



**HAL**  
open science

# Study of the maturation and degradation mechanisms of carbon-based perovskite solar cells

Cynthia Farha

► **To cite this version:**

Cynthia Farha. Study of the maturation and degradation mechanisms of carbon-based perovskite solar cells. Material chemistry. Université Savoie Mont Blanc, 2023. English. NNT : 2023CHAMA009 . tel-04198578

**HAL Id: tel-04198578**

**<https://hal.science/tel-04198578>**

Submitted on 11 Apr 2024

**HAL** is a multi-disciplinary open access archive for the deposit and dissemination of scientific research documents, whether they are published or not. The documents may come from teaching and research institutions in France or abroad, or from public or private research centers.

L'archive ouverte pluridisciplinaire **HAL**, est destinée au dépôt et à la diffusion de documents scientifiques de niveau recherche, publiés ou non, émanant des établissements d'enseignement et de recherche français ou étrangers, des laboratoires publics ou privés.

## THÈSE

Pour obtenir le grade de

### DOCTEUR DE L'UNIVERSITÉ SAVOIE MONT BLANC

Spécialité : **Matériaux, Mécanique, Génie civil, Electrochimie**

Arrêté ministériel : 25 Mai 2016

Présentée par

**Cynthia FARHA**

Thèse dirigée par **Lionel FLANDIN, Professeur, USMB**  
et codirigée par **Emilie PLANES, Maître de conférences, USMB**  
et codirigée par **Lara PERRIN, Maître de conférences, USMB**

préparée au sein du **Laboratoire d'Electrochimie et Physico-chimie des Matériaux et des Interfaces**  
dans l'**École Doctorale I-MEP2 - Ingénierie – Matériaux, Mécanique, Environnement, Energétique, Procédés, Production.**

## Etude des mécanismes de maturation et de dégradation au sein des cellules solaires pérovskites à base carbone

Thèse soutenue publiquement le **07 Mars 2023**

devant le jury composé de :

**Monsieur Lionel FLANDIN**

Professeur, Université Savoie Mont Blanc, Directeur de thèse

**Monsieur Jean-Marc CHENAL**

Professeur, INSA Lyon, Rapporteur

**Monsieur Thanh Tuan BUI**

Maître de conférences, CY Cergy Paris, Rapporteur

**Madame Eliane ESPUCHE**

Professeure, Université Claude Bernard Lyon 1, Examinatrice

**Madame Sylvie NEYERTZ BROWN**

Maître de conférences, Université Savoie Mont Blanc, Examinatrice

**Monsieur David RIASSETTO**

Maître de conférences, Université Grenoble Alpes, Examineur

**Monsieur David MARTINEAU**

Ingénieur, Solaronix, Invité

**Madame Stéphanie NARBEY**

Ingénieure, Solaronix, Invité

**Monsieur Stéphane CROS**

Ingénieur, CEA, Invité

**Madame Emilie PLANES**

Maître de conférences, Université Savoie Mont Blanc, Encadrante invitée

**Madame Lara PERRIN**

Maître de conférences, Université Savoie Mont Blanc, Encadrante invitée



# ACKNOWLEDGMENTS



**To my Uncle Joujo, my funniest best friend, who took the lead to  
heaven just after the completion of this work ...  
I dedicate my thesis to you!**

I thank all who in one way or another contributed in the completion of this thesis. First, I thank God for protection and ability to do this work. Undertaking this PhD has been a truly life-changing experience for me and it would not have been possible to do without the support and guidance that I received from many people.

I would like to first say a very big thank you to my supervisor Lionel Flandin for all the support and encouragement he gave me, during the three years. Without his guidance and constant feedback this PhD would not have been achievable.

Many thanks also to my supervisors Emilie Planes and Lara Perrin for their encouragement and supervisory role and for their valuable input. I greatly appreciate their support received through the collaborative work. They have guided me and encouraged me to carry on through these years and has contributed to this thesis with a major impact.

My deep appreciation goes out to the LEPMI team members that have taken some time to discuss and enrich my work and with whom I shared the daily morning coffee and lunch breaks: Marjorie (our second mom), Nico (I know that I am your favorite PhD student), Gilles (thank you for answering all my silly questions), Johann (I'm sure you have a doctorate in zoology), Christophe, Florence and Julien.

In addition to this, I would like to thank all the doctoral students, post-docs and trainees who were more than colleagues, they were friends with whom I spent precious moments, evenings and unforgettable memories!

Thank you for: Thibault (spending hours answering a yes/no question just to make sure I got it all figured out), Marie (the most beautiful mama), Mylène (I've never tasted cookies better than yours), Félix and Nikoleta (sharing the lab during the day and the dance floor during the night with you was so fun), Noémie (the first to arrive to the lab.. 7:30h, how could you?), Méryll (our representative of PhD students who has no luck in this life), Saman (the calmest guy I have ever met), Fatou (even if we didn't spend too much time in the lab but we clicked right away and you really supported me during the writing), Romain (I know very well that you were waiting for me to leave to take my office, remove my name from the door and turn off the heating, but I forgive you haha!), Saadia (who knows all the series in the world: Turkish, Arabic, French...), Rachel (the funniest! I will never forget our beloved flies, our 'TikTok on the clock' dance and PS: Don't forget your pajamas during your travels) and Ali (with whom I discovered the Savoie with our beautiful road trips and I will never forget your support and my birthday surprises), Abbas (the one who knows and helps all the Lebanese in Savoie), Louai (rawa2, tranquille), Ghinwa (the craziest human being on earth-Em Boninwa), Syreina (the queen of ALD), Joelle (jouja I mar3ousha), Petros (you faced all types of problems in France, especially with Ubers) and Maroun (the only PhD student who had zero struggles during his thesis).

My thanks also go out to the students Thomas, Erica, Lou, Titouan and Célian who were so helpful in numerous ways during their internships.

I want to express my deep gratitude to the closest to my heart: Maroua and Mirella. You have always been by my side and given me a hand to deal with the hard times. You have always gone off your way to make me feel better. I have shared moments of deep anxiety but also of big excitement with you my gorgeous girls (Ento Laaaarge!)

I count myself very lucky to have met the Tunisian community: Maroua thank you once again and it is thanks to you that I learned how to speak Tunisian. Ghaith thank you for asking me all the time how could you cheer me up and help me (Since I have finished let's have some drinks at meltdown!). Hatem, you have always been able to turn my tears into laughs, thank you for your encouragement and for always listening to me and supporting me, you have been my unpaid therapist (K, Yellow, 3, 6, chapati).

Very special words of gratitude to my friends who have always been a major source of support when things would get a bit discouraging: Marleine, Georges and Elia. Maro thank you deeply for always being there for me from the very beginning till now, I am so lucky to have you in my life. Jouj, we started our adventure together in France in 2018 and here we are both doctors with the same defense date! I am so thankful having you both in my life, you are supportive in a way that warms the heart.

I would like to acknowledge how grateful I am for having my childhood friends: Ghiwa, Leila, Carine and Sahar, in my life who are always ready to listen to my rants about research with a smile on their face. It's going to seem a little weird but thank you Covid because it's thanks to you I spent the funniest nights of my life with these girls during the lock down (Nare Nare!)

I owe a huge debt of gratitude to Léa and Elissa, my two best friends (PPG). I am truly grateful for our friendship, you are always by my side no matter what.

Finally, but definitely not the least, a heartfelt thank you goes to my parents, Abou and Em Khalil, who have been great over the years. You are always showing how proud you are of me. I am so appreciative of your constant love and understanding. You always encourage me to follow my dreams. Thank you for believing in me more than I believe in myself. You have been by my side throughout this PhD, living every single minute of it, and without whom, I would not have had the courage to embark on this journey in the first place. And of course a special thank you for my grandma Tata Bahjat and my uncle Père Makhoul. Your prayers have given me hope when I needed it most, I really do appreciate it.

I express my gratitude to my brothers Khalil and Hicham and their wives Alexandra and Nadine. Without your help during this challenging period, I couldn't have finished my thesis so smoothly. Your permanent love and confidence in me have encouraged me to go ahead in my study and career.

Thank you my lovely family for encouraging me to make crazy life decisions, such as coming to France for college, all by myself, and then embarking on a roller-coaster journey: the Ph.D. These decisions left me wiser and more grateful than ever before.

The last word goes for Kai, my nephew, my cutest baby boy, who is the light of our lives and who has given me extra strength and motivation to get things done. This thesis is also dedicated to you Kaio.

## Table of contents

<b>GENERAL INTRODUCTION</b> .....	7
<b>CHAPTER I: STATE OF THE ART</b> .....	11
1. Introduction.....	12
2. Photovoltaic effect .....	13
3. Three generations of PV technology .....	13
4. Generality on Perovskite materials .....	15
4.1. History .....	16
4.2. Crystallography.....	16
4.3. Properties .....	17
5. Perovskite PV solar cells .....	18
5.1. Conventional PV devices architecture.....	18
5.2. Carbon-based perovskite solar cells.....	20
5.3. Transport layers.....	22
5.4. Simple perovskites.....	24
5.5. Mixed perovskites .....	26
5.6. Additives for perovskite .....	27
6. Perovskite deposition techniques .....	31
6.1. Spin-coating deposition method (One-step or Two-steps).....	32
6.2. Thermal/Vacuum evaporation .....	33
6.3. Doctor blade coating .....	34
6.4. Slot die coating .....	34
6.5. Spray coating .....	35
6.6. Drop casting.....	36
6.7. Inkjet printing .....	36
7. Post treatments leading to a maturation phenomenon .....	38
8. Encapsulation systems .....	40
9. Durability qualification testing and accelerated aging tests .....	44
10. Conclusion .....	47
<b>CHAPTER II: EXPERIMENTAL PART</b> .....	49
1. Studied materials: perovskite solar devices fabrication .....	50
1.1. Devices architecture preparation.....	50
1.2. Perovskite filling (precursors formulation, infiltration processes and annealing) .....	50
1.3. Post-treatment: maturation step .....	51
1.4. Encapsulation systems .....	51



2.	Aging campaigns conditions .....	52
3.	Characterization methods .....	52
3.1.	Photocurrent density-voltage measurements (J-V) .....	53
3.2.	Impedance spectroscopy.....	56
3.3.	Light Beam Induced Current (LBIC) .....	57
3.4.	UV-visible spectroscopy (absorbance and diffuse reflectance) .....	57
3.5.	Photoluminescence spectroscopy (PL).....	59
3.6.	Photoluminescence imaging (PL imaging).....	60
3.7.	X-ray diffraction analysis (XRD) .....	61
3.8.	Scanning Electron Microscopy (SEM) and Energy Dispersive X-Ray Analysis (EDX).....	62
3.8.	Raman spectroscopy .....	63
3.9.	Profilometry.....	63
3.10.	Fourier-transform infrared spectroscopy (FTIR) .....	64
<b>CHAPTER III: OPTIMIZATION OF THE ENCAPSULATION SYSTEMS FOR CARBON-BASED PEROVSKITE SOLAR CELLS .....</b>		<b>65</b>
	Introduction.....	66
	Results & Discussion.....	71
	Conclusion .....	93
<b>CHAPTER IV: UNDERSTANDING OF THE MATURATION MECHANISM OBSERVED FOR CARBON-BASED PEROVSKITE SOLAR CELLS.....</b>		<b>95</b>
	Introduction.....	96
	Results and discussion.....	99
	Conclusion .....	114
	Supplementary information .....	116
<b>CHAPTER V: EFFECT OF THE PROCESSING AND OF MATURATION ON THE STABILITY OF CARBON-BASED PEROVSKITE SOLAR CELL UNDER DAMP HEAT CONDITIONS .....</b>		<b>117</b>
	Introduction.....	118
	Results and discussion.....	119
	Conclusion .....	132
	Supplementary information .....	134
<b>GENERAL CONCLUSION AND PERSPECTIVES.....</b>		<b>137</b>
	General conclusion .....	138
	Perspectives.....	140
<b>REFERENCES .....</b>		<b>141</b>

# GENERAL INTRODUCTION

Carbon-based perovskite solar cells have recently shown a huge potential to achieve high efficiency succeeding up to 25.7% certified power conversion efficiencies (PCEs)[1]. Organic–inorganic hybrid halide perovskites belong to an interesting group of semiconductor materials for optoelectronic applications, with important properties such as tunable band structure, low exciton binding energy, high absorption coefficient, high electron and hole mobilities and long carrier diffusion length. This generation of PV technology has emerged the field as a third generation after noticing the high energy production cost of the first generation based on silicon semiconductors and the high toxicity, low abundance or high cost of elements for the second generation most efficient systems (CIS, CIGS, CdTe, GaAs). Therefore, over the past 20 years, semiconductors with electrical performances compatible to high efficiencies at affordable costs have been developed involving organic/polymer PV, dye-sensitized Solar cells, quantum dot sensitized solar cells and hybrid perovskite solar cells. The latter found out a huge success and has produced some of the most rapid growth in cell performance due to their high efficiency, low cost raw materials and the easiness of their manufacturing methods which give them a great potential for industrialization. Nonetheless, despite all the advantages, the biggest challenge for C-PSC is their lack of long term stability caused by main four factors: heat, humidity, UV light and moisture[2].

In this work, HTM-free solar cells substituting the HTM with hydrophobic carbon electrodes have been developed due to promising characteristics like elimination of costly HTM, high stability of the elements selected for device architecture, clean process for perovskite implementation and processability in ambient conditions. This study was conducted in collaboration with the swiss company ‘Solaronix’. Solaronix develops since 1996 devices for the third generation of PV technology aiming to afford innovative solar energy solutions. Replacing the liquid electrolytes in their DSSC with perovskite, Solaronix began working on solid-state hybrid perovskite as early as 2013 with an architecture derived from Grätzel DSSC monolithic cells. The company is considered one of the key players operating in the global Perovskite Solar cells market since they participated in adopting many approaches to improve the efficiency and the stability of the solar cells increasing their lifetime to stay ahead of the competition and expand market footprint[3]. Therefore, all the studied systems in this manuscript are furnished by Solaronix. These solar cells consist of a triple layered mesoporous stack ( $\text{TiO}_2/\text{ZrO}_2/\text{C}$ ) deposited on a glass substrate already containing a FTO (fluorine doped tin oxide) transparent conductive oxide electrode and a thin  $\text{TiO}_2$  compact layer acting as electron transport layer. The common  $\text{MAPbI}_3$  perovskite precursors’ solution is added as a final step. In this work, the 5-ammonium valeric acid iodide additive was used to help the formation of the PK crystals in the mesoporous scaffold. This generates preferential growth in the normal direction and therefore enhance the PCE of the device. In the developed work, two infiltration methods have been compared. The first one consists in a one drop automatized simple injection of the precursors by drop casting in the center of the solar cell[4] and the second one use inkjet printing which consist in automatic managed printing steps of precursor small droplets all over the solar cell’s surface area [5][6]. Whatever the infiltration

method is, adding the PK at the end of the cell fabrication, helps to have very little contact with moisture and oxygen, which certainly explains the greater stability of these devices. Contrary to other main developed planar architectures, this technology allows also eliminate the need for glove boxes in manufacturing, which will facilitate their industrial development. After the addition of all layers, our cells were submitted to a post-treatment called “maturation”, during which they are exposed to 75% of relative humidity at 40°C for a period of time between 100 and 150 hours in an environmental chamber to enhance the cell’s performance [7]. Finally, they are encapsulated between two glass covers thanks to a polymer-based sealing agent.

The solar cells studied here have many advantages, such as the innovative perovskite deposition technique and a process without glove box but are not yet enough developed industrially for commercialization at large scale, like many 3rd generation solar cells. In this thesis work, we have tried to answer in part to questions hindering the development of large-area modules, like stability, performance and process.

After studying the state of art of the photovoltaic devices with a focus on perovskite in the first chapter and explaining the protocols used for solar cell fabrication together with the different characterization techniques used in the second chapter, we have proposed to study different encapsulation systems in the third chapter to first partially address the problem of stability. The perovskite photoactive material in developed cells are often unstable in the presence of moisture, oxygen and temperature. It is therefore necessary to encapsulate these cells to protect them from external agents when operating. Glass covers are usually used with a polymer-based sealing agent. In this chapter, to evaluate the performance of different sealing agents, encapsulated perovskite solar cells have been submitted to damp heat conditions. By monitoring the performance during the ageing campaign and certain functional properties of the full device and of the perovskite layer, the mechanisms of degradation of each cell have been elucidated and the best encapsulation system has been determined.

The fourth chapter concerns the study of the post-treatment procedure. This stage of maturation is little studied in the literature. Thus, the objective of this part is to discern the mechanisms behind this process. For this, the two types of solar cells (pipetting and inkjet) have been studied before and after the maturation step. Thanks to a deepened analysis of the microstructure of the perovskite layer and its functional properties, this maturation mechanism has been understood and seems to be different according to the perovskite deposition method.

The fifth chapter aims to further investigate the cells’ stability and that by launching different aging campaigns at damp heat (85/85) conditions. The studied systems were pipetted and inkjet cells with and without maturation. The performance of about 5 cells from each batch was monitored at regular time intervals. Thanks to the correlation of these various results, a

rather thorough and comparative study of the various devices concerning their performance and their degradation mechanisms will be proposed.

Finally, the last part of this manuscript is devoted for a general conclusion that sums up all that has been mentioned in the previous chapters followed by the perspectives.

# CHAPTER I: STATE OF THE ART

## 1. Introduction

Around the planet, all the developing and developed economies concentrate on renewable energy sources such as solar, wind, and biomass to satisfy human social and economic growth[8][9][10] Renewable energy sources can be represented as the energy obtained from the continuous, frequent and enduring sources of energy in the natural environment or as the energy flows which are renewed at the same rate as they are used[11]. For many years, population and economic growth have generated an increase in global energy demand. To reduce the resulting increase in carbon emissions, renewable energies are attracting an increasing interest, especially for the production of electricity. Solar energy is one of these sources that promises a bright future[12] since it is one of the most important eco-friendly energy sources for many reasons like: abundant, free, pollution-free, and distributed all over the earth given that the sun emits this energy at the rate of  $3.8 \times 10^{23}$  kW, out of which approximately  $1.8 \times 10^{14}$  kW is intercepted by the earth[13][14][15]. Several researches have reported that solar photovoltaic (PV) panels (concentrated or not), and solar heaters have got the highest annual growth rate compared to other renewable energy sources[16], and PV will become the most alternative renewable energy source until 2040[17].

The revolution of PV technology has then started with three generations of PV devices. Our work will be mainly focused on one case of the third generation: Perovskite solar cells. In this chapter, we will rapidly present the different generations highlighting their advantages and disadvantages. Then, the importance of perovskite solar cells these days will be explained: going back to the history behind perovskite materials how they evolved and what are their properties making them so unique in the PV industry.

In the state of art section, we will also present the different layers constituting a perovskite solar cell and point out the influence of each material and its role, without forgetting the essential work of encapsulation. Despite the large variety of architectures, we adopted in this thesis the carbon-mesoporous based perovskite solar cell (C-PSC) one, which present a great interest for industrial developments. As this architecture implies specific methods concerning the implementation of the perovskite layer, the different perovskite deposition methods existing in literature will be also presented together with their advantages and drawbacks. Moreover, we reviewed the potential post-treatments processes existing to enhance the solar cell's performance (maturation). And, finally, the different stresses tests that can be conducted to evaluate the device's stability will be presented.

All these parts were discussed here, since this thesis aims to answer to many questions still not solved in literature, i.e.: What are the mechanisms occurring in the PK layer when the deposition technique is changed? What are the phenomena taking place in 'maturation' post-treatments? What is the impact of different types of encapsulation on the devices lifetime?

How will the solar cell reacts when exposed to extreme conditions such as damp-heat? All the answers will be investigated in detail in this thesis work.

## 2. Photovoltaic effect

The photovoltaic solar energy is when a device containing one or several semiconductor(s) absorbs photons and is able to transform this energy in an electron at its excited state. Then, phenomena of charge separation and conduction within the device conduct to generate electric current in an external circuit. This was discovered by the French physicist Alexandre-Edmund Becquerel in 1839[18]. He noticed that 'electrical currents coming from certain light induced chemical reactions'[18] by exposing a p-n junction to the sun light, as the basic structure of a solar cell, and noticing the electrons and holes drifting to the 'n' and 'p' type region, respectively, while electron-hole pairs were created by absorbing the photon, leading to the creation of a photocurrent from 'n' to 'p' by connecting both sides of the junction together[19]. It was not until 1954 that three American researchers, Chapin, Pearson and Prince developed a photovoltaic cell to identify the possibility of supplying electricity. In 1958, a cell with an efficiency of 9% was developed and at the same time the first satellites with solar panels were sent into space[20].

Therefore, the revolution of PV cell technologies has started. The multijunction structure have been used for the first time by Wolf in 1960[21]. In this device, the power conversion efficiency was increased thanks to the different layers allowing a better absorption of the light on the wider range of wavelengths. In 1981, Guha et al. noticed that the hydrogen dilution in an amorphous silicon create a protocrystalline silicon, more stable than the standard amorphous silicon [22]. In 1972, cadmium based solar cells become promising due to their low cost and with a 5-6% of efficiency[23], followed by  $\text{CuInSe}_2$  (CIS) in 1974[24] which are well-known for their high absorption efficiency.

The progress of such technology depends on materials and structure development. However, the main goal will always be reaching maximum power at minimum cost. In any architecture, solar cells, which are connected in series and in parallel in order to form the desired voltage and current levels, remain the basic semiconductor components of a PV panel[11].

## 3. Three generations of PV technology

Silicon is a very abundant element on earth and is considered a semiconductor material applicable to PV applications with a 1.1eV band gap value [25]. Bell Laboratories developed the first silicon-based solar cell with 4-5% efficiency in 1953 and 6% in 1954[26]. Crystalline silicon PV cells have the longest production history exceeding 60 years of development and constitute the largest part of PV production[27]. Depending on how the Si wafers are manufactured, different types of silicon can be obtained: monocrystalline (c-Si),



polycrystalline (Poly c-Si) and amorphous. All 3 are used in the field of PV: even if the monocrystalline Si is the purest and the most efficient of the three types, polycrystalline and amorphous Si are used because of their lower cost and reasonable efficiency[28].

Second-generation solar cells were then developed, they are also known as thin-layer solar cells, because the thickness of the active material is kept low (1-4  $\mu\text{m}$ ) compared to crystalline silicon-based devices ( $\sim 100\text{-}500\ \mu\text{m}$ )[29]. This generation uses various materials such as amorphous silicon (a-Si), cadmium indium selenium (CIS) and copper-indium-gallium-selenium (CIGS) as light-absorbing materials[27]. The latter offers lower manufacturing costs than c-Si wafer-based solar cells due to material savings. Unfortunately, this generation has some drawbacks like the cost of some materials is increasing (In), or the used material is highly toxic (Cd), and the efficiencies are lower compared with silicon based solar cells[30]. However, in 2019, Solar Frontier company achieves 23.35% of power conversion efficiency as a world record in thin film solar cell technology, on a 1  $\text{cm}^2$  cell using Cd-free CIS technology[31].

Due to high costs of the first and second generation, together with toxicity on non-abundance of used materials of the second generation, a third generation has emerged. Nanoscience et nanotechnology contributed to sustainable energy systems using nano-structured semiconductors with enhanced electrical performances leading to high power conversion efficiencies at lower costs[32]. This generation involves organic PV (OPVs), Dye-sensitized solar cell (DSSC), quantum dot-sensitized solar cell (QDSSC) and hybrid perovskite solar cells (PSCs)[33].

Dye-sensitized solar cells, also known as Grätzel cells named after the developer, discovered in 1991 with a power conversion efficiency of 7.9%[34]. These devices are based on the photoexcitation of dye molecules on the surface of metal-oxide nanostructured semiconductors (usually  $\text{TiO}_2$  used as a paint base in pigment industry) as photoanode[32]. DSSCs found a big success due to many advantages: high efficiency, low cost, simple manufacturing methods, insensitive to environment contaminants and it could be used in darker conditions like in a cloudy weather or in dusk and dawn [35]. These features can be prepared with roll-to-roll technique, which is a continuous low-cost manufacturing method to print the DSSCs on flexible substrates [36]. A tremendous increase in the number of publications was noticed and a considerable amount of work has been made in order to improve this technology leading to 13% of efficiency in 2014[37]. The cell performance relies on many factors as the surface morphology, the thickness if the  $\text{TiO}_2$  layer, the particle size and the nature of the dye. Unfortunately, since high efficiencies have been reached using liquid electrolytes, the latter causes short term stability due to the evaporation of the organic solvent and limited solubility of inorganic salts[27].

Organic semiconductors polymers were in the same time introduced into the PV industry with Tang in 1986 [38]and gain in interest in the year 2000. It seems a promising technology

because material used are flexible, highly abundant and cheaper compared to the inorganic alternatives[39]. These organic photovoltaic materials can be fabricated via low-cost manufacturing techniques in solution[40]. Nonetheless, the power conversion efficiency of this technology is much lower than silicon, which limits unfortunately their commercial growth[41]. However, efficiency of about 18% were reachable using simultaneously complex device architectures and complex organic photoactive materials, which is thus non-industrially viable[1].

In parallel with these devices, quantum dot-Sensitized Solar cells (QDSSC) have been developed, which are based on nano-crystals and nano-porous materials[42]. These materials can double the electricity obtained from other solar cells devices since they can convert more than 65% of the solar spectrum[43]. QDSSCs are characterized with their tunable band gap from the infrared to the ultraviolet region by the control of QD composition and size[44], high optical absorption coefficient and good photochemical stability over dyes[45]. Cadmium chalcogenide QDs like CdS[46], CdSe[47] and CdTe[48] are the most known used sensitizer due to their high stability.

One of the most exciting developments of the third generation of photovoltaics concerns organic and inorganic hybrid lead halide perovskites due to their high efficiency, low-cost raw materials and the simplicity of their manufacturing methods. In 2009, Kojima et al.[49] developed the first perovskite solar cell with 3.8% PCE where hybrid perovskites were used as alternative sensitizer to dye molecules in the DSSC configuration based on liquid electrolyte. Three years later, Park et al. reached 6.5% by increasing the load capacity of perovskite and optimizing the TiO<sub>2</sub> area [50]. Later in 2012, Kim et al. reported the first solid perovskite solar cell (PSC) with 9.7% PCE and long term stability of 500h in ambient atmosphere[51]. Lee et al. replaced TiO<sub>2</sub> with SnO<sub>2</sub> and reduce voltage losses achieving 10.9% efficiency under one sun[52]. Heo et al. reached then 12% of PCE in 2013 using a 3D mesoporous TiO<sub>2</sub> layer filled with MAPbI<sub>3</sub> and a polymeric hole transport layer[53]. The two-step sequential deposition technique where the PbI<sub>2</sub> was firstly deposited followed by the CH<sub>3</sub>NH<sub>3</sub>I was adopted by Burschka et al. where they obtained 15% of efficiency due to the creation of dense and uniform perovskite layer[54]. Subsequently the research enthusiasm in the perovskite field was fueled and the highest efficiency of PSC has reached 25.2% by KRICT (South Korea) where they use NiO<sub>2</sub> as a hole conductor that can withstand high temperature up to 70°C[55]. Despite all the advantages of these devices, poor long-term stability and short lifetime cause hindrances in their path of commercialization. The later perovskite technology will be developed after in a more detailed way as this thesis aims to specifically study the mechanisms of maturation and degradation within carbon based perovskite solar cells.

#### 4. Generality on Perovskite materials

#### 4.1. History

Discovered in 1839 by Gustav Rose in the Ural Mountains in the initial form of the mineral  $\text{CaTiO}_3$  and then named after the Russian mineralogist L. A. Perovski, perovskites are now a wide family of natural and synthetic oxides. The general formula is  $\text{ABX}_3$  with A and B two cations of different sizes (A larger than B) and X is the anion[56]. The most known natural perovskites were  $\text{CaTiO}_3$  and  $\text{BaTiO}_3$  3D structures. Afterwards, in 1893, elements like  $\text{Cs}^+$ ,  $\text{K}^+$  and  $\text{Pb}^{2+}$  were used as cations and  $\text{I}^-$ ,  $\text{Br}^-$  and  $\text{Cl}^-$  as anions in synthetic perovskites. In 1978, Weber discovered the possibility of using the methyl ammonium ( $\text{CH}_3\text{NH}_3^+$ ) as cation[57], which will lead to the hybrid perovskite today used in PV. In 2009,  $\text{MAPbI}_3$  and  $\text{MAPbBr}_3$  ( $\text{MA}=\text{CH}_3\text{NH}_3$ ) perovskite for first used as liquid sensitizers in the DSSC PV technology[55].  $\text{CH}_3\text{NH}_3\text{PbI}_3$  is an ambipolar semiconductor where it can be n or p type, and has intense light absorption. Moreover, due to its charge carriers long diffusion lengths and lifetimes, such perovskite solar cells can reach high PCE[58].

#### 4.2. Crystallography

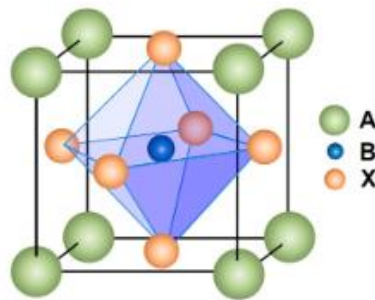


Figure 1 :  $\text{ABX}_3$  perovskite 3D structure[59]

The crystal lattice with the highest symmetry for perovskite is the cubic one. However, the cubic lattice can be distorted depending on the chemical nature of the ions. The size of the ions has a main role in this distortion and therefore the stability of the crystalline structure. Thanks to the Goldschmidt[60] tolerance factor ( $t$ ), perovskite formation can be estimated given that[59]:

$$t = \frac{R_a + R_x}{\sqrt{2} \times (R_b + R_x)}$$

A 't' value between 0.89 and 1 favors the cubic structure. If 't' is lower than 0.89, then a less symmetric orthorhombic or tetragonal structure is obtained[56]. More than one structure can be found for a perovskite depending on the temperature and preparation methods[61]. Goldschmidt factor is insufficient to define the perovskite structure, but an octahedral factor  $\mu$ [62] where the perovskite is stabilized for  $0.44 < \mu < 0.85$  [62] with:

$$\mu = \frac{R_b}{R_x}$$

Considering the most studied perovskite for PV ( $\text{CH}_3\text{NH}_3\text{PbI}_3$ ) and according to the calculation of the tolerance factor (with  $R_a(\text{CH}_3\text{NH}_3^+) = 0.18 \text{ nm}$ ,  $R_b(\text{Pb}^{2+}) = 0.119 \text{ nm}$ ,  $R_x(\text{I}^-) = 0.22 \text{ nm}$  [56],  $t = 0.836$ , this perovskite must be either tetragonal or orthorhombic.

As mentioned previously, the temperature is a main factor on which the structure depends. Table 1 presents that, at room temperature,  $\text{CH}_3\text{NH}_3\text{PbI}_3$  perovskite has a tetragonal structure [63].

Table 1: Temperature dependent structural data of  $\text{CH}_3\text{NH}_3\text{PbI}_3$  [63]

Phase	Temperature (K)	Crystal system	Space group	Lattice (pm)	Volume ( $10^6 \text{ pm}^3$ )	
$\text{CH}_3\text{NH}_3^+ \text{PbI}_3^-$				$c = 1184.9(2)$		
	$\alpha$	> 327.4	cubic	$Pm\bar{3}m$	$a = 632.85(4)$	253.5
	$\beta$	162.2–327.4	tetragonal	$I4/mcm$	$a = 885.5(6)$ $c = 1265.9(8)$	992.6
	$\gamma$	< 162.2	orthorhombic	$Pna2_1$	$a = 886.1(2)$ $b = 858.1(2)$ $c = 1262.0(3)$	959.5

#### 4.3. Properties

The greatest advantage of hybrid perovskite materials is the properties combination of organic and inorganic semiconductors. Organic semiconductors have simple manufacturing methods, versatile for several applications but suffer from low performance. Inorganic semiconductors are highly performing with their important optoelectrical properties leading to stable device despite their high costing fabrication techniques. Therefore, hybrid perovskites offer low-cost and more stable performing solar cells [64]. Moreover, these materials are characterized by their long charge carrier lifetime and diffusion length, the facility of deposition and strong light absorption [65][66]. High optical extinction coefficient of perovskite provides a good light absorption at low film thicknesses. In addition, thanks to their low exciton binding energy, the dissociation into free carriers can be done at room temperature. Also, the intrinsic ferroelectricity property helps to improve the charge separation [67]. The most common used perovskite is the methylammonium lead iodide ( $\text{MAPbI}_3$ ). It has a direct-like bandgap between 1.5 and 1.6 eV [68][69][51]. This value depends on the metal-halogen bond, which can be helpful since the bandgap can be varied depending on the selected halogen [70]. The properties of perovskite materials with PV application are presented in Table 2 [55].

Table 2: Properties of perovskite materials with PV application[55]

Properties	Value Range
Bandgap	1.5–2.5 eV
Absorption coefficient	$10^5 \text{ cm}^{-1}$
Exciton binding energy	Less than 10 meV
Crystallization energy barrier	$56.6\text{--}97.3 \text{ kJ mol}^{-1}$
PL quantum efficiency	70%
Charge carrier lifetime	Greater than 300 ns
Relative permittivity	3
Carrier mobility	$800 \text{ cm}^2/\text{Vs}$
Exciton	Wannier type
Trap-state density	$10^{10} \text{ cm}^{-3}$ (single crystals), $10^{15}\text{--}10^{17} \text{ cm}^{-3}$ (polycrystalline)

## 5. Perovskite PV solar cells

A PV system consists of three functioning steps: absorption of photons followed by free charge generation, charge transport and charge extraction. Generally, perovskite solar cells are constituted with a perovskite layer sandwiched between an electron transport layer (ETL) and a hole transport layer (HTL). When the solar cell receives the light, the latter is absorbed by the perovskite and excitons are generated and subsequently holes and electrons forming the charge carriers are produced upon excitons dissociation. This exciton dissociation takes place at the interfaces between the perovskite layer and the charge transporting layer. The electron-hole separation led to injecting the electrons into the ETL. These electrons migrate to the anode which is generally the fluorine doped tin oxide glass (FTO). The generated holes are injected into the HTL and migrate to the cathode. Since the electrons and holes are now collected by the electrodes, an electric current is produced[71].

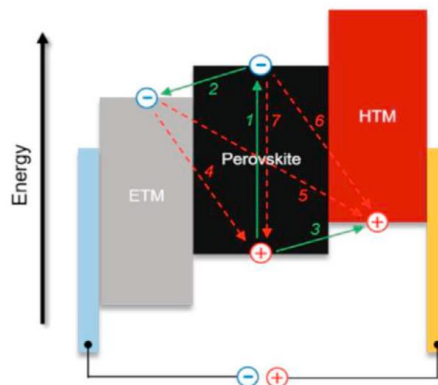


Figure 2: schematic representation of energy levels and charge transfer processes in a perovskite solar cell[72]

### 5.1. Conventional PV devices architecture

Recently, several structures of Perovskite solar cells have evolved. The typical solar cell structures can be divided into two categories: standard (NIP) and inverted (PIN) structures. This depends on which transport material layer (electron or hole) is receiving firstly the incident light. Moreover, these two structures can be also divided into two categories: mesoscopic and planar structures. Mesoscopic consists of a mesoporous layer whereas for the planar structure, only planar layers exist as presented in Figure 3.

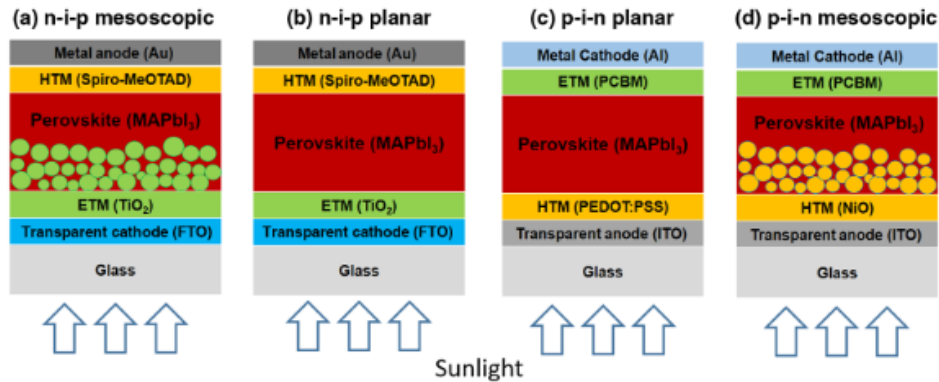


Figure 3: Schematic diagrams of perovskite solar cells in the (a) NIP mesoscopic, (b) NIP planar, (c) PIN planar, and (d) PIN mesoscopic structures[73]

NIP mesoscopic structure was the first architecture used and was adapted from DSSC in 2009[49]. It consists of a glass cathode, ETL, mesoporous metal oxide containing the perovskite, HTL and then the metallic anode. The mesoscopic layer is usually thick but less than 300 nm to have a good crystallinity since above this thickness the grain growth is confined by the pores of the structure leading to disordered and amorphous phases[73]. To enhance the efficiency of the solar cell by avoiding non-radiative recombination, a compact blocking layer is added on the FTO/Glass [74]. One of the most usually used is the mesoporous TiO<sub>2</sub> and this by adding it on a TiO<sub>2</sub> compact layer. Generally the compact and the mesoporous TiO<sub>2</sub> should be heated at 450°C to obtain an anatase phase[75]. The addition of the mesoporous layer offers a lower contact resistance for forward electron transfer for the PK enlarging the interface area between the perovskite layer and the TiO<sub>2</sub> and showing a significant reduction in the severity hysteresis previously present due to the low conductivity in intrinsic TiO<sub>2</sub> in a planar PSC.

The planar architecture is an evolution of the mesoscopic structure and is also a copy of what is traditionally used in OPV[76]. The perovskite layer is placed between the ETL and the HTL without the mesoporous metal oxide layer, inducing to a simpler architecture. Generally, perovskite solar cells in NIP structure are more efficient than those in PIN[77] but both structures allowed high efficiencies in PV devices exceeding 20% whether in a planar[78] or mesoscopic[79][80] architecture. However, this is often achieved with complicated multi-components and multi-layered architectures.

## 5.2. Carbon-based perovskite solar cells

The high costs of noble metals such as gold and silver as back electrodes and HTL materials block the commercialization of the perovskite solar cells and limit their large-scale application. Moreover, gold and silver require to be deposited by vacuum evaporation, which is a highly energy-consuming method. Their main disadvantage is that they can decrease the solar cell performance due to formation of silver and gold halides after the migration of halogen atoms from the perovskite layer[81][71]. Therefore, to reduce the fabrication costs and at the same time improve the durability of devices, carbon-based perovskite solar cells (C-PSC) have been developed based on cheap and stable carbon electrode. This architecture could be either HTL-free or not. Graphite/amorphous carbon, graphene and carbon nanotubes are the most common used as carbon-based materials in the perovskite solar cell field. They are characterized by their low cost, high conductivity, and work function(5 eV)[82] close to that of the gold(5.1 eV)[83]. In addition, the instability issues have been solved due to the hydrophobic nature of carbon preventing the moisture ingress into the solar cell, and reducing the complexity of the device fabrication.

In the C-PSC, generally no HTL is required, because carbon electrodes can extract photo-generated holes by themselves which makes it possible to manufacture an HTL-free perovskite solar cell [74]. Mei et al. from Grätzel center reported in 2014 a C-PSC HTL-free yielding a stable PCE of 12.8% exceeding 1000h under ambient temperature and full sunlight without encapsulation[5]. In 2017, Grancini et al. from Grätzel center in collaboration with the Swiss Company Solaronix demonstrated with similar devices 10 000 h stability without PCE loss under 1 sun stress. Whereas, with a gold electrode and Spiro-OMeTAD as HTL, the PCE decreases of more than 25% only after 300 h of illumination[6]. Since the absence of HTL in C-PSC may cause excessive surface recombination at the counter electrode, Xu et al. proposed to add NiO<sub>x</sub> as HTL to the C-PSC and were able to reach 14.9% PCE[84]. Then, Ye et al. demonstrated a C-PSC with CuPc as HTL giving 18% of PCE[85].

Carbon electrodes can be prepared in two ways: high and low temperature (see Figure 4). The high temperature process consists of first depositing the carbon layer by screen printing or doctor blading on a stack without perovskite, then performing a high temperature pyrolysis between 400 and 500°C, to break down all organic and solvent binders and eventually infiltrate the perovskite layer through the mesoporous carbon electrode obtained. For the low temperature process, perovskite can be deposited before electrode deposition since the carbon electrode layer is deposited by doctor blading and annealed at a temperature below the degradation of perovskite[74]. The composition of the carbon pastes used to make the carbon electrodes is therefore different depending on the type of process used.

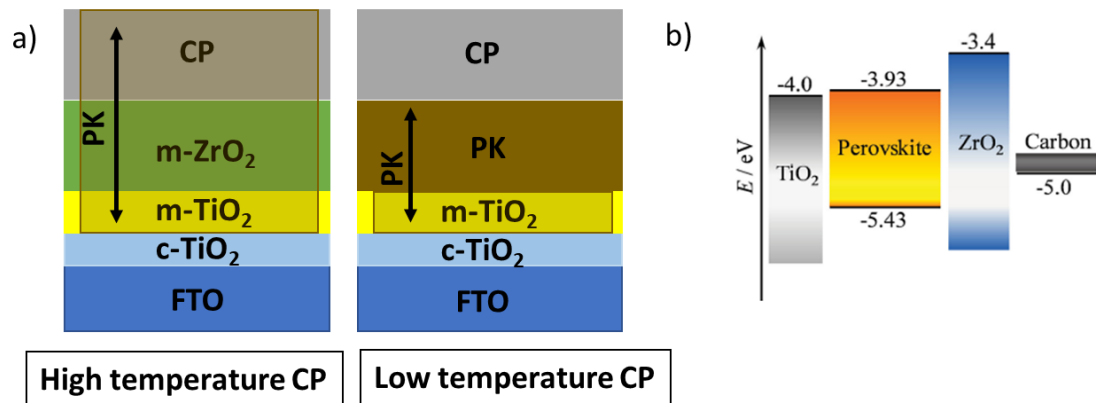


Figure 4: a) Schematics of perovskite solar cells with high- and low-temperature carbon-based electrodes ;b) energy level diagram of mesoscopic carbon-based perovskite solar cell[86]

In this manuscript, the first method is used. A typical high temperature carbon-based perovskite solar cell consists a front FTO/glass substrate, a mesoporous ETL, an insulating intermediate layer and then the mesoporous carbon electrode[87]. In this architecture, an insulating layer is crucial between ETL and carbon layer to prevent the contact between the front and back electrode thus avoiding Ohmic shunts and a photocurrent leakage[81]. The most commonly insulating mesoporous material used are ZrO<sub>2</sub>[88] or Al<sub>2</sub>O<sub>3</sub>[89]. ZrO<sub>2</sub> has larger pores than Al<sub>2</sub>O<sub>3</sub> which facilitate the infiltration of the perovskite and its contact with the anode and thus makes a better spacer material in the C-PSC and more efficient[89]. Liu et al.[88] and Barichello et al.[90] highlighted the importance of the thickness of this layer. They optimized the ZrO<sub>2</sub> thickness at 1  $\mu\text{m}$  and reported that under this value, most of the generated photoelectrons recombined with holes leading to an energy loss. Additionally, over 1  $\mu\text{m}$  it risks to surpass the limit of carrier diffusion length. As the perovskite is added as a final step for completing the solar cell. The latter can be deposited using different techniques that will be discussed later in this manuscript. The main advantage of this manufacturing method is that it is possible to perform all the steps in open air without degrading perovskite, since it is infiltrated in the mesoporous scaffold at the end of all the fabrication steps, potentially just before the encapsulation stage.

In 2013, Ku et al. reported the first HTL-free C-PSC with high stability and a PCE of 6.64%[82]. The perovskite was here deposited by drop casting on the top of the m-TiO<sub>2</sub>/m-ZrO<sub>2</sub>/m-carbon architecture. Mei et al. fabricated in 2014 a solar cell with enhanced 12.8% performance using MAPbI<sub>3</sub> perovskite 5-ammonium valeric acid iodide (5-AVAI) additive[5]. In 2016, Hashmi et al. studied a carbon based perovskite solar cell with a 5-AVAI doped perovskite deposited by inkjet printing and obtained 7.65% in terms of efficiency[4]. In 2017, Grancini et al. reported a one year-equivalent stable perovskite solar cell yielding a PCE of 12.9% in a carbon based perovskite HTL-free device also with the use of 5-AVAI additive. Moreover, when these devices are fabricated with larger modules (10 x 10 cm<sup>2</sup>), a close 11.2% PCE value was obtained [6]. During the same year, Hashmi et al. discussed a new post-treatment to enhance the devices



performances. The PCE increased from 9% to 13.1% by exposing them to 75% of R.H and 40°C for 200 hours. The studied cells were carbon based using  $\text{MAPbI}_3$  doped with 5-AVAI and drop casting method. When exposed to illumination at 40°C, the cells retained 92% of their initial efficiency after 350 hours[7]. In 2019, Zimmermann et al. reported a C-PSC with perovskite doped with both 5%mol 5-AVAI and 4%mol  $\text{CuSCN}$ , the later to improve the hysteresis. The power conversion efficiency reaches 15%, and a good stability under 1 sun was obtained with less than 10% PCE loss after 1000h[91]. In 2020, Verma et al. reported a C-PSC when all  $\text{m-TiO}_2$ ,  $\text{m-ZrO}_2$  and the PK precursor solution were deposited by inkjet, demonstrated a 9.1% of PCE for a device area larger than  $1 \text{ cm}^2$  [92]. In 2020, Tsuji et al. reported that the graphite material is essential to achieve high-quality penetration of the PK precursor by comparing two graphite types and demonstrating that PSC based on pyrolytic graphite has higher efficiency than that based on amorphous graphite[93]. In 2021, Kobayashi et al. developed encapsulated mesoporous-carbon perovskite solar mini-modules and reported the high stability of these devices under damp heat conditions (85°C/85%R.H.). More than 92% of PCE was retained after 300hours of accelerated ageing, equivalent to 20-year stability in outdoor use. They also demonstrated a light-induced performance increase phenomenon[94]. In 2023, Bogachuk et al. demonstrated that adding by inkjet printing a sacrificial film of polystyrene nanoparticles between  $\text{TiO}_2$  and  $\text{ZrO}_2$  allowed to obtain larger PK crystals and therefore enhanced efficiency by suppressing non radiative recombinations and thus improving the Voc and consequently the PCE (15.7%) of the device[95]. In 2021, Ye et al. introduced perfluorotetradecanoic acid in the perovskite and reached the highest PCE (18.9%) of HTL-free C-PSC, by suppression of the ion migration and reduction of the crystal defects in perovskite[96].

In addition, carbon-based perovskite solar cells possesses a great potential for easy recyclability. Bogachuk et al. [97], Ku et al. [98] demonstrated that the triple mesoporous scaffold ( $\text{m-TiO}_2/\text{ZrO}_2/\text{C}$ ) can be reused after perovskite removal by washing. In addition, thanks to a thermally-assisted mechanochemical approach, the constituents of the device architecture can be reused since it was shown that is it possible to remove the encapsulants, the electrode and the PK without using any toxic solvent[97]. Furthermore, Binek et. al [99] reused  $\text{PbI}_2$  and the most expensive part which is the FTO for manufacturing new solar cells using a multi-step procedure that separate the different layers. In order to decrease the environmental impact, recycling waste materials is an important step.

### 5.3. Transport layers

The solar cell performance depends in part on the materials chosen materials as ETL and HTL. Efficiency can be affected by the optical and electrical properties of these materials. They must have a good energy alignment with the PK, a high transmittance in the UV-visible region, and therefore a suitable thickness, an appropriate conductivity, as well as good thermal stability. Organic and inorganic transport materials have been used in the perovskite solar cell

development[100]. Figure 5 shows the different materials, that can compose a perovskite solar cell with their energy levels[73]. For an HTL material, the Highest Occupied Molecular Orbital (HOMO) must be greater in energy than the valence band (VB) of the perovskite. The Lowest Unoccupied molecular orbital (LUMO) of the HTL must be less than the conduction band (CB) of the perovskite. ETL should be able to transmit photons in the UV-visible range so that they can be easily absorbed by the active layer, and must also have good electron mobility in order to guarantee charge collection at the electrodes. Moreover the mobility of the holes in the HTL material must be quite high in order to assure good transport of the loads and reduce losses to the electrodes[101][102].

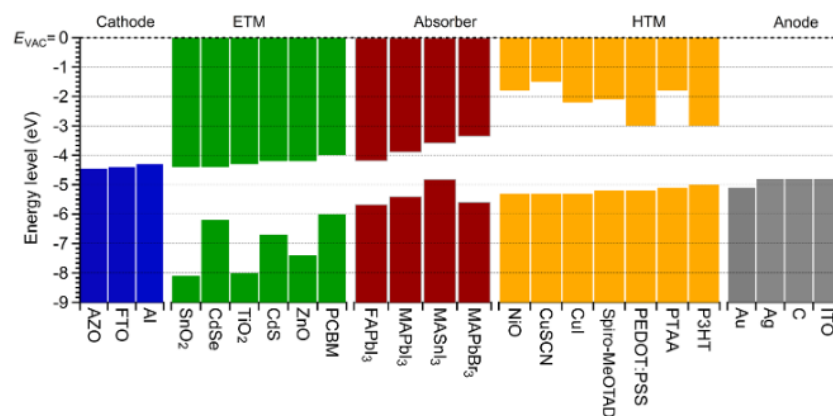


Figure 5: Diagram showing the energy levels, from left to right, for representative cathode, n-type (ETM), absorber, p-type (HTM), and anode materials[73]

#### a) Electron transporting layer

The most frequently used ETL materials in NIP structure are  $\text{SnO}_2$  and  $\text{TiO}_2$ .  $\text{SnO}_2$  has a high mobility and a wide bandgap. Xing et al. achieved 21.6% PCE using  $\text{SnO}_2$  as ETL. But despite the high efficiency, it suffers from degradation in high temperature. Moreover, it has much lower CB compared to that of the perovskite generating voltage losses in the PSC and deploying  $\text{SnO}_2$  on large scale is challenging [103].  $\text{TiO}_2$  is the most popular ETL either in its planar form on which the perovskite layer is deposited or in its mesoporous form. In this case, perovskite is infiltrated into this layer. It has suitable bandgap alignment with the perovskite and transparency for visible light. In addition in its mesoporous form, it improves the electron transport properties with a better pore filling leading to an enhancement in the interface between the ETL and the perovskite[104][105].

In a PIN structure, fullerene and its derivatives like PCBM[76], ICBA[106] are used as ETLs. PCBM was widely used since it passivates the perovskite surface with eliminating the hysteresis and recombination losses[107][108]. PCBM has decent electron mobility and can be used at low-temperature[109]. But since the PCBM/metal contact is not optimal for electron extraction due to the energy level mismatch, ZnO layer was added in between

increasing the air stability of the device and blocking the reaction between metal electrode and the perovskite that causes breaks in the PK structure[110].

#### b) Hole transporting Layer

Although our work will concern HTL-free architectures, here is a description of materials usually selected as HTL. The main role of HTL is to act as hole-selective contact in order to extract the photo-generated holes and carry them to the cathode, forbidding the contact between the perovskite layer and the electrode[111]. Various HTL materials can be used in a NIP structure including organic materials like small molecules of spiro-OMeTAD (2,2',7,7'-tetrakis(N,N-di-p-methoxyphenyl-amine)9,9'-spirobifluorene)[112], polymers like PTAA (poly(triaryl amine)) and P3HT (poly(3-hexyl-thiophene))[53], inorganic materials such as CuI (copper iodide)[113], CuSCN (Cuprous thiocyanate) [114]. In a PIN structure, polymers like PEDOT:PSS (poly(3,4-ethylenedioxythiophene) polystyrene sulfonate)[115], PTAA[76] and inorganic materials like NiO<sub>x</sub> (Nickel oxide)[116], CuSCN[117] can be used as HTLs.

If inorganic materials are more stable, Spiro-OMeTAD is the most commonly used material as HTL due to its efficient transporting holes capability and his ability to reduce the series resistance as well as the interfacial recombination losses which will subsequently improve the FF and the V<sub>oc</sub>. However, to achieve the best efficiencies, it needs ionic additives such as bis(trifluoroethane) sulfonimide lithium salt (Li-TFSI) and 4-tert-butyl pyridine (TBP) to improve the conductivity and hole mobility[111]. But the high cost of this material and its weak stability remain a problem and blocks its use for commercialization[118]. Therefore, polymeric HTL (PTAA, P3HT, *PCPDTBT* (Poly[2,6-(4,4-bis-(2-ethylhexyl)-4H-cyclopenta[2,1-b;3,4-b']dithiophene) - alt - 4,7(2,1,3-benzothiadiazole)), *PCDTBT* (Poly[N-9'-heptadecanyl-2,7-carbazole - alt - 5,5-(4',7'-di-2-thienyl-2',1',3'-benzothiadiazole), *POWT* (poly(5-amino-5-carboxy3-oxapentyl)-2,5-thiophene)[119] [120] have been adopted since they are cheaper. Moreover, some of them offer higher hole mobility compared to the Spiro-OMeTAD[121], without additives.

#### 5.4. Simple perovskites

Currently, the methylammonium lead iodide (MAPbI<sub>3</sub>) has revolutionized the field of emerging photovoltaic technologies for being the most common and most extensively investigated organic-inorganic hybrid perovskite[122]. This absorbing material has a tetragonal perovskite structure and presents different phase transitions as a function of temperature. Below 162.2 K it is orthorhombic, between 162.2 K and 327.4 K it is tetragonal and above the prementioned temperature it adopts a cubic structure[63]. One of the most interesting features of MAPbI<sub>3</sub> is the low carrier recombination at the solar cell interfaces which is supported by long-range carrier diffusion lengths (100-1000 nm) and high absorption coefficient[123] [124][125]. Despite these properties, MAPbI<sub>3</sub> biggest challenge is the sensitivity to moisture and polar solvents leading solar cells based on this active layer to have stability issues, in addition to its bandgap (1.55 eV) which is not ideal for solar cells[126].

However, to overcome these complications, other hybrid perovskite components exist and could be classified based on substitutions of the monovalent cation, the divalent metal and the halide positions. These different formulations make it possible to modify the value of the perovskite band gap and may improve the solar cell's performance and modify the properties. Moreover, plenty of grain boundaries, voids and surface defects within the perovskite material can be detected, causing efficiency losses and recombination sites[127].

#### a) Halide substitution

To tune the optoelectronic properties, the iodine can be substituted by chlorine or bromine since the bandgap value is directly related to the bond between the metallic anion and the halogenated anion. Therefore, the adaptability of the bandgap depending on the material composition is one of the most important properties of the hybrid perovskites. The MAPbCl<sub>3</sub> bandgap is 3.11 eV and is suitable as a single light absorber, while MAPbBr<sub>3</sub> with 2.3 eV bandgap value favorable energy level with respect to TiO<sub>2</sub> is interesting for tandem applications whereas MAPbI<sub>3</sub> is suitable for single band gap absorber [128][129]. Moreover, MAPbBr<sub>3</sub> is characterized by its high V<sub>oc</sub> thanks to the high conduction band minimum forming a barrier to confine electrons and forbid recombination effects[130].

#### b) Cation substitution

Furthermore, the cation can be replaced since it can also impact the bandgap value depending on its size given that the crystal lattice can expand or contract varying the Pb-X bond distance. Thus, when the ionic radius of the organic cation increases, the crystal lattice is dilated and therefore the bandgap value decreases and a shift towards the infrared is detected[131]. The most commonly used cations that can replace the methylammonium are formamidinium (FA: NH<sub>2</sub>CH=NH<sub>2</sub><sup>+</sup>)[132][133][134], cesium (Cs<sup>+</sup>)[135] or rubidium (Rb<sup>+</sup>)[136][137]. FA is slightly larger than MA, causing an expand in the lattice and consequently decreasing the band gap from 1.59eV for MAPbI<sub>3</sub> to 1.45-1.52 eV for FAPbI<sub>3</sub>[128]. In addition, it was demonstrated that replacing the MA by FA leads to better thermal stability[138]. However, the best PCE reported for FAPbI<sub>3</sub> perovskites is lower than the MAPbI<sub>3</sub> despite the smaller bandgap which was considered to enhance the solar cell performance, but it is the poor FF behind this PCE loss[139] and this is due to the transformation of FAPbI<sub>3</sub> from the α-FAPbI<sub>3</sub> (the alpha or black phase) to δ -FAPbI<sub>3</sub> (the photo-inactive delta or yellow phase) at room temperature making the device unstable[61]. As well, the Cs is a good cation substitute since its ionic radius is compatible with structure and it has the same effect as FA.

#### c) Metal substitution

Replacing lead would be favorable from toxicological perspective and therefore many studies have been directed towards tin perovskites[140] where it was reported for the first time a completely lead-free, CH<sub>3</sub>NH<sub>3</sub>SnI<sub>3</sub> perovskite solar cell processed on a mesoporous TiO<sub>2</sub> scaffold, reaching efficiencies of over 6% [141]. CH<sub>3</sub>NH<sub>3</sub>SnI<sub>3</sub> has the advantage of reduced band gap, however, Sn gets oxidized easily leading to poor long-term stability and low

reproducibility of these films demanding a careful re-evaluation of the  $\text{CH}_3\text{NH}_3\text{SnI}_3$  system[129].

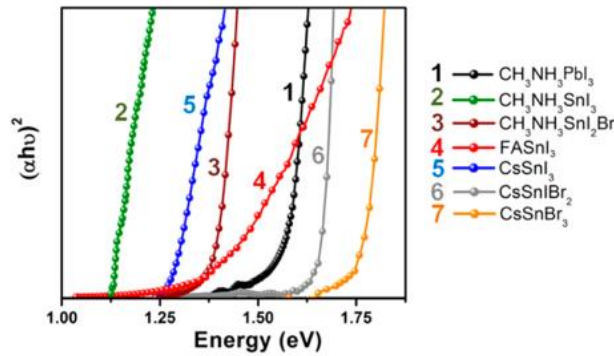


Figure 6: Tauc plots of several lead-free perovskites films[129]

### 5.5. Mixed perovskites

Pellet et al. reported the first mixed cation perovskite using a mixture of formamidinium ( $\text{HN}=\text{CHNH}_3^+$ , FA) and methylammonium ( $\text{CH}_3\text{NH}_3^+$ , MA) cations in the A position of the  $\text{APbI}_3$  perovskite structure with  $(\text{MA})_x(\text{FA})_{1-x}\text{PbI}_3$  ( $x = 0-1$ ). This combination improved the short-circuit current and showed great potential as a versatile tool to tune the structural, electrical, and optoelectronic properties of the light-harvesting materials. This device reached a 14.9% by adding 20% MA to the FA dipping bath completely avoiding the undesirable formation of the  $\delta$ -phase while maintaining the red-shifted band gap of  $\text{FAPbI}_3$  [138].

To further enhance the MA/FA mixed cation perovskite performance, mixed anion/cation perovskite were then developed. The Bromine (Br) was introduced to partially replace the iodide (I). Jeon et al developed  $(\text{FAPbI}_3)_{0.85}(\text{MAPbBr}_3)_{0.15}$  showing a more stabilized perovskite phase of  $\text{FAPbI}_3$  and improves the power conversion efficiency of the solar cell up to 20.1% [142][143]. Moreover, Jacobsson et al. varied the MA/FA and the I/Br-ratio achieving a PCE of 20.67% with  $\text{MA}_{2/6}\text{FA}_{4/6}\text{Pb}(\text{Br}_{1/6}\text{I}_{5/6})_3$  [144]. Other than Br, Isikgor et al. introduced Cl into the cation mixture and developed  $\text{MA}_{1-x}\text{FA}_x\text{PbI}_{3-y}\text{Cl}_y$  obtaining high-power conversion efficiency (PCE) of 18.14%. The mixed cations and mixed halides lead to long charge diffusion lengths. The superior performance is mainly explained by the  $J_{sc}$  enhancement [145].

One of the biggest challenge of the inorganic-organic hybrid halide perovskites is the degradation due to the volatility of the organic cations[146]. But researchers studied ternary cation perovskites using MA, FA and Cs, where the first triple cation perovskite solar cell was reported by Saliba et al. [147]. They showed that the Cs can successfully improve the MA/FA mixture with more thermally stable devices containing fewer yellow phases impurities, highly uniform perovskite grains extending from electron to hole collecting layer and reaching 20.1% of efficiency.

## 5.6. Additives for perovskite

Additives play a main role in enhancing the morphology of the perovskite films, their crystal growth and thus the performance of the solar cell. Therefore, using additives has proven to be an adequate method for facilitating homogeneous nucleation or for modulating the crystallization kinetics. Moreover, additives help to control the surface uniformity, crystal size and contribute in reducing electrical shunt and the recombination effects [148][149]. Additives can be divided into categories depending on their functionalities as shown in Figure 7. Given that, some can play a role in the morphology and the crystallinity of the perovskite film, whereas others can improve the optical and electrical properties. Additives can interact with components in the perovskite solution (by chemistry or physics paths) or can passivate the PK film facilitating the charge extractions or can modify the crystallinity to enhance it.



Figure 7: Classification of the additives used in current perovskite solar cells[149]

### a) Polymer additives

Oxygen atoms in a polymer can form bond H-bonds with the MA hydrogen atoms helping to resist to humidity for long-time operation. Moreover, bonds between Pb ions in the perovskite with atoms like S and N in polymers can stabilize the frame structure of the perovskite. In addition, polymer additives can improve the perovskite coverage films thanks to their good solubility reducing the contact angle and therefore helping for a better spreading. Therefore, polymers are considered efficient additives in promoting uniform crystallization. Chang et al. demonstrated that the use of 1wt% of the poly(ethylene glycol) (PEG) additive can tune the morphology of the perovskite layer by retarding the crystals growth and aggregation which helped to form an uniform film [150]. Zhao et al. reached a 16% PCE using PEG and as an additive showing how it facilitates the formation of a uniform and homogeneous polymer-scaffold perovskite layer in addition to a strong humidity resistance thanks to the hydrogen

bonding between PEG and PK molecules ensuring a compact moisture barrier around the PK crystal grains[151]. Tripathi et al. added the amine-polymer poly [(9,9-bis(3'-(N,N-dimethylamino)propyl)-2,7-fluorene) - alt - 2,7-(9,9-dioctylfluorene)] (PFN-P1) to a simple spin-coating process as a surfactant that promotes uniform crystallization with a uniform distribution of grain sizes and improved open circuit voltage with 13.2% PCE[152]. Guo et al. fabricated a 90-nm-thick film prepared with 3wt% polyvinylpyrrolidone (PVP) additive, showing an increase in the thermal stability against decomposition into  $\text{PbI}_2$ , and a stable crystal size and morphology, with increased open circuit voltage (Voc), fill factor (FF), and PCE[153].

#### b) Fullerene additives

Fullerene can fill the pinholes and vacancies between PK grains reducing the photocurrent hysteresis[154]. And since the diffusion length of electrons is shorter than that of holes in PK films, fullerene additives can construct electron transport channels to facilitate the extraction and enhance the performance. Xu et al. reported the first perovskite- $\text{PC}_{61}\text{BM}$  hybrid solid with reduced hysteresis, due to an in situ passivation of the halide-induced deep traps by  $\text{PC}_{61}\text{BM}$  adsorption during the perovskite self-assembly[143]. Chiang et al. used [6,6]-phenyl-C71-butyric acid methyl ester ( $\text{PC}_{71}\text{BM}$ ) to play a critical role in improving the quality of the light-absorbing layer by filling pinholes and vacancies between perovskite grains, resulting in a film with large grains and fewer grain boundaries to obtain a solar cell with 16% of PCE and a highly FF of 0.82[154].

#### c) Metal halide salt additives

Metal halide salt additives can significantly increase the grain size and contribute for smoother perovskite surfaces. Boopathi et al. introduced alkali metal halide salts (KCl, NaCl and LiCl) and found a PCE improvement since these additives can enhance the crystallinity and the morphology and reduce the grain boundaries. Perovskites with KCl have larger crystallites and better stability than those with NaCl or LiCl[155]. Bag et al. incorporated a controlled amount of sodium iodide into the  $\text{PbI}_2$  precursor of the perovskite film which led to larger grain size reaching 14.2% efficiency with low hysteresis[156]. Chen et al. demonstrated that adding  $\text{CaCl}_2$  as an additive can improve the  $\text{MAPbI}_3$  film with forming uniform crystals and good surface coverage. This result is obtained after an annealing process where the Cl anions process induces a preferred orientation of the  $\text{MAPbI}_3$  crystal grains[157].

#### d) Inorganic acid additives

Inorganic acid additives like hydriodic acid (HI), hydrobromic acid (HBr), and hydrochloric acid (HCl) increase the solubility of perovskite solutions, promote nucleation, help to have a continuous perovskite film with large grains, prevent from decomposition by reducing oxidized  $\text{I}_2$  back to  $\text{I}^-$  and therefore improving long term stability and contribute in controlling the crystallization[149]. Heo et al. fabricated a pinhole-free  $\text{MAPbI}_3$  perovskite films by using  $\text{MAPbI}_3/\text{DMSO}$  solution and  $\text{MAPbI}_3/\text{DMF}$  with HI additive solvent that helped to improve the

solubility and converted the  $\text{PbI}_2$  to perovskite attaining a 17.2% PCE[158]. Eperon et al. used HI additive in the  $\text{CsPbI}_3$  that stabilized the perovskite in the black phase and improved the crystal growth[158]. By comparing HI, HCl and HBr, Huang et al. discovered that HBr is the most efficient additive showing a better crystallization with fewer pinholes and low series resistance and good homogeneity with 15.76% of PCE[159]

#### e) Solvent additives

Jen et al. incorporated 1,8-diiodooctane (DIO) into the precursor solution and demonstrated how it controlled the crystallization and contributed to homogeneous nucleation[148]. Li et al. introduced the acetonitrile (ACN) as an additive into the  $\text{PbI}_2$ /DMF solution and found out that a proper ratio of ACN/ $\text{PbI}_2$  lead to a uniform perovskite film with low grain boundaries and longer carrier lifetime. The best efficient solar cell using this additive arrived to a PCE of 19.68%[160]. Wu et al demonstrated that a small amount of  $\text{H}_2\text{O}$  (2 wt%) added to  $\text{PbI}_2$ /DMF can improve the  $\text{PbI}_2$  properties and therefore the perovskite film making it homogeneous without any pinholes[161].

#### f) Nanoparticles additives

Li et al. were the first to intermix precursor-capped inorganic nanoparticles of PbS which were covered with perovskite precursor molecules of methylammonium iodide ( $\text{CH}_3\text{NH}_3\text{I}$ , MAI). Through this intermixing-seeded growth technique, morphological improvements, such as increased crystal domains, enhanced coverage, better uniformity, were performed in the perovskite thin films, and the corresponding solar cell devices achieved a power conversion efficiency of 17.4%[162]. Zhang et al. incorporated core-shell metal-dielectric NPs of  $\text{Au@SiO}_2$  into the solar cell and remarked an enhanced short circuit photo-current due to a reduced exciton binding energy and hence enhanced generation of free charge carriers[163]. Chang et al. improved the crystallinity of the perovskite film by incorporating metal-organic framework nanocrystals (MOFs) which are a class of 3D porous crystalline materials fabricated of organic linkers and metal-based nodes. MOFs have regular nanostructured pores which allowed them to integrate into the perovskite precursor solution, hence enhanced the formation of uniform grain size perovskite crystals[164]

#### g) Organic halide salt additives

These additives contain heteroatoms in organic components, which form hydrogen bonds with H atoms in  $\text{MA}^+$  interconnecting the perovskite crystals. This yields to larger grains on a homogeneous surface. Docampo et al. highlighted that chloride is critical in MA lead halide perovskites via a controlled addition of methylammonium chloride (MACl) to the MAI immersion solution. In fact, the incorporation of MACl helps the  $\text{PbI}_2$  conversion to  $\text{MAPbCl}_{3-x}\text{I}_x$  perovskite improving the  $J_{\text{sc}}$ . Moreover, MACl reduces the series resistance which enhance the FF and hence the charge diffusion length become longer[165]. Hsu et al. incorporated ethyl ammonium iodine (EAI) into the perovskite precursor and higher absorbances and degrees of crystallinity were achieved correspondingly with higher surface coverage.  $\text{EA}^+$



incorporating coordinately with MA<sup>+</sup> in the 3D lattice of the MAPbI<sub>3</sub> can move the 3D structure into a 2D one which will help to improve the stability having a 2D/3D mixed structure[166].

Mei et al. were the first researchers group that has used and investigated the occurring mechanism of 5-ammonium valeric acid iodide (5-AVAI) addition leading to nucleation and growth optimization of MAPbI<sub>3</sub>. The additive partially replace the MA cations to form (5-AVA)<sub>x</sub>(MA)<sub>1-x</sub>PbI<sub>3</sub> perovskite, where the COOH groups of the additive form hydrogen bonds with NH<sub>3</sub><sup>+</sup> groups and I<sup>-</sup> ions from PbI<sub>6</sub>. Hence these COOH anchor a monolayer of the amino acid to the TiO<sub>2</sub> and ZrO<sub>2</sub> layers by binding to the exposed Ti and Zr ions. The NH<sub>3</sub><sup>+</sup> groups in the 5-AVAI play the role of nucleation sites for MAPbI<sub>3</sub> and help its filling into the pores. The acidic property of this additive contributes to reduce the colloid size ensuring a slow crystallization in porous structure as the one used in this manuscript. Moreover, XRD analysis highlighted that perovskites with 5-AVAI have a dominant orientation ensuring better contact with TiO<sub>2</sub>. An improved PCE (Figure 8) was noticed since 5-AVAI cations induce preferential growth in the normal direction of the perovskite crystals with better coverage. These devices also showed promising stabilities under different stress conditions Figure 9[5][167][149][168][169], see example in Figure 9. A one-year stable perovskite device was then fabricated by Grancini et al. by engineering an ultra-stable 2D/3D (HOOC(CH<sub>2</sub>)<sub>4</sub>NH<sub>3</sub>)<sub>2</sub>PbI<sub>4</sub>/CH<sub>3</sub>NH<sub>3</sub>PbI<sub>3</sub> perovskite junction by incorporating 3% of 5-AVAI with zero PCE loss under ISOS standard conditions[6][170].

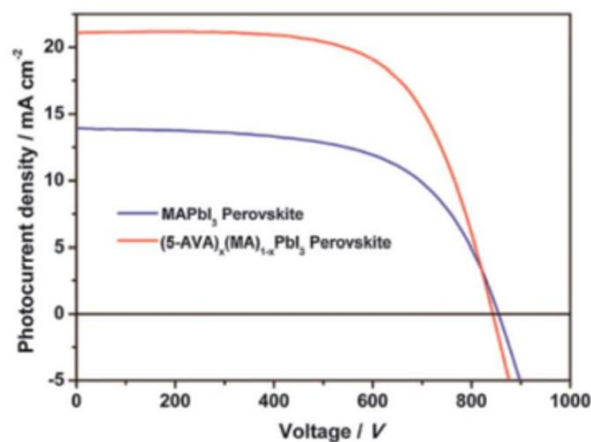


Figure 8: J–V curves of carbon-based perovskite solar cell with and without 5-AVAI additive in the PK formulation [149]

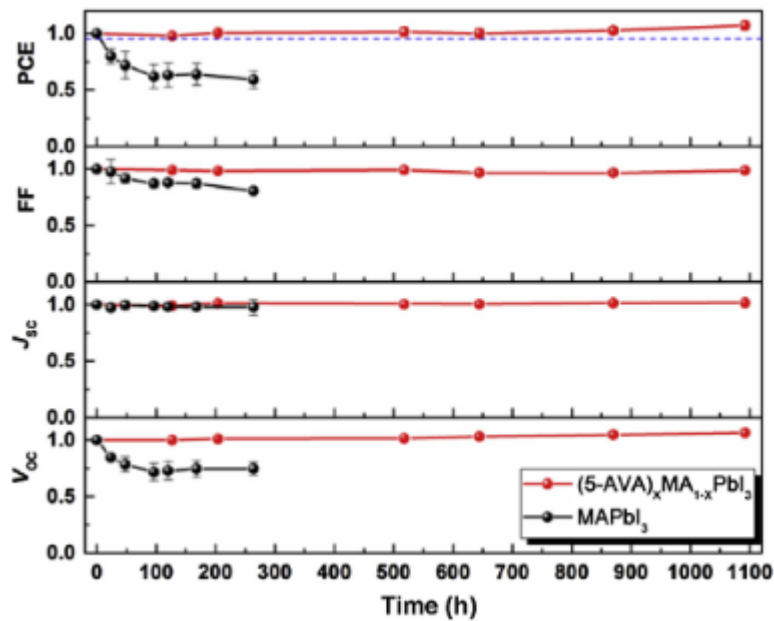


Figure 9: Performance evolution of C-PSCs under damp heat (85 C/85%RH) with or without the AVAI additive[171]

#### h) Other additives

Shahiduzzaman et al. employed the ionic liquid 1-hexyl-3-methylimidazolium chloride as an additive in the perovskite precursor solution. Analysis revealed a uniform surface with good morphology and showed that the incorporation of the ionic liquid prevented rapid crystal formations which led to an homogeneous nucleation[172]. Chen et al. reported a high-quality perovskite film by adding NH<sub>4</sub>Cl, demonstrating how it can affect the crystallization and make the perovskite film smoother with no need of thermal annealing and with no hysteresis behavior appearing[173].

Moreover, Qin et al. introduced benzoquinone (BQ) into MAI and PbI<sub>2</sub> to improve both morphology and stability since it was shown that BQ reduces the speed of crystallization which will help to obtain a uniform, flat surface with larger grains reducing carrier recombination and improving the electron transfers[174].

## 6. Perovskite deposition techniques

The main achievement of perovskite solar cells is their ability to achieve high performance by limiting problems of recombination and stability with simple and low cost manufacturing methods. But this is very dependent on the PK deposit technique and on the layer on which it is deposited. In this thesis, we adopted two different deposition techniques, both using the mesoporous scaffold ability for infiltration: the drop casting and the inkjet methods. Given that our solar cell's architecture consists a triple mesoporous layer scaffold, adding the PK as a final step with the prementioned techniques makes is an easy and clean way for

manufacturing the devices without overflowing or spilling out the precursor. Moreover, these techniques does not require a glove box facilitating the fabrication procedure.

To date, several other methods have been developed to improve the quality of perovskite film. The morphology, crystallinity and uniformity of the latter depends heavily on the choice of the deposition method. This will have a direct impact on the PCE of perovskite solar cells. The main ones are described thereafter.

#### 6.1. Spin-coating deposition method (One-step or Two-steps)

Peroskites can be obtained via a spin-coating technique. This technique is widely used because of its low-cost and simplicity. Two methods have been proposed in one or two step(s).

For the one-step technique, precursors of lead ( $PbX_2$ ) and organic halide (AX) are usually dissolved in a highly polar solvent like dimethylformamide (DMF), dimethyl sulfoxide (DMSO), gamma butyrolactone (GBL), dimethylacetamide (DMAc), N-methy-2-Pyrrolide (NMP) or isopropyl alcohol (IPA)[175][176][177][178][178][179]. The resulting precursor is spin-coated on the substrate. A crystallized layer of perovskite results due to the strong ionic interaction between halogen anions and metal cations coupled with the evaporation of the solvent during the spinning[180], with potential the help of the addition of an anti-solvent[181]. Spin-coating of the precursors solution is then followed by a drying and heating at mild-temperature (70-170°C)[142], where the annealing process are expected to impact the  $MAPbI_3$  morphology and crystallinity. Moisture should be avoided while depositing the perovskite to prevent from its decomposition[179][55][59]. However, controlling the film thickness, morphology, uniformity is so difficult using this technique since it forms layers with pin-holes due to the slow crystallizations and leads to voids because of the viscous coating solution[59] [182].

In 1998, Mitzi et al. proposed a two-steps deposition technique to overcome all of the aforementioned drawbacks of the one-step method and especially the poor surface coverage and unavoidable non-uniformity[183]. This research group deposited  $PbI_2$  film with DMF on a  $TiO_2$  film using the spin-coating technique at 70°C and followed by a spin-coating or by dipping in a MAI solution to obtain  $CH_3NH_3PbI_3$ [183]. It was shown that the quality of the perovskite depends on the spinning time and speed of the spin-coating of the MAI [184]. Moreover increasing the MAI concentration reduces the grain sizes[185]. This technique produces better film compared to the one-step method. The average power conversion efficiency for a one-step spin coating was 7.5%, whereas for the two-steps it was 13.9% mainly due to improvements in the morphology of  $CH_3NH_3$ [186][185].

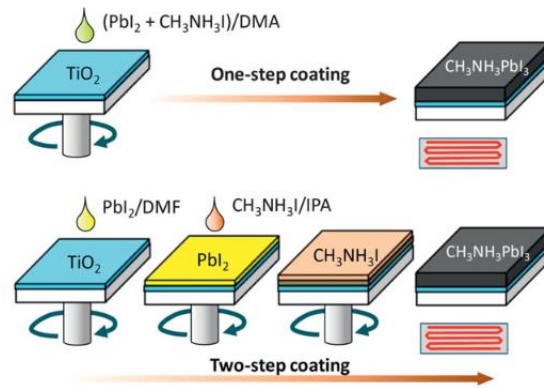


Figure 10: One-step and two-steps coating procedures to deposit MAPbI<sub>3</sub> perovskite films. The one-step coating procedure was conducted using a single precursor solution containing MAI (CH<sub>3</sub>NH<sub>3</sub>I) and PbI<sub>2</sub>, while the two-steps coating method was performed by reacting the spin-coated PbI<sub>2</sub> film with the MAI solution[179]

It is quite simple to manufacture devices by spin coating on a laboratory scale, even if this process leads to a significant waste of the solutions used. Despite the good efficiency, this method also presents some disadvantages. Two main problems were highlighted: the incomplete conversion of PbI<sub>2</sub> and the uncontrolled perovskite crystal sizes, especially in planar structure. Moreover, this technique is applicable on the laboratory scale but it is not realistic for large scale industrialization [187][188].

## 6.2. Thermal/Vacuum evaporation

In 2013, Liu et al. were the first to fabricate a perovskite film using the Vapor deposition technique[189]. The recently mentioned group co-evaporated organic (MAI) and inorganic (PbCl<sub>2</sub>) with a molar ratio on substrate of about MAI:PbCl<sub>2</sub>=4:1, using dual-source vapor deposition. A uniform flat perovskite film with high coverage was obtained[189]. In 2021, Feng et al. reported a highly efficient solar cell of 21.32% PCE with a high-quality formamidinium perovskite film on a 400 cm<sup>2</sup> substrate[190]. However, despite that vapor deposition avoids the use of solvents, this technique requests a lot of vacuum, which is too much energy consuming and costs and thus slows down the possibility of mass production[191].

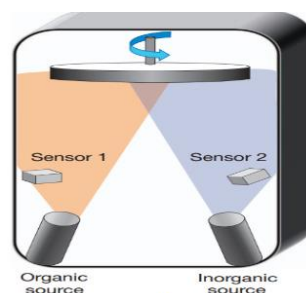


Figure 11: Schematic representation of the dual-source thermal evaporation system for depositing the perovskite layer[189]

### 6.3. Doctor blade coating

This technique is applicable on a large scale, is very simple and low cost. It consists of pouring a fixed amount of perovskite on the substrate then sweeping it linearly at high speed. For this technique, it is recommended to keep the substrate at high temperature to have a smoother and more uniform pinhole-free film. Moreover, heating substrate and applying an airflow over it improve the evaporation rate of the added solvent boosting the nucleation and crystal growth[192]. Three factors can control the film's thickness and the crystallization: the concentration of the precursor ink, the speed of the blade's movement and the gap between the substrate and the blade[193]. Tang et al. reported a 19.3% PCE using this technique[194]. Compared to the spin-coating method, Doctor blading requires lower quantity of the precursor solutions as there is no/few waste[195].

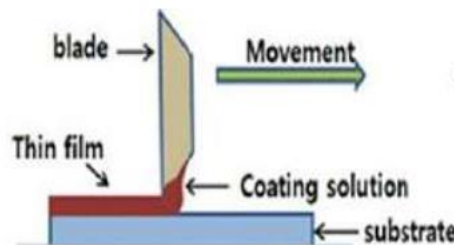


Figure 12: Schematic representation of the doctor blade deposition method[196]

### 6.4. Slot die coating

Slot die coating technique is very analogous to the doctor blade technique. The only difference is instead of using a blade to spread the ink over the substrate, an ink reservoir is applied as presented in Figure 13. The ink flow can be better controlled and the film quality is improved compared to the doctor blade technique. However, larger ink quantity is required to fill the ink reservoir[197]. Burkitt et al. fabricated a solar cell with 7% of PCE (FTO/c-TiO<sub>2</sub>/m-TiO<sub>2</sub>/PK/spiro-MeOTAD/Au) using the slot die coating for each layer except the gold electrode [198]. Kim et al. achieved 12.7% PCE for a perovskite solar cell fabricated by slot-die coating with a blowing step and a heating procedure improving the perovskite film coverage[199].

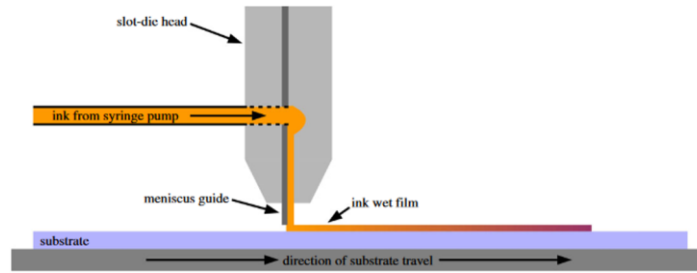


Figure 13: Schematic representation of the slot die process[198]

## 6.5. Spray coating

The spray coating technique consists of the dispersion of tiny liquid droplets over the substrate through a nozzle as shown in Figure 14. This technique can be classified into three categories depending on the dispersing method: (i) pneumatic spraying (through fast gas flow), (ii) ultrasonic spraying (through ultrasonic vibration) and (iii) electro spraying (through electrical repulsion) [193]. The most commonly used technique for the fabrication of the perovskite layer is the ultrasonic spraying[200]. Spray coating has two systems: atomizing system which consists of converting the perovskite solution into droplets, and deposition system where a low-pressure gas stream guides the PK droplets into the substrate. While the deposition process is proceeding, the solvent is getting evaporated. Both systems are connected by a quartz nozzle through which the perovskite solution is added[55]. In 2014, Borrows et al. realized a solar cell with 11% PCE and 85% coverage adopting the spray pyrolysis method[201].

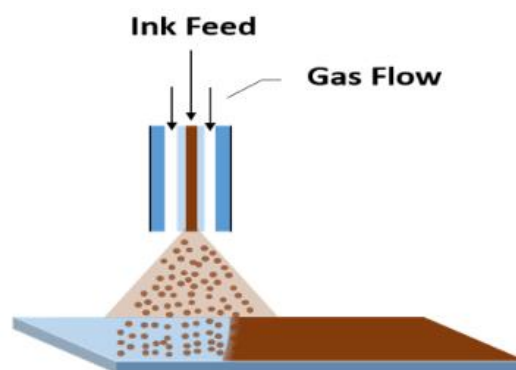


Figure 14: Schematic representation of the spray coating technique[193]

## 6.6. Drop casting

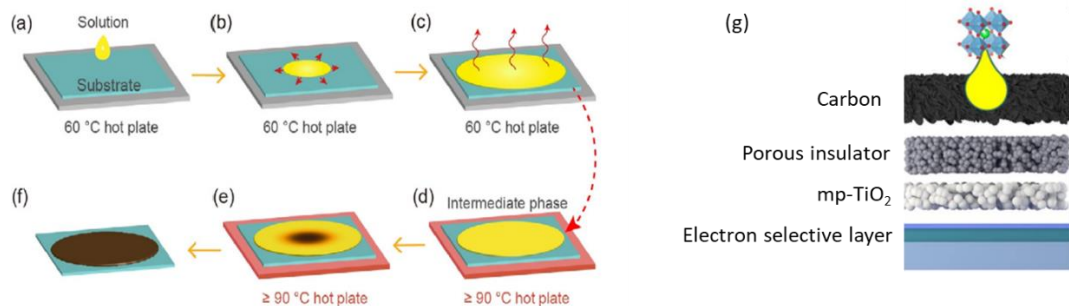


Figure 15: Illustration of the drop-casting method for preparing MAPbI<sub>3</sub> film: a) The solution is dropped onto the center of a substrate on a 60 °C hot plate. b) The solution spreads on the substrate. c) The solution stops spreading, resulting in a round wet film. d) The substrate is transferred to a hot plate with a temperature above 90 °C. e) The film color turns black, indicating the formation of MAPbI<sub>3</sub>. f) Round brown MAPbI<sub>3</sub> film forms [202] g) into the mesoporous scaffold [203]

All the above-mentioned techniques require either an inert atmosphere, a low air humidity or a high vacuum to obtain good performance of the devices. To avoid complicated conditions for the fabrication of an efficient solar cell, scientists recently headed to the drop casting method [202][204][205][206]. This technique is an easy, low-cost, low-waste and productive method performed in air [206] [207][208]. It was firstly reported by Mei et al. in 2014 which consists of infiltrating the metal halide perovskite precursor into a triple layer mesoporous scaffold (TiO<sub>2</sub>/ZrO<sub>2</sub>/C) where they obtained a PCE of 10.4% [5]. Using this technique on planar architecture is usually less good than simple spin-coating. However, Zuo et al. demonstrated that by avoiding the airflow around the drop casted PK, they reached 18.7% of PCE for a planar perovskite solar cell without the use of any antisolvent and with a 88% R.H ambient condition [208].

This technique is composed of several steps: a drop of the precursor solution is deposited on the center, the solution spreads all over the substrate, the solvent evaporates with the help or not of annealing leading to a dark brown film resulting from perovskite crystallization. This technique is advantageous due to no waste of the precursor solution. It will be used in our work to fill the mesoporous layers of our C-PSC stacks.

## 6.7. Inkjet printing

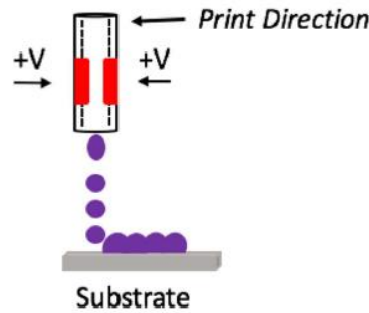


Figure 16: Schematic representation of inkjet method[209]

This technique is a digital method that can be controlled by a computer program to obtain the desired patterns with no specific requirements for the shape and materials of the substrate since there is no contact[184]. It aims to replace the drop casting method since the whole device may be produced on a larger scale in an easy and fast way[210][4]. Inkjet has been chosen for several fabrications of optoelectronic devices[211]. It can be used for the fabrication of functional layers from homogeneous or colloidal liquid phase inks. The principle of this technique relies on a piezo material dispersing the ink precursor while controlling the droplet size as shown in Figure 16. This technique presents several advantages: low cost, contactless, scalable, freedom of design and it reduces the irreproducibility observed in other techniques[212]. When applied on a large active surface area, it showed higher PCE compared to the spin coating method (Figure 17)[213].

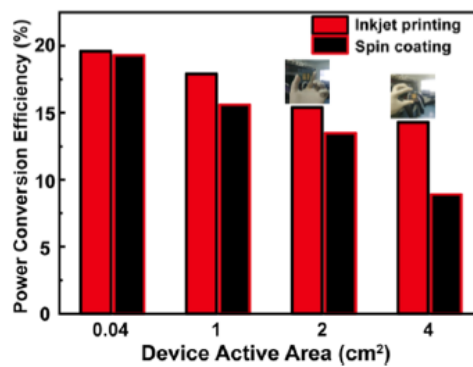


Figure 17: Diagram of PCE comparison for PSCs based on inkjet printing and spin-coating methods with different device areas (0.04, 1.0, 2.0, 4.0 cm<sup>2</sup>)[213]

The first perovskite solar cell was fabricated using inkjet printing technique in 2014, affording 11-12% efficient PSCs[214]. In fact, they printed a mixed solution of MAI with Carbon on a PbI<sub>2</sub> layer (previously deposited using spin-coating). This allowed a one-step realization of MAPbI<sub>3</sub> and carbon layer without the use of an insulating intermediate ZrO<sub>2</sub> layer.

Then, this method was applied for mesoporous[210] and monolithic hole-conductor-free PSCs[4]. Hashmi et al.[4], Verma et al.[92] adopted this infiltration technique and reached 7.65% and 9.1% PCE respectively.

The highest PCE achieved with an inkjet perovskite layer is 16.78% for 120 cm<sup>2</sup> surface area[212]. Nevertheless, inkjet has many limitations such as the clogging of the nozzles in the



printing cartridges due to the transformation of PK crystals from the liquid precursor on surfaces. This leads to less precise material deposition. Therefore stable precursor inks are more required in order to avoid the print head damages[4].

Perovskite drop casting and inkjet infiltration methods will be studied more deeply in the upcoming chapters of the manuscript on C-PSC type devices configuration. The aim will be to scout their impact on the solar cells' performance and on durability. Some works relate on this subject in literature, but the impact of the deposition technique choice on both the microstructure of the perovskite and the mechanisms occurring into the layers has not yet been deeply studied. Thus, it seems interesting to investigate the effect of the process on both the perovskite morphology and performance.

## 7. Post treatments leading to a maturation phenomenon

Solar cells do not always achieve their maximum of efficiency after deposit and annealing, but require sometimes an additional procedure. Maturation is a process that helps to improve the solar cell PV parameters and therefore its performance. This step can occur into the solar cell during the manufacturing or can be imposed by external factors.

Wagner et al. highlighted a maturation process when they demonstrated a relationship between crystal formation and PV performance of perovskite solar cells. They introduced a novel time-resolved real-time probing of photophysical and electrical solar cell parameters in a C-PSC. Thanks to PL measurements in real-time depositing, an intensity increase was firstly noticed and a redshift was detected reflecting the crystal size growth during the PK conversion. In a second stage, a redshift is still detectable despite the PL decreasing explaining that a crystal growth is still going, arriving to a stage where boundary effects quench the PL intensity. A stable grain size was then observed, after the total conversion from  $\text{PbI}_2$  to PK, with an enhanced photocurrent improving the electrical connections and explaining the 'maturation' process that was occurring [215].

Another type of maturation step was demonstrated by Ho et al. where they reported an annealing in ambient air and in oxygen environment. In fact, this annealing method helped to reduce the oxygen vacancy density causing defects into the solar cell, and improve the optical transmission of the  $\text{TiO}_2$ , thus enhancing the electron transport layer. Hence, changing the annealing environment from ambient air to oxygen contribute in enlarging the optical band gap and improving the  $\text{TiO}_2$  compact layer which plays the role of an ETL and decreases the recombination rate at the PK/ $\text{TiO}_2$  interface. Moreover, this maturation step increases the  $J_{sc}$  and the FF and consequently the PCE of the solar cell[216].

Liu et al. reported perovskite solar cells using  $\text{TiO}_2$  as ETL showing that these devices have improved more by twice after light soaking for 15 mins showing that this light soaking increased the concentration of oxygen vacancies in the  $\text{TiO}_2$  film, increasing the film conductance and accelerating the charge extraction rate in the PK/ $\text{TiO}_2$  interface and upgrading the PCE[217]. The use of light-soaking treatments was also considered as a

maturation step since it was noticed that this procedure may improve the solar cell performance. Schneider et al. showed two types of maturation: natural and induced by light-soaking. The first one was by measuring the solar cells after 5 days of their fabrication after leaving them in the dark in a moisture-free nitrogen atmosphere glove box (matured as presented in Figure 18). Whereas for the light-soaking, it was applied after 7 days of fabrication, for 1.5h hours and a 12 hours rest period. Natural maturation increased the  $J_{sc}$  while the  $V_{oc}$  increases thanks to the light-soaking process as presented in Figure 18[218].

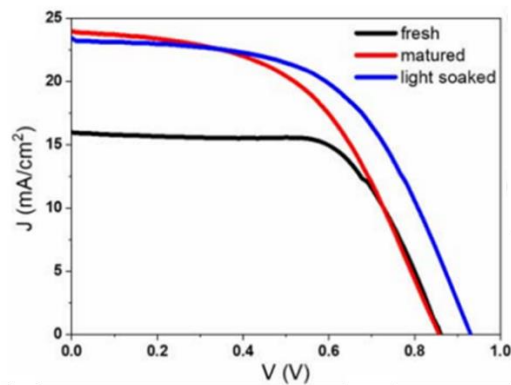


Figure 18: Current density versus voltage ( $J$ - $V$ ) curve of a typical C-PSC at the three measured stages of maturation; fresh (black), matured (red), and light soaked (blue)

Ginting et al. observed a 24% improvement after 24h of storage in dark conditions in air, due to partial oxidation of spiro-OMeTAD by  $O_2^-$  species, leading to a hole transporting conductivity enhancement and therefore a more efficient charge transfer from the HTL to the anode [219]. Wu et al. proved that a 30% efficiency improvement can be achieved after 1000h of storage under  $N_2$  for  $MAPbI_3$  solar cells which was explained by the infiltration of the PK into ETL which was ZnO nanorods crystals[220]. Commandeur et al. presented a positive maturation effect with a  $40 \pm 10\%$  PCE increase after 14 days of storage in dark ambient conditions for  $CsPbBr_3$  perovskite solar cells. This improvement is due to a  $V_{oc}$  and  $J_{sc}$  increase. The  $V_{oc}$  indicates a reduced number of pinholes and defects decreasing the number of deep states within the bandgap that take place at the edges of grain boundaries. Whereas for the  $J_{sc}$  increase, it explains the more efficient extraction of photogenerated charge at the EL and HTL interfaces [221]. You et al. showed the positive impact of mild moisture (humidity =  $35 \pm 5\%$ ) on perovskite films formation during the thermal annealing(2h at  $90^\circ C$ ), explaining that humidity can induce perovskite grain growth with enhanced PV parameters[222]

Hashmi et al. adopted the humidity assisted thermal exposure (HTE) as a post-treatment for printed carbon-based perovskite solar cells. This maturation step consists exposing the devices to high humidity ( $70 \pm 5\%$ ) and a constant temperature ( $40^\circ C$ ) for around 200h in an environmental chamber. This step demonstrated an improvement on the cells' performance with low hysteresis. The maturation process increases the interconnectivity of carbon nanoparticles through the perovskite crystals growth, which can be enhanced within the porous stack leading to higher PV parameters as presented in Figure 19. It is good to mention that the carbon layer is thick enough to block the rapid intrusion of large water droplets

coming from the humid environment and only allows the gaseous state of the moisture to pass through it and then continues through more dense mesoporous  $ZrO_2$  to assist the irreversible perovskite crystal growth without changing its chemical structure. In this approach they reported a PCE increase from 9% to 13.8% for C-PSC after the maturation process. To better investigate the long term stability of these enhanced devices they exposed them to full sun illumination at  $40^\circ C$ . The study was conducted till 350h of aging where 92% of the PCE was retained with no comparison to cells without the HTE treatment [7].

Therefore, in this manuscript one next chapter is fully devoted to mainly understand the mechanisms behind this performance enhancement comparing solar cells before and after the maturation step at T0. We will also scout the impact of the deposition technique (pipetting vs. inkjet) on this post-treatment to better understand what is occurring in the perovskite layer and at the interfaces, and if there is a dependent between the PK infiltration technique and the mechanism leading to PCE enhancement. Moreover, another chapter will be devoted to the investigation of the impact of this maturation on the lifetime of our devices under damp heat conditions.

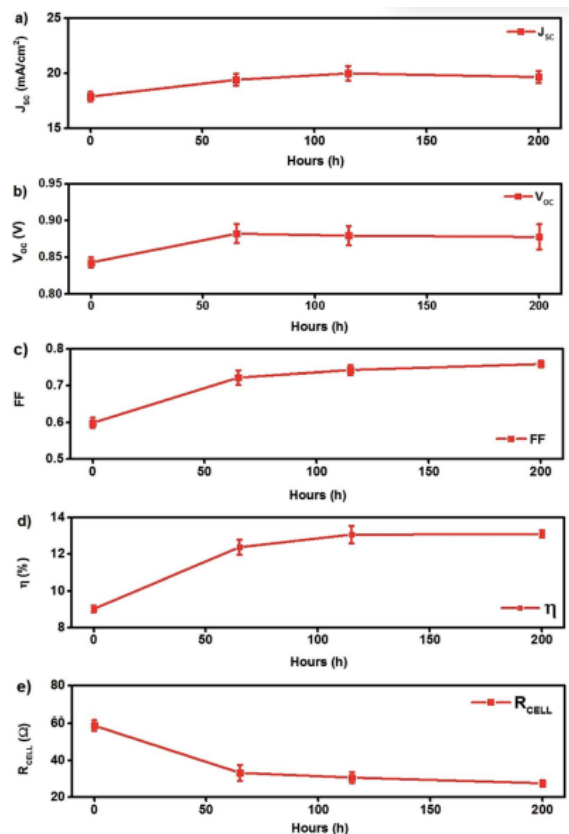


Figure 19: Photovoltaic parameters of a batch (7 cells) of C-PSCs exposed in the environmental chamber for the HTE treatment. The values represent the average of forward- and reverse-scanned J–V curves[7]

## 8. Encapsulation systems

The interest in the encapsulation techniques has progressively increased since it is one of the main reasons to develop a stable perovskite solar cell surviving all the testing conditions. The encapsulation should act as a barrier for the degradation factors as oxygen, UV radiation, temperature and moisture (Figure 20). An ideal encapsulant should have a low OTR (Oxygen Transmission Rate) and WVTR (Water Vapor Transmission Rate), high resistance to UV and thermal oxidation, good adhesion to the perovskite, chemically inert, high flexibility and dielectric constant and has similar coefficient of thermal expansion of PSCs materials[223].

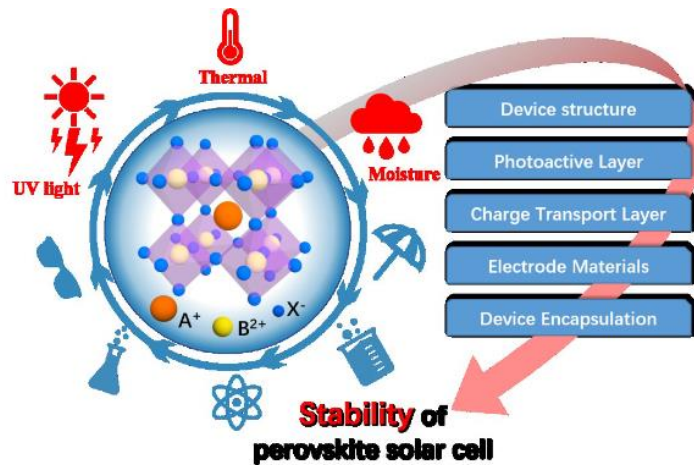


Figure 20: Schematic representation of different factors affecting the stability of perovskite solar cells[224]

The encapsulation systems today applies to PV devices are divided into two main categories: sealed glass to glass systems and polymer encapsulations.

Regarding polymer encapsulations, these systems are well known for their high flexibility facilitating their deposition method (roll to roll lamination). Many types of polymer encapsulants exist such as: poly(methyl methacrylate (PMMA), polyethylene terephthalate (PET), polytetrafluoroethylene (PTFE), polycarbonate (PC), polydimethylsiloxane (PDMS), ethylene-vinyl alcohol copolymer (EVOH), polyethylene- naphthalate (PEN), flexible polymer-based hybrid multilayers, and polymer composites[225]. Weerasinghe et al. used indium doped zinc oxide coated polyethylene terephthalate (IZO-PET) as an encapsulant for perovskite solar cells (IZO-PET/TiO<sub>2</sub>/CH<sub>3</sub>NH<sub>3</sub>PbI<sub>3</sub>/Spiro-OMeTAD/Au). The permeation testing revealed its efficient role against moisture ingress through the adhesive layers and around electrical contacts compared to solar cells without encapsulation. They achieved 12% in terms of efficiency and reported a stable PCE with no variation during storage under ambient conditions for more than 500h for encapsulated cells[226]. Castro-Hermosa et al. evaluated PET, flexible ultra-high permeation barrier films, and rigid glass as encapsulation barriers for PSCs and demonstrated that by adding an adhesion promoting layer on the standard ultra-high permeation barrier films, it reduces the WVTR by a factor of 5 compared to barriers without it. A lifetime test was conducted in a dark room with constant temperature and humidity. For ultra-high permeation barrier and glass, respectively 91% and 76.6% of initial

PCE value were retained after 840h (against 6% for PET), and then respectively 60% and 30% after 4000h [227].

For glass to glass systems, it consists in placing the device between two sealed glass sheets. Indeed, as generally known, glass is one of the best encapsulating materials, but most glass covers need a sealant to completely encapsulate the device. Unfortunately this technique requires high temperature exceeding 100°C which is challenging regarding the temperature sensitive PSCs. Therefore, thermo-curable or UV-curable sealants have been studied such as Surlyn ionomer, butyl rubber, polyisobutylene (PIB), epoxy resin/glue and so on[228][229][54][230][231].

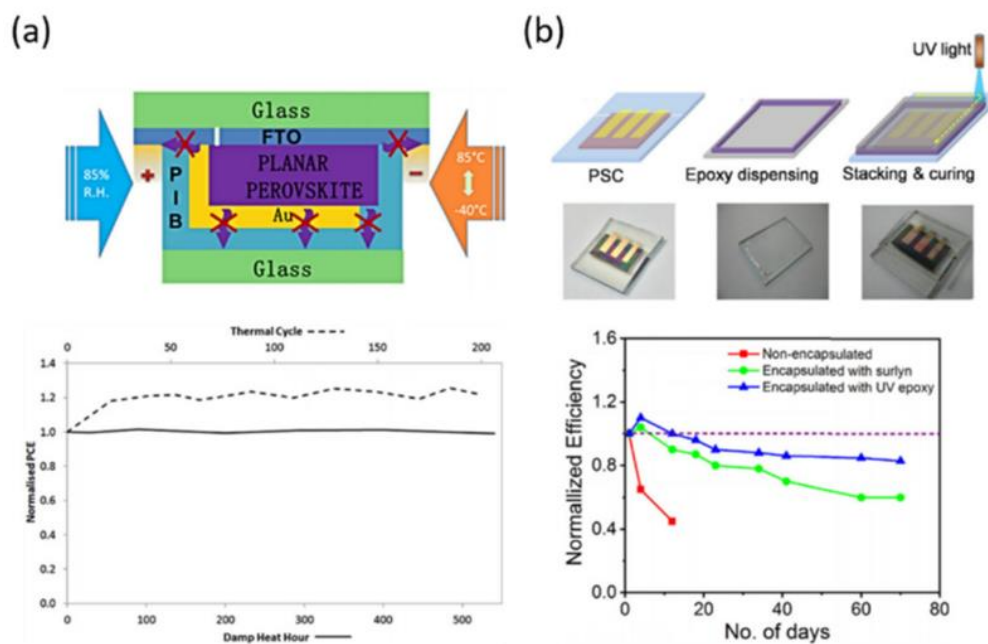


Figure 21: (a) Schematic illustration of polyisobutylene (PIB) blanket used as cover encapsulant and edge sealant for perovskite solar cell and its corresponding normalized PCE during thermal cycle test (b) Top-row of glass-to-glass encapsulation of PSC with UV-curable epoxy edge sealant and its corresponding normalized PCE during stability test[225]

Shi et al. adopted the PIB as edge sealant or blanket layer at low temperature as demonstrated in Figure 21 a). PIB was cut and deposited in a way to cover and protect the PSC. The complete device was hot-pressed to avoid the formation of bubbles and ensure good bonding. Compared to EVA and UV-cured epoxy, PIB is more inert in terms of reactivity with the PK layer[228]. Ramasamy et al. [232] used UV-curable epoxy and Surlyn gasket (SG), both used as edge sealant as shown in Figure 21 b). Right after encapsulation, the SG device's PCE decreases of 24.43% whereas it decreases of 14.72% for UV-epoxy. This decrease is caused by the high temperature during the SG sealing (125°C) and the UV irradiation for the UV-epoxy crosslinking, both inducing decomposition of the perovskite layer. The stability of the devices was then studied in the dark at 30°C and 50% of R.H. showing that unencapsulated devices degraded after 14 days with 60% PCE loss, compared to the SG and UV-epoxy sealed devices showing first an increased efficiency after 1 week and then a slightly more severe decrease for SG however maintaining 60% of initial PCE value after 70 days, against 83% for epoxy gasket.

In this manuscript, glass-glass encapsulation was selected, and five different systems were scouted in order to seal the glass-glass encapsulation. The idea was to investigate the impact of those various systems on our various developed devices. Indeed, glass lids were sealed together by lamination with different hot-melt thermoplastic films: Surlyn (SG or SF according to its gasket or film usage) (WVTR = 0.66 g/m<sup>2</sup>/day)[233], polyolefin (PO) (WVTR = 0.8–5.5 g/m<sup>2</sup>/day) [234], Polyurethane (PU) (WVTR = 1.6 g/m<sup>2</sup>/day)[235], trilayer polyolefin (tPO ENLIGHT™) (WVTR = 1.1 g/m<sup>2</sup>/day)[236] and tPO together with PIB (tPO+PIB)(PIB WVTR = 10<sup>-2</sup> to 10<sup>-3</sup> g/m<sup>2</sup>/day)[228].

Surlyn is an ionomer resin-copolymer that consists in methacrylic and ethylene moieties. These ionomers can automatically form a cross-linking between the ionic components of the polymer during the synthesis[237]. They are thermoplastic materials and are characterized by their high weathering stability and water vapor barrier. They found a huge success when applied as encapsulant with an epoxy edge seal by Grancini et al. with no decline in performance after 10 000 h under continuous illumination at 50°C in a carbon based perovskite solar cell[6]. However, Cheachoroen et al. demonstrated that the Surlyn encapsulated PSC lead to delamination with a drop in performance after thermal cycling due to the high elastic modulus (394 MPa) and low fracture energy[233].

Polyurethane is formulated by step-growth polyaddition of diisocyanates and polyols in order to obtain urethane bonds. PU possess high transmittance (exceeding 90%), chemical inertness and good UV and thermal stability. Moreover, this encapsulant system is low-cost and does not require an expensive polymerization procedure. PU has been used as an additive in the PK precursor enhancing the device performance as showed Huang et al. when they reported how PU retarded the crystallization, reduced the trap states, carrier recombination and improved the bendability thanks to its elasticity forming cross linking network at the grain boundaries[238][235]. Kaltenbrunner et al. used PU as an encapsulant and obtained very stable devices in outdoor environment in a perovskite solar cell [239]. Fu et al. reported that PU encapsulation can be carried out at 80°C and enhance the thermal stability preventing the moisture ingress[240].

Polyolefins (PO) have no chemical reactions with the perovskite when applied as an encapsulant and possesses low elastic modulus which was demonstrated to withstand 200 thermal cycle tests. These encapsulants have high electrical resistivity, low WVTR, high transmittance, high chemical inertness and excellent moisture barrier [241]. They can be divided into polyolefin elastomer and thermoplastic polyolefin families. The first one contain crosslinking agents which form a 3D network during the lamination process, whereas in the latter no crosslinking occurs but only a melting during the lamination process that takes less than 10 mins[242]. Both consist of a polyethylene backbone with different side groups.

In addition to PO, in our work an additional sealant named “tPO” for tri-layer PO was also used. It is the ENLIGHT™ Polyolefin Encapsulant, which is a composite film commercialized for silicon PV encapsulation as sole backsheet (WVTR = 1.1 g.m<sup>-2</sup>.d<sup>-1</sup>). It consists in three layers:

encapsulant layer, bonding layer and high-temperature-resistant outer layer as shown in Figure 22 that eliminate delamination and ensure easy lamination.

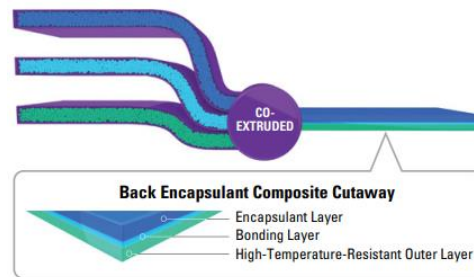


Figure 22: ENLIGHT™ Polyolefin Back Encapsulant Composite Films[243]

Polyisobutylene edge-seal is widely used in industrial silicon photovoltaic modules. PIB is known for its low moisture diffusivity and low glass transition temperature ( $T_g = -75^\circ\text{C}$ ) and is widely used as an edge sealant with a thickness of 0.2-0.6 mm as showed Kempe et al. since it has good adhesion and electrical insulation properties [244]. Moreover, PIB has low WVTR =  $10^{-2}$ - $10^{-3} \text{ gm}^{-2} \text{ d}^{-1}$  and low elastic modulus (9 MPa). According to literature [228], it can improve the stability of perovskite devices under damp heat testing and thermal cycling. Hence, in our study it was added to the tPO film in order to test its potential to enhance the sealing system, as illustrated in Figure 23.

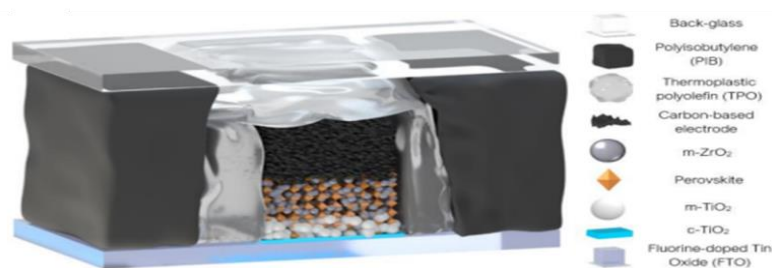


Figure 23: Illustration of C-PSC device stack used in this work when encapsulated glass-glass sealed with tPO and PIB[97]

## 9. Durability qualification testing and accelerated aging tests

Many stability studies have been reported to better understand the reasons behind the degradation of the perovskite solar cells. All these studies were based on the International Summit on Organic Photovoltaic Stability (ISOS) protocols, which are the standardized ageing experiments[245]. These tests are for lab-scale devices and aim to ensure the comparability of PV testings in order to improve the quality of published data. These protocols can be applied on solar cells or even on neat materials, or half cells to better explain the degradation processes.

Perovskite solar cells degradation could be caused by many factors including: high temperature[246], exposure to visible[247] and UV light[248], humidity[249], and electrical bias[250]. The most known applied tests are: dark storage testing, outdoor testing, light soaking testing, thermal cycling testing and light-humidity-thermal cycling testing as shown in Table 3[245]. All of these tests could be conducted at different temperature and relative humidity conditions.

Table 3: Overview of existing ISOS protocols and suggested additional protocols that account for the properties of perovskite[245]

Test ID	Light source	Temperature	Rel. humidity	Environment/Set-up	Characterization light source	Load
<b>Dark storage (ISOS-D)</b>						
ISOS-D-1	None	Ambient (23 ± 4 °C)	Ambient	Ambient air	Solar simulator or sunlight	OC
ISOS-D-2	None	65, 85 °C	Ambient	Oven, ambient air	Solar simulator	OC
ISOS-D-3	None	65, 85 °C	85%	Env. chamber	Solar simulator	OC
<b>Bias stability (ISOS-V)</b>						
ISOS-V-1	None	Ambient (23 ± 4 °C)	Ambient	Ambient air	Solar simulator	Positive: $V_{bias}$ , $V_{oc}$
ISOS-V-2	None	65, 85 °C	Ambient	Oven, ambient air	Solar simulator	$E_p/q$ , $J_{sc}$
ISOS-V-3	None	65, 85 °C	85%	Env. chamber	Solar simulator	Negative: $-V_{oc}$ , $J_{mp}$
<b>Light-soaking (ISOS-L)</b>						
ISOS-L-1	Solar simulator	Ambient (23 ± 4 °C)	Ambient	Light only	Solar simulator	MPP or OC
ISOS-L-2	Solar simulator	65, 85 °C	Ambient	Light & temperature	Solar simulator	MPP or OC
ISOS-L-3	Solar simulator	65, 85 °C	- 50%	Light, temperature & RH	Solar simulator	MPP
<b>Outdoor stability (ISOS-O)</b>						
ISOS-O-1	Sunlight	Ambient	Ambient	Outdoor	Solar simulator	MPP or OC
ISOS-O-2	Sunlight	Ambient	Ambient	Outdoor	Sunlight	MPP or OC
ISOS-O-3	Sunlight	Ambient	Ambient	Outdoor	Sunlight and Solar simulator	MPP
<b>Thermal cycling (ISOS-T)</b>						
ISOS-T-1	None	RT to 65, 85 °C	Ambient	Hot plate/ oven	Solar simulator	OC
ISOS-T-2	None	RT to 65, 85 °C	Ambient	Oven/env. chamber	Solar simulator	OC
ISOS-T-3	None	-40 to + 85 °C	< 55% <sup>(1)</sup>	Env. chamber	Solar simulator	OC
<b>Light cycling (ISOS-LC)</b>						
ISOS-LC-1	Solar simulator/ Dark Cycle	Ambient (23 ± 4 °C)	Ambient	Light only	Solar simulator	MPP or OC
ISOS-LC-2	period: 2, 8, or 24 h Duty cycle:	65, 85 °C	Ambient	Light & temperature	Solar simulator	MPP or OC
ISOS-LC-3	1:1 or 1:2	65, 85 °C	< 50%	Light, temperature & RH	Solar simulator	MPP
<b>Solar-thermal cycling (ISOS-LT)</b>						
ISOS-LT-1	Solar simulator	Linear or step ramping between room temp. and 65 °C	Monitored, uncontrolled	Weathering chamber	Solar simulator	MPP or OC
ISOS-LT-2	Solar simulator	Linear ramping between 5 °C and 65 °C	Monitored, controlled at 50% beyond 40 °C	Env. chamber with sun simulator	Solar simulator	MPP or OC
ISOS-LT-3	Solar simulator	Linear ramping between -25 °C and 65 °C	Monitored, controlled at 50% beyond 40 °C	Env. chamber with sun simulator and freezing	Solar simulator	MPP or OC

Dark storage testing (ISOS-D) aim to evaluate solar cell's lifetime with no exposure to light. It tests the tolerance of the device to components present in the air like oxygen and CO<sub>2</sub> or when moisture and high temperature are existing. This testing is important since ambient species can impact the mobile defects density, ions and electronic traps within the PK layer. Dark storage can decompose the perovskite and ambient species may charge the PK surface leading to ion distribution modifications [251][249][252]. Thermal stability can be studied by applying high temperature to PSC in the dark, chemical and structural instabilities of the different layers



could be detectable[253][254]. Since the tests should be applicable independently of the PK phase transitions, ISOS protocols suggest keeping the testing temperatures above the tetragonal to cubic phase transition for MAPbI<sub>3</sub> (ISOS-D1: ambient, ISOS-D2: 65 or 85°C). ISOS-D3 correspond to the so called “damp-heat test” highlighting the impact of the humidity (85% R.H) when the studied solar cells are kept at high temperature [245]. According to the IEC 61215 standards, the 85°C/85% R.H. damp-heat test is the only one accepted by both module manufacturers and buyers (for silicon devices). A controlled ageing chamber should be used to maintain high humidity and temperature and avoid condensation[255].

ISOS-V tests consist exposing the solar cells to electrical bias in the dark and study its behaviour. This latter can degrade the PSC by causing ion migration or charge carrier accumulation. Both positive and negative biases are potentially damaging for the device. A  $V_{MPP}$  or  $V_{OC}$  is generally applied as a positive bias condition. This test has not been applied to PSC to date, only on Si PV devices. The reverse bias is applied for partly shaded solar modules to match the current flow through the rest of the device. When the solar cell passes this test, it is recommended to keep it in the dark for a period of time to trace its recovery in order to arrive to a stable state since bias tests cause a redistribution of charges and it is reversible once the stress has stopped[245].

Light soaking tests (ISOS-L) can cause chemical reactions leading to perovskite degradation and defects formation[256][257]. This test is know to promote phase segregation[258]. As especially UV light increases the non-radiative recombination rate, UV blocking layers are required for devices to become more stable[259].

Concerning the outdoor stability studies (ISOS-O), it happens with natural sunlight in the ambient conditions. This type of testing is unstable since many factors can impact it like the weather, the location, the season... Many studies have been made trying to correlate between lifetime under real weather conditions to that obtained under accelerated stresses.

The problem is that it will depend of used materials (photoactive and non-photoactive materials constituting the full device). As for example, according to either mountain or tropical climate, respectively 1000h or 4000h of stability under 85°C/85%RH damp-heat test will be equivalent to a 25 years lifetime for silicon devices[260].

Thermal cycling in the dark (ISOS-T) and light-humidity-thermal cycling (ISOS-LT) evaluate the solar cells degradation caused by solar radiation, temperature, and humidity upon cycling conditions. PSCs may degrade more severely in a variable ambiance than in under constant conditions due to ion accumulation at the contacts[261]. To simulate day-night cycles, cycling through light-dark periods can be also conducted (ISOS-LC). It was shown that a PCE increase may be detected under illumination after storage in the dark and this is due to a neutralization of interfacial defects by photogenerated charge carriers or due to some changes causing ion migration. Therefore, the PSCs suffer from ‘Fatigue’ effect where after each light-dark cycle, the PCE restoration is reduced despite its increase after the dark storage. Hence, a reversible and irreversible degradation mechanism is taking place into the device[262][263][94].

## 10. Conclusion

In summary, being the cleanest and the most exploitable resource of energy, solar energy can potentially meet the developing requirements for the planet's energy needs. In recent decades, great attention has been paid to perovskite solar cells thanks to their facile and low manufacturing processing achieving power conversion efficiencies exceeding 25%[264]. In this chapter, we showed the three different generations in the PV field and focused on the perovskite solar cells (PSCs) constituting the third generation. PSC are characterized with their  $ABX_3$  structure. Several advantages allowed these materials to show great potential to positively devote to the development of large-scale production processes such as: strong absorption, tunable band gap, low exciton binding energy, and prolonged carrier migration length as we previously discussed and highlighted the crystallography importance[265]. In addition, we described the architecture of a perovskite solar cell and its different layer and we pointed out on the carbon based perovskite solar cells since one of the main drawbacks of the commercialization of the PSCs is the use of noble metals like gold and silver as back electrodes. Therefore, carbon based perovskite solar cells have emerged the field[81]. Simple perovskite  $MAPbI_3$  is the most common and extensively investigated hybrid perovskite[122]. So our work adopted this type of PK. The biggest challenge for carbon based perovskite solar cells is their lack for long-term stability. Hence, the use of additives and a post-treatment can strengthen the perovskite structure and enhance the device performance as we demonstrated[168]. Moreover, we explained that determining the PK deposition method is a crucial step to achieve high performance and eliminate recombination and stability issues. Regulating the crystallinity and consequently the morphology and the uniformity of the perovskite film is controlled by the deposition technique[55]. Among many techniques, drop casting is an easy, low-cost and without waste method performed in ambient air[5]. Another deposition technique is the inkjet controlled by a computer program in order to obtain the desired pattern. This method allow the large scale productions in an easy and rapid way [214]. In the upcoming study, drop casting and inkjet methods will be adopted as the PK infiltration techniques for the Carbon-based perovskite solar cells. The studied systems will be encapsulated with different encapsulants in order to better optimize the best sealant. In addition, this manuscript highlights the maturation step that ensures an efficient improvement of the device. Therefore, comparative analyzes evaluated the difference between cells before and after maturation. And finally, damp heat (ISOS-D3) studies were conducted as stability tests to better understand the causes behind the device degradation.



# CHAPTER II: EXPERIMENTAL PART

## 1. Studied materials: perovskite solar devices fabrication

### 1.1. Devices architecture preparation

The architecture of typical monolithic carbon-based, hole transport layer-free, perovskite solar cells produced by Solaronix S.A. and studied in this manuscript consists of: a front FTO/glass substrate (TCO22-7/LI, Solaronix low-iron sodalime glass coated with a 7 Ohm/sq. fluorine doped tin oxide layer of about 400 nm, electrode size: 25 x 20 mm), electron-selective layers to avoid the non-radiative recombination at the front electrode (TiO<sub>2</sub> compact and mesoporous layers), a mesoporous ZrO<sub>2</sub> insulating layer to avoid ohmic shunts and a mesoporous carbon back electrode.

A 18±3 nm compact layer of TiO<sub>2</sub> was deposited by spray pyrolysis over the FTO glass substrates of titanium diisopropoxide bis(acetylacetonate) diluted in ethanol at 400-500°C. A 550±75 nm thick mesoporous TiO<sub>2</sub> layer was then obtained by screen-printing a nanoparticle paste (Ti-Nanoxide T165/SP, Solaronix) followed by a 45 min firing at 500°C. Similarly, a 1±0.1 µm thick mesoporous ZrO<sub>2</sub> layer was obtained by screen-printing a nanoparticle paste (Zr-Nanoxide ZT/SP, Solaronix) followed by firing at 500°C. Finally, a 17±1.5 µm conductive porous carbon electrode was obtained by screen-printing a high-temperature graphite/carbon paste (Elcocarb B/SP, sheet resistivity: ≤25 ohm/sq, Solaronix) followed by 30 min firing at 400°C, affording a 12.5 x 12.0 mm active area.

Thicknesses were measured using mechanical profilometry after each deposition step, the perovskite precursors solution being added at the end using either drop casting or inkjet printing deposition method.

### 1.2. Perovskite filling (precursors formulation, infiltration processes and annealing)

The perovskite precursor solution (5-AVA)<sub>x</sub>MA<sub>1-x</sub>PbI<sub>3</sub> (reference 76802, Solaronix) in gamma-butyrolactone (GBL) solvent containing lead iodide (PbI<sub>2</sub>) and methylammonium iodide (MAI) in equimolar concentration with 5mol% of 5-ammoniumvaleric acid iodide (5-AVAI) was infiltrated within the mesoporous layers of the previously described stack using one of the two following procedures.

- *Drop casting process:*

A polyimide adhesive mask is first applied around the TiO<sub>2</sub>/ZrO<sub>2</sub>/carbon filled area. This protection prevents the solution from spreading outside the active area of the solar cell (it will be removed after the perovskite drying step). Then, 5.76µL of the perovskite precursor solution (1.2 mol/mL) is dispensed at the center of the active area with the help of a home-made automated micropipette. The samples are first left in a box (lid on) on a perfectly leveled support for 30 min, allowing liquid spreading over the active area mesoporous surface. Then, annealing is performed in an oven at 50°C for about 60 min.

- *Inkjet printing process:*

The perovskite precursor solution (1.2 mol/mL) is transferred to an inkjet printer cartridge, and a total quantity of 3.3  $\mu\text{L}$  was infiltrated all over the  $\text{TiO}_2/\text{ZrO}_2/\text{carbon}$  filled area with a drop-on-demand inkjet printer (PixDro LP50, 512 nozzle printhead) at a resolution of 1200 x 1200 dpi. The samples are annealing for 10 min on a hot-plate set to 50°C to form the desired perovskite crystal structure.

### 1.3. Post-treatment: maturation step

The fresh solar cells were eventually exposed to a post-treatment in order to achieve maximal performance. As reported in literature [7], this maturation step was performed at 40°C with 75% RH atmosphere for 100–150 h. Considering the interest of this step, a large part of the manuscript will be devoted to the elucidation of occurring mechanisms.

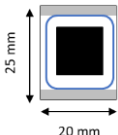
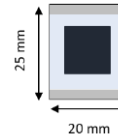
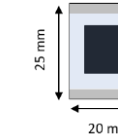
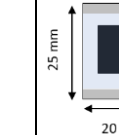
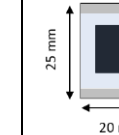
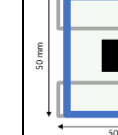
### 1.4. Encapsulation systems

As generally known, glass is one of the best encapsulating materials, but most glass covers need a sealant to completely encapsulate the device. Individual cells were here encapsulated soon after completion using 5 different sealing systems.

A 1.8 mm thick soda-lime glass lid was thus used as back glass. It was sealed by lamination together with different hot-melt thermoplastic films, using a vacuum membrane laminator with integrated pump, programmable heat and duration (1 atmosphere pressure). The back glass was sealed either to only the front glass substrate of the solar device in the case of gaskets, or additionally to also the entire solar device for full covering films.

Tableau 4 presents the references and characteristics of used sealants: a thermoplastic ionomer as edge sealant (Surlyn gasket: SG) or full covering film (SF), three full covering thermoplastic sealants (polyurethane: PU, polyolefin: PO and an ENLIGHT™ polyolefin: tPO), and finally a double system with a polyisobutylene (PIB) edge sealant added to full covering tPO. As indicated, for the latter, larger glass substrates 50x50 mm (with identical active area cells) were used in order to make room for the extra PIB edge sealant. In other cases than TPO, it was necessary to use several layers to obtain a complete fusion overall the surface. This is due to the fact that the active part is a little in relief.

Tableau 4: The references and characteristics of the used sealing systems: SG, PO, PU, tPO and tPO with PIB

<b>Sealing material</b>	Surlyn gasket (1 mm wide)	Surlyn film	Polyurethane film	Polyolefin film	ENLIGHT™ polyolefin film	ENLIGHT™ polyolefin film + PIB gasket (4.5 mm wide)
<b>Acronym</b>	SG	SF	PU	PO	tPO	tPO+PIB
<b>Commercial Reference</b>	Meltonix 1170-60 (Solaronix), DuPont Surlyn®	Meltonix 1170-60 (Solaronix), DuPont Surlyn®	Polyurethane hot melt adhesive film (Hengshenglong)	Polyolefin hot melt adhesive film (Hengshenglong)	XUS62250 (Hangzhou First Applied Material), Dow ENLIGHT™	XUS62250 (Hangzhou First Applied Material), Dow ENLIGHT™ + Quanex SET Tape
<b>Thickness</b>	60 μm	5x60 μm	2x150 μm	2x180 μm	400 μm	400 μm
<b>Lamination conditions</b> (T°C, evacuation and lamination times)	105°C, 1 + 1 min	105°C, 1 + 1 min	105°C, 1 + 1 min	105°C, 1 + 1 min	105°C, 1 + 1 min	110°C, 2 + 8 min
<b>Illustration</b> (light blue colors represent the sealing agent)						

## 2. Aging campaigns conditions

To compete with other PV technologies and to investigate the solar cells' long-term stability for commercial desires, the aging behavior of the devices has been evaluated. According to International Electrotechnical Commission tests standards (IEC 61215), the only test accepted by both module manufacturers and buyers (for silicon devices) is an exposition of solar devices to air atmosphere at 85°C with 85% of relative humidity.

In this manuscript, only one accelerated aging has been used on encapsulated solar cells: 85°C and 85% R.H. in a humidity chamber (HCP150, Memmert), also called Damp-Heat test. Cells were aged in the same orientation than for end-use operating conditions, i.e. transparent FTO electrode side up. For non-encapsulated devices, softer conditions were also tested: 85°C, and 85°C + 45% R.H. Two configurations were tested: PK upwards receiving severe humidity and oxygen stress, or PK downwards placed on a glass slide. Regular sampling of cells was realized to monitor certain functional and/or structural properties. The aim was to track relevant aging markers in order to determine the degradation mechanisms involved.

## 3. Characterization methods

### 3.1. Photocurrent density-voltage measurements (J-V)

The photocurrent density-voltage curve of a solar cell is the superposition of the J-V curve of the solar cell diode in the dark with the light-generated current density of the solar cell. The light has the effect of shifting the J-V curve down where power can be extracted from the diode as shown in Figure 24.

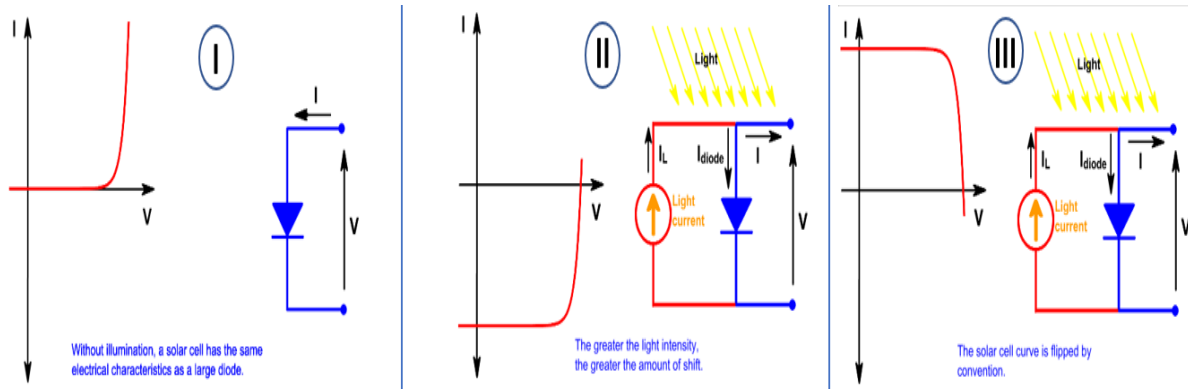


Figure 24: Current-voltage (I-V) curves of solar cell (I) at dark, (II) under illumination, (III) flipped by convention towards positive currents [266]

Photocurrent density-voltage (J-V) curves were recorded under illumination with a solar light simulator Newport Oriel LCS-100 providing an AM 1.5G spectrum of 1000 W/m<sup>2</sup> light intensity and using a SP-150 potentiostat/galvanostat of Biologic (Software EC-Lab-11.26). Before any J-V acquisition, the solar simulator lamp was left heated for 30 min. The power calibration (1000 W.m<sup>-2</sup>) was systematically carried out each day using a calibrated reference silicon cell with a readout meter (Oriel, Model: 91150V - Series Number: 801/0871). Measurements were done either on full cells (1.5 cm<sup>2</sup>) or by positioning an opaque mask on the solar cells with square aperture size equal to 0.64 cm<sup>2</sup>. This allows to better compare inkjet printing and drop casting obtained cells by excluding potential unfilled edges in the case of drop casting process. The J-V measurement was divided into three parts: first a V<sub>oc</sub> measurement under dark, followed by another one under illumination for around 10 mins till reaching a stable V<sub>oc</sub>, then a reverse J-V scan (from the V<sub>oc</sub> to -0.2V).

In order to elucidate the “bump” phenomena, various scan rates were used going from low scan rates (1mV/s) up to fast ones (1000 mV/s). Thanks to the resulting curve, the photovoltaic parameters (PCE, J<sub>sc</sub>, V<sub>oc</sub>, FF, R<sub>s</sub> and R<sub>sh</sub>) were estimated using a homemade program on Spyder software. For this, experimental data were fitted with an analytical formula taken from the electrical model presented in Figure 25. It consists of a real diode (I<sub>D</sub>) in parallel with an ideal current source (I<sub>ph</sub>). Two resistive elements accounting for power losses have been added: a parallel (or shunt) resistance R<sub>sh</sub> and series resistance R<sub>s</sub>.



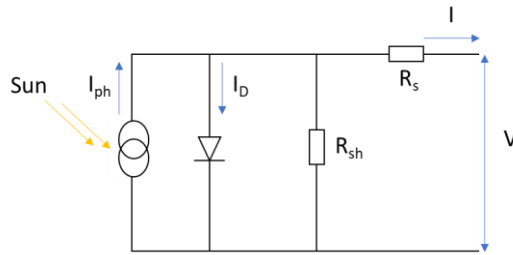


Figure 25: The equivalent circuit for a PV solar cell  
(with  $I_{ph}$  – the photogenerated current;  $I_D$  – the diode current;  $R_s$  – the series resistance;  $R_{sh}$  – the shunt resistance)

a) Short-circuit current density ( $J_{sc}(\text{mA}/\text{cm}^2)$ )

The short-circuit current density is the current density that the solar cell delivers under illumination when the voltage across the device is zero. This parameter is directly related to the photo-generation which means that the stronger the intensity of the light radiation, the greater the  $J_{sc}$  since more electron-hole pairs can be generated. The short-circuit current depends on many factors which are:

- the number of photons generated by the incident light source as mentioned before, here =  $1000 \text{ W}\cdot\text{m}^{-2}$ ,
- the spectrum of the incident light, here AM1.5G spectrum was selected. This coefficient is the one generally used for solar applications in temperate regions. It corresponds to a zenith distance of  $48.2^\circ$ ,
- the optical properties (absorption and reflection) of the solar cell and the carrier collection probability of the solar cell, which depends especially on the surface passivation and the carrier lifetime in the photoactive layer,
- the area of the solar cell (here =  $0.64 \text{ cm}^2$ ). That is why we instead present the short-circuit

current density ( $J_{sc} = \frac{I_{sc}}{\text{illuminated area}}$ )

b) Open circuit voltage ( $V_{oc}(\text{V})$ )

The open-circuit voltage corresponds to the maximum voltage measured at the solar cell's terminals under illumination at zero current crossing it. Light radiation generates electron-holes pairs within the PV device leading to a shift in the thermodynamic equilibrium which is manifested by the generation of a voltage across the PV cell. The  $V_{oc}$  mainly depends on the studied device and therefore of its forbidden band gap energy ( $E_g$ ). It also depends on non-radiative recombinations that take place within the cell. These recombinations can be issued from different causes such as surface recombinations (surface defects), Shockley-Read-Hall recombinations (impurities, gaps, insertions etc.) or Auger recombinations (if the charge carrier density is very high).

c) Filling Factor (FF)

The short-circuit current and the open-circuit voltage are, respectively, the maximum current and voltage collectible from a solar cell. Nonetheless, at both of these operating points, the power from the solar cell is zero. The fill factor is a parameter corresponding to the ratio between the maximum power that can be reached by the solar cell  $P_{mp}$  (Power at maximum power point, with  $V_{mp}$  and  $J_{mp}$  the voltage and the current density for which the solar cell delivers its maximum power) to the product of  $V_{oc}$  and  $J_{sc}$ :

$$FF = \frac{P_{mp}}{V_{oc} \times J_{sc}} = \frac{V_{mp} \times J_{mp}}{V_{oc} \times J_{sc}}$$

This PV parameter is particularly sensitive to the quality of the charge carriers' movements within the PV system, caused by shunt resistive losses (punctual short circuits) and the imbalance between the transport of electrons and holes [267]. Graphically, the FF is a measure of the "squareness" of the solar cell and is also the ratio of the area of the smallest rectangle which will fit in the IV curve (in green on Figure 26) on the largest one (in yellow on Figure 26).

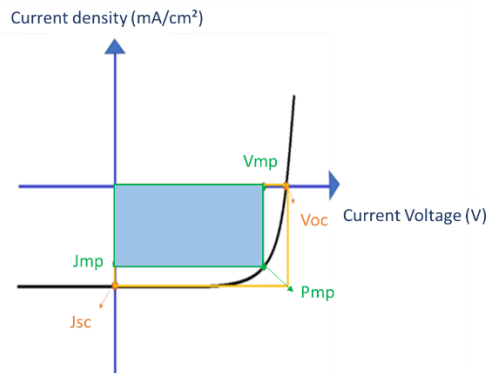


Figure 26: J-V curve of a solar cell showing the different PV parameters ( $J_{sc}$ ,  $V_{oc}$ ,  $FF$ ,  $V_{mp}$ ,  $J_{mp}$  and  $P_{mp}$ )

#### d) Power Conversion Efficiency (PCE)

To compare the PV solar cell performances, the power conversion efficiency is the most commonly used parameter. This efficiency is defined as the ratio between the maximum power delivered by the cell and the incident light power  $P_{inc}$  ( $1000W/m^2$ ), and is generally presented in percentage. Therefore, the efficiency can be calculated as a function of the three previously mentioned PV parameters and is defined as:

$$PCE = \frac{P_{mp}}{P_{inc}} = \frac{V_{oc} \times J_{sc} \times FF}{P_{inc}}$$

#### e) Series ( $R_s$ ) and shunt ( $R_{sh}$ ) resistances

The  $R_s$  and  $R_{sh}$  parameters of our solar cells were evaluated using a homemade program on Spyder software using the equivalent circuit presented in Figure 25.

The solar device architecture can limit the solar cell's performance inducing resistive losses like leakage current, trapping charge carriers at the PK/TiO<sub>2</sub> interface and recombination

effects issued from the applied voltage and the illumination intensity. These losses are piloted by the series and shunt resistances. Shunt resistance are typically due to manufacturing defects. Low shunt resistance causes power losses in solar cells by providing an alternate current path for the light-generated current. Series resistance in a solar cell has three causes: firstly, the movement of current through the emitter and base of the solar cell; secondly, the contact resistance between the metal contact and the photoactive material; and finally, the resistance of the top and rear metal contacts. The main impact of series resistance is to reduce the fill factor, although excessively high values may also reduce  $I_{sc}$ .

### 3.2. Impedance spectroscopy

Impedance spectroscopy (IS) offers a simple method referring to an equivalent circuit to evaluate the different resistances and capacities linked to ionic and electronic mechanisms taking place into the cell in order to extract its dynamic parameters. This characterization is performed with or without a solar light simulator Newport Oriel LCS-100 providing an AM 1.5G spectrum of  $1000 \text{ W/m}^2$  light intensity and using a potentiostat/galvanostat (SP-300 with impedance measurement option, Biologic).

In a first way, the impedance was measured under one sun at three different cycles of low voltage amplitude: 0.6, 0.7 and 0.8V with  $\Delta V = 30 \text{ mV}$  where the modulated current response is evaluated. Moreover, before any measurement, a five minutes wait is recommended to better stabilize the short-current circuit of the device. The frequencies go from high (1MHz) to low (0.5 Hz). Thanks to the EC-Lab-11.26 software where all the parameters were fixed, a  $\text{Re}(Z) = -\text{Im}(Z)$  is plotted from which different resistances and capacities are extracted, with reference to the following circuit [268]:

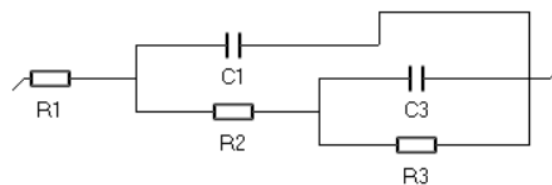


Figure 27: The equivalent circuit for the IS measurement

Consequently, the Nyquist Diagram generated from the impedance spectroscopy where two semi-circles appear, one at high frequencies and the second at low frequencies, is fitted to the equivalent circuit with: R1 the series resistance, C1 the capacitance associated with the dielectric response of the perovskite controlling the capacitance at high frequencies exceeding 1 kHz which is also called the geometric capacitance, R2 the recombination resistance in the perovskite, R3: the recombination resistance at the interfaces and C3 the capacitance associated to the surface charge accumulation at the interfaces appearing at low frequencies ( $\sim 1 \text{ Hz}$ ) especially between  $\text{TiO}_2$  and the perovskite [268].

Besides, two other impedance measurements were also made using the same equivalent circuit for the fitting. In the first case, the illumination intensity is varying (0.2, 0.4, 0.6, 0.8 and 1 Sun) at open circuit voltage where charge recombination impact was evaluated. Whereas, at the second one, the illumination is fixed at 1 Sun under non-open circuit but instead, modifying the voltages (0, 0.18, 0.36, 0.54, 0.72 and 0.9 V) to better study the charge extractions. [268][269]

### 3.3. Light Beam Induced Current (LBIC)

LBIC-mapping measurements enable to know the short-circuit current at a local level within the entire cell active surface. The main defects can be identified and the performance homogeneity of the solar cell can be evaluated. The device used was developed in the laboratory, following the principle of commercial devices. The cell is excited with a green laser beam (5 mW, 520 nm), with a diameter of 0.7 mm which moves with steps of 1 mm on the surface of the cell. It scans a line path starting from left to right for 18 mm on the X axis (starting point: red dot), then goes up by 1 mm following the Y axis attached to a moving X-Y stage and controlled by a computer to end after a 18 x 18 mm path (ending point: blue dot), see illustration in Figure 28-a. As shown in Figure 28-b, a map is then obtained showing the dispersion of the local short-circuit current within the cell. The obtained maps were post-treated by ImageJ to extract Isc values and to have a distribution for each studied cell.

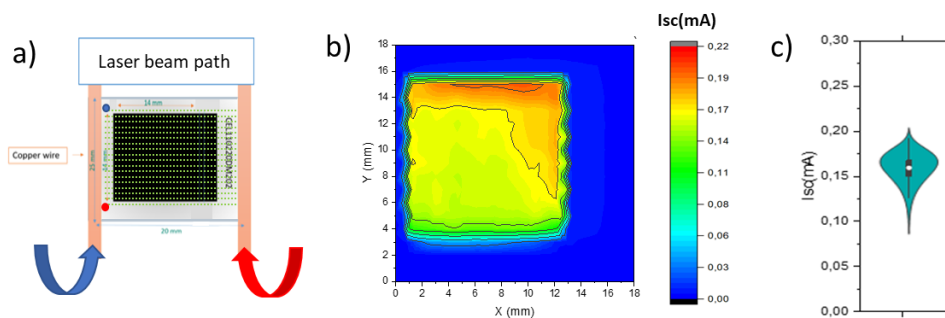


Figure 28: a) Schematic representation of the laser beam path on all the active area surface of typical studied solar cells, b) Example of LBIC mapping for an inkjet perovskite solar cell, c) Violin plot of the previous LBIC mapping

### 3.4. UV-visible spectroscopy (absorbance and diffuse reflectance)

For optical properties, UV-visible diffuse reflectance and absorbance spectra were measured with a Shimadzu UV-2600 spectrophotometer equipped with an integration sphere accessory. Measurements were made out between 200 and 1100 nm at the average speed fixed by equipment (0.5 nm step). In the case of perovskite solar cells, UV-Visible spectroscopy is used to identify optical transitions associated with perovskites and other degradation materials like the  $\text{PbI}_2$ . This technique is very widespread for the analysis of perovskite films, because of its speed and simplicity. In this manuscript, two main modes were used: absorbance and diffuse reflectance. For both modes, a standard white plate of  $\text{BaSO}_4$  is placed at each exit window of

the integration sphere to correct the baseline as shown in Figure 29. For the measurement, in the diffuse reflectance mode, the BaSO<sub>4</sub> plate on the side of the sample is replaced by the latter. All measurements were carried out with no reference sample.

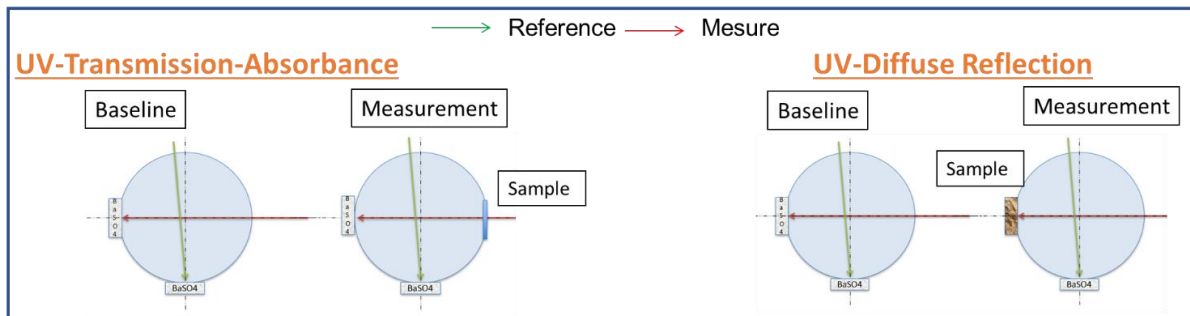


Figure 29: Spatial configuration of the UV-visible integration sphere and its principle for placing the sample into it at the transmission-absorbance and the diffuse reflectance modes

Absorbance measurements require a previous step of CP removal. Indeed, the opacity of the thick CP layer avoid any possible transmission of light within the entire device. This was realized using adhesive scotch peeling method, and could present the disadvantage to remove also a small quantity of the perovskite layer. However, this technique allows the detection of the different materials constituting the active layer of the solar cell like: 3D PK at 780 nm, PbI<sub>6</sub> octahedron or PbI<sub>2</sub> at 550 nm, monohydrated PK at 380 nm and 2D PK at 420 nm. In a more convenient way, diffuse reflection measurements were used mainly to confirm the presence of the PK layer and to evaluate its bandgap value. It can also give information on important modifications during the aging campaigns.

Optical band gaps were calculated thanks to the Tauc plot method though the following equation using Kubelka-Munk function in order to be applied to reflectance spectra:

$$[F(R) \times hv]^{\frac{1}{r}} = \left[ \frac{(1 - \frac{R(\%) }{100})^2}{2 \times (\frac{R(\%) }{100})} \times hv \right]^{\frac{1}{r}} = f(hv) \quad [270]$$

with R(%) is the reflectance obtained from the spectra,  $h\nu$  the photon energy, and the coefficient  $r$  being 2 or 1/2 for respectively indirect or direct allowed transitions. The latter is the case to consider for perovskite[271].

As illustrated in Figure 30-b, a linear region of the plot is identified and a straight line is fitted in order to find the bandgap value using the tangent method.

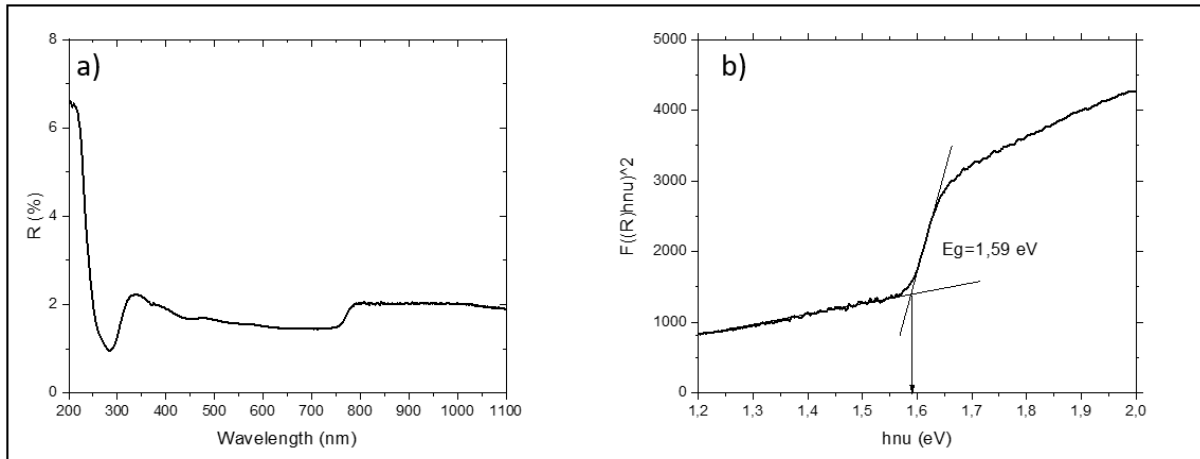


Figure 30: a) UV-visible diffuse reflection spectrum on a typical studied cell, b) Illustration of optical bandgap determination using the Tauc plot method according to diffuse reflection data

### 3.5. Photoluminescence spectroscopy (PL)

To obtain a PL spectrum, solar cells were analyzed in a Shimadzu RF-6000 spectrofluorometer with a 520 nm excitation wavelength using a scan rate of 6000nm/min, an excitation slit of 5 nm, an emission slit of 5 nm and a measurement range of 600-900 nm. The typical analyzed area of our solar cells is represented in green on Figure 31-a. The excitation was oriented through the FTO/TiO<sub>2</sub> side of PK solar cells, since the opaque carbon paste screens the excitation beam (typical obtained spectrum presented in Figure 31-b). Samples were placed between two filters: the first (575 nm low-pass) located in front of the excitation source and the second (600 nm high-pass) in front of the source of emission beneficial to abolish any artefact coming from the spectrophotometer (see illustration in Figure 31-c).

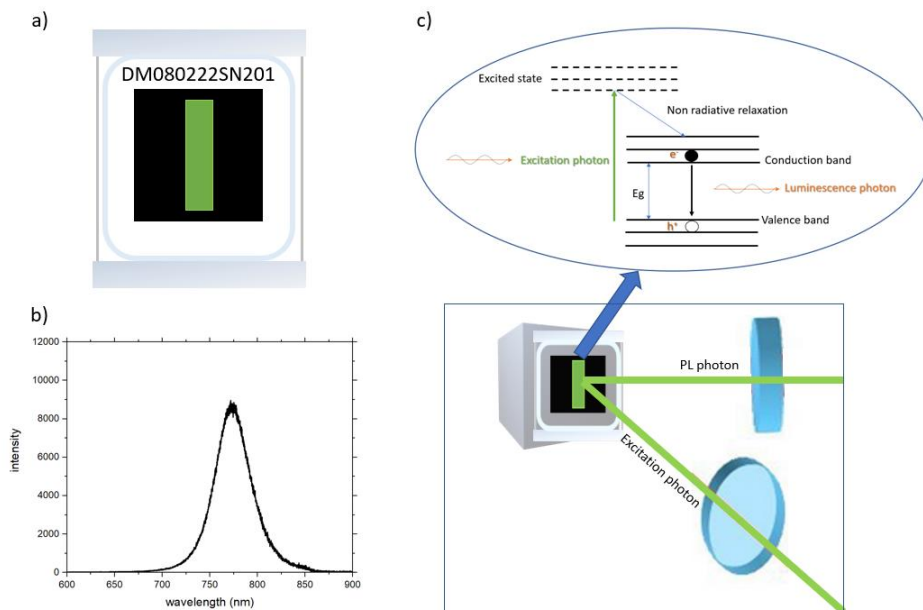


Figure 31: a) Schematic representation of typical studied solar cells and highlight of the excited area (in green), b) Example of typical PL spectra obtained by excitation through the FTO/TiO<sub>2</sub> side of PK solar cells c) Schematic representation of the photoluminescence excitation measurement and phenomena.

The objective of this technique is based on the radiative excitation of the solar cell, which then emits in return an emission spectrum characteristic of the studied perovskite present in the device. In the case of semiconductors, which is our case, the incident photons must have an energy greater than that of the semiconductor's band gap to participate to the photovoltaic mechanism. The photon is then absorbed by the material and leads to the formation of electrons in the conduction band and holes in the valence band. When an electron in an excited state recombines with a hole, this recombination can lead to the emission of a photon (radiative transition). The photons emitted by the material have less energy than that of the absorbed photons due to non-radiative relaxation. The energy of these photons is measured in order to obtain the photoluminescence spectrum. The band gap transition of the perovskite being around 765 nm, the wavelength of excitation must be at a higher energy in order to be able to observe photoluminescence specific to perovskite. Typically, an excitation wavelength at 520 nm seems optimal to observe the emission line of the perovskite. Therefore, it is possible to follow both the evolution of the recombination rate (mainly radiative) taking place in the material and at the interfaces, and of the value of the forbidden band thanks to the position of the photoluminescence peak. This characterization is complementary to UV-visible spectroscopy.

### 3.6. Photoluminescence imaging (PL imaging)

PL imaging allows to study the solar cell local characteristics in order to highlight the mechanisms of degradation taking place within the cell. It was performed in open-circuit condition with a homemade device. The cell is placed in a dark chamber under a camera with two green light-emitting diode (LED) flashing the cell with an emission spectrum between 400 and 550 nm during 1 second. Just after the flash, a photograph is taken by the camera. The camera is equipped with a 650 nm high-pass filter from Edmund Optics (York, UK) in furtherance of minimizing reflection artefacts originating from the excitation light. Thus, an image in grey level of local PL emitted by the solar cell is obtained. As previously demonstrated in the work of Planes et al. [272], each pixel of the taken photo, is responded by the gray level (GL) according to the sample, the time of exposure, the focal length, the aperture of the camera and the filter. Referring to the prementioned work, we recalibrated our set up where the camera's gain takes part of the relationship linking the measurement of the gray level with the illumination (E) produced by the light source of the solar cell as following:

$$GL = k \times T^\alpha \times P_{gain}^\beta \times E$$

with k a constant specific to the camera (0.00125), T the exposure time (1000 ms),  $\alpha(1)$  and  $P_{gain} = 10^{G/10}$  with G the gain of the camera,  $\beta(0.57)$  are pre-determined constants, and E the radiant flux intensity ( $W/m^2$ ) produced by the solar cell (which corresponds to the flux emitted per unit of surface)[272]. Thanks to this relation and to a previous determination of these parameters within our lab, it is possible to post-treat the photo to evaluate the radiation flux intensity emitted by the cell (see Figure 32.b). This technique has several advantages, it is

relatively rapid and it is a non-destructive characterization since no connection at the electrodes level is required.

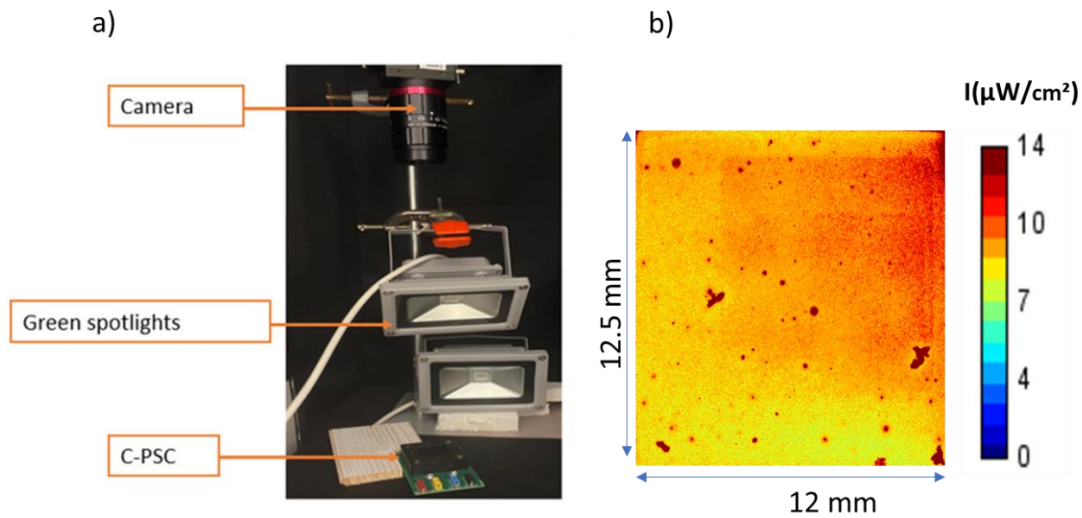


Figure 32: a) Set up of the PL imaging, b) Example of obtained images after the post treatment with ImageJ of the PL photo

### 3.7. X-ray diffraction analysis (XRD)

The crystalline composition of all perovskite layers has been determined by X-ray diffraction (XRD). An X-ray tube generates an X-ray beam directed to the sample at an angle  $\theta$  (Figure 33-a). This beam is then diffracted by the crystal lattices of the different crystalline structures existing in the solar cell. These lattices are oriented in diffraction network according to the Bragg equation:  $2d_{hkl} \sin(\theta) = n\lambda$

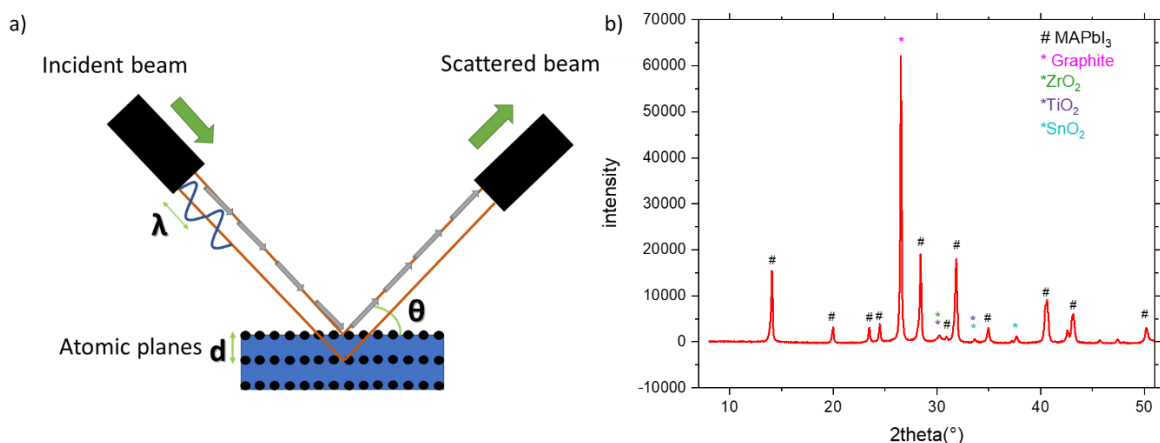


Figure 33: a) Schematic representation of the XRD technique b) XRD patterns of the carbon-based perovskite solar measured at the center of the cell

where  $d_{hkl}$  (nm) is the spacing of the crystal layers,  $\theta$  ( $^\circ$ ) is the incident angle (the angle between incident ray and the scatter plane),  $n$  is the diffraction order and  $\lambda$  (nm) is the wavelength of the incident X-rays. The structural composition of the cell's layers were



determined thanks to XRD analysis using a PANalytical X'Pert PRO MPD X-Ray diffractometer between 2-theta of 8° and 50° with Cu-Ka source. Before analyzing the samples, the solar cells were opened and the carbon paste layer was peeled off, for the reason that the carbon peak detected in the XRD diffractogram is so intense that it covers the rest of the peaks. Data were then treated on Match! Software, that identifies the different phases and lattice parameters composing the solar cell (see Figure 33-b). In addition, a background subtraction was carried out after integrating the XRD diffractogram to evaluate the crystalline and the amorphous phases ratio. Thus, the relative crystallinity of the elaborated perovskites and of the PbI<sub>2</sub> amount could be evaluated for each sample thanks to the following equations:

$$\text{PK Relative crystallinity (\%)} = \frac{\sum(\text{PK areas})}{\text{Integrated Area} - \sum(\text{other peaks areas})} \times 100$$

$$\text{PbI}_2 \text{ Relative crystallinity (\%)} = \frac{\sum(\text{PbI}_2 \text{ areas})}{\text{Integrated Area} - \sum(\text{other peaks areas})} \times 100$$

This technique is very useful for studying the degradation of the perovskite layer. Thus, it is possible to define degradation signature, such as the amount of the crystalline PbI<sub>2</sub> present in the active layer. The disadvantage of this technique is that it only allows to evaluate the crystalline phases of the solar cell, then it is necessary to associate it with other characterizations in order to completely study the cells.

In the fourth chapter, we adopted the XRD-2D with Hypix2D detector for the center and corner's analyses. For the third and fifth chapter conventional XRD diffractometer was used.

### 3.8. Scanning Electron Microscopy (SEM) and Energy Dispersive X-Ray Analysis (EDX)

The morphology and thickness of the solar cell layers were evaluated by scanning electron microscopy (SEM) using FEG ZEISS Ultra 55 in secondary electrons mode at the Consortium of Common Technological Means (CMTC) in Grenoble. The surfaces were prepared by cross polishing, which is an ionic polisher allowing to better observe the cells in cross section while preserving the structure. This technique consists of an argon beam with a low angle of incidence, where the argon does not implant itself on the sample's surface but only polishes it cleanly, leaving it free of any artefacts. Thanks to an integrated camera, the solar cell is placed with an excellent precision assuring a successful preparation. SEM images were made using secondary and back-scattered detectors. To complete the detection of all the present elements in the solar cell, some EDX analysis were performed, allowing precisely to identified the depth filled by perovskite infiltration (within the TiO<sub>2</sub>, ZrO<sub>2</sub> and carbon layers) as shown in Figure 34. This analytical technique excites the solar cell with an electron beam dissipating some of the absorbed energy by ejecting a core-shell electron. To fill its place a higher energy outer-shell electron proceeds, releasing the difference in energy as an X-ray which has a characteristic spectrum based on its atom of origin. Therefore, the position of the peaks allows

to identify the elements, and the intensities correspond to their concentration. The layers thicknesses were calculated using ImageJ.

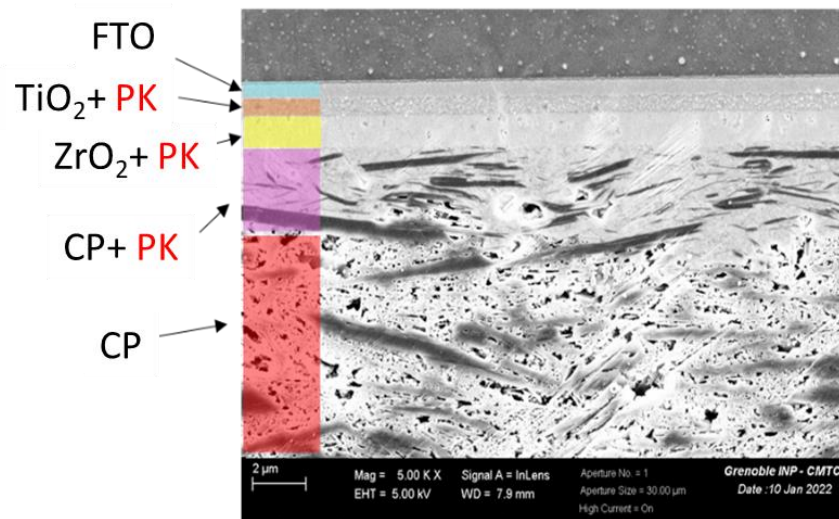


Figure 34: Cross-section SEM images of a typical studied solar cell with the identification of the layers realized thanks to complementary EDX analysis

### 3.8. Raman spectroscopy

Raman spectroscopy is a scattering technique presented as an intensity-versus-wavelength shift. It is based on the inelastic scattering of incident radiation through its interaction with vibrating molecules where it probes the molecular vibrations. This technique consists to illuminate the solar cell with a 520 nm monochromatic laser beam which interacts with the molecules of the sample and a scattered radiation arises. The latter having a frequency different from that of incident light which is used to generate a Raman spectrum. Therefore, the molecular vibrations excited by the laser allow chemical identification of the sample [273]. In this study, Raman spectroscopy is performed with a x50 objective with an integration time of 20 seconds repeated 3 times in confocal mode. The studied solar cell is opened (without an encapsulation) and the CP was already peeled off. While measuring, it is important to evaluate the PK layer without reaching to the TiO<sub>2</sub>. After the measurement, the spectra are normalized to the CP band at 1400 cm<sup>-1</sup>. The intensities can not be evaluated since the CP band depends on the amount of carbon still present. Consequently, only the presence or absence of the different bands will be considered in this study like the MA<sup>+</sup> band or to the MAPbI<sub>3</sub> band.

### 3.9. Profilometry

To measure the layer thicknesses and roughness before and after maturation, each layer was measured (Stack 1: FTO+TiO<sub>2</sub>-c, Stack 2: FTO+TiO<sub>2</sub>-c+TiO<sub>2</sub>-m, Stack 3: FTO+TiO<sub>2</sub>-c+TiO<sub>2</sub>-m+ZrO<sub>2</sub>, Stack 4: FTO+TiO<sub>2</sub>-c+TiO<sub>2</sub>-m+ZrO<sub>2</sub>+CP) with a KLA Tencor model D500 profilometer after scratching the sample with a scalpel in its center. For each given value, a total of nine

profiles on three different samples were made. The measurement range used with this equipment was: 2.5  $\mu\text{m}$  for the three first stacks, 10  $\mu\text{m}$  for the fourth one and for complete cells (with the infiltrated PK layer). A scan speed of 0.05 mm. s<sup>-1</sup> and a force equivalent to 0.2 mg were applied, together with 10 000 data points in each profile with a filter-level average equal to 4 points. Finally, each time the software was started, a calibration was systematically performed using a certified height of 9425 Å.

### 3.10. Fourier-transform infrared spectroscopy (FTIR)

Fourier transform infrared spectroscopy is a non-destructive, sensitive and precise technique that determines the nature of the chemical functions present in a solution, powder or a solid film. FTIR uses the vibrational and rotational properties of the chemical bonds of a molecule when submitted to an infrared wavelength since the molecule's covalent bonds will selectively absorb radiation of specific wavelengths causing this vibration. Therefore, after applying the Fourier transform (a mathematical function that takes apart waves and returns the frequency of the wave based on time), obtaining an infrared spectrum allows the identification of infrared bands characteristic of a chemical bond. Hence, it is then possible to go back to the chemical structure of the studied sample by analyzing the spectrum. The latter presents absorbance in a function of the wavenumber (1/wavelength corresponding to the vibration energy of the molecular bonds). This characterization technique was adopted in our work to study the encapsulation systems sealing our devices to better understand the chemical bonds formulating the films, together with their potential aging upon damp-heat test. The analyses were carried out using a PerkinElmer FT-IR Spectrometer Spectrum 3. The used crystal is diamond from PIKE MIRacle and the measurement was completed in a spectrum range going from 4000 cm<sup>-1</sup> to 600 cm<sup>-1</sup> with a 2 cm<sup>-1</sup> resolution in Attenuated Total Reflectance mode (ATR). The background is settled without the use of any sample before starting the measurements. Each presented spectrum is the average of 16 analyses. All these parameters are fixed on the 'Spectrum' software.

# CHAPTER III: OPTIMIZATION OF THE ENCAPSULATION SYSTEMS FOR CARBON-BASED PEROVSKITE SOLAR CELLS

## Introduction

Long term stability of carbon-based perovskite solar cells is one of the fundamental issues to be resolved for the upcoming production of this technology since the devices are sensitive to many factors such as oxygen, moisture, UV, heat and more. Therefore, suitable encapsulation systems protecting the perovskite layer are critical and mandatory to prevent degradation and to move on from laboratory scale to the industrial one[274][275]. The choice of the encapsulating material(s) is depending on several parameters: optically transparent where light is incident on the PSC, wide thermal stability, efficient barrier stability against moisture and oxygen ingress causing the degradation and chemically inert towards the layers in contact without releasing by-products harmful to the electrical contacts and the active layer[235].

Generally, the most know encapsulating material is glass having low water vapor transmission (WVTR) and low oxygen transmission (OTR) rates[227]. However, another critical component is needed to prevent the contact of the PV device with the surrounding environment[276], i.e. an adhesive material ensuring the sealing of the glass-glass encapsulation, comprising of not the sealing of the solar device itself. For silicon industrial devices, EVA is often used. Its damp-heat aging resistance and ultraviolet aging resistance are not good, however crosslinking has been proved to be effective for improving its aging resistance, together with the addition of antioxidant, UV absorber, and light stabilizer [277]. Nevertheless, EVA is not suitable for perovskite device encapsulation due to its high 140°C needed temperature for hot-melt lamination[234] and to its acetic acid by-product of degradation which is harmful for perovskite[241]. In this work, six different hot-melt sealants will be laminated using a 105-110°C lamination temperature. All possess interesting permeation rates: Surlyn ionomer (WVTR = 0.66 g/m<sup>2</sup>/day) [233], polyolefin (PO) (WVTR = 0.8–5.5 g/m<sup>2</sup>/day) [234], polyurethane (PU) (WVTR = 1.6 g/m<sup>2</sup>/day) [235], trilayer polyolefin (tPO ENLIGHT™) (WVTR = 1.1 g/m<sup>2</sup>/day) [236] and tPO together with PIB (tPO+PIB)(PIB WVTR = 10<sup>-2</sup> to 10<sup>-3</sup> g/m<sup>2</sup>/day) [228].

All the studied cells have undergone the maturation process already discussed in the first chapter and for which the next chapter is devoted, where the devices' performance are enhanced after exposure to 40°C and 75% R.H for 100-150 hours[7]. In this chapter, we reported two major sections: the first one covers the differences at T0 for all inkjet and pipetted cells encapsulated with the previously mentioned different systems. Whereas as for the second part, we mainly focused our attention on moisture and oxygen protection and studied the devices' stability under damp heat conditions according to International Electrotechnical Commission tests standards (IEC 61215)[278] to better evaluate the impact of extreme conditions on the devices' lifetime.

Figure 35-a presents the architecture of perovskite devices studied here, together with the type of encapsulation considered, i.e. a back glass sealed using the lamination of a thermoplastic sealant. The advantages of the C-PSC architecture used is that the perovskite precursors can be incorporated within the mesoporous stack (m-TiO<sub>2</sub>/m-ZrO<sub>2</sub>/m-Carbon) afterwards the fabrication of this stack, by simple injection. This makes it a very clean method for perovskite deposition, which has been here performed either using drop casting or inkjet printing methods, illustrated in Figure 35-b and respectively called “pipetted PK” and “inkjet PK” in the following. Pipetted PK is obtained by a one-spot injection of the perovskite precursor solution, and a simple polyimide mask allows the perovskite not to overflow the mesoporous pattern after diffusion. Inkjet PK is an advanced mass reproducible technique allowing homogeneous large area deposition. The small deposited drops allowed a clean and precise filling of the mesoporous pattern. In order to fill the same area than with pipetted PK method, without rewetting dry-areas, a 42.7% less quantity of precursor solution was used. A stable precursor ink is essentially recommended to produce precise infiltration and printing of perovskite absorbing layer while not damaging the print head of the printer. For this purpose, the perovskite ink used is a gamma-butyrolactone ( $\gamma$ -GBL) solution of methylammonium lead iodide (MAPbI<sub>3</sub>) perovskite precursors with 5-ammonium valeric acid iodide (5-AVAI).  $\gamma$ -GBL is an interesting solvent as the perovskite precursor solution in  $\gamma$ -GBL possesses a reversible solubility allowing its regeneration[279]. In addition, 5-AVAI is an additive improving the formation of the perovskite crystals into the mesoporous layers especially into the TiO<sub>2</sub> by enhancing the contact strength between the active layer and the ETL. This additive modifies the 3D PK architecture into a quasi-2D one linking the (-COOH) group in the 5-AVAI to the TiO<sub>2</sub> surface and therefore generating a preferential growth in the normal direction, which is important for thick perovskite layers as in our C-PSC architecture [5][94].

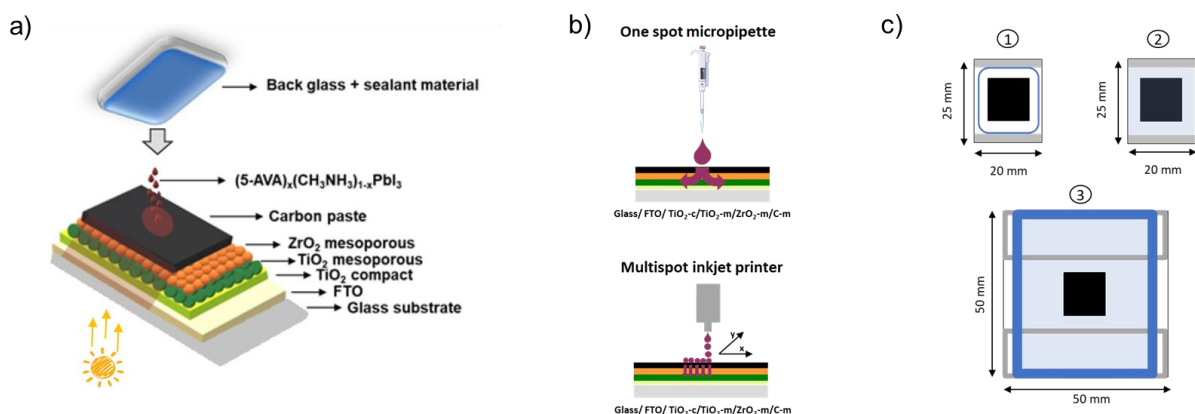
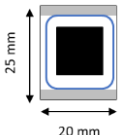
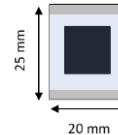
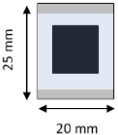
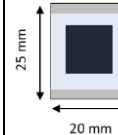
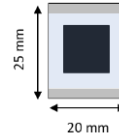
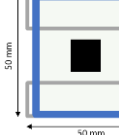


Figure 35: a) Presentation of the C-PSC architecture of perovskite devices studied, b) Schematic representation of the two perovskite infiltration methods used and compared, c) Guide for the different encapsulation systems using: ① Surlyn Gasket edge sealant, ② PO or PU or tPO or Surlyn full covering films and ③ tPO film + PIB edge sealant.

The final step, illustrated in Figure 35-a and detailed in Figure 35-c, is the solar devices encapsulation. Individual cells were here encapsulated soon after completion using 6 different sealing systems. As generally known, glass is one of the best encapsulating materials, but glass

covers need a sealant to completely encapsulate the device. A soda-lime glass back sheet and a soda-lime front substrate were here used as the outer skins of the C-PSC solar cells as main protection against moisture and oxygen stresses. These two glass protections were sealed by lamination together with different hot-melt thermoplastic films. Used sealing systems were: a thermoplastic ionomer as edge sealant (Surlyn gasket: SG) or full covering film (SF), three full covering thermoplastic sealants (polyurethane: PU, polyolefin: PO and an ENLIGHT™ polyolefin: tPO), and finally a double system with a polyisobutylene (PIB) edge sealant added to full covering tPO. Table 5 presents the references and characteristics of used sealing materials. Given the different nature of the studied encapsulation systems, it is likely that the lamination conditions may differ. Figure 35-c show the location of each type of sealing materials within the device: SG gasket is illustrated by a blue thin line in the draw ①, full covering films by light blue coverages in the draws ② and ③, PIB edge sealant by a blue thick line in the draw ③. As indicated, larger glass substrates of 50x50 mm were used for the latter to make room for the extra PIB edge sealant. However, identical active area cells were used for all configurations (indicated by the 1.5 cm<sup>2</sup> black area).

Table 5: the references and characteristics of the used sealing systems: SG, PO, PU, tPO and tPO with PIB

<b>Sealing material</b>	Surlyn gasket (1 mm wide)	Surlyn film	Polyurethane film	Polyolefin film	ENLIGHT™ polyolefin film	ENLIGHT™ polyolefin film + PIB gasket (4.5 mm wide)
<b>Acronym</b>	SG	SF	PU	PO	tPO	tPO+PIB
<b>Commercial Reference</b>	Meltonix 1170-60 (Solaronix), DuPont Surlyn®	Meltonix 1170-60 (Solaronix), DuPont Surlyn®	Polyurethane hot melt adhesive film (Hengshenglong)	Polyolefin hot melt adhesive film (Hengshenglong)	XUS62250 (Hangzhou First Applied Material), Dow ENLIGHT™	XUS62250 (Hangzhou First Applied Material), Dow ENLIGHT™ + Quanex SET Tape
<b>Thickness</b>	60 μm	5x60 μm	2x150 μm	2x180 μm	400 μm	400 μm
<b>Lamination conditions</b> (T°C, evacuation and lamination times)	105°C, 1 + 1 min	105°C, 1 + 1 min	105°C, 1 + 1 min	105°C, 1 + 1 min	105°C, 1 + 1 min	110°C, 2 + 8 min
<b>Illustration</b> (light blue colors represent the sealing agent)						

The adhesion of Surlyn® gasket or film on glass is excellent, leading to a fully transparent sealing[240]. This material is an ionomer resin, i.e. an "ionically cross-linked" thermoplastic copolymer, adding flexibility and resistance. It is a copolymer of ethylene with a polar vinyl monomer (methacrylic acid), and the cross-linkages are obtained by partial neutralization of acid sites with a metal salt. They found a huge success when applied as encapsulant with an epoxy edge seal by Grancini et al. with no decline in performance after 10 000 h under continuous illumination at 50°C in perovskite solar cells [6]. Lertngim et al. showed that it was also possible to apply the Surlyn composite film as an encapsulant for OPV cells [280]. Cheachoroen et al. demonstrated that the Surlyn encapsulated PSC could lead to delamination with a drop in performance after thermal cycling due to the high elastic modulus (394 MPa) and low fracture energy in PSC[233]. Polyolefins thermoplastics (PO and tPO) are also well known for their excellent adhesion on glass[242][281]. These encapsulants have high electrical resistivity, low WVTR, high transmittance, high chemical inertness and excellent moisture barrier[282] [241]. The tPO ENLIGHT™ material consists in three layers: encapsulant layer, bonding layer and high-temperature-resistant outer layer. This encapsulant has already been used in literature to study the degradation behavior in Si-cells[242], in perovskite solar cells[241] and organic solar cells[283]. Polyurethane is formulated by step-growth polyaddition of diisocyanates and polyols in order to obtain urethane bonds. PU possess high transmittance (exceeding 90%), chemical inertness and good UV and thermal stability.



Polyurethane films can be also used as sealant since they can efficaciously improve the thermal stability of the cells and prevent the intrusion of moisture[238][235]. Kaltenbrunner et al. used PU as an encapsulant and obtained very stable PSC devices in outdoor environment[239]. Fu et al. reported that PU encapsulation can be carried out at 80°C and enhance the thermal stability preventing the moisture ingress in perovskite solar devices[240]. Kim et al. reported a packaging process for OPV using PU as an oxidation barrier to improve the stability[284]. Polyisobutylene edge-seal is widely used in industrial silicon photovoltaic modules. It helps delaying moisture ingress, which protects cells, connections, and conductive oxide coatings from corrosion and degradation. According to literature [228], it can also improve the stability of perovskite devices under damp heat testing and thermal cycling. Hence, it was added to the tPO film in order to test its potential to enhance the sealing system.

### **A- Impact of the encapsulation sealing step on C-PSC initial properties**

The potential impact of the encapsulation step was first evaluated by comparing the photovoltaic parameters before and after encapsulation for the 6 different sealing systems used. Figure 36-a presents typical PV parameters for pipetted and inkjet C-PSC devices before encapsulation: power conversion efficiency (PCE), short-circuit current density ( $J_{sc}$ ), open-circuit voltage ( $V_{oc}$ ), and fill factor (FF). PCE obtained for pipetted and inkjet solar cells are quite equivalent, respectively  $13.2\% \pm 0.4$  and  $12.9\% \pm 0.3$  in reverse scan (or  $12.7\% \pm 1.2$  and  $11.7\% \pm 0.9$  in forward scan). If,  $V_{oc}$  and FF values are quite similar,  $J_{sc}$  is a little higher of  $1 \text{ mA/cm}^2$  for pipetting cells. This could be due to the additional 42.7% quantity of precursor solution used.

After the sealing, no visual modification was noticed for all the encapsulations systems. Figure 36-b bar charts represents the percent deviation of each PV parameters right after each encapsulant sealing using lamination process. Pipetted cells are represented in full colored bars and inkjet cells in hatched colored bars. It was observed a slight improvement of PCE for both pipetted and inkjet solar cells sealed using Surlyn gasket (about +1 to +1.5% of deviation), whereas a decrease is noticed for all sealings based on full films: PO (-7 to -8 % of deviation), PU (-3.4 to -5.7 % of deviation), tPO (-3.7 to -4.2 % of deviation), tPO with PIB (-8.9 to -9.6 % of deviation) and SF (-7.3 % of deviation). If the link with  $J_{sc}$  and  $V_{oc}$  variations is not always obvious, the link with FF is clear. Indeed, when only a sealing gasket is used, the FF is less impacted than when using full covering sealing films (about -0.2/-0.5 % versus -4.1 to -11.4 % of FF deviation).

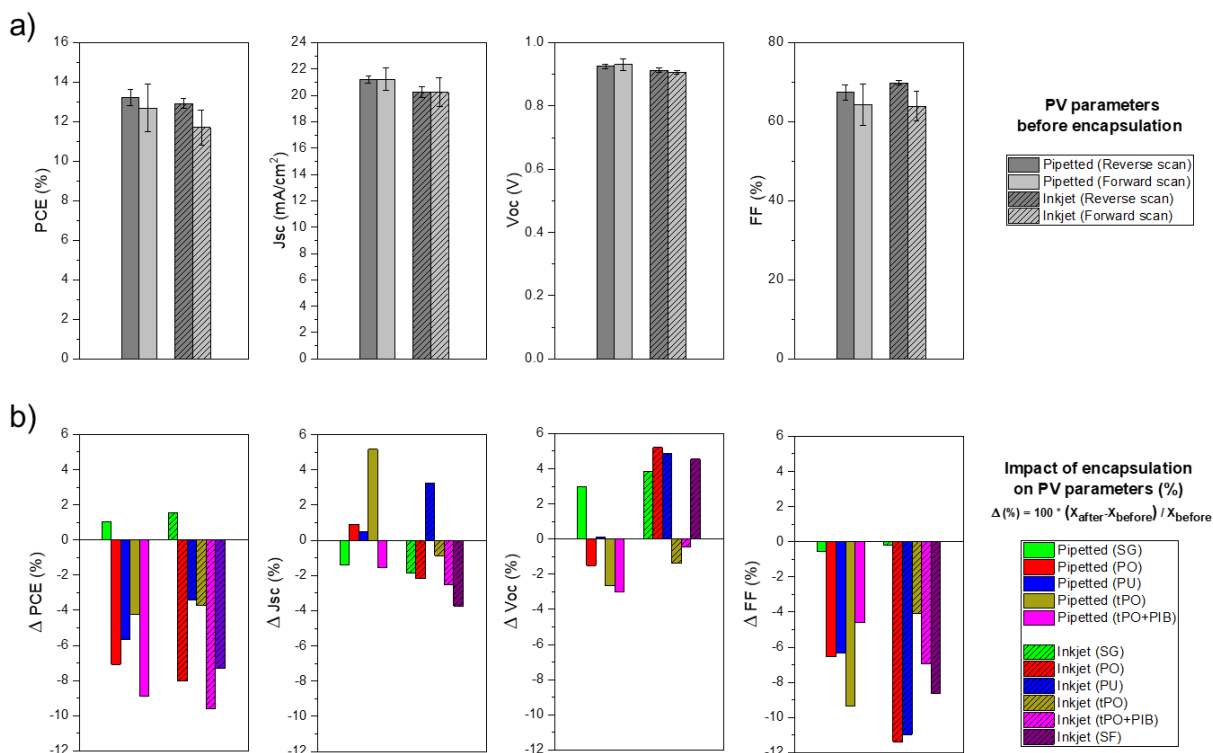


Figure 36: a) PV parameters of pipetted and inkjet C-PSC solar cells before encapsulation (average values and standard deviations for both reverse and forward scans), b) Impact of the encapsulation step on PV parameters for each studied sealing system (results are presented in percent deviation and were calculated on the average value between reverse and forward scans). J-V parameters were recorded at a 4mV/s scan speed, and representative batches of 18 cells were used for the evaluation of each sealing system impact.

UV-visible diffuse reflection spectroscopy, photoluminescence (PL) spectroscopy and X-ray diffraction (XRD) analysis were then used to better examine the impact of the encapsulation sealing step at initial stage. Reflection and emission data are presented in Figure 37 and XRD spectra are given at the end of the manuscript in Figure 47 together with their variation under ageing. The XRD parameter of interest at this stage is presented in Table 6, i.e. the perovskite relative crystallinity rate for each encapsulated system.

Table 6: XRD perovskite relative crystallinity of the pipetting and inkjet cells for each encapsulating system.

XRD Relative crystallinity rate(%) at T0	SG	PO	PU	TPO	tPO+PIB	SF
Pipetting	21,8% ± 2%	22% ± 2%	22% ± 2%	23,4% ± 2%	22,7% ± 2%	-
Inkjet	12,57% ± 2%	11,35% ± 2%	11,67% ± 2%	11,05% ± 2%	12,98% ± 2%	11,1% ± 2%

According to XRD spectra, no PbI<sub>2</sub> was detected before or after encapsulations, phases and species in presence were almost identical corresponding to tetragonal MAPbI<sub>3</sub> and the calculated relative amounts of crystallinity were similar whatever the encapsulation (i.e. about 22-23% for pipetted perovskite and 11-13% for inkjet perovskite). For this latter calculation of relative crystallinity, it was taken care to realize it on same cell batches (same electrodes and same perovskite solution) as small variations could increase the discrepancy of obtained values. The difference of relative crystallinity obtained between pipetted and inkjet cells originates from the difference of infiltration process and resulting perovskite quantity and/or

quality. This is more detailed in the next chapter together with MEB, Raman and UV-visible absorption showing a more ordered PK structure for pipetting cells.

Diffuse reflectance spectra show similar patterns and reflectance values for all encapsulating systems, except for tPO+PIB. If the spectra baseline can be slightly different for pipetted versus inkjet devices (2.0 % versus 2.49 % at 600nm), the baseline is strongly impacted with a 0.9 % value at 600nm for tPO+PIB devices. The difference between pipetted and inkjet devices is explainable as a lower content of perovskite can lead to a lower perovskite absorption band leading to a potential higher reflection within the device (devices are fully opaque due to the final carbon paste layer). As for tPO+PIB, it should be mentioned that, due to PIB edge-sealant thickness, strongest lamination conditions were needed to obtain a complete fusion of tPO overall the surface as compared to the use of tPO alone and to other films studied here. To keep reasonable the PCE impact of encapsulation process, larger glass substrates were used to make room for the extra PIB edge sealant (as illustrated in Figure 35-c-③), and a temperature of 110°C (instead of 105°C) with a duration of 10min (instead of 2 minutes) was selected for tPO+PIB lamination conditions. In spite of the impact on reflectance level, the spectra pattern and perovskite band edge were still similar (reflectance band edge at 780 nm corresponding to the end of perovskite absorption at a 1.59 eV band gap, as highlighted in Figure 37-a and-b insets).

For PL, Figure 37-c presents bar charts for average emission measured intensities according to the various encapsulations, together with typical corresponding spectra in insets. Slight variations were observed in PL intensities. They are more pronounced in the case of inkjet cells but remains largely reasonable. However, as highlighted in Figure 37-d, a wavelength blueshift occurs only for cells encapsulated with tPO+PIB. As it is not correlated with an optical bandgap shift, it can be related to either a decrease in the PK grain size or to a passivation of the PK layer during the strongest condition used for tPO+PIB lamination process [286]. In the case of other encapsulants, the tendency is more to a smaller redshift. Such redshift has already been observed, it might notably be related to a photon-recycling phenomenon, i.e. the process of reabsorption (and re-emission) of photons that results from radiative recombination [287].

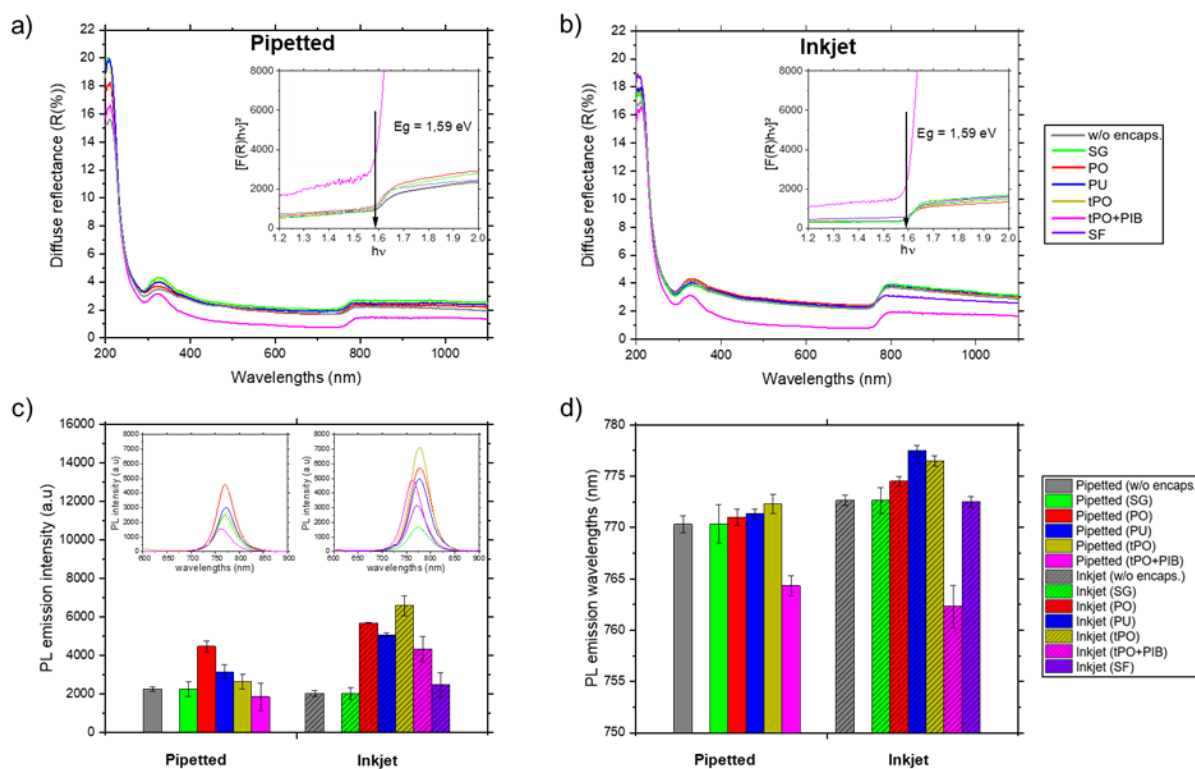


Figure 37: a) and b) UV-visible diffuse reflection spectra of respectively pipetted and inkjet cells according to different encapsulations (Tauc plots in insets), c) and d) photoluminescence emission intensities and wavelengths for an excitation at 520 nm (examples of typical obtained spectra in c insert).

To sum up this part, 6 different sealing systems were compared for pipetted and inkjet solar cells: Surlyn Gasket (SG), Surlyn Film (SF), Polyolefin (PO), Polyurethane (PU), trilayer Polyolefin (tPO) and tPO together with Polyisobutylene (tPO+PIB). At first, before any encapsulation, carbon-based perovskite solar cells have quite equivalent PV performance whatever the precursor infiltration method despite the lower 42.7% quantity of PK used for inkjet versus pipetted. Once the devices are encapsulated, it was noticed that SG may enhance the PCE of both pipetted and inkjet cells whereas an efficiency decrease occurs when using PO, PU, tPO and tPO+PIB as sealants. This variation is mainly due to the FF modification showing a less impact with the edge sealant compared to full covering films. On another note, the encapsulation step does not generate any degradation component like  $PbI_2$  referring to XRD and UV-visible analyses. Therefore, sealing systems do not impact negatively the initial solar cell performance. However, for tPO+PIB double system, since the lamination conditions were stronger than for the rest of the sealing systems, different behavior in UV spectra with lower reflectance is noticed together with blue shift of PL emission probably related to a PK grain decrease or passivation during lamination. In order to evaluate the impact of the sealing systems on the carbon-based perovskite solar cells durability, the second part is consecrated to the monitoring of an aging campaign with a full set of characterizations conducted at each sampling point.

## B- Impact of the encapsulation system on C-PSC cells durability

To investigate our C-PSC solar cells' long-term stability, the aging behavior of the different encapsulated devices has been evaluated under damp heat conditions (85°C/85% R.H.). According to International Electrotechnical Commission tests standards (IEC 61215), the only test accepted by both module manufacturers and buyers (for silicon devices) is an exposition of solar devices to air atmosphere at 85°C with 85% of relative humidity.

To verify that solar cell's lifetime is successfully extended thanks to the sealing procedure, the stability of open cells (not encapsulated) was first evaluated using softer conditions. As shown on Figure 38-a, at 85°C/45%R.H. ageing conditions, the stability of open cells do not exceed a few hours for inkjet devices and 50h for pipetted devices (respectively, open or solid round grey symbols). At 85°C without humidity (but with oxygen), their individual lifetime is extended to about 10 hours for inkjet devices and 200 hours for pipetted devices (respectively, open or solid triangle grey symbols). According to our device architecture, with a perovskite filling of the insulating ZrO<sub>2</sub> mesoporous layer overflowing in all the TiO<sub>2</sub> mesoporous layer and in a fraction of the mesoporous carbon layer to insure a good electronic contact, it seems rational to interpret the stability difference between inkjet (dotted lines) and pipetted (solid lines) devices by the fact that a 42.7% less quantity of precursor solution was used. This should lead to a lower stock of perovskite materials to face oxygen and humidity stresses, rapidly leading to non-sufficiently filled mesoporous layers, resulting in insulating devices.

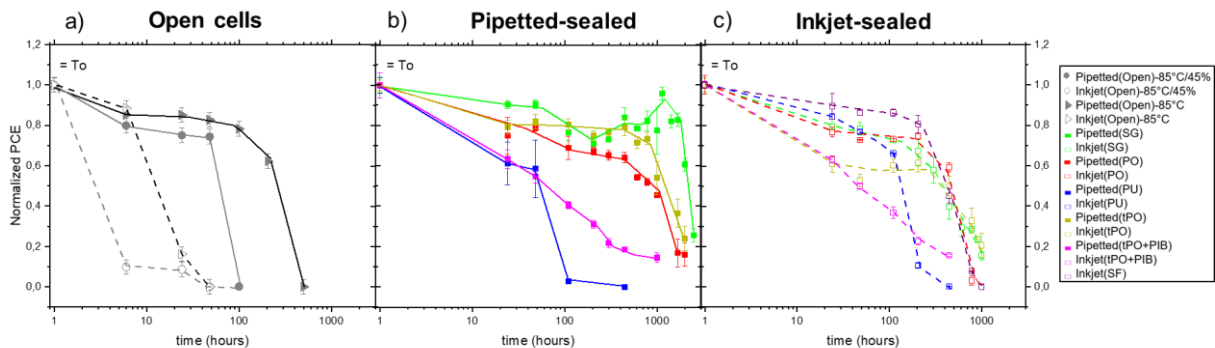


Figure 38: PCE variation with time for a) non encapsulated cells, b and c) respectively pipetted and inkjet encapsulated cells (non encapsulated cells were aged in soft conditions, i.e. 85°C/0%R.H. and 85°C/45%R.H. as indicated in the caption on the right; encapsulated cells were aged at damp heat conditions 85°C/85% R.H.).

Figure 38-b and Figure 38-c respectively shows the PCE variation with time for pipetted and inkjet devices encapsulated with various encapsulant materials. Surlyn full covering film is only presented for inkjet devices as it was decided recently to add this technology. However, an additional ageing campaign is ongoing at present time also on pipetted devices to better scout the potential of Surlyn full covering film.

Data are presented in a scale normalized to one at initial stage not to have crossed tendency curves and a logarithmic scale was selected for aging time representation for a better separation and reading of sampling points (the point positioned at 1h corresponding in reality to the performances at initial stage, i.e. right after encapsulation).

By looking at the PCE evolution with aging time, as for non-encapsulated cells, a better durability is generally observed for pipetted cells compared to the inkjet ones. As displayed, pipetted cells encapsulated with SG have the best stability with only 20% loss of initial PCE after 1500 hours of damp heat aging, followed by pipetted tPO cells with 72% loss, pipetted PO with 80% loss at 1500h. From pipetted devices, we can conclude that the less stressing sealing process not covering the active area of the device (surlyn gasket) is the most adapted sealant for the device durability. Sealing processes with full covering polyolefin-based films (tPO and PO) are close behind but with poorer results leading to a strong loss of performances after 1000 hours of damp heat ageing. The double tPO+PIB process is obviously detrimental for the functionality of the device with a strong decrease of PCE from the beginning of ageing and with a 50% loss after only 100h. It should be mentioned that, due to PIB edge-sealant thickness, strongest lamination conditions were required to totally melt the tPO overall the surface, as compared to the use of tPO alone and to other studied sealants. The pipetted PU cells studied here are the worst. Most cells become fully passive after 100 hours of ageing. This premature degradation might be related to the chemical nature of the sealing PU film that appear to undergo chemical changes in the studied conditions: the solid and flexible film having turned into a soft and sticky material.

Concerning inkjet cells: tPO+PIB and PU encapsulating materials lead to a very similar degradation mechanism already observed with pipetted cells. In contrast, SG, SF, PO and tPO all ended up with quite comparable behaviors: a relative stability with about 60-80% of initial performances up to about 200 hours of aging, followed by a fast drop of PCE for all cells. They were all described as non-functional after about 1000 hours of ageing. However, SG, SF, PO and tPO all provide a beneficial hindering of both oxygen and humidity degradation. As a result, the lifetime of all type of devices was found largely improved as compared to the non-encapsulated cells. On another note, we can make the hypothesis that the 42.7% less quantity of perovskite needed in the case of inkjet devices leads to a loss of electrical contact between the perovskite remaining layer and the carbon paste more rapidly than with pipetted devices. This will be investigated after though the study of other PV parameters (see Figure 39), together with a physico-chemical and morphological analysis of the perovskite layer.

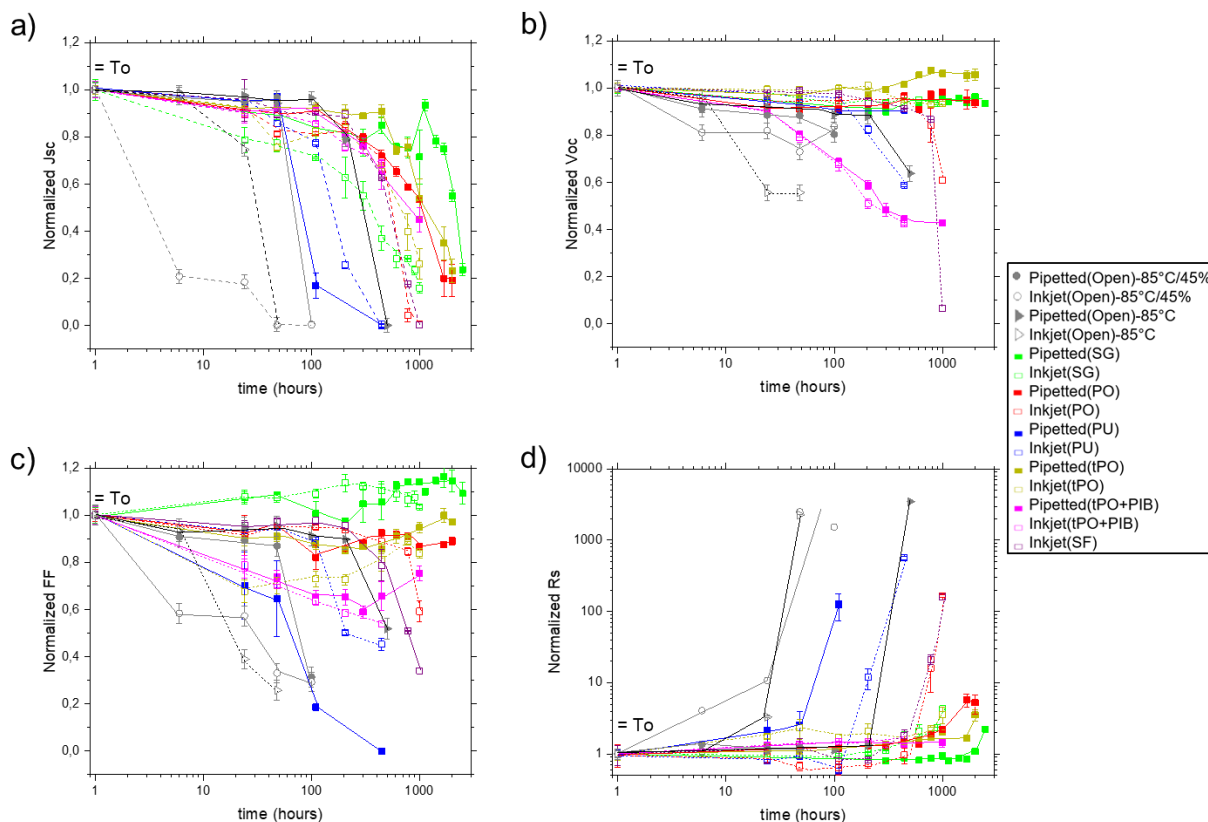


Figure 39:  $J_{sc}$ ,  $V_{oc}$ ,  $FF$  and  $R_s$  variation with time for both non-encapsulated cells (grey) and encapsulated cells (colors).

According to Figure 39, it can be seen that the  $J_{sc}$  evolution exactly follow the PCE evolution for all cells (open and encapsulated), except for the double tPO+PIB system. For the latter,  $J_{sc}$  trend is close to the one of both tPO and PO, but its  $V_{oc}$  drastically drops after 48 hours of ageing (J-V curves evolutions are also represented in Figure 40 for a better visualization). For other systems, the  $V_{oc}$  value only drops when cells are close to 0% in efficiency, and the  $V_{oc}$  of SG, SF, PO and tPO remains quite constant till the end of devices lifetime.

Concerning the  $FF$ , its value is quite constant till the end for pipetted SG, PO, PU, tPO. It seems even to increase for both pipetted and inkjet Surlyn gasket devices. Its decrease is generally related to the end of lifetime of devices. However, for the double tPO+PIB system, a decline of  $V_{oc}$  is obvious but quite reasonable. The latter system is also the only one not showing a rise of  $R_s$  simultaneously to the drop of PCE, indicating clearly a difference in the occurring mechanism. It seems that for SG, SF, PO, PU and tPO films, the end of lifetime is related to a progressive degradation of the perovskite layer (within the insulating mesoporous  $ZrO_2$ ), leading to a non-conductive path between  $TiO_2$  and carbon layers. On the other hand, for the double tPO+PIB system, the devices are still conductive without observing neither a huge decrease of  $J_{sc}$  nor an increase of  $R_s$ , but a decrease of  $V_{oc}$ . According to literature[288][289], the  $V_{oc}$  of perovskite solar cells can be related to several factors: the band gap of the perovskite (here not impacted), the energy level difference between FTO and carbon paste, deep-level traps within the perovskite layers or its interfaces. If the lamination conditions are stronger in the tPO+PIB case, it would be surprising to induce a modification of the energy



levels of oxide or carbon layers. Since a blueshift of the perovskite emission was observed, it sounds more likely that traps could have been created within this layer.

To support Figure 39 illustration, the evolution of J-V curves during the aging is represented in Figure 40 for representative examples of pipetted and inkjet cells with each different encapsulation systems. It highlights the rapid decrease of FF for PU-sealed devices, the rapid  $V_{oc}$  drop for tPO+PIB-sealed devices, and the main  $J_{sc}$  control on PCE value for other sealing systems.

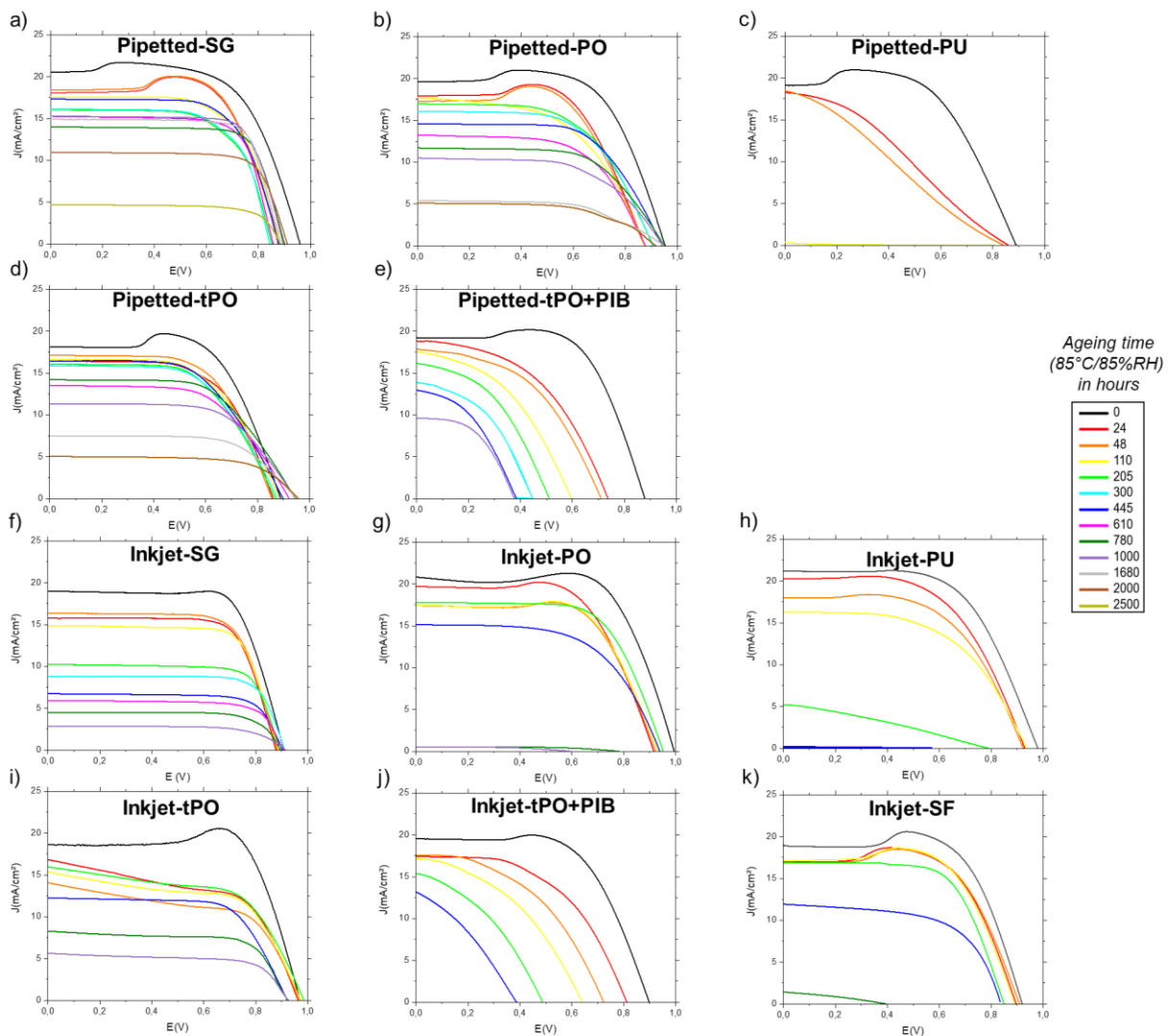


Figure 40: J-V curves evolution during the aging (representative examples for pipetted and inkjet cells with each different encapsulation systems, at a 4mV/s scan speed in reverse scan).

If the macroscopic J-V characterizations give a first strong information about the potential degradation mechanism occurring during aging, it is necessary to complete our observations using a full set of other characterization techniques. A first simple one is the direct observation of the visual aspect of solar devices. For this purpose, Figure 41 shows both sides of the encapsulated devices after the last measurement point of damp-heat aging campaigns. At initial state, right after the lamination, all devices presented equivalent aspect as illustrated

by the SG-sealed pipetted device example presented here at T<sub>0</sub>. During aging, the aspect of SG-sealed samples does not change a lot within the active area. It is however possible to notice a slight degradation of the small little content of perovskite overflowing the carbon paste area (indeed to secure the absence of short-circuit between TiO<sub>2</sub> and carbon, the intermediate mesoporous ZrO<sub>2</sub> layer was deposited a little larger and it is filled by perovskite). Furthermore, the Surlyn material itself undergoes a change of color (yellow to brown, observable after 2000h of ageing). The analysis of the sealing materials will thus be an interesting perspective to determine if they undergo themselves a degradation (due to damp-heat conditions or to perovskite degradation by-products) or simply a coloration due to the release of iodine. For PU-sealed devices, a yellow coloration rapidly spread within the polymer sealant, beginning from the edge of the photovoltaic active layer to all the sealant. Furthermore, it was observed that the sealant undergoes a degradation as it became a sticky paste but not solid anymore, allowing a delamination of both sealed glasses with hands at the end of aging campaigns. This time also, it would be interesting to identify the potential of perovskite degradation by-product to accelerate or not the PU-polymer degradation. For, PO, tPO and SF films, no coloration was observed but some bubbles were identified for carbon side. These bubbles appear at early stage for PO devices, then SF devices, followed by tPO devices. They indicate a delamination of the sealing film only on the carbon top layer of the active solar cell and not on the edges of the glass/glass encapsulation. This could be due to both mechanical stresses or to a release of gas by-products during ageing. For the double tPO+PIB system, the end of lifetime was express but we can observe that even the small little content of perovskite overflowing within the larger ZrO<sub>2</sub> mesoporous layer is still present with no change of color at the end of the aging campaign. This indicates that the rapid loss of performance is not due to a failure of protection from tPO+PIB encapsulation, but to the initiation of defects during the initial stage of lamination.

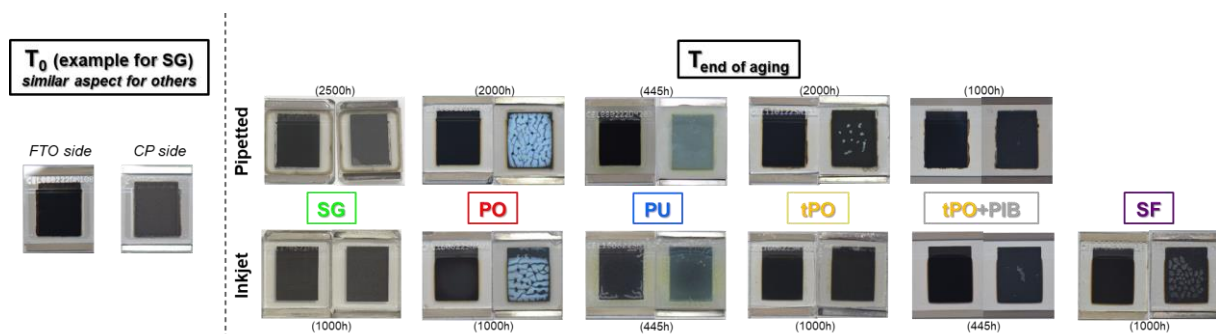


Figure 41: Photographs of encapsulated solar devices before and after damp-heat aging (both FTO and CP side are shown).

### C- In-depth characterizations of aging mechanisms for full devices and perovskite/sealants materials

A full set of characterization techniques has been used with the objectives to elucidate degradation mechanisms occurring in both device and encapsulation under the previous damp heat aging test: physicochemical characterizations (infrared spectroscopy), local mapping characterizations (LBIC & PL imaging), optical characterizations (absorption / reflection / emission spectroscopies), and morphology (XRD).

First of all, as a change was visually observed in some sealing films, we investigated the possible aging of sealing materials during the damp-heat test. The following Figure 42 presents UV-visible absorption and infrared spectra (ATR reflectance mode) for each sealing material in two different cases: fresh films not aged and films aged within the solar device. In order to be sure not to pollute the analyses with the PV device materials, samplings were made in the sealant section between glass-glass. For SG and PU films, they were not possible to extract in a shape compatible with UV-visible spectroscopy at the end of ageing. So, for UV-visible spectroscopy measurements of SG and PU, the sampling was realized at an intermediate ageing time for which the impact of ageing was however already visible.

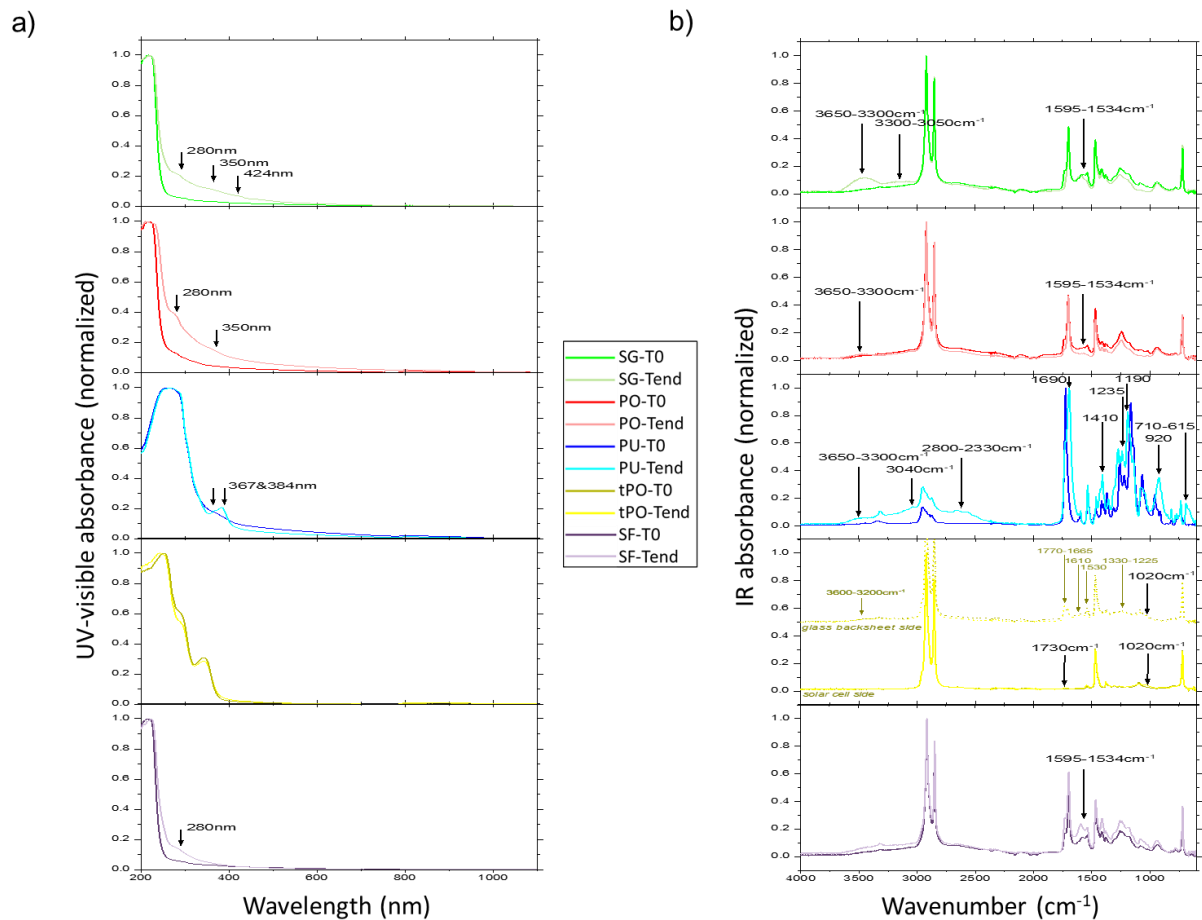


Figure 42: a) UV-visible absorption spectra and b) infrared spectra of sealing materials at: T0 and Tend of ageing within the PV device.

From UV-visible absorbance in Figure 42 a, it is possible to detect an identical emerging peak at 280nm for aged SG, SF and PO. For aged SG, more peaks (350 and 423 nm) were present than from aged SF, the 350 nm peak being also present for aged PO. PU highlight two different peaks at 367 and 384 nm, even at early stage. In the case of tPO, no additional peak was found but slight variations of the absorbance pattern could occur.

For PU, the additional peak should originate from the polymer degradation by-products also observed using infrared spectroscopy. UV-visible spectra of the device layers will be however scouted to see if this transition could be found within the device as it could correspond to hydrated perovskite transition value. For others, the three peaks between 280 and 450 nm could be related to the iodine compound[290] if it is able to migrate through the polymers films together with water vapor. The quantity of these signals could even be related to the visual observations in Figure 41. First, SG which is more colored than other materials possesses more peaks, then PO which contains lots of bubbles between device and sealant at end of ageing, followed by SF with less bubbles and finally tPO with quasi-inexistent bubbles.

According to infrared spectra, it could also be seen that SG is the more impacted by water ingress with a large  $3650-3300\text{ cm}^{-1}$  band. When compared to SF, this could originate from the beginning of its sealing property leakage as its end of ageing time is 2500hours against 2000h for SF. Analyzing obtained infrared spectra at initial state, it could surprisingly be observed that PO possesses a quasi-similar spectrum than the surlyn ones. The PO polymer used is thus also an elastomer, like surlyn. They possess exactly the same ratio between characteristic bands of the various  $\text{CH}/\text{CH}_2/\text{CH}_3$  groups ( $3000-2800$ ,  $1465$ ,  $1405$ ,  $1360\text{ cm}^{-1}$ ) and of the  $\text{C}=\text{O}$  groups ( $1700$  and  $1230\text{ cm}^{-1}$ ). Only characteristic bands of the tetra coordinated metallic complex ( $1595$ ,  $1534\text{ cm}^{-1}$ ) showed a slight change in pattern and intensity, which could be due to a difference with the metal used[291]. The latter bands are also the only ones that seems to be impacted by ageing for the three SG, SF and PO configurations.

For tPO, as ENLIGHT™ materials are known to be a coextruded composite layer[236], both film sides were scouted using ATR-infrared spectroscopy. For the film side laminated on the solar device, it was found to correspond to polyethylene and more specifically to “linear low-density polyethylene (LLDPE)”[292]. The other side of tPO was discovered to possess additional peaks, indicated in brown on related spectra, and more likely corresponding to acrylate functions [293] in small quantity within a LLDPE polymer. Both layers were found to present very few modifications after ageing, with however the appearance of tiny bands at  $1020$  and  $1730\text{ cm}^{-1}$  (indicated in black), compatible with typical oxidation results in such LLDPE polymers[294].

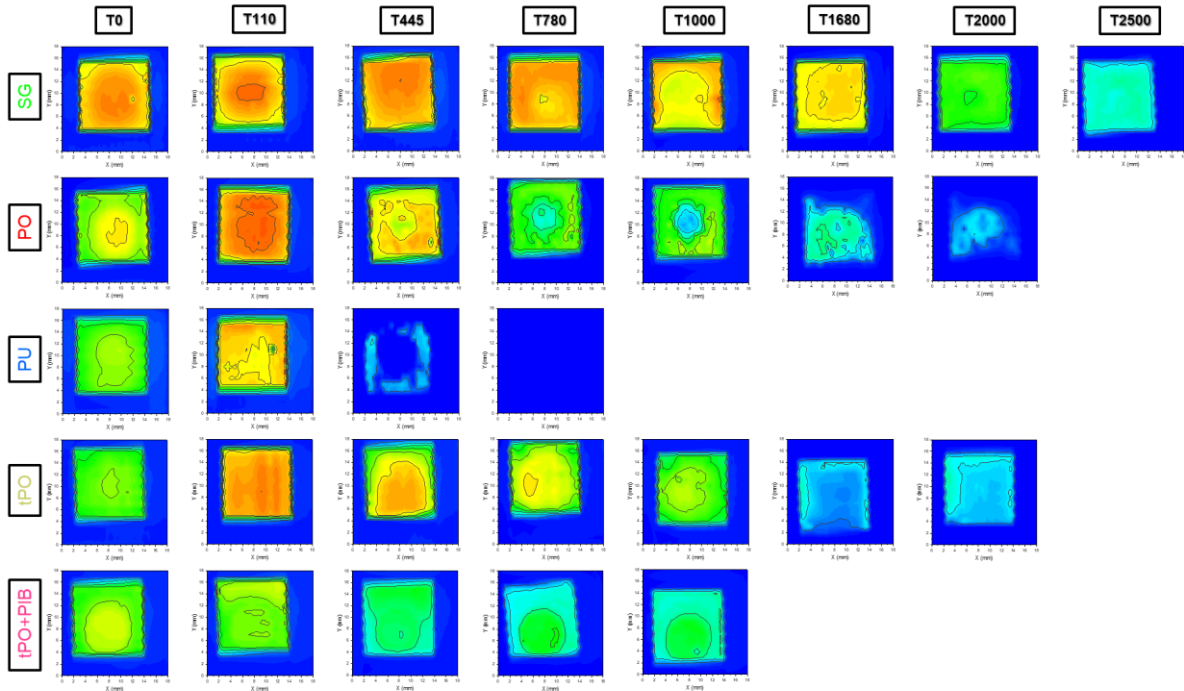
For PU, according to literature it should be more stable to sole thermal aging[295]. However, release of HI vapors by perovskite may act on enhancing its degradation and acid exposure can provide such obtained infrared pattern[296]. In order to confirm this hypothesis, we will soon conduct aging campaign of sole sealant films in either  $85^\circ\text{C}$  or  $85^\circ\text{C}/85\%\text{R.H.}$  ageing conditions.

Knowing the modest aging state of encapsulation systems at end of aging (except for PU), local performances of full devices were then evaluated during aging using LBIC and PL imaging

characterizations, respectively displayed in Figure 43 and Figure 44. Figure 43 clearly highlights the central drop of the perovskite solution for the pipetted cells. For inkjet cells, a more homogenous aspect is observed, as expected.

LBIC results are also summarized in Figure 45-a and -b presenting the evolution with aging time of the LBIC short-circuit current average value (the value is normalized according to the value measured at T0, and uncertainty bars represent the  $I_{sc}$  dispersion within the active area of a cell). The LBIC- $I_{sc}$  evolutions are overall in accordance with  $J_{sc}$  evolutions of the macroscopic J-V measurements (Figure 39-a), even if J-V measurements were performed using a 0.64 cm<sup>2</sup> centered-mask whereas LBIC imaging studies the entire available photoactive area (1.5 cm<sup>2</sup>). It should be however noticed a general tendency to a first step of LBIC- $I_{sc}$  increase during the first 100 hours of aging which is not reported with J-V measurements. Then, all LBIC- $I_{sc}$  decreases with similar levels than in J-V measurements. The  $I_{sc}$  decrease is quite homogeneous for SG and tPO+PIB encapsulations (for both pipetted and inkjet devices). In accordance with J-V, LBIC- $I_{sc}$  of the double tPO+PIB systems are always honorable at the end of the ageing process with a drop of less than 10% for inkjet devices and less than 50% for pipetted devices. The absence of inactive zones on the contrary of tPO alone attests of the good protection of PIB edge sealant. For PO, PU, tPO and SF encapsulated devices, the appearance of non-active zones were noticed before the end of life of devices. It could be either on the middle or the edges of devices, no specific rule could be established.

a) LBIC- *Pipetted devices*



b) LBIC- *Inkjet devices*

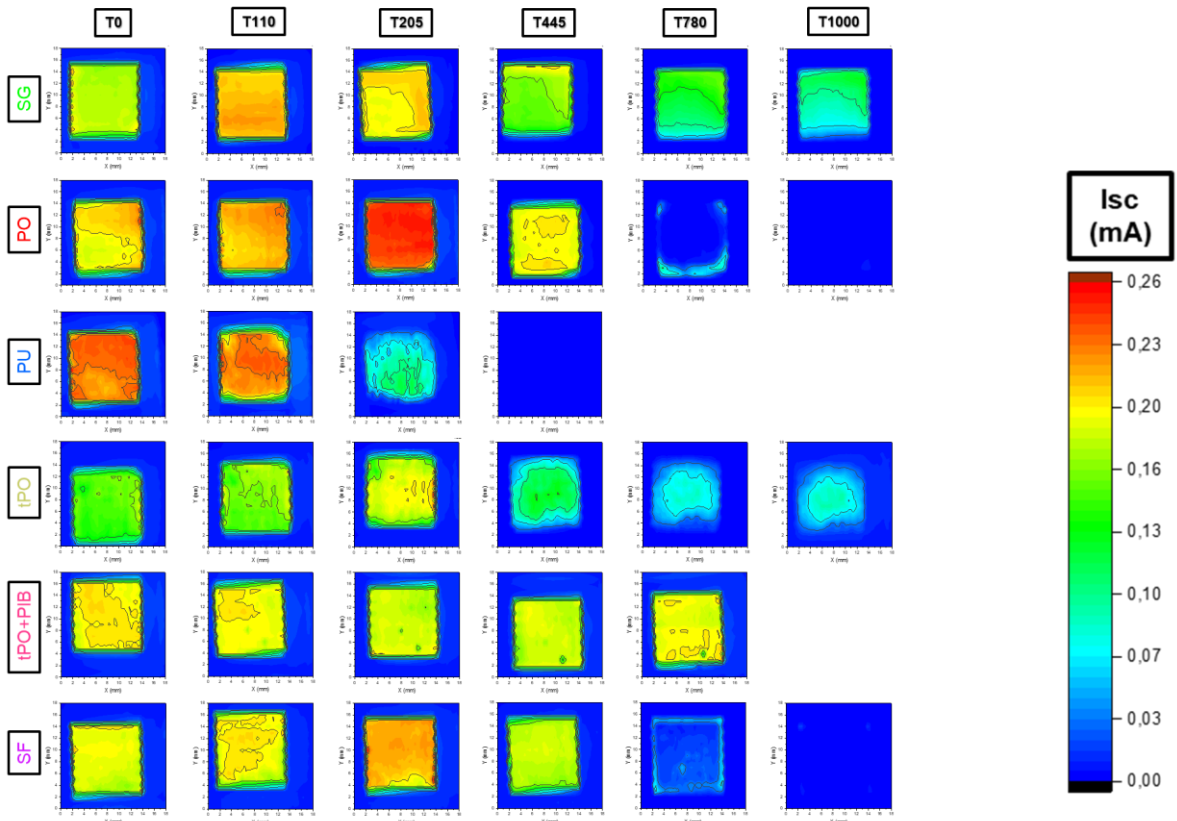
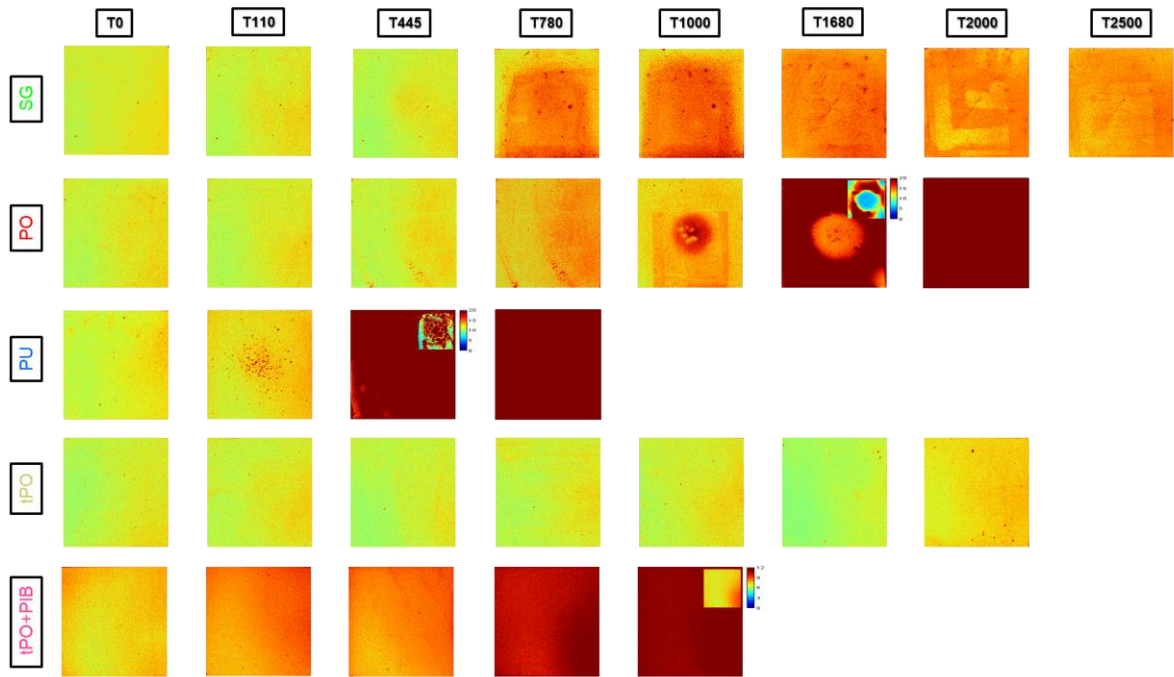


Figure 43: Variation with aging time of LBIC mapping images according to the different encapsulation systems for a) pipetted cells and b) inkjet cells.

a) PL imaging- *Pipetted devices*



b) PL imaging- *Inkjet devices*

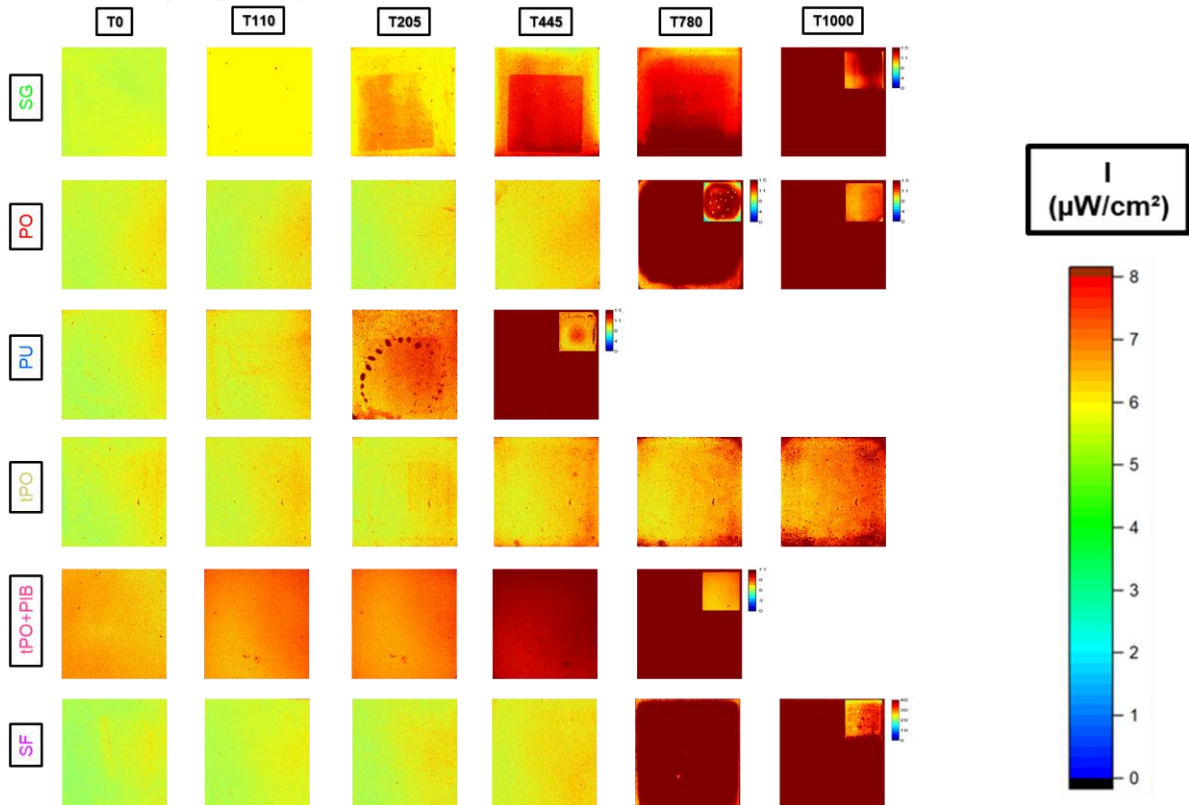


Figure 44: Variation with aging time of PL mapping images (12 cm x 12.5 cm) according to the different encapsulation systems for a) pipetted cells and b) inkjet cells. (Miniature replica are also presented with a different irradiance scale for some end times of the aging sampling)

Figure 44 presents homogeneous photoluminescence irradiance levels all over the surface whatever the system studied (different PK injection method and encapsulation sealing). Thanks to our PL imaging device, it is possible to recalibrate the images according to the time and gain of the camera. In view of the variations in intensity observed during the ageing period, we have chosen to present the evolution of the PL imaging irradiance levels in terms of the percent deviation according to initial value (i.e.  $\Delta (\%) = 100 * (PL_{\text{after}} - PL_{\text{before}}) / PL_{\text{before}}$ ), which could be compared to the evolution of the PL spectral intensity represented in Figure 45-e and-f also in terms of percent deviation. As concerns PL results, we can first observe that PL imaging data are in accordance with PL spectral data (Figure 45). The range of variation is emphasized when using PL spectroscopy but the PL evolution of all different configurations (different PK injection method and encapsulation sealing) follow the same trend whatever the PL method used. According to PL imaging, we can detect some specific phenomena as for SG devices. Indeed, the PL images of SG devices reveal the J-V solicited area as a square shape caused by the mask used during J-V measurements. This was sometimes a little present for other sealants, but really more pronounced for SG devices. This more solicited area undergoes a faster aging affording in this square the color corresponding in fact to the following sampling point of the area outside the square. If SG devices are the best ones in terms of PCE lifetime, it is not the last one evolving in terms of PL. This highlights different occurring ageing mechanisms according to the sealing method used. With the help of a more frequent sampling with PL spectroscopy, we can even observe that PL first increases till about 1500 hours for SG-pipetted devices before to finally decrease together with the rapid drop of PCE. It is the only case like this in the present study. As it also corresponds to the appearance of the Surlyn gasket staining, it is more likely that the acceleration of aging could be due to a leakage of the sealant and that the quantity of perovskite within the active layer really decreases after 1500 hours producing a decrease of photoluminescence. This happens after a first stage of photoluminescence increase due to a progressive apparition of defaults like  $PbI_2$  in small quantities playing the role of passivating agent[297]. This allows a conservation of PCE with some fluctuation till 1500 hours.

As SG was the more powerful encapsulation, we also finally decided to study SF as full sealant. The sensitized square area was this time not highlighted. It means that the little pouch remaining within the gasket area should act in the aging mechanism (either by providing a small quantity of oxygen or by allowing the release of degradation gases without the devices layers). Indeed, as highlighted in Figure 41, some bubbles were this time created between the carbon layer and the surlyn sealant. For inkjet devices, both PL irradiance and intensity increase more using SF than SG. The decrease of PCE and of  $LBIC-I_{sc}$  was quite equivalent with a more rapid drop for SF on last points. However, the effect of SF instead of SG has still to be confirmed on more resilient pipetted devices (ongoing campaign).

For other sealing films (PO and tPO) with similar impact on PCE lifetime, their answer in PL is strongly different. If PO shows a strong PL (represented by a burgundy color on PL images) for a PCE loss > 70%, this is not the case for tPO always showing smaller PL for an identical PCE. This seems in accordance also with the number of bubbles observed in Figure 41 between



carbon layer and sealing PO and tPO films. Their quantity was really huge for PO and sporadic for tPO. During aging, the more photoluminescent first appearing areas in PO also correspond to the area with the first bubbles appearing. PO devices presents also a more rapid  $R_s$  increase than tPO. Regarding the tPO+PIB double system, Figure 45 confirms that the PL increases more rapidly than with tPO alone. As  $J_{sc}$  is not so strongly impacted but  $V_{oc}$  is when using this double system (with stronger solicitation during lamination), it seems reasonable to think that PL highlight the presence of defaults acting as deep-level traps that could have been initiated during lamination.

Finally, the worse sealing material PU rapidly generates first the appearing of strong photoluminescent spots (burgundy color). This corresponds to the appearing of bubble at the same location than these spots, but rapidly disappearing to the benefits of a yellow color diffusing within the PU material. PL images are thus in accordance with the harsh PCE and LBIC degradation of related cells. As highlighted with UV-visible and infrared spectra, the polymers undergo strong degradation during the conducted ageing campaign. It would be interesting to also age this polymer alone (85°C, and 85°C/85%R.H.) in order to scout the impact of perovskite degradation by-products release on the PU degradation rate.

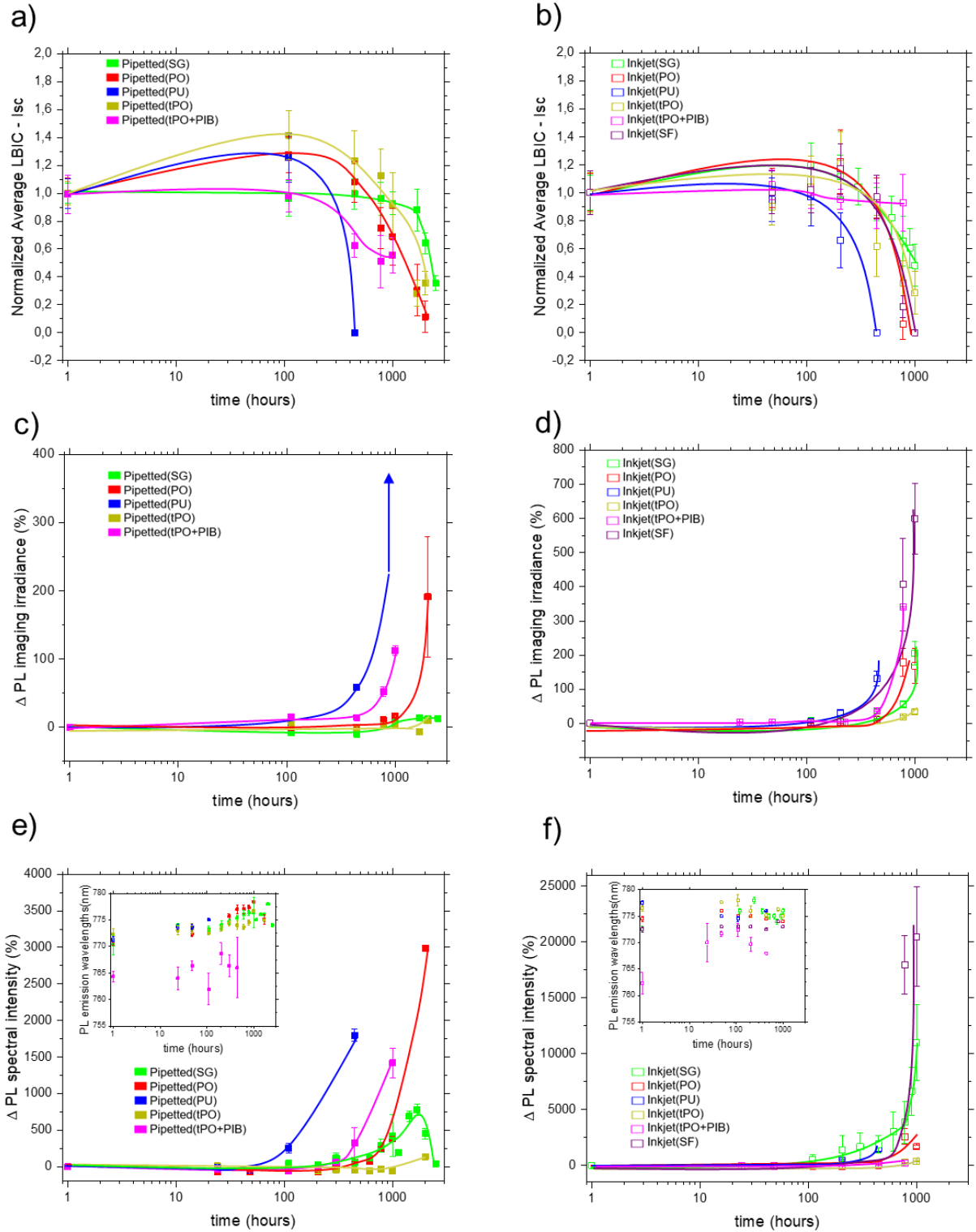


Figure 45: Variation with time of a) and b) the LBIC-Isc value normalized by LBIC-Isc value at T<sub>0</sub>, c) and d) PL imaging irradiance in terms of percent deviation according to initial value, e) and f) PL spectral intensity in terms of percent deviation according to initial value (uncertainty bars represent the typical dispersion within the active area of one cell for LBIC and PL imaging values, and the standard deviation on 3 samples for PL spectral values).

To correlate previous results with potential degradation of the active layer, UV-Visible spectroscopy analyses were performed using either reflectance mode or absorbance mode (presented in Figure 46 a and -b respectively). Due to the presence of an opaque carbon

electrode, absorbance analyses require to open the encapsulation and peel the carbon layer which is destructive for the cell. This method was thus used only at T0 and at Tend of aging. Reflectance is less instructive than absorbance but is non-destructive and thus allowed a full follow-up during aging.

As compared to reflectance spectra at initial state T0 (Figure 37-a and-b), patterns of reflectance spectra during the aging campaigns were quite similar. Spectra at Tend of aging are presented in Figure 46-a. The bandgap of perovskite is at the same value than before ageing, and is clearly observable at 1.59 eV (780nm) for quite all systems excepted inkjet devices encapsulated using PO, PU and SF. Indeed, these systems present a very small or quite inexistent perovskite transition by reflectance at end of aging. This is coherent with the fact that their PCE is equal to 0. What we can observe is mainly the reflectance of the Glass/c-TiO<sub>2</sub>/m-TiO<sub>2</sub>/m-ZrO<sub>2</sub>/m-carbon stack as presented also bellow in Figure 46-a. Two situations however present a different pattern with the presence of additional peaks. This is the case for PU-sealed devices with the presence of a transition beginning at 510 nm (peak with number ①), and for SG-inkjet devices with the presence of a transition beginning at 400 nm (peak with number ②). For PU-devices, this should correspond to PbI<sub>2</sub> as to the yellow shade propagating in PU itself is more around 380nm. For SG-inkjet devices, the 400 nm peak correspond to the mono-hydrated perovskite phase[298][299]. It begins to be slightly noticeable at 500h of ageing and is clearly visible at 1000h which is the beginning of degradation also for pipetted cells. This may thus highlight the start of water permeation through SG. It is also correlated to a general increase of the reflectance on all the 400-1100 nm range.

To better understand the ageing mechanisms within the different devices, additional analyses were performed using absorbance after peeling the carbon layer (Figure 46-b). Obtained data should however be considered with care as the level of removed material was obviously not always the same. At T0, all devices could be peeled in quite the same conditions (i.e. quite the same number of carbon delamination using scotch before to obtain an absorption spectra without signal due to carbon). After ageing, some devices could be difficult de peel due to either a strong adhesion of carbon to its under layer (for PO, PU, SF) or to a bad adhesion of perovskite-ZrO<sub>2</sub> filled layer to its under layer (for tPO+PIB).

As already reported, at the initial state, we can note the presence of others compounds such as PbI<sub>2</sub>, monohydrated perovskite and 2D perovskite. The attributions were realized according to literature[299][6][300][301][299]. For pipetting solar cells, monohydrated (350 nm) and 2D perovskites (420 nm) are present in all cases except for tPO+PIB system presenting a flat pattern. This highlight a strong modification due to the specific lamination conditions applied. A flat absorbance pattern is reported to correspond to a perovskite layer with either lots of voids between crystals or holes[302]. In the case of inkjet solar cells, only a slight PbI<sub>2</sub> peak appearing around 550 nm was observed, together also with a flat pattern which could be due to the lower quantity of perovskite used for filling inkjet devices.

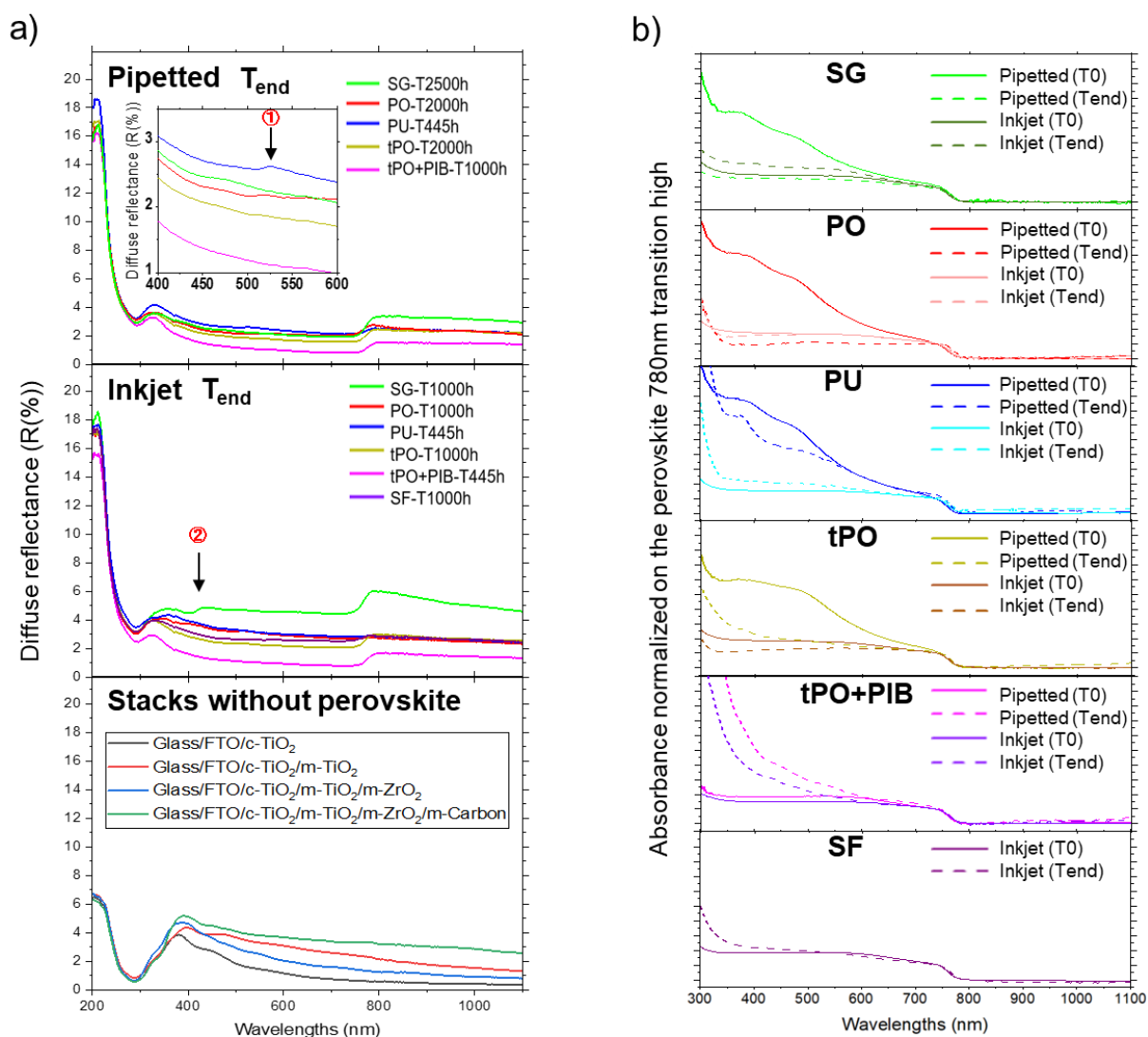


Figure 46: a) the variation over the aging time of the UV-visible diffuse reflection at 600 nm for of the pipetted and inkjet cells encapsulated with SG, PO, PU, tPO and tPO with PIB, b) their tauc plot, c) their wavelengths extracted from the photoluminescence spectra excited at 520 nm, d) their XRD patterns, e) their relative crystallinity as a function of the PK percentage present in the C-PSC

After 2500h of aging, pipetted-SG normalized absorption was as flat as the one of inkjet-SG at T<sub>0</sub>. This highlights a perovskite layer containing lots of voids between crystals. It is exactly the same for PO and tPO pipetted devices at the end of lifetime (2000h). For pipetted PU devices, no additional signal was observed at 500 nm as for reflectance spectra. This means that the signal was due to the color within PU, also corresponding to the additional UV-visible peak observed for PU analyzed alone in Figure 42. As the intensity of the normalized spectra increases at 300 nm, this means that the quantity of perovskite in presence is lower than at T<sub>0</sub>. In addition, the ratio between monohydrated perovskite and perovskite transition increases. This seems to indicate that the degradation of pipetted devices with SG, PO, tPO is more likely due to an amorphisation because of temperature stress, while for PU devices the degradation is due to the ingress of water through the sealing material.

For tPO+PIB devices, it was difficult to obtain a meaningful information for both pipetted and inkjet devices. Indeed, carbon peeling rapidly conducts to also a peeling of ZrO<sub>2</sub> layer leading to a high substrate (300nm) /perovskite (780nm) absorbance ratio. However, the presence of a small quantity of PbI<sub>2</sub> is noticeable at 550 nm.

Regarding inkjet devices, most of absorbance patterns were quite similar between initial state and end of lifetime. The patterns are all flat, which is in accordance to a less filled mesoporous network. After ageing, SG present exactly the same pattern with a slight PbI<sub>2</sub> peak increase. PO, PU and tPO devices all present also quite similar patterns but with a decrease of the perovskite/substrate ratio.

In all analyzed cases, perovskite is present even at end of devices lifetime without lots of degradation by-products visible using UV-visible spectroscopy. In fact, our C-PSC architecture act differently than traditional spin-coated devices: the perovskite layer is thick (~1µm) but spread within an insulating ZrO<sub>2</sub> mesoporous layer. Indeed, a simple amorphization of perovskite, leading to a smaller perovskite volume is potentially able to conduct to an insulating device. To scout further the perovskite layer degradation, peeled samples were thus also analyzed using XRD.

Figure 47-a presents the XRD diffractograms of each studied configuration both at initial time (T<sub>0</sub>) and at the end of aging (T<sub>end</sub>). The latter corresponding to a PCE loss > 80%. Figure 47-b represents the relative crystallinity of both perovskite and PbI<sub>2</sub> phases at corresponding times thanks to the following equations:

$$\text{PK Relative crystallinity (\%)} = \frac{\sum(\text{PK areas})}{\text{Integrated Area} - \sum(\text{other peaks areas})} \times 100$$

$$\text{PbI}_2 \text{ Relative crystallinity (\%)} = \frac{\sum(\text{PbI}_2 \text{ areas})}{\text{Integrated Area} - \sum(\text{other peaks areas})} \times 100$$

For all devices, we can observe that the crystallinity rate has decreased during aging. For PU and tPO+PIB sealing systems, crystalline PbI<sub>2</sub> is not present in significant quantity at the end of lifetime of device. This combined with UV-visible data and other observations, allowed us to conclude to different aging mechanisms for this both encapsulation systems. For PU, the sealant material undergoes degradation and was obviously able to infiltrate through the perovskite and mesoporous scaffolds leading to 28% crystallinity loss in pipetted cells and 50% loss with inkjet ones. This even leads to difficulties in removing the carbon paste material. For tPO+PIB, the degradation of PCE is more related to the creation of deep-level traps within the perovskite layers or its interfaces during the lamination stage driving to 32.8% crystallinity loss for pipetted devices versus 8.6% for inkjet solar cells. In addition to this, both systems undergo an amorphization of the perovskite due to temperature stress.

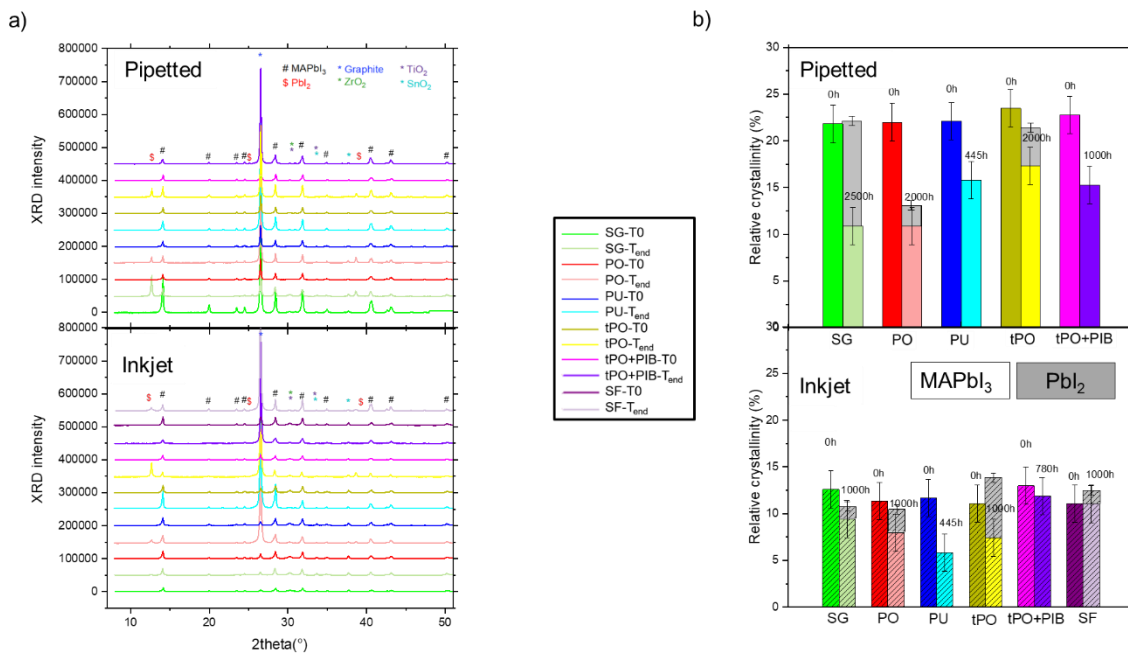


Figure 47: a) XRD diffractograms of pipetted and inkjet devices for each studied encapsulation at T0 and at T end of lifetime, b) relative crystallinity percentages for perovskite (color) and PbI<sub>2</sub> (grey) phases at T0 and at T end of lifetime for each configuration.

As regards SG, PO and tPO encapsulations, they all lead to the production of PbI<sub>2</sub>. At the end of the aging, the best PCE was recorded for pipetted-SG. However, the PbI<sub>2</sub> production was more important for SG (11.3%), followed by tPO (4%) and then PO (2.1%) for pipetted cells. Whereas it was the opposite for inkjet cells, with the highest PbI<sub>2</sub> production for tPO encapsulated devices (6.4%) followed by PO (2.4%) and then SF (1.47%) and SG (1.22%) at the end of the aging.

The perovskite can crystallize under several orientations. In our mesoporous scaffold, the AVAI doped MAPbI<sub>3</sub> is mainly oriented according to the orientations named 1 (110 and 220 at 2θ = 14° and 28.4°) and 2 (200 and 400 at 2θ = 20° and 40.6°). Figure 48 gives the perovskite orientation proportions during aging for the different studied systems. Analyses were conducted on devices originating for the same batch. At initial state, the orientation proportion is a little different between pipetted and inkjet devices, but is similar whatever the encapsulation. For the different systems, except SG-pipetted devices, the orientation proportions of the perovskite are quite similar between initial state and end of aging. For SG-pipetted devices, the orientation 1 proportion increase after 2500h of ageing. As huge increase in the proportion of crystalline PbI<sub>2</sub> is observed, this could explain the change in the perovskite orientation proportions. Obviously, the orientation 1 is the one less impacted by the encapsulation breakage.

a) *Pipetted devices*

b) *Inkjet devices*

Perovskite orientations

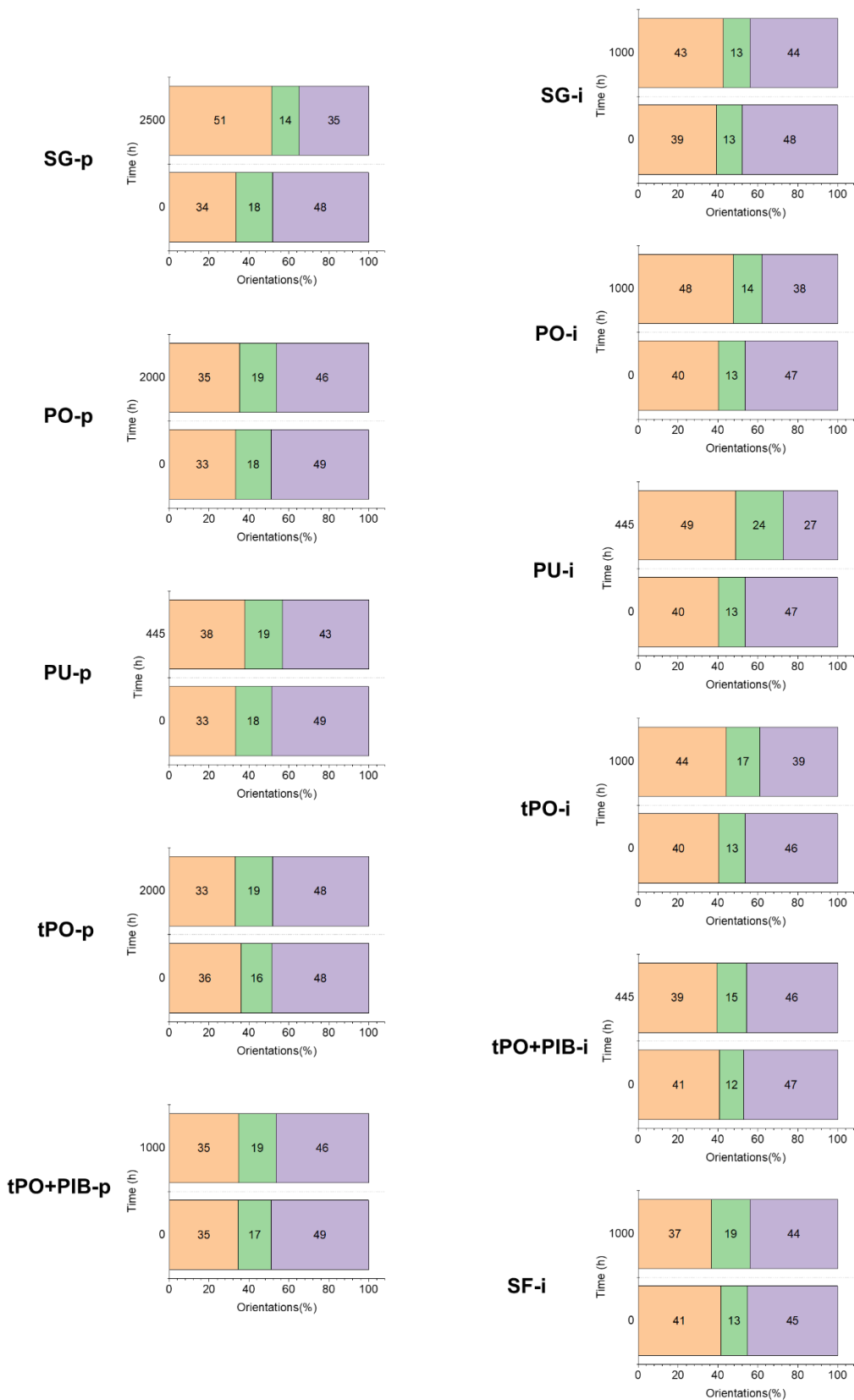
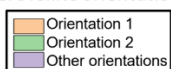


Figure 48: Variations of perovskite orientation proportions during aging for a) pipetted and b) inkjet devices.

## Conclusion

The surlyn gasket was found to be the best encapsulant for longer C-PSC devices lifetime. This could originate from two findings. First, this edge sealant demonstrates lower impact on performances after lamination. Secondly, it allows the production of a small amount of  $\text{PbI}_2$  more rapidly (could be due to either the small non-empty and thus filled with air envelope on top of the cell, or to some permeation of surlyn gasket to water ingress). However, this default somehow helps to maintain the PCE of pipetted C-PSC on a longer time. For inkjet cells, a different degradation mechanism occurs as main encapsulates led to an identical preterm end of life of SG, SF, PO and tPO concerned devices. This is due to less filled mesoporous networks, which have proved to produce a less compact and less crystallized perovskite layer.

According to the results obtained in this first chapter, the following C-PSC devices will be all encapsulated with SG, and we will now concentrate our interest on the impact of combined impact of both maturation and perovskite deposition process on enhancement and durability mechanism.





# CHAPTER IV: UNDERSTANDING OF THE MATURATION MECHANISM OBSERVED FOR CARBON-BASED PEROVSKITE SOLAR CELLS

## Introduction

In the past few years, halide perovskites based solar cells have undergone an incredible rise in the efficiencies compared to traditional inorganic solar cell semiconductors such as cadmium telluride, multicrystalline Si or copper indium gallium selenide[303]. Very large PCE reaching 25.7% have been achieved with organic-inorganic lead halide perovskite in recent studies[1][304][305]. These values originate from a unique combination of intrinsic features: remarkable optical and electrical properties such as high absorption efficiency ( $10^4 \text{ cm}^{-1}$ ), direct band gap, and high charge transport capacity to name but a few. This PV technology is also interesting for realistic low-cost processing[301]. There is however a need nowadays for improvement in the long-term stability[306]. Amongst the possible architectures, Hole transport material (HTM)-free carbon-based perovskite solar cells (C-PSCs) look especially promising, because of a further reduction of the low cost compared to previous used devices using gold as a back contact. HTM-free C-PSCs also benefit of a simplified processing protocol with FTO/TiO<sub>2</sub>/ZrO<sub>2</sub>/carbon structure[82]. Much like with more conventional PSCs setup, the addition of 5-ammonium valeric acid iodide (5-AVAI) results in a significant improvement of the devices both in the initial state and after ageing[86]. The active layer in highly efficient PSCs are typically prepared using a spin coater. The latter however limits the surface coverage and induces structural and morphological variation of the perovskite (PK) layer with the distance to the center. This will probably prevent its use for large scale developments[307]. As a result, a variety of PK manufacturing procedures have been developed including blade coating, slot-die coating and spray pyrolysis. These techniques overcome the major problem of the spin coating, but need to be conducted in an inert atmosphere with a very low-humidity to achieve good efficiencies[308]. Recently, remarkable techniques have been proposed to prepare perovskite based solar cells in ambient conditions[208]. These stable cells also have higher PCEs, and rely on a perovskite with a better crystallization.

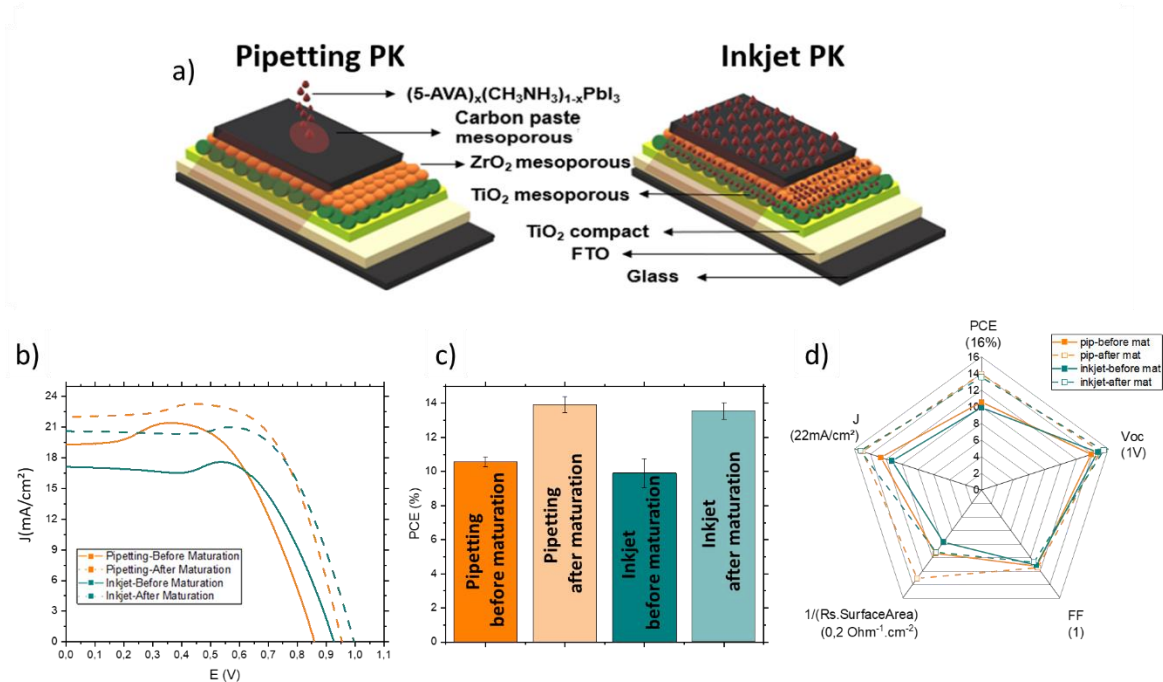


Figure 49: a) Cell architecture with a simplified representation of the perovskite deposition; b)  $J(V)$  measurements of "Pipetting" and "Inkjet" solar cells before and after the maturation step (reverse scan at 4 mV/s); c) Average PCE obtained on 9 cells; d) Star diagram to represent others PV parameters measured on "Pipetting" and "Inkjet" solar cells before and after the maturation step

This experimental work concerns the development of a new generation of PK solar cells derived from dye-sensitized solar cell technology[309]. A mesoporous TiO<sub>2</sub> layer is utilized as ETL with a large surface of interface that facilitates the electron transport, and reduces the charge recombination, Figure 49 a). An insulating space layer is then added with ZrO<sub>2</sub> backbone which is also a mesoporous structure. The last applied layer is a mesoporous carbon paste that will play the role of upper electrode and HTL layer. The absence of a specific HTL layer represent a major distinctive characteristic in the PK technology. All these stable layers may safely be deposited one on top of the other. They are not sensitive to moisture or oxygen. The perovskite, most delicate component, is infiltrated at the end of the process. This is the other distinctive characteristic of these cells, the entire process can be performed in ambient conditions without a glove box. The incorporation of perovskite at the end of the process for a limited time just before the encapsulation prevents its degradation. In this specific study, two processes were compared for the deposition of perovskite, Figure 49a): The "pipetting" process consists of a central injection by drop casting while for the "inkjet" process a "step printing" technology is used allowing a better control of the deposited volume. This approach was employed for comparison, it is supposed to be the most effective way to fabricate cells with large areas and to promote a more homogeneous deposit on the surface. In both cases, the initial solution was prepared with the desired relative amount of PK and AVAI. This latter is known to facilitate the PK crystallization in this mesoporous skeleton and promoting

preferential growth in a normal direction[310][311]. This perovskite is also known to develop a better contact surface with  $\text{TiO}_2$  with a lower defect concentration and to be more stable[312][313][170][168]. With these innovative devices it is possible to obtain right after fabrication interesting performances of about 10.5% and 10% for the "pipetting" and "inkjet" cells, respectively.

With most of the PV technologies, the cells and modules present the best performances just after being processed. In contrast, the most recent PK-based cells experience a "maturation step". This phenomenon refers to the initial increase in the PCE, just after being processed. The maturation step has already been revealed in the literature [7]. Although it may be viewed as a somewhat positive phenomenon at first glance, it could actually represent an industrial problem if the systems had to be matured prior to commercialization. We first performed a comparative study of the amplitude and speed of the maturation changes depending on the environmental conditions: temperature, humidity, and light exposure. The goal was to underline the maturation to better track it. With our systems, we observed that the best maturation condition, with the most changes in performances was achieved at 40°C/75% RH for 150h. The synergistic effect of the temperature and humidity on the maturation confirms previous studies[7].

## Results and discussion

For comparison, Figure 49 b) shows the  $J(V)$  measurements of the two types of studied cells before and after maturation. Corresponding PV parameters and performances are represented in Figure 49 1 c) and d). The maximized maturation step was indeed very efficient in increasing the performances. The procedure also reduced the difference between the processing ways. The inkjet method increased more to match the pipetting, they eventually both reached about 14%. Both the shape of the curve and the extracted parameters indicate that the PCE enhancement mainly resulted from the  $J_{sc}$  parameter, also in agreement with the literature data. Different explanations have already been proposed, such as the improvement of the carrier recombination processes partly induced by an improvement of the crystalline microstructure of the perovskite [218]. However, few articles were published that specifically studied this phenomenon. Because of the large applied and basic interest, it seems appropriate to try and better understand the relationships between the mechanisms and the plausible consequences on the functional properties of solar cells. The current study relies on a set of characterization methods used at different scales of the cell, from the perovskite layer to the complete solar cell.

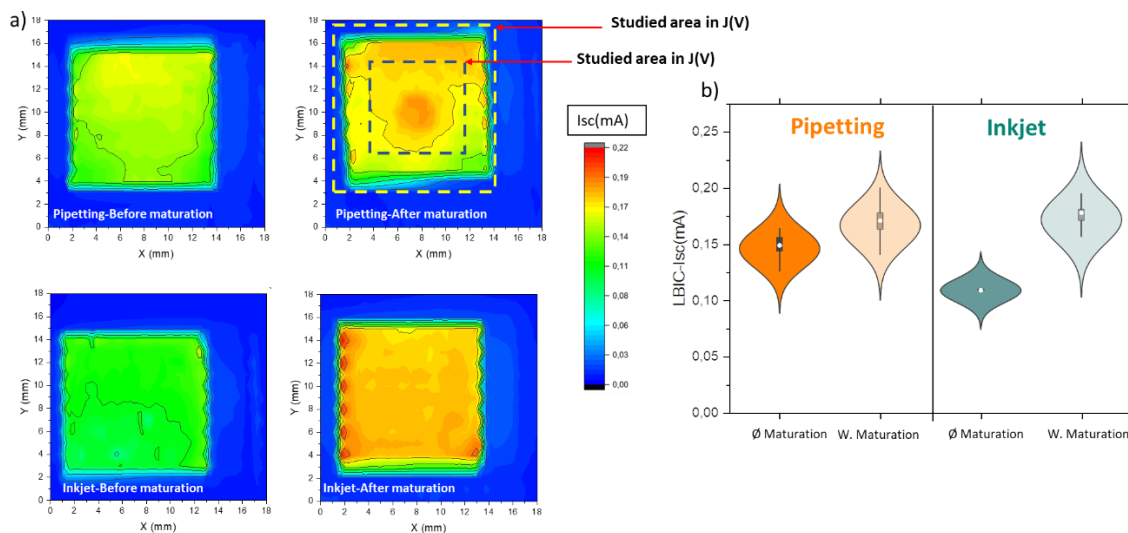


Figure 50: a) LBIC maps of “pipetting” and “inkjet” solar cells before and after the maturation step, b) Statistical representation of LBIC maps under violin plots (box plots (average, minimum, maximum, first and third quartiles) with kernel density plot of each side)

The macroscopic PCE represent an average value on the cells. The differences in the processing conditions may however induce a spatial distribution of the performances. The LBIC characterization is thus the appropriate tool to investigate these differences, since a local short circuit current measurement is performed. The experimental results are presented in Figure 50. The maturation step increases the values of the short-circuit currents ( $I_{sc}$ ), especially for the inkjet cells, in good agreement with the macroscopic  $J(V)$  measurements. The violin plot, further reveal that even if the local performances seem quite homogeneous before the maturation step, they become more heterogeneous after this step, especially for the pipetting

cells. The raw LBIC data show that the central area seems perform better. The center of the cells is the location where the infiltration of the PK was performed in the case of pipetting cells, this might induce a thicker PK layer and thereby better properties. For the correlation it is important to note that the macroscopic  $J(V)$  measurements are performed with a mask of  $0.64\text{cm}^2$ , placed on the center of the cell (Illustration of measurements without mask for pipetting cells is shown in the Figure 61 in Supplementary Information). Thus, for pipetting cells, the maturation stage essentially induces an improvement in cell performance at the center of the cell. In the case of inkjet cells, there is a much more homogeneous improvement in performance.

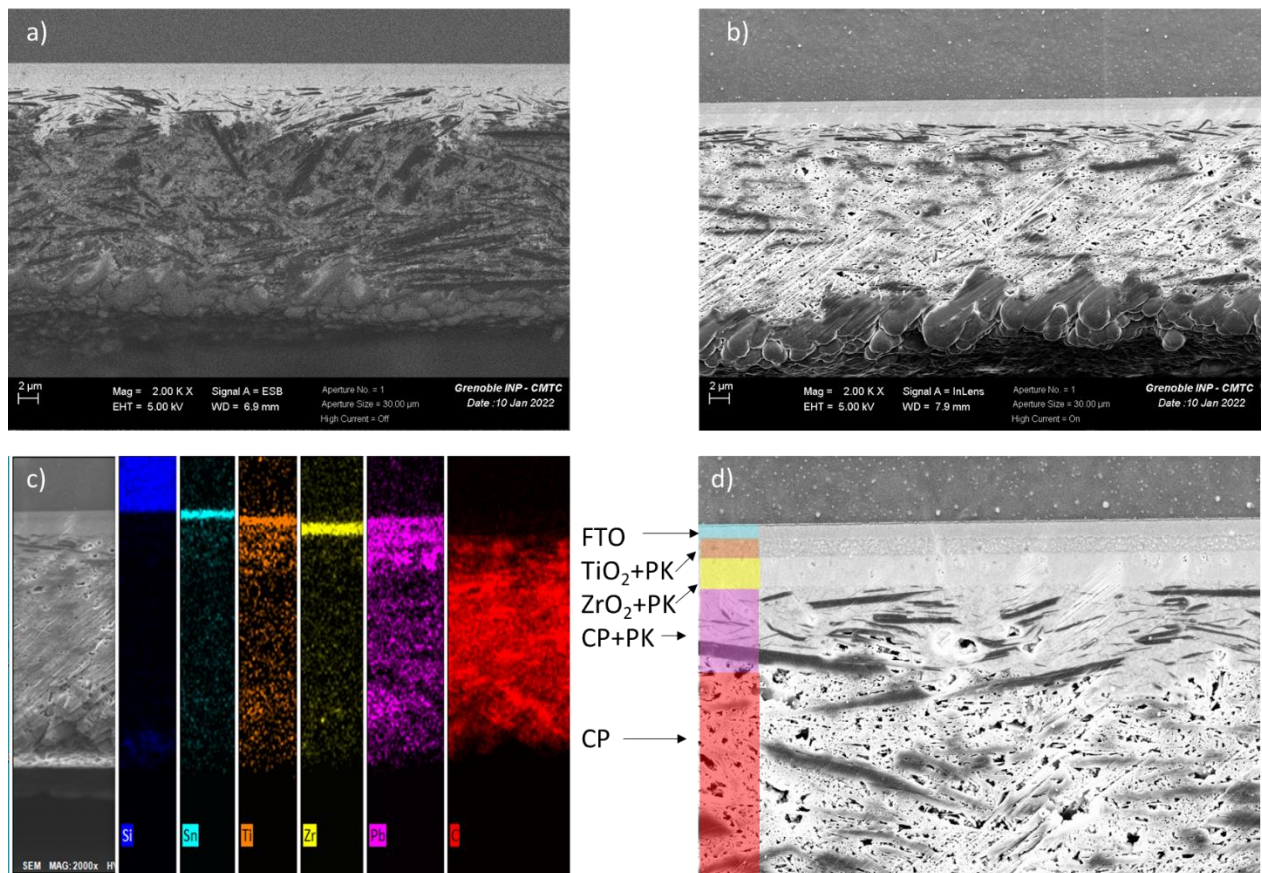


Figure 51: Layer identification of solar cells by SEM at the center of a "pipetting" solar cell: a) EBSD images, b) SEM images, c) EDX maps, d) Another SEM image with a magnification and the identification of the layers

Tableau 7: Estimation of PK layers in carbon paste for "pipetting" and "inkjet" solar cells (at the center and in a corner of a cell)

	PK + CP ( $\mu\text{m}$ )
Pipetting – Center	2,5-3
Pipetting – Corner	1,5-2
Inkjet – Center	1-1,5
Inkjet - Corner	1-1,5

SEM observations were carried out to correlate these heterogeneities of performances, observed for "pipetting" solar cells, to the method of perovskite layer deposition (Figure 51 and Figure 52). The identification of the different layers within the stack was carried out with the backscattered electron detector (EBSD) and EDX analyses. On the EBSD images, the perovskite layer presents a clear contrast because of the presence of lead that contrasts with the lighter elements found in the other layers. Next the images obtained with the secondary electron detector further helped to distinguish the layers. Although the dissimilar layers are thin and intimately mixed with one another, the EDX analyses made possible a clear identification of each individual phase. Figure 51 indicates that the perovskite fully permeated within the  $\text{ZrO}_2$  layer, and partly the  $\text{TiO}_2$  and carbon layers. For  $\text{TiO}_2$ , the filled part corresponds to the mesoporous  $\text{TiO}_2$  layer, the compact  $\text{TiO}_2$  layer cannot be filled by perovskite. The PK thickness within CP is contrasted enough to allow a meaningful thickness measurement of a PK richer CP phase and thereby a comparison not only of the two types of cell ("pipetting" and "inkjet") but also of the differences between the center and the edges, Figure 52 (see red arrows). As shown in Tableau 7 and Figure 52, the thicknesses are significantly larger in the "pipetting" cells than in the "inkjet" cells. This means that the PK impregnation in the carbon layer is much more efficient in the pipetting than for the inkjet method. This is to correlate with the fact that, to fill the same active area without rewetting dry-areas, a 42% less quantity of precursor solution was needed in the case of inkjet method. Finally, the differences between the centers and the corners are also observable, showing a better quality and thicker layer in the center of the cell than in the corners, especially for the "pipetting" cells. These morphological features are likely to induce the measured local heterogeneities of performances for the pipetting cells. Because these heterogeneities become even more contrasted after maturation, it appears essential to better understand this phenomenon.



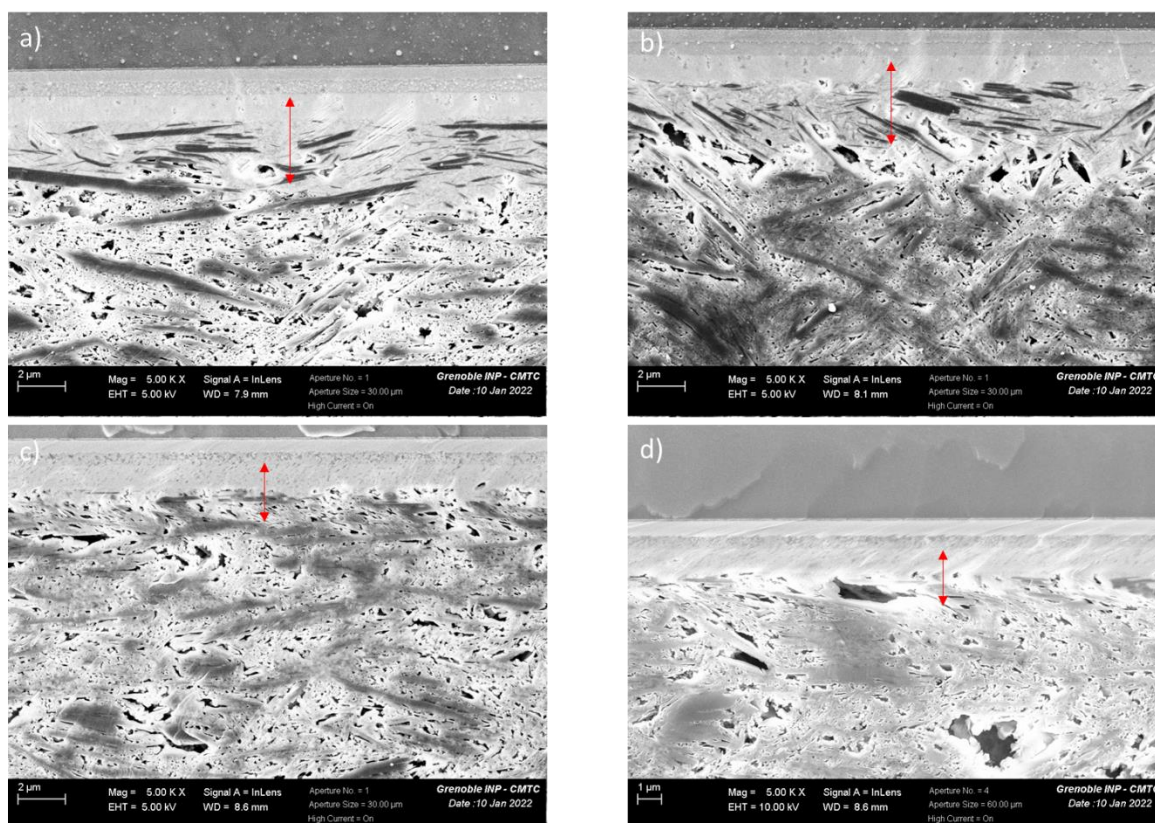


Figure 52: SEM images (with SE detector) for "pipetting" solar cells a) at the center b) in a corner and for "inkjet" solar cell c) at the center d) in a corner.

A large series of characterization tools and methods have been employed to track the changes within the active layer of the solar cells. Unfortunately, most of the techniques require to break the cells open and remove the carbon layer to obtain quantitative and sensitive results. The process tends to irreversibly damage the active layer. This prevents the further usage and characterization of the cell. Each sample was thus characterized thoroughly to use the interrelationships between the experiments. X-ray diffraction (XRD) analyses were performed at the center and at the edge of the cells after removal of the carbon layer. The diffractograms for both types of cells before and after the maturation step are presented in Figure 53. With the third-generation photovoltaics, very thin layers are used and the XRD spectra present a large number of peaks, many of which originate from the materials surrounding the active layer. An attribution of the different contributions is proposed in Table 8, based on the literature data. The results indicate that the PK in the active layers presents a tetragonal XRD pattern with two main orientations: (110) and (220) and (200) and (400) [314][315]. This is thus very similar to the  $\text{MAPbI}_3$  perovskites deposited by spin-coating. However, other orientations may be observed with a minor amount. In a planar spin-coated perovskite solar cell, only the aforementioned orientations (110,220,200,400) are to be seen [315][316]. In contrast, the mesoporous pipetted or inkjet perovskite solar cells exhibit new additional PK peaks with very different orientations like (121) at  $23.4^\circ$ , (202) at  $24.4^\circ$  and (134) at  $43.1^\circ$ [94][317]. This feature may result from the AVAI addition that impedes the PK crystallization by adding complexity to the structure[168]. It may also be the consequence of

the mesoporous architecture of the host layer that geometrically hinders the crystallization with its high surface and narrow structure.

As shown in Figure 53 c), it is also possible to evaluate the relative amount of crystallinity. The experimental data show that this parameter does not change much spatially on the cell. The crystallinity remains at 20-22% with the pipetting cells. With the inkjet cell method, a slight decrease between edge and center and before/after the maturation step, where they remain below 20%, i.e. between 15-17%. A similar data treatment with spin-coated perovskite deposited on a planar architecture would give a very different amount of crystallinity, close to 50%[316]. The infiltration in a mesoporous scaffold thus seems to hinder the PK crystallization.

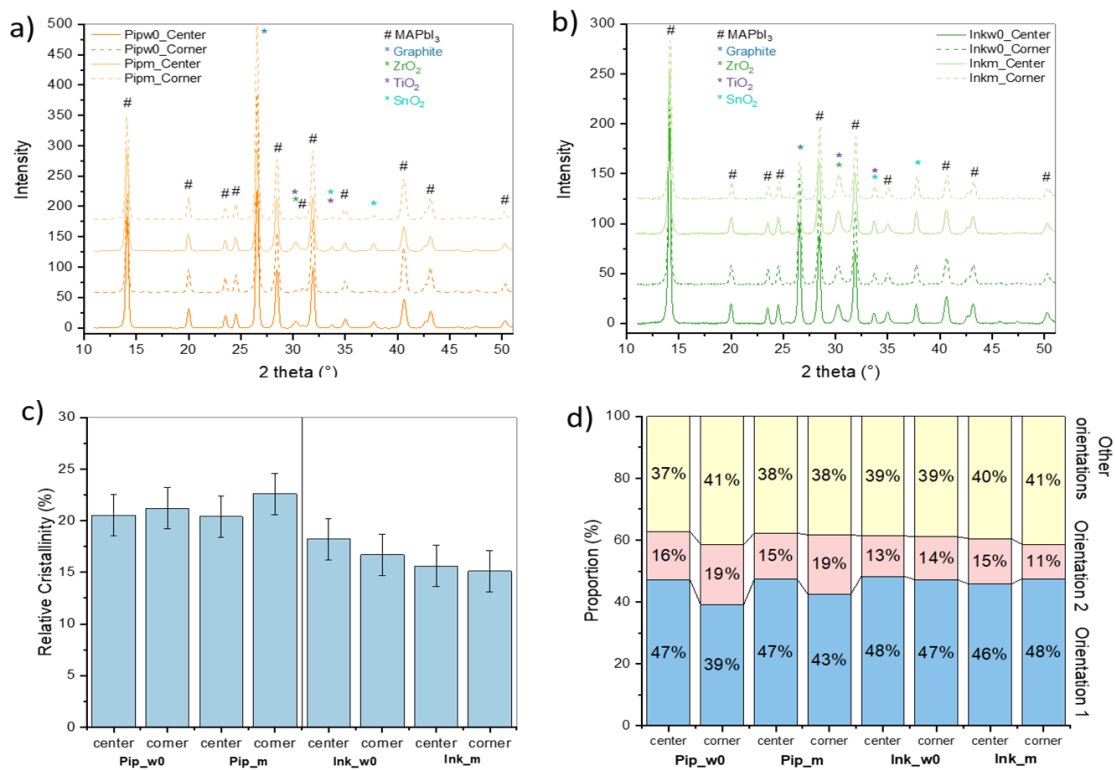


Figure 53: XRD patterns of a) “pipetting” and of b) “inkjet” solar cells at the center and in a corner before and after the maturation step; c) Relative crystallinity (%); d) Proportions of the two main orientations and others orientations in the perovskite (the orientations are defined in the Table 8)

Table 8: Attribution of main diffraction lines

2 theta (°)	Attribution	PK orientation
14	<b>PK (110)</b>	<b>Orientation 1</b>
20	<b>PK (200)</b>	<b>Orientation 2</b>
23,4	PK (121)	Others orientations
24,5	PK (202)	Others orientations
26,5	Graphite	-
28,4	<b>PK (220)</b>	<b>Orientation 1</b>
30,2	ZrO <sub>2</sub> /TiO <sub>2</sub>	-
30,8	PK (123)	Others orientations
31,2	PK (222)	Others orientations
33,7	SnO <sub>2</sub> /TiO <sub>2</sub>	-
35	PK (132)	Others orientations
37,7	SnO <sub>2</sub>	-
40,6	<b>PK (400)</b>	<b>Orientation 2</b>
42,6	PK (141)	Others orientations
43,2	PK (134)	Others orientations
50,3	PK (404)	Others orientations

Figure 53 d) shows that orientation 1 is always the most prominent one and relatively constant, close to 50%. This is also true for all kind of cells. The preferred orientation is rather straightforward to understand in planar structure because the horizontal surface helps the texture development during the crystallization. This is obviously not the case with mesoporous structure where the host presents surfaces with all possible 3D orientations. Even if incorporating perovskite into a mesoporous structure should not result in a highly ordered structure, preferential orientations are still found. For the pipetting cells, the proportion of orientation 1 is lower in the corners of the cell, as compared to the center. This could be due to a difference of diffusion of the components of the perovskite precursor solution as it is known that the AVAI additive can interact with TiO<sub>2</sub> and ZrO<sub>2</sub>[318]. It seems that the process used for the inkjet cell leads to a fairly homogeneous deposition of the perovskite. In all cases, the combined proportions of both orientations 1 and 2 never exceeds 60%, contrasting with the spin-coated case, where the same orientations represent up to 90% [315][316].

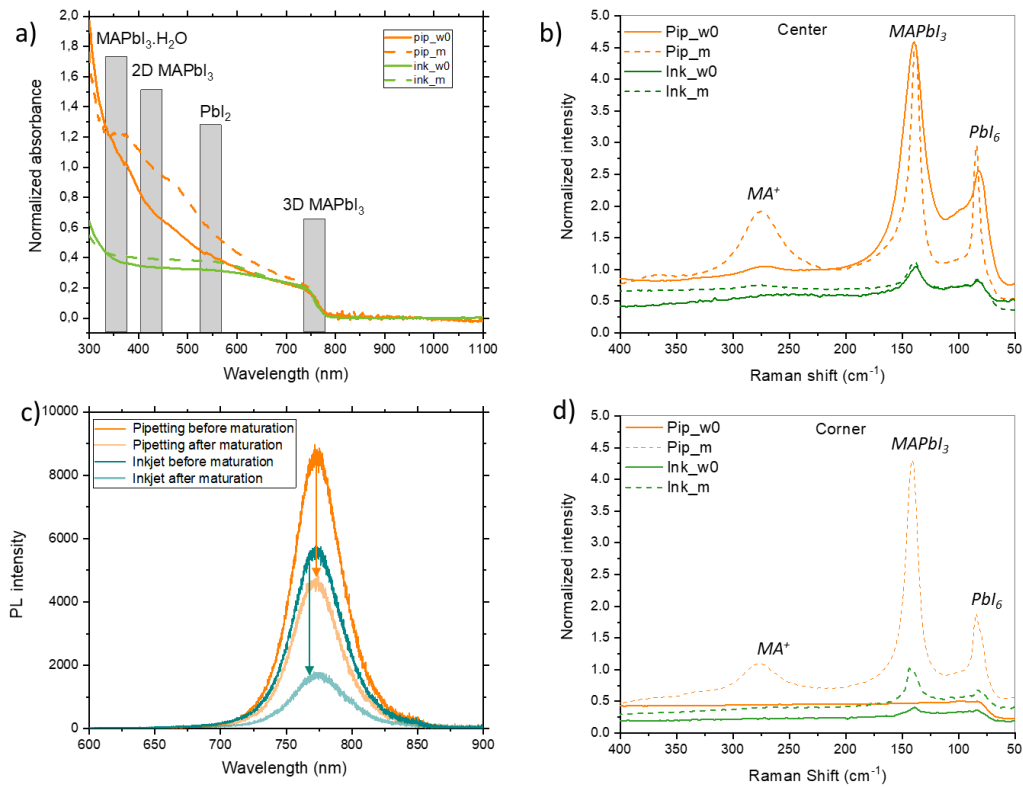


Figure 54: For « pipetting » and « inkjet » solar cells, before and after maturation step, a) UV-Visible absorbance spectra (normalized at 0.2 on perovskite band gap), b) Raman spectra performed at the center, c) Photoluminescence spectra, d) Raman spectra performed in the corner of the solar cells (UV-visible and Raman spectra were performed on opened solar cell after removal of carbon layer)

This study was completed by other analyses. The perovskite material of the different cells seems to have quite different optoelectronic properties. UV-Visible absorption analyses were first conducted, Figure 54 a). They all have a main transition near 780 nm, characteristic of the 3D phase of perovskite[319]. The bandgaps were evaluated and measured 1.59 eV for all types of cell. First, for inkjet devices, we note a flatter pattern than for pipetted ones. This could be related to the perovskite infiltration process used as a flat absorbance pattern is reported to correspond to a perovskite layer with either lots of voids between crystals or holes[302][320]. For matured pipetted solar cells, we note the appearance of new transitions around 350 nm and 420 nm. According to the literature, these phases can be associated respectively with the formation of hydrated MAPbI<sub>3</sub> and 2D MAPbI<sub>3</sub> phases [298][299][6][301]. In the presence of AVAI, a 2D perovskite, possibly with a stoichiometry of (AVA)<sub>2</sub>PbI<sub>4</sub> can be formed. As the ammonium valeric acid moiety can adsorb on the TiO<sub>2</sub> and ZrO<sub>2</sub> surfaces via its carboxylic acid group[6], this could lead to a suppression of defects in these layers. This type of PK was also reported to present a better stability than pure 3D MAPbI<sub>3</sub>[171]. For the other monohydrated perovskite phase, this is probably an effect of the treatment of maturation occurring in temperature and humidity. This means that the maturation process promotes the formation of two others phases based on PK phases, with one of her apparently beneficial for the cell's

behavior. Nevertheless, for the matured “inkjet” cells, we do not note the formation of such phases, only an intensification of the phase around 550 nm, characteristic of the  $\text{PbI}_2$ . It is however known that a small amount of  $\text{PbI}_2$  can play the role of passivating agent and be beneficial for PV performances[321].

Next, Raman analyses were performed to track the changes in chemical functions within the perovskite. The spectra obtained are presented in Figure 54 b) and d). In order to better scout the perovskite phase, the carbon paste was peeled out of samples just before the analyses. The Raman analyses were thus performed on the  $\text{PK}+\text{ZrO}_2$  surface, which is confirmed by the fact that we do not observe the  $\text{TiO}_2$  specific peaks ( $143\text{ cm}^{-1}$ ,  $196\text{ cm}^{-1}$ ,  $395\text{ cm}^{-1}$ )[322]. Thanks to the work of Jain et al. [323] and Selvarajan et al. [324], the different bands could be identified. The band at  $80\text{ cm}^{-1}$  is attributed to the symmetric and asymmetric breathing mode of the  $\text{PbI}_6$  octahedron. This peak, when shifted towards larger wavenumbers, can also be used to track the formation of the  $\text{PbI}_2$ . The band at  $145\text{ cm}^{-1}$  is characteristic of the perovskite, and more specifically to its MA group. This vibration is important because it results from the intercalation of  $\text{MA}^+$  in  $\text{PbI}_2$  to form a fully crystalline perovskite. In the center of the cells, the presence of both bands ( $80$  and  $145\text{ cm}^{-1}$ ) can be observed, indicating the good conversion of the perovskite. The only difference between the two types of cells is the intensity of the signal. Because the experiments were performed in the same condition, a larger intensity indicates a larger amount of PK or a better quality of the perovskite, which is in accordance with the less flat UV-visible absorbance spectra pattern observed for pipetting cells. After maturation, the two spectra obtained for the inkjet cells are similar, indicating no physicochemical modification of the material during the process. In contrast, a new band at  $270\text{ cm}^{-1}$  appeared during the maturation of the pipetting cells. It was attributed to higher ordering of the MA cations in a periodic system, and thus a second harmonic of the  $140\text{-}150\text{ cm}^{-1}$  band[323]. In the cell corners, uncomplete perovskite conversion is observed for pipetted cells before maturation. After maturation, a completion of the conversion is evidenced, more intense for the pipetting cell. The first two bands are more pronounced, and we note the formation of the  $\text{MA}^+$  band at  $270\text{ cm}^{-1}$ .

It seems that the deposition process of perovskite and the maturation step induces some microstructural and physicochemical modifications of perovskite. In the case of pipetting cells, after the maturation step: formation of a 2D perovskite improving the charge transfer, and better conversion of the perovskite on the entire solar cell inducing a more ordered structure. In the case of the “inkjet” solar cells, a different behavior was observed with only the formation of a slight amount of  $\text{PbI}_2$  and a slight better conversion of the perovskite in the corner of the solar after the maturation. This assumes that the post-treatment step for inkjet cells does not really improve the PK layer itself. To go further within the maturation impact and scout interfaces, PL spectroscopy is shown in Figure 54 a). PL measurements were realized from the  $\text{TiO}_2$  side, as the opaque carbon paste do not allow to scout the other side. The absolute intensities measured for the “inkjet” solar cells are lower than that measured on “pipetting” solar cells which is in accordance with the smaller content of perovskite. In

addition, the maturation step systematically induces a reduction in the PL intensity for all studied type of solar cells, indicating an improvement of the interfaces and a reduction of the recombination after maturation. On another note, Figure 55 presents roughness measurements realized on the top carbon electrode before and after maturation for both deposition techniques. It can be observed that in both cases the value increases after maturation. This is even more pronounced for inkjet cells presenting before maturation a roughness close to virgin carbon paste. As observed with MEB images, the carbon layer is not fully filled by perovskite. However, as the perovskite precursor solution is infiltrated through the mesoporous layer, some perovskite could remain within carbon and the increase of roughness can be considered as an evidence of either a small perovskite reorganization or a small perovskite passivation in  $\text{PbI}_2$  compatible with an enhancement of the perovskite/carbon interface.

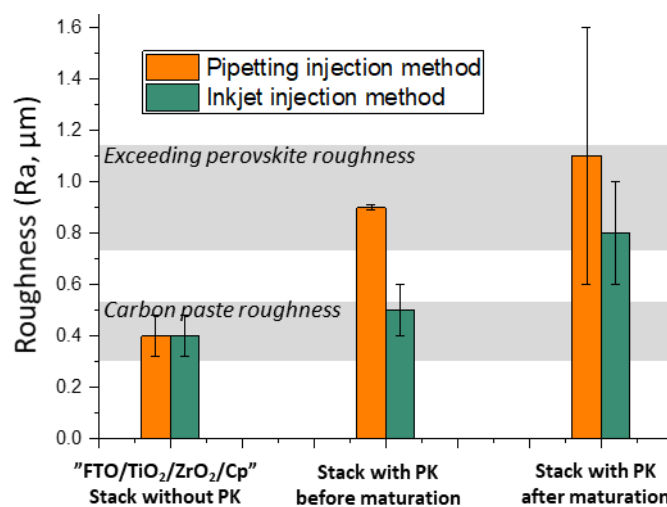


Figure 55: Roughness measurements using contact profilometry on the top carbon layer

To better understand the functional changes within the cells induced by the maturation, impedance spectroscopy measurements (EIS) have been conducted. This technique is widely used to extract the dynamic parameters within the cells. The study of the complex impedance in a Nyquist diagram reveals a series of semicircle attributed to resistance and capacitances. The experimental data may then be fitted to various types of lumped circuits, supposed to describe the different physical contributions in the system, in the present case the ionic and electronic conduction mechanisms and the polarisations at different interfaces[268]. Here the cells were tested under two different conditions: (1) at open circuit (OC) under varying illumination intensities (parameters are extracted, analyzed and plotted as a function of the resulting open-circuit photopotential and (2) under non open circuit (NOC) conditions with varying DC potential (Voltage) with light intensity is fixed to 1 Sun. All impedance plots were presented in the Figure 56 and Figure 57. Our Nyquist graphs typically revealed two semicircles with dissimilar characteristics times, therefore observed at lower and higher frequencies. The specificity of the cells could be quantified with the amounts the extracted parameters (resistance and capacitance). For pipetting cells, the low frequency semicircle is really small in OC conditions, and not visible in NOC conditions before maturation stage. The

inkjet cells show a different behavior: only a second arc is visible after maturation under OC conditions and under NOC conditions, this second arc is barely visible. The equivalent circuit used to adjust the data was chosen from the many options in the literature. We picked one with few parameters (3 resistances and 2 capacitances) enough to describe the set of experimental results and yet contain some physical background for the parameters [269][325][326][327].

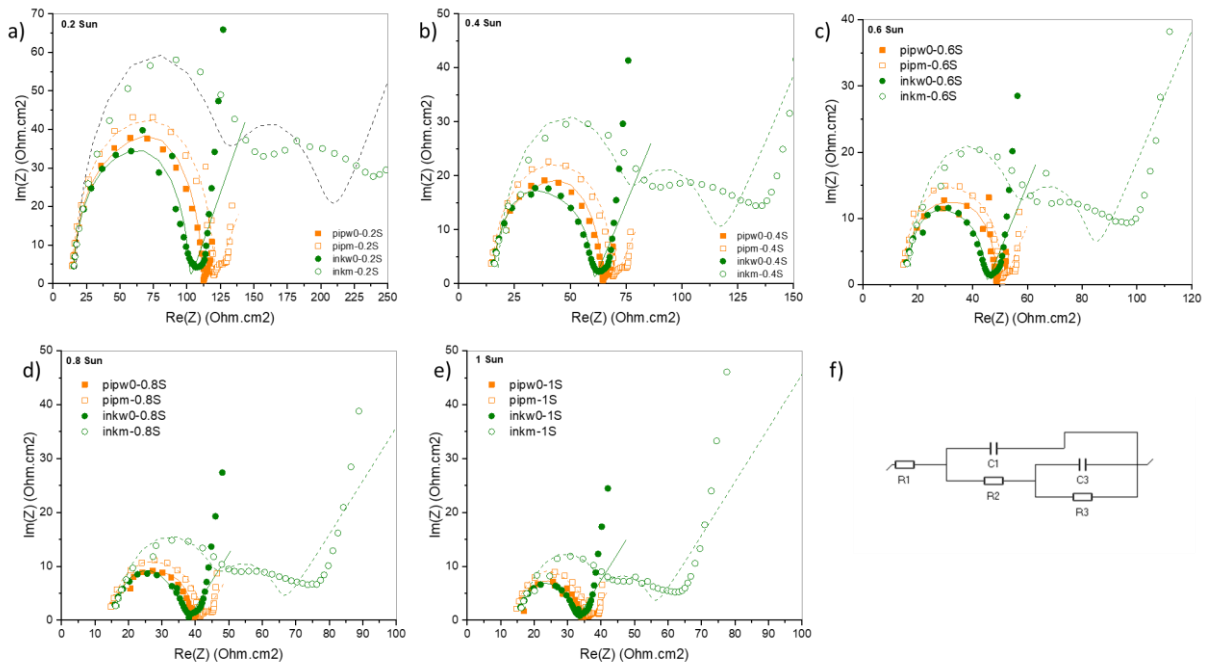


Figure 56: Impedance plots ( $Z''$ - $Z'$ ) measured on "pipetting" and "inkjet" solar cells before and after maturation step under a voltage equal to the open-circuit voltage ( $V=V_{oc}$ ) for different illumination intensities: a) 0.2 Sun; b) 0.4 Sun; c) 0.6 Sun; d) 0.8 Sun; e) 1 Sun; f) Equivalent circuit used for fitting impedance data.

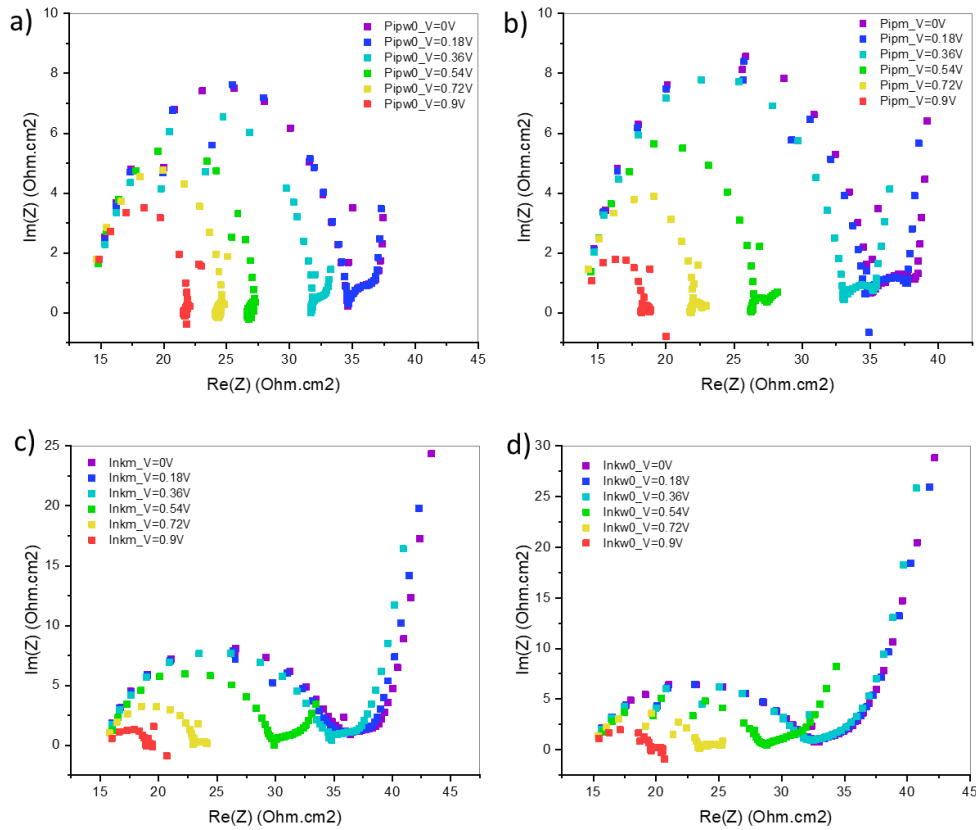


Figure 57: Impedance plots ( $Z''$ - $Z'$ ) measured under variable voltage for an illumination of 1 Sun on a) and b) “pipetting”; c) and d) “inkjet” solar cells before and after maturation

According to various authors, the changes in the five parameters of the lumped model may be attributed to physical changes within the cells. The first and most straightforward one is the series resistor R1, it mimics ohmic contributions of the contacts and wires. The equivalent circuit also includes two capacitances (C1 and C3) and two resistances (R2 and R3). The capacitances C1 and C3 are respectively associated with the bulk response of the perovskite layer and the interfacial polarization due to charge accumulation at the surfaces surrounding the PK. C1 is associated to relatively fast relaxation, it predominates at high frequencies (> 1 KHz). In contrast C3 results from slower charges movement and is visible at lower frequency (1 Hz). With this assumption, the dielectric constant of the perovskite layer  $\epsilon$  may be directly used to estimate the geometrical capacitance of the parallel plate capacitor as  $C1 = \epsilon\epsilon_0 / d$ , where d is the layer thickness and  $\epsilon_0$  the permittivity of the free space. C3 is attributed to space charges accumulation at the interfaces. R2 and R3 represents the low and high frequency resistance related to the recombination process at the interface of the perovskite and the extraction. As a result, total recombination resistance may be obtained with  $R_{rec} = R2+R3$ .



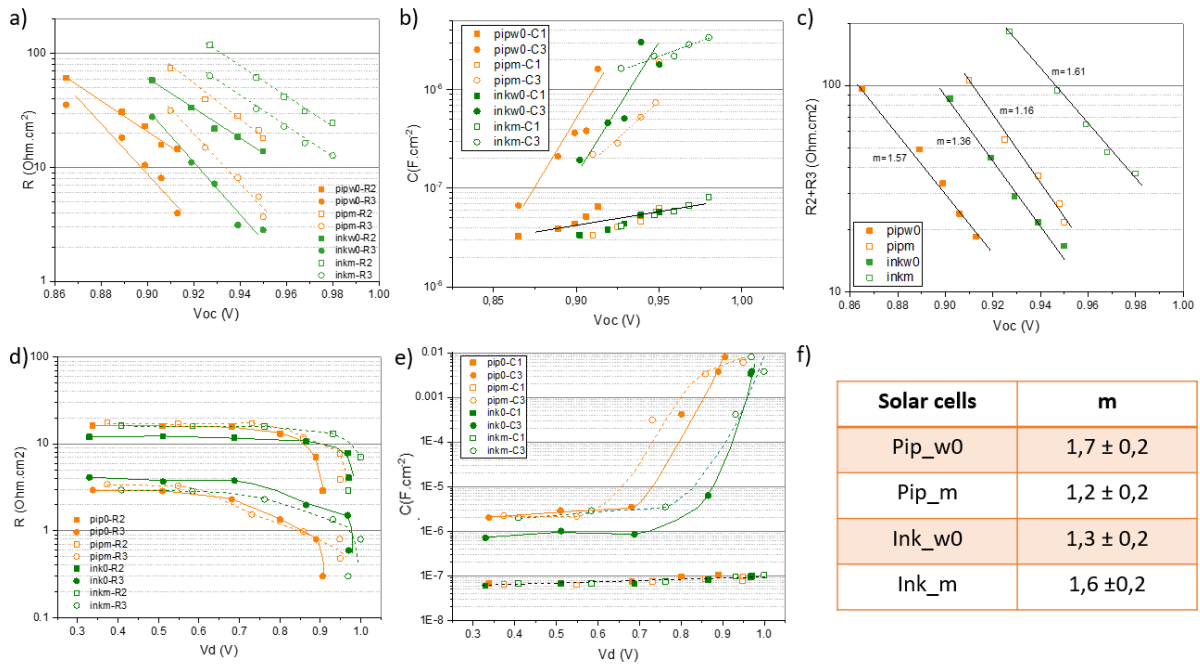


Figure 58: Resistances, Capacitances, Time constants under open-circuit conditions (OC) (a, b, c) and under non-open circuit (NOC) conditions (d, e, f)). Under NOC conditions, parameters are plotted versus the series corrected potential  $V_d = V_{app} - V_{series}$

All the EIS spectra could be fitted fairly with this relatively simple model. The extracted parameters are presented in the Figure 58 for all studied solar cells before and after maturation. Under OC and NOC conditions, the C1 value is remarkably stable when the light intensity and the applied potential are varied, leading to a fairly constant value of  $C_1 \approx 0.08 \mu F \cdot cm^{-2}$ . Surprisingly the capacitance value was not altered by the thickness variations, shown in Figure 51. In other word the C1 value does not seem to reflect the polarization of the PK layer but should be related to an interface. This lumped model was initially designed for fitting the EIS spectra in planar structure, it could seem reasonable to adapt it to account for the mesoporous structure of the studied material, that develops a large amount of interface surfaces. In contrast, C3 was not constant and especially depended on the intensity of the light utilized during the EIS measurements. C3 has a very low value in the dark and increases gradually to reach about  $1 \text{ mF} \cdot \text{cm}^{-2}$  at 1 sun. This is in line with the bibliographic observation, that led the authors to associate C3 with the light-induced buildup of an electronic accumulation zone formed by majority carrier (holes) in the vicinity of the cathode contact (TiO<sub>2</sub>/Perovskite interface [268]). For pipetting solar cells under illumination and OC conditions, the range of C3 decreases during the maturation process, with no variation of R2 and R3. In contrast, we note an increase in C3 and R3 with no variation of R2 for inkjet solar cells in the same conditions. In EIS experiments, each semicircle is associated with a characteristic time. In the present case, two may be defined:  $\tau = R_2 C_1$ ;  $\tau' = R_3 C_3$ , corresponding to high and low frequencies. For pipetting solar cells, very slight modification is to be noted. For inkjet cells, the maturation induces an increase in  $\tau'$  suggesting the accumulation of electrically charged species at the TiO<sub>2</sub>/perovskite interface.

The dependence of the resistance with the illumination may be described mathematically with an Arrhenius equation describing an activation energy [269]. This equation also allows to determine the nonideality coefficient. R2 and R3 were adjusted with the following the expression:

$$R = R_0 \exp\left(\frac{-qV}{mk_B T}\right)$$

Where  $R_0$  is the pre-exponential coefficient,  $q$  is the electron charge,  $k_B$  is the Boltzmann constant,  $T$  is the temperature, and  $m$  is the nonideality factor. The recombination resistance or charge transfer resistance  $R_{rec}$  within the cells may be simply determined with the addition of the two resistances R2 and R3 [269]. The Figure 58 c) displays the result of this calculation as a function of the light intensity. The samples presented a very similar slope, suggesting the meaningful determination of the nonideality factors. This useful parameter helps understand the recombination process in solar cell. Its absolute value allows to identify the nature of the mechanisms. The tested materials may be divided in three categories corresponding to discrete value,  $m=1$  for band-to-band,  $m= 1.5$  to band-to-defect within the absorber bulk,  $m=2$  for the band to defect recombination at the space-charge region in the vicinity of the surface. In summary the smaller  $m$  values indicate better cells, closer to ideality. In the case of the pipetting solar cells, the maturation step induces a decrease in  $m$  from almost 2 to close to 1. This clearly reveals that the maturation improves the recombination process for pipetting solar cells. As little variation in the R3 and C3 parameters is observed after maturation for these cells, it seems that this recombination improvement is partly due to a change in the perovskite layer. This seems entirely in line with the results obtained previously. In contrast, the  $m$  value increased after the maturation for inkjet cells, favoring the band-to-defect recombination process. Indeed, only a variation of parameters C3 and R3 seems to be observed after maturation, indicating essentially a modification of the interfaces and probably the one between  $TiO_2$  and perovskite. This seems to confirm the results obtained previously, which indicates little modification of the perovskite layer microstructure after maturation.

Under NOC conditions, an exponential dependence is observed at high DC potential but becomes flat as the experiment approaches SC conditions, which suggests that the device is ruled by the shunt resistance at fixed light intensity and low applied bias. The transition between the two regimes occurs at voltages right below the maximum power point (MPP) of the corresponding  $J(V)$  curves. At high voltage, the behavior is similar than that observed under OC conditions. Concerning the maturation impact, we note after maturation a shift of the transition to higher voltage for all studied solar cells, probably explained by a shift of the MPP, inducing an improvement of the performance after the maturation step. As under OC conditions, C1 is constant whatever the tested potentials and similar for all tested solar cells before and after the maturation. This is in agreement with observations under OC conditions. An increase in C3 was observed for inkjet solar cells after the maturation process. There are also variations for parameters R2 and R3 but much less marked than in OC conditions. For pipetting solar cells, no variation was observed. Globally, the trends are similar for both types

of solar cells, whatever the tested conditions (NOC and OC), which seem indicate only a modification of the interfaces for inkjet solar cells after the maturation step.

In addition of all conducted analyses, it seems also relevant to take an interest on the detailed procedure for measuring the PCE in solar cell. For instance, many authors have noticed that varying the scan rate can directly alter the results. In our case, we have noticed that the shape of the J(V) curve strongly varied depending on the scan rate. The J(V) curves presented in Figure 59 (b-e) are measured in reverse scan at variable scan rates comprised between 1 mV/s and 1000 mV/s.

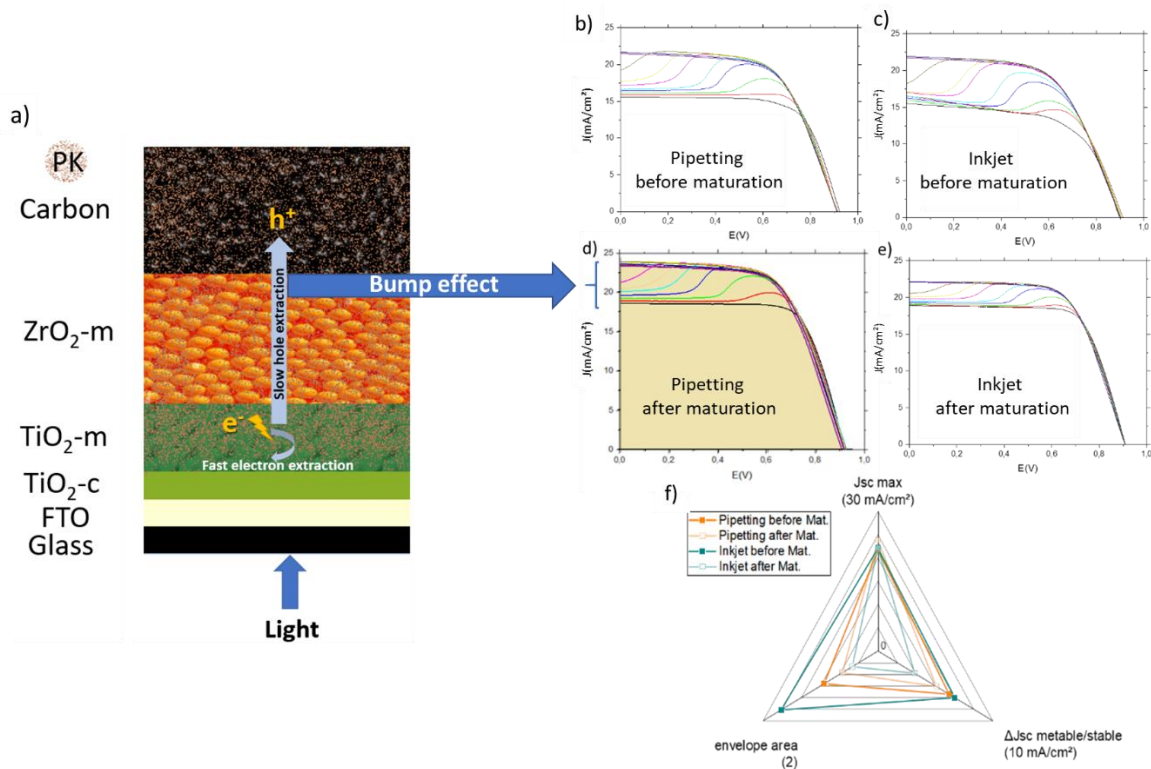


Figure 59: a) Schematic representation of the electrons and holes shifts into the solar cell; J(V) measurements performed at variable scan rates comprised between 1 mV/s and 1000 mV/s for pipetting solar cells: b) before maturation, d) after maturation and for inkjet solar cells: c) before maturation, e) after maturation; f) Representation of the key parameters extracted from JV measurements

A major problem with the configuration of HTM-free devices with a zirconia buffer layer is the relatively long distance ( $\sim 1\mu\text{m}$ ) that the holes must travel to reach the conductive carbon cathode as illustrated in Figure 59. Incident light in the visible range that reaches the solar cell is mainly absorbed in the first few hundred nanometers of the cell's perovskite layer, which means that most of the electron-hole pairs are generated near the photoanode. Therefore, free electrons can be extracted quickly by simple injection into the mesoporous titanium, while the generated holes must pass through the mesoporous zirconium oxide to reach the carbon contact. This can lead to an imbalance in charge extraction, which often results in hysteresis behavior as well as the appearance of a "bump" in the reverse J(V) scan. This bump

begins to shift towards lower voltage while increasing the scan rates. Besides, as highlighted in Figure 59(b-e), this phenomenon is due to a transition from a stable state (at low scan rate) to a metastable one (fast scan rate), where in both cases there is no bump effect, by a relaxation mechanism from where we can estimate a characteristic time (not presented here, in study elsewhere in the lab). As shown in Figure 59, it appears that the maturation stage reduces the amplitude between the stable and the metastable states, by mainly increasing the stable state  $J_{sc}$ . Consequently, it seems that this process leads to an improvement of the charge transfers within the cell. For pipetting cells, this seems to be partly confirmed by the previous results which show an improvement of the microstructure, the formation of a 2D PK phase, limiting the formation of defects and by the IS measurements showing an improvement of the recombination process. In the case of inkjet cells, other elements may explain these results. Indeed, the fact that the characteristic time of low frequency processes characteristic of charge transfer at the  $TiO_2$ /PK interface increases can partly explain the decrease of the appearance of this bump. In literature, one of the strategies used to limit this phenomenon is the introduction of CuSCN in the perovskite to accelerate the mobility of the holes [91].

## Conclusion

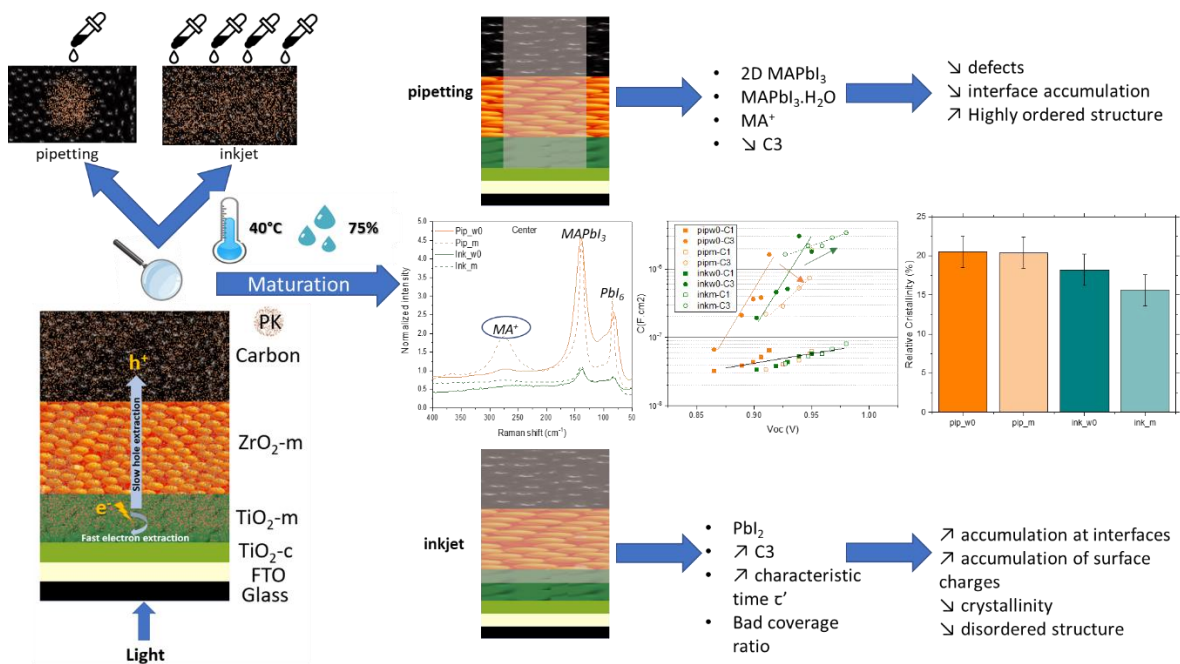


Figure 60: Schematic representation summarizing the performance of pipetting and inkjet cells after maturation

To sum up, the mechanism of a beneficial maturation process was here studied through two different perovskite deposition processes. The studied solar cells consist of a triple mesoporous layer TiO<sub>2</sub>/ZrO<sub>2</sub>/C where the perovskite is added as a final step either by pipetting or inkjet. Once the devices are completed, they undergo or not a maturation step during 150h at 40°C with 75% of relative humidity. This study successfully demonstrated that this post-treatment improved the photovoltaic performances of the cells whatever the infiltration PK method used. This enhancement was certified by many characterizations: J(V) measurements, LBIC, MEB, XRD analysis, Raman, UV-visible and PL spectroscopies and Impedance spectroscopy. As a result of the maturation, the PCE greatly increased from 10.5% to 14% and from 10% to 14% for pipetted and inkjet cells respectively. This increase is mainly due to the appearance MA<sup>+</sup> in pipetted cells improving the charges transfer with more ordered PK structure. Moreover, the formation of a 2D MAPbI<sub>3</sub> phase detected in the UV measurements, allows the formation of a better interface between perovskite and TiO<sub>2</sub> electron transport layer reducing the defects. Whereas for the inkjet cells, an homogeneous aspect is noticed in LBIC and MEB images with the same PK amount in the middle as in the corners of the cell, which is not the case for pipetted cell. Pbl<sub>2</sub> appearance after maturation, led to lower crystallinity rate for inkjet cells. These devices undergo a C3 decrease detected in impedance spectroscopy causing accumulation of surface charges at the TiO<sub>2</sub>/perovskite interface. However, PL spectroscopy highlights a reduction of the recombination after maturation, which should thus occur to the carbon/perovskite interface according to the roughness measurements. To further investigate the impact of the maturation step on stability of the

recent studied devices, aging campaigns were conducted in the next chapter where damp heat 85°C/85% R.H. tests were applied.

Supplementary information

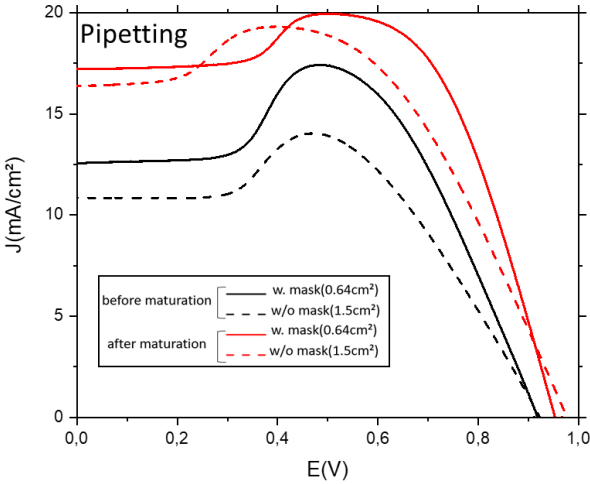


Figure 61: J(V) measurement of a pipetted cell with and without a mask before and after maturation

**CHAPTER V: EFFECT OF THE  
PROCESSING AND OF  
MATURATION ON THE  
STABILITY OF CARBON-BASED  
PEROVSKITE SOLAR CELL  
UNDER DAMP HEAT  
CONDITIONS**



## Introduction

Intensive efforts have been recently made to enhance the power conversion efficiency of perovskite solar cells like optimizing the perovskite and interfacial layers or the deposition method of the active layer or the post treatments. In this manuscript, two deposition processes of perovskite were compared: the first one, called "pipetting process" (single injection of the perovskite solution at the center of the solar cell) and the second one called "inkjet process" (several injections similar to a printing process). As demonstrated in the previous part, these solar cells do not achieve their maximal performance at the end of the manufacturing, but require a so-called maturation process. After a "running-in" period of 150h at 40°C/75% RH, the performance of these cells improves from about 10% to roughly 14% for both pipetting and inkjet cells. The mechanisms at the origin of this maturation have been largely described in the previous section. To cut a long story short, the large increase mainly results from the improvement of the charger transfers due to a passivation either from 2D MAPbI<sub>3</sub> or PbI<sub>2</sub> formation depending of the perovskite infiltration process used.

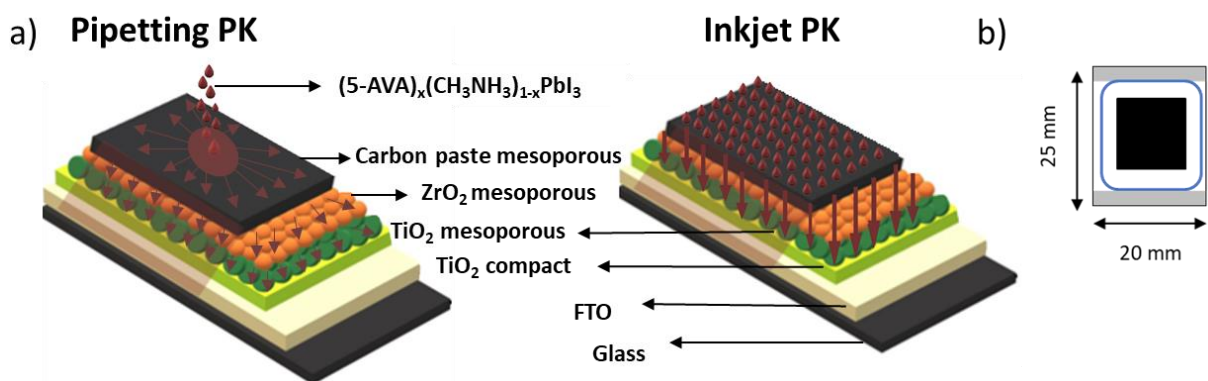


Figure 62: a) C-PSC cell architecture with a simplified representation of the perovskite deposition processes (active area = 12\*12.5 mm<sup>2</sup>); b) Dimension of solar cells after encapsulation (glass-glass laminated with a Surlyn gasket sealant, represented by a blue line)

In this study, the stability of these perovskite solar cells has been evaluated under damp heat conditions. The architecture as well as the geometry is shown in Figure 62. The main objective of the present study is to evaluate if the long-term stability of the cells may be altered by the perovskite deposition process or the maturation step. Various types of cells were therefore subjected to accelerated aging at 85°C/85%RH for 3000h. The performance of about 5 cells from each batch was monitored at regular time intervals. Other cells were also prepared, and aged with the same conditions to track possible structural and chemical changes within the active layer. A detailed study of the correlation among this large series of results, allows to develop new insight of the performance and the degradation mechanisms of these type of solar cells.

## Results and discussion

The Figure 63 presents the variation of PV parameters of the studied solar cells during the aging campaign. As mentioned, at initial stage matured solar cells show better performance as compared to the freshly processed counterparts, Figure 63 d). As a tradeoff, the cells exhibit a significant decrease in performances during the first day of aging up to 220h. They interestingly ended up to PCE very close to that of non-matured solar cells. The latter were found relatively stable during this first step, "Phase 1" in Figure 63 d). The changes in the PCE in matured cells were governed by a decrease in both  $J_{sc}$  and  $V_{oc}$  (Figure 63 c)) and (Figure 63 e)). This combination of results suggests that the maturation step presents little interest on a practical standpoint. The performances improve only momentarily, and the overall energy production is not altered significantly.

A comparison of the processing condition reveals a balance between both inkjet cells with a better  $V_{oc}$ , and we can note that  $V_{oc}$  of inkjet solar cells are better throughout the aging campaign than the ones of pipetting solar cells, contrary to  $J_{sc}$ , which is similar for all tested solar cells during this phase 1. This leads globally to a decrease in FF for pipetting solar cells (Figure 63 b)) up to 220h, whereas this parameter is globally stable for inkjet solar cells. For all tested solar cells, the  $R_s$  value is relatively weak during this stage, Figure 63 f). After this first stage of aging, a continuous decrease in performance can be observed for inkjet cells, whatever the initial treatment. It is the second phase of aging, called Phase 2 in the Figure 63 a). After 1000 hours of ageing, these cells show performances too low to be qualified as functional. We note a more important degradation of the performances for the matured cells. This decrease of performance is partly explained by the decrease of  $J_{sc}$ , which is also more important for the matured cells, then at the end of aging by a drastic increase of the  $R_s$ . The FF and  $V_{oc}$  parameters of inkjet cells are globally quite stable during these 1000h of aging.

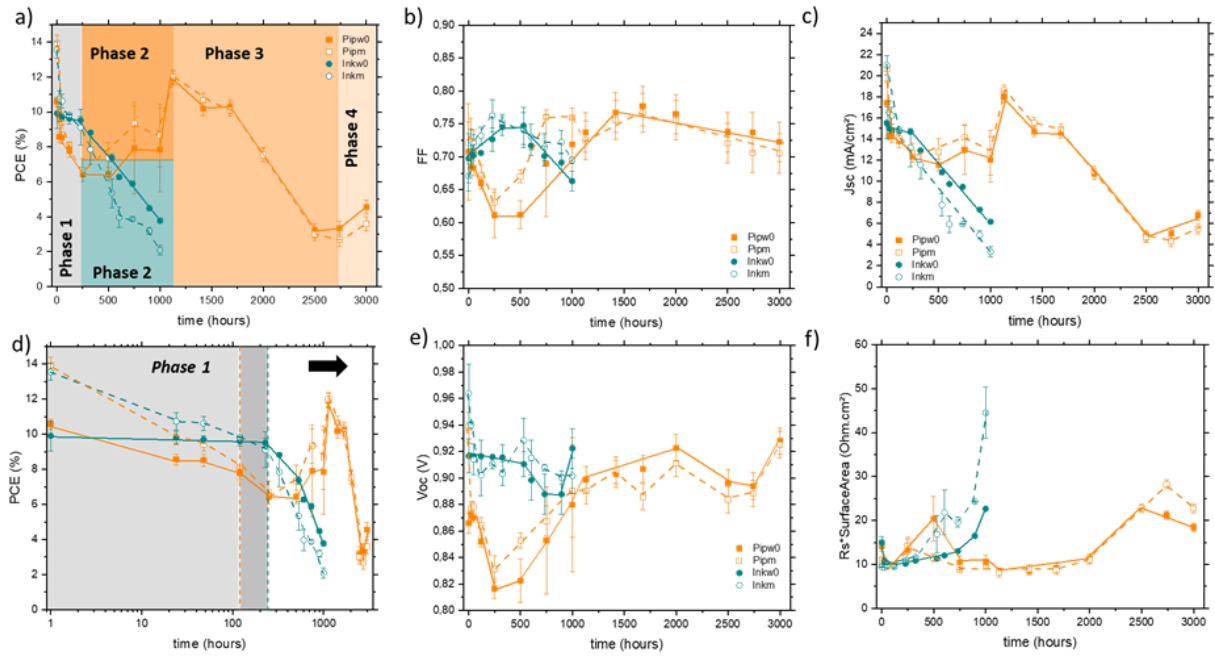


Figure 63: Variations of PV parameters (Power Conversion Efficiency (PCE) presented respectively in normal and logarithmic scales (a; d); Fill Factor (FF) (b); Short Circuit Current density ( $J_{sc}$ ) (c); Open circuit voltage ( $V_{oc}$ ) (e); Series resistance ( $R_s$ ) (f)) during aging campaigns for “Pipetting” and “Inkjet” solar cells with (m) and without (w0) the maturation pre-treatment step. ( $J/V$ ) measurements performed at  $4mV/s$  in reverse scan)

For the pipetting cells, we note three additional aging phases, called Phases 2, 3 and 4 on Figure 63 a): after the decrease of performances observed in Phase 1, a reincrease of the performances is observed until 1130h of aging to reach quasi initial performances (Phase 2), then a decrease until 2750h of aging (Phase 3), followed by a slight increase till 3000h (Phase 4). It is important to specify that the matured cells present higher performances during phase 2 then a quite similar behavior for both types of cells in phase 3 to end with a slight performance increase for non-matured cells in phase 4. The increase in performance observed during phase 2 is explained by an increase in FF,  $J_{sc}$  and  $V_{oc}$ , Figure 63 b), c) and e). The performance decrease observed at phase 3 is mainly due to a decrease in  $J_{sc}$  Figure 63 c). The improvement at phase 4 is essentially induced from the  $J_{sc}$  and  $V_{oc}$  increase. On another note, the  $R_s$  increases for pipetted cells till 500h in correlation with the PCE decrease, this parameter remains then low till 2000h in accordance with the PCE reincrease. It increases again at the end of Phase 3 explaining the PCE decrease, followed by a slight decrease coordinating with the PCE increase in Phase 4, Figure 63 f).

Consequently, even if the two types of cells (pipetting and inkjet) present a similar architecture, the process of deposition of the perovskite seems to have a determining effect on the long-term stability of these devices. The inkjet cells present a rather low stability, at 1000h no more cell is functional, while the pipetting cells have yields close to 8% at 1000h of aging and 4% at 3000h. It seems that the mechanism of degradation is different, since the degradation of the performances for the inkjet cells is partly due to a fall of  $J_{sc}$ , which is generally rather traditional. For the pipetting cells, the first decrease of performance is due to a decrease in  $J_{sc}$ ,  $V_{oc}$  and FF, then the reincrease in performance is partly due to variations in

$V_{oc}$  and FF, and after the major decrease is mainly caused by the  $J_{sc}$  variation whereas the slight improvement at the end of the aging is originating from a  $V_{oc}$  and  $J_{sc}$  increase.

A major problem with the configuration of carbon-based devices is that the high temperature, needed to obtain an optimal carbon layer, implies a post-deposition of perovskite. If this post-deposition of perovskite is an advantage for a clean industrial process development, it implies first the use of an insulating mesoporous zirconia buffer layer between electron transport and carbon layers. According to previous results, it seems rational to interpret the stability difference between inkjet and pipetted devices by the fact that less precursor solution was used. This should lead to a lower stock of perovskite materials to face ageing, leading quickly to a non-sufficiently filled  $ZrO_2$  mesoporous layer, resulting in insulating devices.

In addition, the relatively long distance ( $\sim 1\mu m$ ) that the holes must travel to reach the conductive carbon cathode could engender another problem which is visible on our  $J(V)$  curves. The later generally show significant hysteresis (see Figure 73 in supplementary info), are very variable depending on the scan speed used, and may show a more or less significant bump. To better understand the first phase of aging, an in-depth study of this bump phenomenon was carried out and represented in Figure 64.

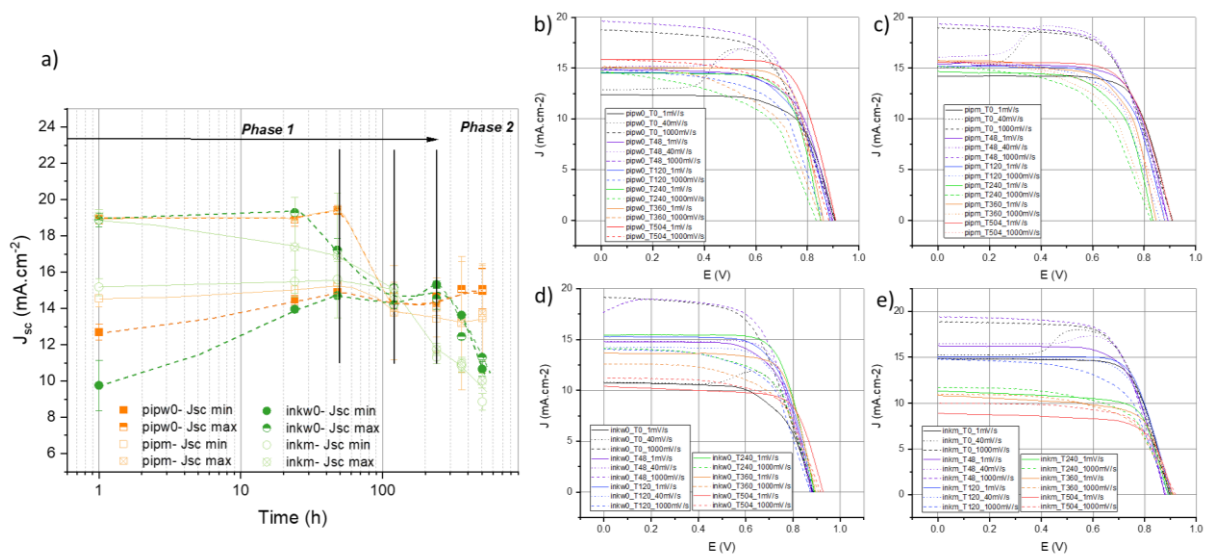


Figure 64: a) Variations of minimum and maximum  $J_{sc}$  values (from  $J(V)$  measurements performed at different speeds) as a function of aging time for “pipetting” and “inkjet” solar cells with and without pre-maturation;  $J(V)$  measurements performed in reverse scan at different speeds as a function of aging time for unmaturation (w0) and maturation (m) pipetting (respectively b) and c) and inkjet (respectively d) and e) solar cells.

When the scan speed of the  $J(V)$  measurement varies from 1 mV/s to 1000 mV/s, we note an important variation of the curve obtained, with for these two limit speeds mainly an increase of the  $J_{sc}$ , for example from approximately 12 to 20  $mA \cdot cm^{-2}$  for a not matured pipetting cell in the initial state. No bump is observed for these two speeds, which is why the  $J(V)$  curves obtained at low and high speeds will be called stable and metastable states respectively. When intermediate scan speeds are tested, we note the appearance of a bump, as shown in Figure 64b), c), d) and e).

As shown in Figure 64 b), c), d) and e), this bump phenomenon seems to be particularly intense and visible at initial state to completely disappear after 120h of aging, whatever the cell type studied. We can also observe that the difference between the  $J_{sc}$  obtained in the stable and metastable states seems to be very important at the initial state to become null during the aging. These two parameters were therefore chosen and plotted as a function of aging time for all the solar cells tested, Figure 64a). In the initial state, we can observe that whatever the type of cell, the value of  $J_{sc-max}$  is identical, only the value of  $J_{sc-min}$  varies. Globally the difference between these two parameters is more important for non-matured cells than for matured cells. As mentioned in the previous section, one of the mechanisms observed during the maturation phase is the improvement of the electron and hole transfers to the electrodes of the cell. As shown previously for the  $J(V)$  measurements, phase 1 occurs up to 120-200h. The study of the  $J(V)$  measurements as a function of the speed and more particularly of the difference between  $J_{sc-max}$  and  $J_{sc-min}$  shows that this phase can be divided into three sub-phases. Up to 48h,  $J_{sc-max}$  remains relatively stable, close to  $20 \text{ mA.cm}^{-2}$  except for inkjet solar cells, which showed a slight decrease in this parameter. During this stage,  $J_{sc-min}$  is globally stable for matured solar cells, whereas an increase in this parameter is observed for non-matured cells, inducing a decrease of the gap between these two parameters. This also explains the increase of FF and the  $R_s$  decrease observed for non-matured solar cells respectively in Figure 63 c) and f). This step seems to resemble a maturation or post-maturation step, with the objective of improving charge transfer within the cell, essentially by balancing electron and hole transfer rates explaining the performance approach of non-matured cells to matured ones during phase 1 demonstrated in Figure 63. This also explains the increase of FF and the  $R_s$  decrease observed for non-matured solar cells respectively in Figure 63 c) and f). Between 48h and 96h, a significant decrease of  $J_{sc-max}$  and to a lesser extent of  $J_{sc-min}$  is observed, so that at 120h, all the cells studied present an identical  $J_{sc-min}$  and  $J_{sc-max}$ . The bump phenomenon has completely disappeared indicating a good balance of the charge transfers within the cell. This confirms the previously shown  $J(V)$  results, which indicate that the matured and non-matured cells present identical performances at 120h. We can therefore see this phase as a culmination of the maturation phenomenon, induced for matured solar cells by the post-treatment performed just after the process and for non-matured solar cells by aging from 100h to  $85^\circ\text{C}/85\%RH$ . Thus, the solar cells studied in this thesis presenting a somewhat special architecture have the particularity of presenting a transient phase after their process, during which the transfers of load within the cell must be balanced. There is a slight lag between the pipetting and inkjet solar cells, probably explained by the fact that the performance is not only influenced by the  $J_{sc}$ . After 120h, during phase 2, similar values for  $J_{sc-min}$  and  $J_{sc-max}$  are still observed, confirming the disappearance of this bump phenomenon. For pipetting cells, we observe a maintenance of the values of  $J_{sc-min}$  and  $J_{sc-max}$ , whereas a significant decrease of these parameters is observed for inkjet cells. These results are in good agreement with those presented previously, even though for the first 100 hours we move over the bump at intermediate speeds.

To elucidate the degradation mechanisms occurring during phase 2, a set of characterization methods were used. In addition to the J(V) measurements, classically performed during aging tests, imaging techniques allowing to better evaluate the local performance of a cell have been implemented on our devices.

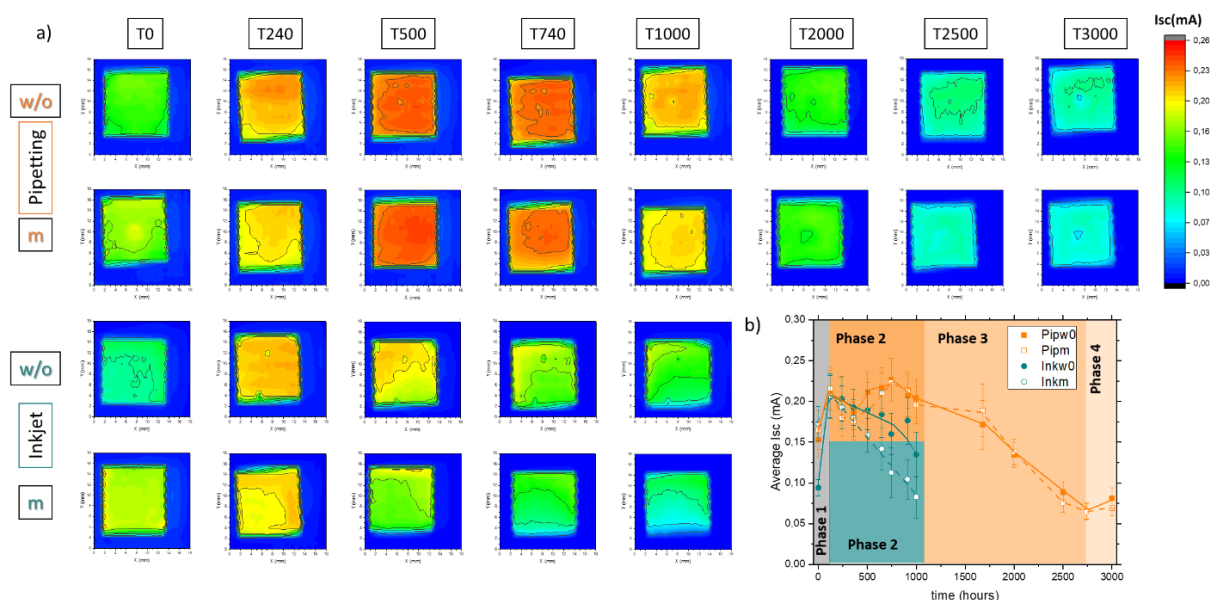


Figure 65: a) LBIC map for all studied cells for different aging times, the color scale represents the short circuit current variation; b) Variations of the LBIC measured average circuit current  $I_{sc}$  (averaged over the active cell area, the uncertainty bar represents the variation over the area of one cell) during the aging campaign for pipetting and inkjet cells with or without maturation before T0.

One of the techniques often used in our team is the measurement of local short-circuit current induced by laser beam. This last one is relatively relevant to evaluate the local performance of a cell. As it has already been shown, in the initial state, inkjet cells are much more homogeneous in terms of local performance than pipetting cells. It is also possible to see that the maturation stage leads to a homogenization of the performances between pipetting and inkjet processes. Up to 120h, the transient phase, previously highlighted seems to be confirmed, since a clear improvement of the average LBIC- $I_{sc}$  observed. Then follows phase 2, which is divided into three sub-phases for pipetting cells. As for the J(V) measurements, the same sequence seems to be confirmed, indicating a good correlation of the results. Up to 500h, a stabilization or a slight decrease of the average short-circuit current is respectively observed for the non-matured and matured pipetting cells, confirming the previously observed PCE and  $J_{sc}$  results. Still, we note much smaller variations for the LBIC measurements than for the J(V) measurements. It is also important to reiterate that the J(V) measurements are performed with a  $0.64 \text{ cm}^2$  mask while the LBIC measurements provide an overview of the entire active surface of the cell ( $1.5 \text{ cm}^2$ ). Thus, it appears that the center of the cell experiences more performance changes than the edges. We then note an increase of this parameter until 740h and then its decrease up to 2750h of aging to be slightly increasing till the 3000h in correlation with the PCE and  $J_{sc}$  variations observed in the J(V) measurements. The maps for the two pipetting cells are very similar at 240h and 1000h, confirming the

excellent stability of these devices. Then, a constant decrease in local current measurements is observed. We can note a small stabilization at the end of aging (between 2500h and 3000h of aging). These observations are in full agreement with the J(V) measures previously studied.

At phase 1, we note an LBIC- $I_{sc}$  increase for non-matured inkjet cells as for pipetting ones explaining the  $J_{sc-min}$  increase in Figure 64 a) and reaching the same level than matured cells whatever the process used. After 120h, i.e passing to the phase 2, a continuous decrease of the average LBIC- $I_{sc}$  is observed for both types of the inkjet cells confirming the results of the J(V) measurements. The results seem to be a little less correlative with the J(V) measurements for inkjet cells at this aging time since LBIC- $I_{sc}$  is not so much altered as J(V)- $J_{sc}$ . But, like for PCE and  $J_{sc}$ , the decrease of LBIC- $I_{sc}$  is much smaller for inkjet non-matured cells than for inkjet matured-cells.

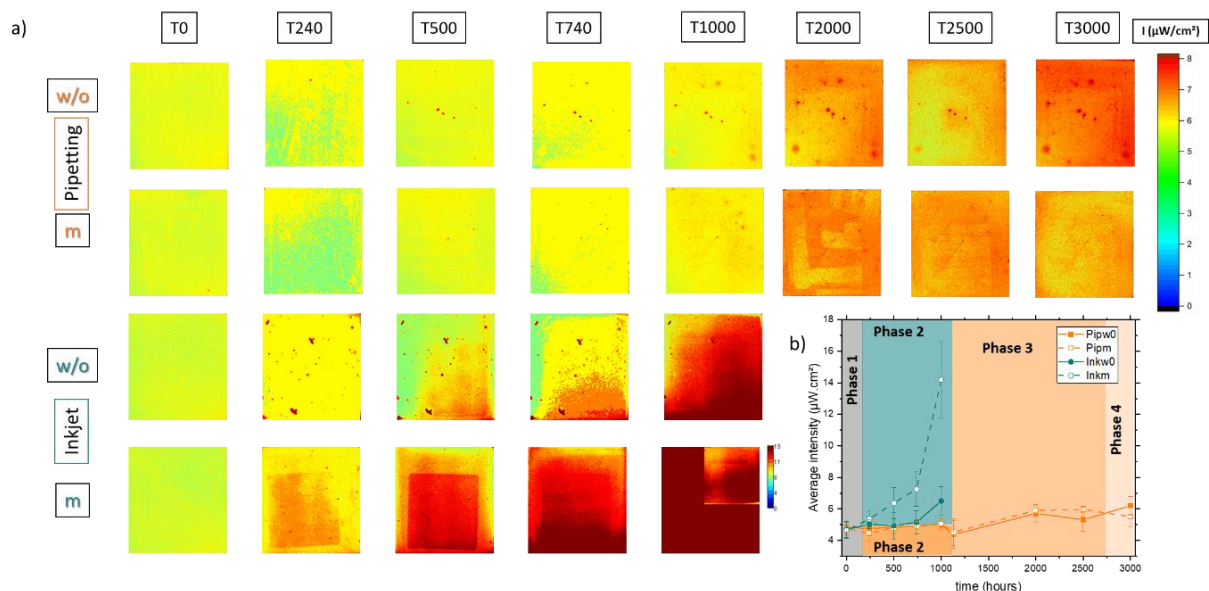


Figure 66: a) PL imaging photos for all studied cells for different aging times, the color scale represents the photoluminescence intensity variation ; b) Variation of photoluminescence intensity measured by imaging (averaged over the active cell area, the uncertainty bar represents the variation over the area of one cell) during the aging campaign for pipetting and inkjet cells with or without maturation before T0.

Our PV results can be combined with photoluminescence imaging. The results are presented in the Figure 66. During the phase 1, no strong evolution of PL emission of solar cells can be observed. After 120h, the behavior is very different following the solar cell type. For pipetting solar cell, a stabilization in the PL signal during phase 2, respectively to that observed in the PCE with a slight decrease at 1100h explaining the PCE increase at the end of this phase. Nevertheless, we note no difference between non-matured and matured solar cells, contrary to the previous results where matured cells showed a quite better performance. This technique may not be sensitive enough, the spectroscopy analyses will probably go further. Recall that this technique is more used for observations of homogeneity of PL emissions. Concerning this aspect, we note a quite homogeneous signal with only a few defects during the phase 2 for pipetting cells, confirming the good quality of the encapsulation till 2000h of

aging. Then, the PL mapping show more pronounced defects and heterogeneous PL increase, highlighting the degradation effect and in correlation with the PCE decrease at this stage. This is confirmed by the plot in Figure 66 b since a slight increase in the uncertainty bar was observed with the aging time. Regarding the inkjet solar cells, a different trend has been observed. The PL imaging show a non-homogeneous signal since the beginning of phase 2 with a large number of observable defects for non-matured cells and a high and continuous increase of PL for matured cells up to 1000h. It seems that these cells are much more sensitive to aging. The uncertainty bars plotted in Figure 66 b also confirms the more heterogeneous degradation increasing with aging time. One again, the lower quantity of perovskite used to fill the mesoporous scaffold probably lead more rapidly to voids within the perovskite layer. In addition, we note the appearance of a square for matured solar cells indicating a preferential degradation of the area subject to illumination during measurements J(V) (use of a 0.64 cm<sup>2</sup> square mask in order to avoid measuring potential non-filled border areas in the case of pipetting process). The observed variations seem however to be in relatively good agreement with the results previously shown. One can just notice a difference in behavior between matured and non-matured cells, apparently not obvious when studying performance variations during aging. To conclude, deepening of these results seems interesting to be conducted using photoluminescence spectroscopy.

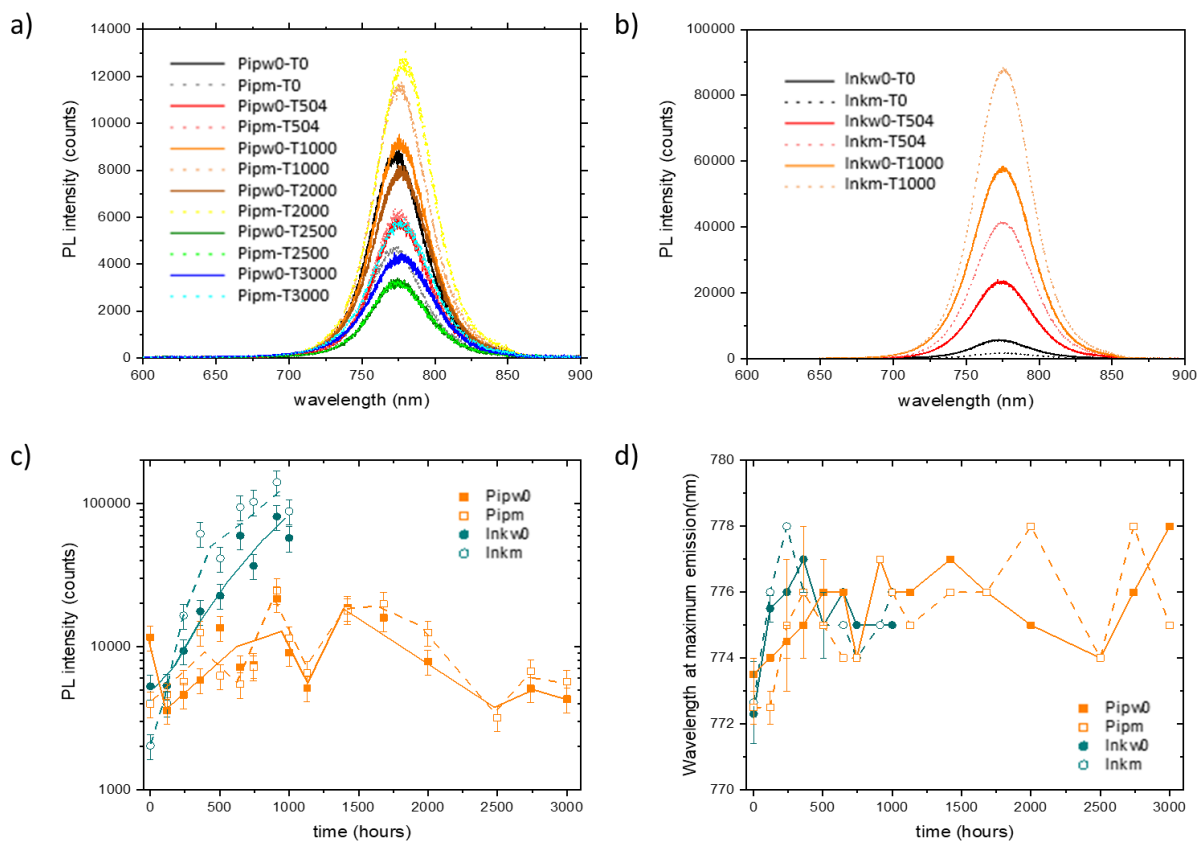


Figure 67: Photoluminescence spectra during aging for a) pipetting and b) inkjet solar cells; Variation of c) maximum emission intensity and d) wavelength at maximum emission intensity as a function of aging time for pipetting and inkjet solar cells with or without maturation before T0.



The photoluminescence spectroscopy results are presented in Figure 67. As with other characterizations, the transient phases are also visible, Figure 67c). The difference in behavior between the inkjet and pipetting cells is clearly confirmed. For pipetting solar cells, after a first PL decrease for non-matured cells in phase 1 to reach matured value and thus confirming the occurring of a post-maturation of non-matured solar cells by the first 100h of aging, a slight increase in maximum signal intensity is then observed during all aging. This increase is much more drastic for inkjet solar cells, with clearly more marked degradation for matured solar cells. As a result, the recombination mechanism seems clearly affected by aging for this type of cells. Moreover, the good stability of the pipetting solar cells also seems to be confirmed by this technique. Regarding the variation of the wavelength to the maximum intensity of emission peak, a significant increase in early aging can be observed during the first 500h for all solar cells. This redshift probably indicates an improvement in the crystalline microstructure of perovskite during phase 1.

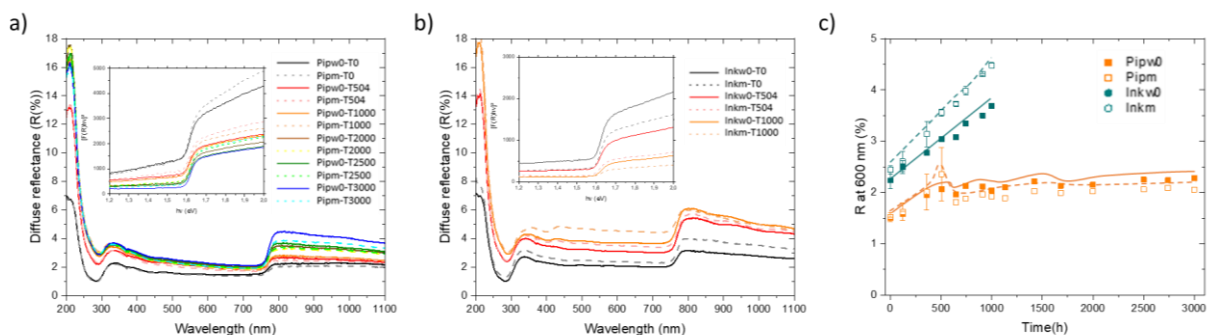


Figure 68: UV-Visible reflectance spectra performed on complete cells (FTO side) during the aging campaign for a) pipetting and b) inkjet solar cells, c) Variation of reflectance value at 600 nm versus aging time for all solar cells studied

To correlate these results with potential degradation of the active layer, UV-Visible spectroscopy analyses were performed. These results are presented in Figure 68 and Figure 69. Two types of analyses were carried out: reflectance analyses allowing follow-up throughout aging since this is a non-destructive test, and absorbance analyses which require the opening of the cell and the peeling of the carbon layer. While the latest analyses are more relevant, they are destructive and could not be done as frequently during the aging campaign. As shown in Figure 68 a) and b), the bandgap of 3D MAPbI<sub>3</sub> perovskite constituting mainly the active layer is clearly observable in reflectance and is around 780 nm. Thanks to the Tauc plots presented in inset, we can see no evolution with aging of the bandgap at 1.59 eV regardless of the type of solar cell. Although this may seem a bit surprising, the degradation of perovskite must be significant enough to observe a change in the bandgap[328], and according to the high of reflectance difference around MAPbI<sub>3</sub> transition it is obvious that MAPbI<sub>3</sub> is always present in a consequential quantity at the end of all ageing campaigns. With this technique, however, it was possible to observe a non-negligible increase of the reflectance of the global spectra (from 200 to 1100 nm). Since the reflectance is increased all over the observation range, this does not signify the observation of a degradation product but more a modification

of the filling of the device. Indeed, it was measured that a Glass/TiO<sub>2</sub>/ZrO<sub>2</sub>/C stack without perovskite possesses a reflectance level higher than both pipetting and inkjet filled stacks at T<sub>0</sub> (see SI-Figure 74).

In order to compare the different cells studied, the reflectance level at 600 nm was plotted as a function of aging time for all the cells studied, Figure 68 c). If a similar slope was firstly observed for all devices until 500h, pipetting cells then stabilized which is related to the re-increase of PCE observed while inkjet cells continue its rise. There is also a more intense increase for matured inkjet solar cells, confirming their greater sensitivity to aging. These results appear to be consistent with previous results. Indeed, less filling perovskite inside inkjet devices compared to pipetting ones already allows a higher reflectance level at T<sub>0</sub>. Then, the degradation or amorphization of perovskite allows the pursuit of the reflectance level increase to converge towards the level of a stack without PK. The low stability of the inkjet solar cells seems to be confirmed and the drop-in performance observed during the ageing campaign, contiguous to a significant decrease in the J<sub>sc</sub>, seems partly explained by a significant reduction of the perovskite layer. By the way, it is possible to observe the emergence of perovskite degradation by-products on reflectance spectra for inkjet devices at 1000h with the presence of a transition with a 400 nm bandgap, corresponding to hydrated MAPbI<sub>3</sub>[299][298]. To observe PbI<sub>2</sub> transition, one should continue the aging campaign long after the reaching of null PCE values, see in SI-Figure 75 Figure 75: UV-Visible reflectance spectra performed on unmaturred and matured inkjet cells at 1600 hours of aging (after the 1000h aging time corresponding at PCE=0). the reflectance spectra at 1600 hours for inkjet cells. Pipetting solar cells appear to be much more stable. This may seem a priori surprising, since these two devices have a similar architecture. Only the deposition process of perovskite differs. But as shown in the previous part, the thickness of the perovskite layer in the inkjet solar cells is much lower and the resulting microstructure appears to be more defective than that obtained in the pipetting solar cells. It can be assumed that this perovskite is much more sensitive to aging.

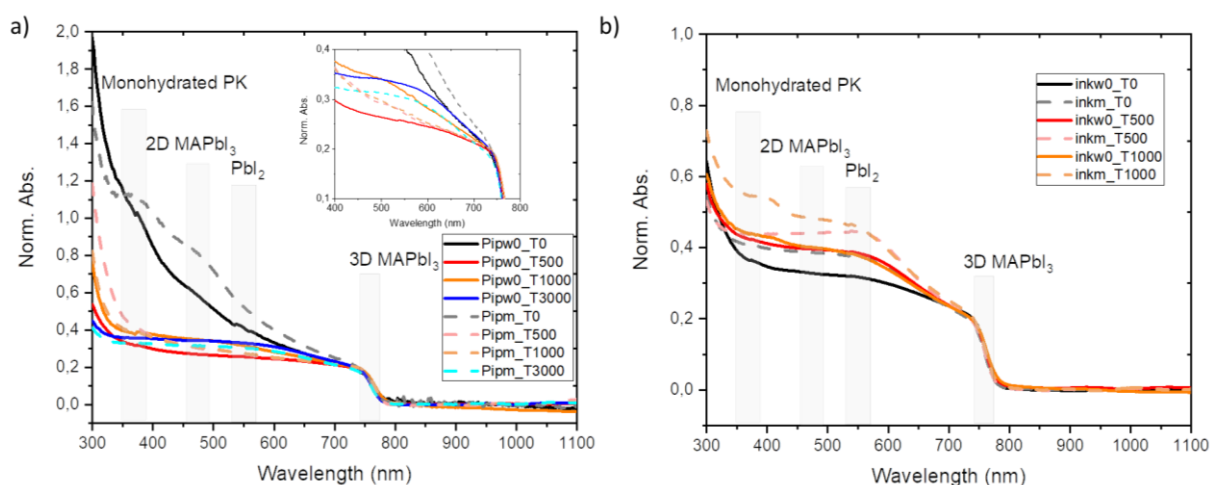


Figure 69: UV-Visible absorbance spectra performed on opened cells after carbon layer peeling as a function of aging time for a) pipetting cells and b) inkjet solar cells.

To better understand the performance variations, especially for pipetting cells, additional UV-visible analyses were performed on opened solar cells after peeling the carbon layer. The Figure 69 presents the obtained Absorbance spectra at different aging times for pipetting and inkjet solar cells. At the initial state, we can note the presence of others compounds such as monohydrated perovskite, 2D perovskite and  $\text{PbI}_2$  at respectively about 350, 450 and 550nm. These attributions can be done thanks to several literature works[298][6][300][301][299]. For pipetting solar cells at T0, monohydrated and 2D perovskites are present for matured solar cells, while for non-matured solar cells, only a slight wave could be distinguished for 2D perovskite. In the case of inkjet solar cells at T0, we do not notice the formation of such phases only an intensification of the  $\text{PbI}_2$  peak appearing around 550 nm for matured solar cells. After 500h of aging, a disappearance of 2D and monohydrated perovskites is observed for pipetting cells,  $\text{PbI}_2$  is still present and even increases during aging for all cells. For pipetting cells, the perovskite spectra flatten out to be close to the one of inkjet cells at T0, which is compatible with a less compact perovskite phase as highlighted also by the previous increase of reflectance level between 0 and 500h of aging. According to the zoom presented in Figure 69 a, a slight continuous increase of  $\text{PbI}_2$  is observable during aging of both pipetting cells. For inkjet cells, a significant increase of  $\text{PbI}_2$  is observed between 0 and 500h of aging, then followed by the presence of monohydrated  $\text{MAPbI}_3$  before 400nm. Finally, there is also no variation in the 780 nm transition attributed to the majority 3D  $\text{MAPbI}_3$  perovskite phase till the end of aging.

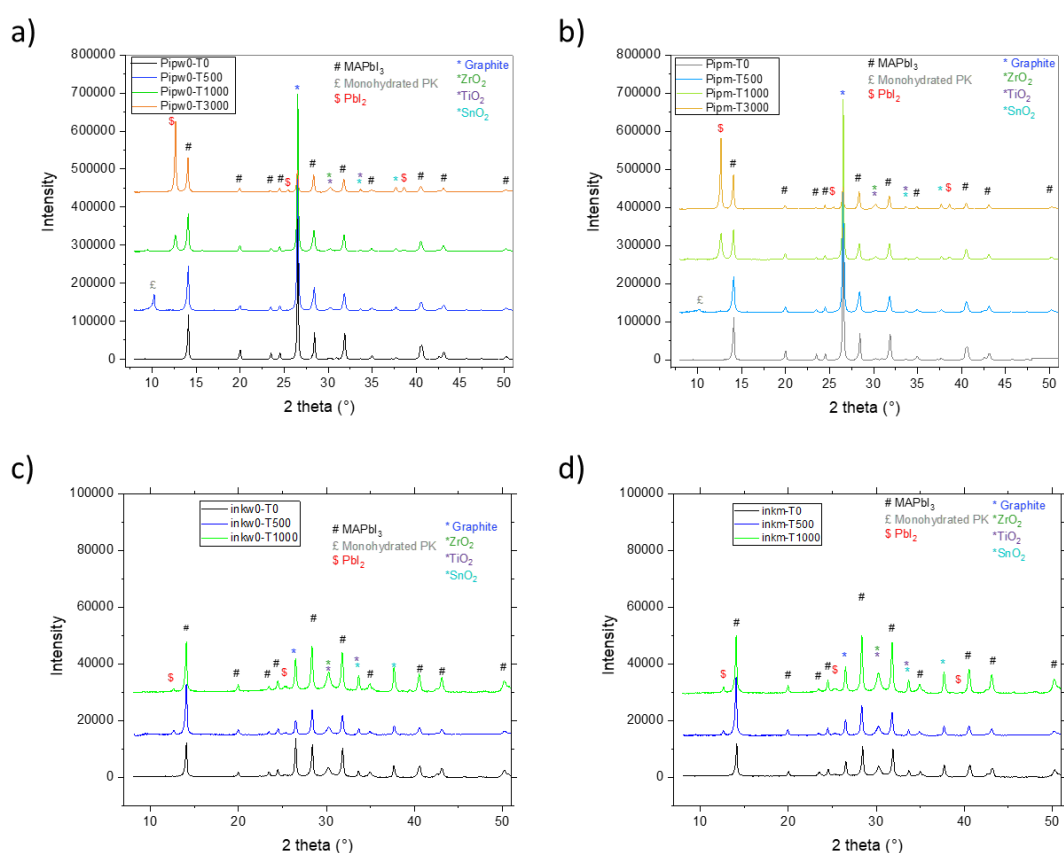


Figure 70: XRD patterns evolution during aging for of a) non-matured pipetting solar cells, b) matured pipetting solar cells, c) non-matured inkjet solar cells, d) matured inkjet solar cells.

The Figure 70 presents the results of XRD analyses performed on pipetting and inkjet solar cells during the aging campaign. Through careful analysis of the diffractogram, it is possible to evaluate a relative crystallinity rate as well as the proportion of certain phases such as perovskite monohydrate and  $\text{PbI}_2$ , Figure 71. For pipetting solar cells, we can observe that the crystallinity rate decreases up to 500h and then increases to a value very similar to the initial state at 1000h, then decreases up to 3000h. Little impact of maturation is visible. We also note the increase in the proportion of the monohydrated perovskite phase at 500h, then its complete disappearance at 1000h till the end of aging. As this compound seems to be present in UV-Visible spectroscopy and increased during aging, it seems indicated that its crystallization is possible up to 500h, then completely disadvantaged afterwards leading to its amorphous phase. Thus, the drop-in performance observed for the pipetting cells from 120h to 500h is probably explained by a decrease in crystallinity and the apparition of this monohydrated perovskite phase. Then, a phenomenon of reorganization of the microstructure of the perovskite allows an increase in the rate of crystallinity, allowing an increase in performance between 500h and 1000h, with a level equivalent to the initial performance. According to literature, the formation of monohydrated perovskite may be reversible[299]. It is thus possible to hypothesize that the 85°C temperature during aging leads to a recrystallization of  $\text{MAPbI}_3$  perovskite from the hydrate, water vapor may be captured by the surlyn gasket. After 1000h, the  $\text{PbI}_2$  formation keeps increasing to reach around 8% and 12% for non-matured and matured cells respectively after 3000h of aging in accordance to the decreasing crystallinity PK rate. This explains the drastic drop of the PCE meaning the major conversion of the perovskite into the degradation compound  $\text{PbI}_2$ .

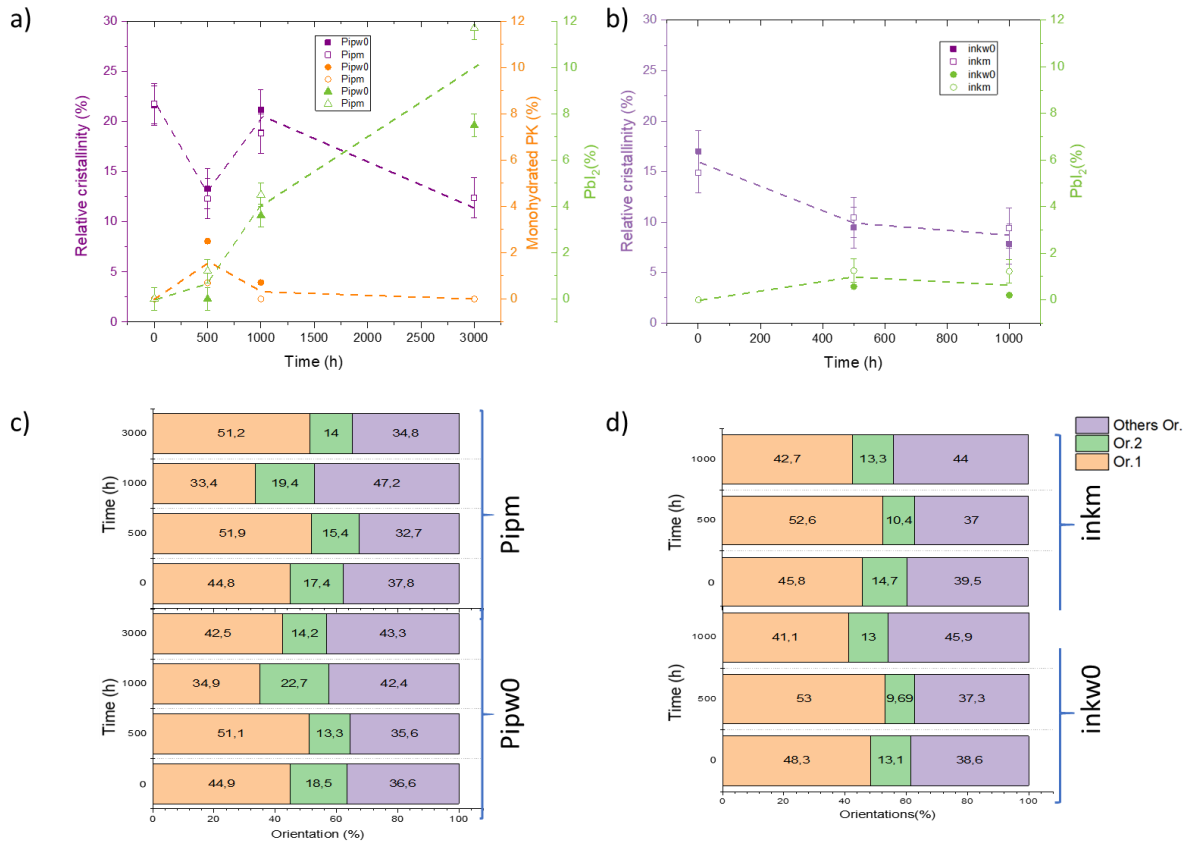


Figure 71: Variation of XRD relative crystallinity of PK,  $PbI_2$  and monohydrated perovskite versus aging time for a) pipetting and b) inkjet solar cells; Variation of PK orientation proportions during aging for c) pipetting and d) inkjet solar cells.

We can observe a different XRD behavior for inkjet solar cells from that observed for pipetting solar cells. We can note a continuous decrease in the rate of crystallinity, which explains the continuous decrease in performance and  $J_{SC}$  after phase 1. By comparing inkjet and pipetting processes, it can be observed that the crystalline rates of perovskite in both cell types are equivalent at 1000h and 3000h of aging for respectively inkjet and pipetting cells, whereas these cells have fairly similar yields at the same time. It therefore seems that pipetting solar cells have 3 times longer lifespan than inkjet cells. There is also no formation of crystalline monohydrated perovskite and very few formation of the degradation product  $PbI_2$  in its crystalline form. Widely present in UV-Visible spectroscopy during aging, they seem almost non-existent in the crystalline state.

As shown in the previous part, perovskite can crystallize under several orientations due to the mesoporous structure of  $TiO_2$ . For both types of cells and for non-matured and matured states, perovskite is mainly oriented according to orientation 1. At 500h of aging, we then note an increase in this contribution, more important for inkjet cells and in favor of all other orientations including orientation 2. Thus, the decrease in the crystallinity rate observed between 0 and 500h is mainly due to the disappearance of orientations 2 and others. At 1000h of aging, there is again a decrease in orientation 1 percentage, in favor of orientation 2 and other orientations for both pipetting and inkjet cells. This decrease is more pronounced for pipetting cells. This is to correlate with the different changes in the crystallinity rate between

500h and 1000h for the two cell types studied, and allows to think that the previously hypothesized recrystallization of  $\text{MAPbI}_3$  perovskite from the hydrate in pipetting cells mainly lead to other orientations than orientation 1. In the case of inkjet solar cells, a decrease in relative crystallinity with the appearance of monohydrated perovskite and  $\text{PbI}_2$  in relatively high proportion mainly in amorphous form is observed over the same aging time range mainly originating from a degradation of the orientation 1. At 3000h of aging for pipetted solar cells, an increase in orientation 1 proportion is observed leading to think that the newly recrystallized perovskite from the hydrate is the first one to degrade in  $\text{PbI}_2$ . Between 1000h and 3000h, a significant decrease in the crystallinity rate with a significant increase in the proportion of crystalline  $\text{PbI}_2$  is observed. However, perovskite orientations proportions quite equivalent to the initial state are found.

## Conclusion

The purpose of this section was to study the stability of pipetting and inkjet cells under damp heating conditions and more particularly the effect of the maturation stage. If in the previous part, which had as its objective the study of the maturation phenomenon, it seemed that the latter had a real importance on the initial performances of the cells, the study of the stability of the cells allows to nuance its effect. After a rather careful study of the performances, the PV parameters and the phenomenon of observed bumps by varying the speed of measurements of  $J(V)$ , it seems that this phenomenon is mainly due to the specific architecture and perovskite (effect of AVAI) used in these cells. These cells undergo a transient phase during which the charge transfers in the cell must be rebalanced. As shown here, this transient phase is accelerated during the so-called maturation stage performed just after the process or occurs during the first 200 hours of aging. Then, it seems that this stage of maturation has little impact or at least can accelerate the degradation of cells.

As expected, this study showed the decisive role of the process of depositing perovskite. If the pipetting and inkjet solar cells in the non-matured and matured states have fairly similar performances, the latter have quite different behaviors during aging. For inkjet cells, after a first soft aging phase until 200h, there is a gradual decrease in performance to obtain completely degraded cells at 1000h of aging. This decrease in performance is mainly due to a decrease in  $J_{sc}$  and a significant increase in  $R_s$  at the end of the ageing campaign. However, these cells show  $V_{oc}$  values that are much higher than those measured for pipetting cells until the end of ageing. For pipetting solar cells, a decrease in performance is observed up to 500h of aging, followed by an increase in performance up to 1000h of aging to reach values very similar to the initial values, then a continuous decrease is observed till 3000h of aging. The 1<sup>st</sup> drop in performance is mainly due to a drop in  $V_{oc}$  ( $J_{sc}$  is fairly stable) to reach values similar to those obtained with inkjet cells, while the 2<sup>nd</sup> drop can be explained by a significant drop in  $J_{sc}$ . For these cells between 0 and 1000h, it seems that a reorganization of the crystalline structure of perovskite occurs with the formation and then the disappearance of the amorphous and then crystalline perovskite monohydrate. Then, the mechanism operating during the 2<sup>nd</sup> decrease of PCE is very similar to that observed for inkjet cells and quite conventional. It is mainly related to a decrease in  $J_{sc}$  and due to a decrease in the crystalline rate of perovskite.

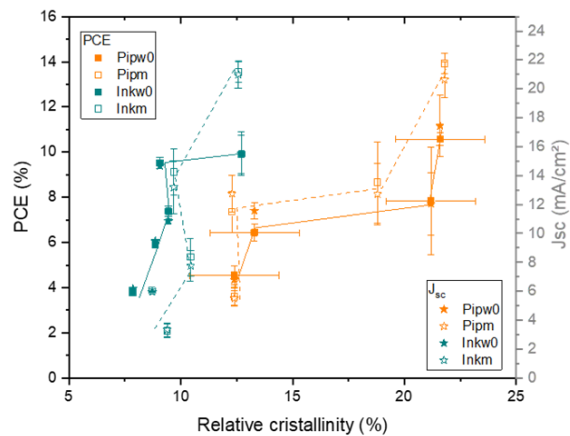


Figure 72: Variation PCE and  $J_{sc}$  versus relative crystallinity for pipetting and inkjet cells with or without maturation

The two cell types exhibit different behaviors. As shown in the figure above, changes in PCE are mainly due to changes in  $J_{sc}$ . For pipetting cells, the increase in PCE may be correlated with an increase in crystallinity, which cannot be observed for inkjet cells. PCE values,  $J_{sc}$  and  $V_{oc}$  were fairly similar to 1000h and 3000h of aging for respectively inkjet and pipetting cells, the rate of crystalline  $PbI_2$  is much higher in pipetting cells while the values of  $R_s$  are much higher for inkjet cells. Consequently, it seems that the second degradation factors of these two cell types are quite different, namely greater degradation of perovskite for pipetting cells and degradation of interfaces for inkjet cells.



## Supplementary information

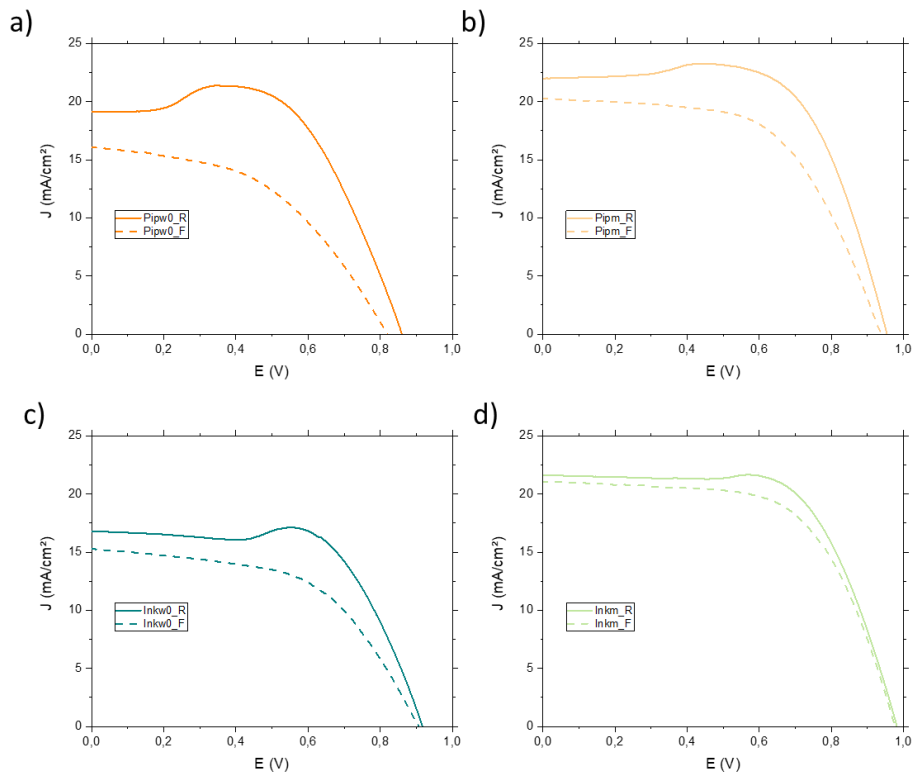


Figure 73: Examples of  $J(V)$  measurements performed in reverse (R) and forward (F) scans at 4 mV/s for unmaturing (w0) and maturing (m) for respectively a), b) pipetting and c), d) inkjet solar cells.

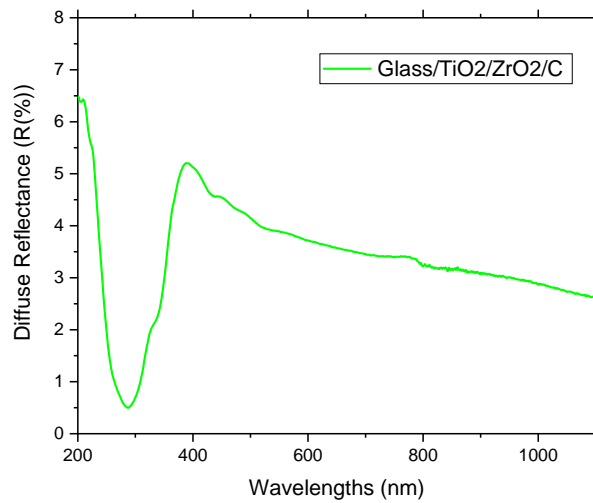


Figure 74: UV-Visible reflectance spectra performed on a Glass/TiO<sub>2</sub>/ZrO<sub>2</sub>/C stack without perovskite (from Glass side).

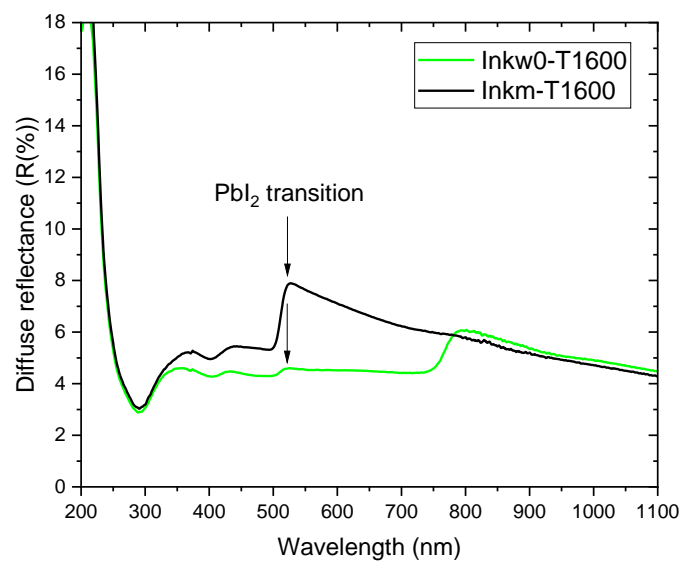


Figure 75: UV-Visible reflectance spectra performed on unaged and aged inkjet cells at 1600 hours of aging (after the 1000h aging time corresponding at PCE=0).



# GENERAL CONCLUSION AND PERSPECTIVES

## General conclusion

In this thesis, the carbon-based perovskite solar cells developed by Soloronix have been largely studied. The easy manufacture method of the C-PSC without using a glove box and the reduced fabrication costs with improved devices' stability, compared to older generations in the PV technology field, make our studied systems very unique and interesting to evaluate.

In the first chapter of results, the very weak stability of C-PSC without encapsulation has been demonstrated. To improve this point, an encapsulation system composed of two glass covers and a sealing agent based on polymer can be used to protect the perovskite layer from external agents like humidity and oxygen. Several sealing agents (SG-SF-PO-PU-tPO-tPO+PIB) have been compared for two types of solar cells enabling the comparison of two different PK deposition techniques (Pipetting and Inkjet solar cells). Just after encapsulation, SG sealing agent can slightly enhance the cell's performance for both types of solar cells (pipetting and inkjet solar cells), whereas for the others sealing agents tested a minor PCE drop is noticed. All solar cells seem to have the same behaviour during the encapsulation step except for tPO+PIB, which has shown a lower diffuse reflectance with a photoluminescence blueshift meaning a decrease in the PK grain size or a passivation during lamination given that the latter conditions are harsher for this sealant. Indeed, due to PIB edge-sealant thickness, strongest lamination conditions were needed to obtain a complete fusion of tPO overall the surface. To better understand the impact of the encapsulant systems on the C-PSC lifetime, our devices have been exposed to damp heat conditions (85°C/85% R.H). A better durability is observed for pipetted cells compared to the inkjet ones. Pipetted SG cells with the less stressed sealing during the lamination not covering the PK area, represent the highest stable devices with only 20% PCE loss after 1500h of aging followed by covering films, tPO (72% PCE loss) and the PO (80% PCE loss). The tPO+PIB system must be detrimental for the functionality of the device caused by the lamination conditions with 50% PCE loss due to its  $V_{oc}$  loss only after 100h of aging meaning a creation of traps within the PK layer. The worst sealant is PU film which turns into a soft sticky material, suffering from chemical changes at initial stages of aging and losing its performance up to 100h. For inkjet solar cells, a similar behaviour was noticed for tPO+PIB and PU films as those for pipetting cells. For SG, SF, PO and tPO all ended up with quite similar behaviour with 60-80% PCE drop up to 200 h followed by a decrease till the end of aging where they become non-functional after 1000 h. Therefore, it appears that the perovskite infiltration process seems to largely influence the stability of these solar cells. For both types of studied solar cells, it seems that the best encapsulation system is based on SG. This latter will be used for further study.

To explore this aspect, in the next chapter, the role of the beneficial maturation process has been deepened for two different perovskite deposition techniques (pipetting and inkjet solar cells). We demonstrated that exposing the solar cells to 40°C and 75% R.H. during 150 h will improve the performances whatever the PK infiltration technique used. The PCE has increased from 10.5% to 14%, and 10% to 14%, respectively for pipetting and inkjet cells. It has been

shown that the performance are more spatially heterogeneous for pipetting cells. After this maturation step, this heterogeneity is less present. Thanks to a deepened study, it has been shown that this process induces different changes following the type of solar cells. For pipetting solar cells, the maturation induces essentially an improvement of the microstructure of the perovskite. A better organization was demonstrated by Raman spectroscopy analyses due to the appearance of MA<sup>+</sup> in pipetted cells. This is confirmed by the XRD analyses which showed an increase in the crystallinity ratio. UV measurements showed also the presence 2D PK phase in allowing a better TiO<sub>2</sub>/PK interface and consequently reducing the defects. As shown in litterature, the charge transfer was improved with a highly ordered PK structure. For inkjet cells, it seems that only interfaces phenomena have been demonstrated: impedance spectroscopy demonstrated that after the maturation step an increase of the capacity associated with the TiO<sub>2</sub>/PK interface indicating an intensified phenomenon of charge accumulation at this interface. Moreover, PL spectroscopy proved that maturation is a beneficial step since its intensity decreases, meaning the reduction of charge recombinations at PK/CP interface. Moreover, XRD analysis indicated Pbl<sub>2</sub> presence after the maturation explaining the slightly lower crystallinity rate after maturation for inkjet cells. This small Pbl<sub>2</sub> amount could even be the role of a positive passivation agent.

The last chapter aims to study the stability under accelerating ageing of the pipetted and inkjet cells, both subjected or not to a maturation pre-treatment. The idea is to see if this initial maturation step plays any role on the cells lifetime. The cells were exposed to damp heat conditions (85°C/85%RH). Contrary to what was demonstrated in the previous chapter, the maturation step seems much less relevant during the stability study. Regardless of the cell type, at about 200h of aging, all unmaturred and matured devices show similar performance. For the non-matured cells, we note a maturation effect during the first days of aging while for the matured cells, only a decrease in performance is observed. For inkjet cells, after 200h of aging, a very harsh decrease in performance was noticed leading to a complete degradation after 1000 h. This result is due to the J<sub>sc</sub> decrease and the R<sub>s</sub> significant increase. For pipetted cells, a first PCE decrease occurs up to 500 h due to a V<sub>oc</sub> decrease, followed by an increase till 1000 h reaching similar values than initial state related to a crystallinity increase, and then finally followed by a decrease up to 3000 h caused by the J<sub>sc</sub> drop correlated to a crystallinity decrease observed in the XRD analysis. In summary, it seems that pipetting solar cells have a much better stability than inkjet solar cells. Thanks to a complete study from device to material, all degradation mechanisms were elucidated and seem to be different in both types of solar cells: it was demonstrated that perovskite degradation is taking place for pipetted cells while interfaces degradation is occurring for inkjet devices.

## Perspectives

Once a clean industrialisable process have been defined leading to efficient and stable devices, the major remaining issues for the commercialization of perovskite solar cells modules is the increase of devices durability, together with the substitution of the toxic lead PK materials as they could release lead within the environment after their usage.

The durability could be further enhanced by improving the morphology of the perovskites films and that can mainly be done by scouting new additives to help in the crystal growth and the dynamics of the crystallinity. This should also enhance the performance of the cells. Many additives have been employed but to date there is no general concept as guidance to choose the appropriate additive. Furthermore, the relation between the additive used and the final perovskite stability needs to be investigated in a more systematic way to optimize how to both control the micromorphology and the resistance against external factors.

On another note, since this work showed that less PK quantity can lead to lower durability of performances in inkjet cells, may be it would be interesting to optimize the PK quantity in C-PSC with for instance the thickness of reservoir mesoporous layers, or to investigate the potential of refilling the devices with perovskite.

To go further, it seems also important to increase the researchs in developing lead-free perovskite for C-PSC devices in order to accelerate its potential for industrialization. This could be achieved by substituting the lead with alternatives such as Sn, Ge, Cu and much more. Bi for example is a non toxic element with quite similar characteristics and radius than Pb, and the research activity around bismuth is actually increasing.

## REFERENCES

- [1] "NREL updates interactive chart of solar cell efficiency," 2022. <https://www.nrel.gov/pv/cell-efficiency.html>.
- [2] S. W. Lee *et al.*, "UV Degradation and Recovery of Perovskite Solar Cells," *Sci. Rep.*, vol. 6, no. 1, pp. 1–10, 2016, doi: 10.1038/srep38150.
- [3] "Insights on the Perovskite Solar Cells Global Market to 2028 - Featuring Oxford Photovoltaics, Solaronix and Dyesol Among Others - ResearchAndMarkets.com," Accessed on January 2023 , 2021. <https://www.businesswire.com/news/home/20211122006432/en/Insights-on-the-Perovskite-Solar-Cells-Global-Market-to-2028---Featuring-Oxford-Photovoltaics-Solaronix-and-Dyesol-Among-Others---ResearchAndMarkets.com>
- [4] S. G. Hashmi *et al.*, "Air Processed Inkjet Infiltrated Carbon Based Printed Perovskite Solar Cells with High Stability and Reproducibility," *Adv. Mater. Technol.*, vol. 2, no. 1, pp. 4–9, 2017, doi: 10.1002/admt.201600183.
- [5] A. Mei *et al.*, "A hole-conductor-free, fully printable mesoscopic perovskite solar cell with high stability," *Science (80-. )*, vol. 345, no. 6194, pp. 295–298, 2014, doi: 10.1126/science.1254763.
- [6] G. Grancini *et al.*, "One-Year stable perovskite solar cells by 2D/3D interface engineering," *Nat. Commun.*, vol. 8, no. 1, pp. 1–8, 2017, doi: 10.1038/ncomms15684.
- [7] S. G. Hashmi *et al.*, "High performance carbon-based printed perovskite solar cells with humidity assisted thermal treatment," *J. Mater. Chem. A*, vol. 5, no. 24, pp. 12060–12067, 2017, doi: 10.1039/c7ta04132b.
- [8] P. A. Owusu and S. Asumadu-Sarkodie, "A review of renewable energy sources, sustainability issues and climate change mitigation," *Cogent Eng.*, vol. 3, no. 1, pp. 1–14, 2016, doi: 10.1080/23311916.2016.1167990.
- [9] A. Qazi *et al.*, "Towards Sustainable Energy: A Systematic Review of Renewable Energy Sources, Technologies, and Public Opinions," *IEEE Access*, vol. 7, pp. 63837–63851, 2019, doi: 10.1109/ACCESS.2019.2906402.
- [10] Z. A. Baloch, Q. Tan, H. W. Kamran, M. A. Nawaz, G. Albashar, and J. Hameed, "A multi-perspective assessment approach of renewable energy production: policy perspective analysis," *Environ. Dev. Sustain.*, vol. 24, no. 2, pp. 2164–2192, 2022, doi: 10.1007/s10668-021-01524-8.
- [11] L. El Chaar, L. A. Lamont, and N. El Zein, "Review of photovoltaic technologies," *Renew. Sustain. Energy Rev.*, vol. 15, no. 5, pp. 2165–2175, 2011, doi: 10.1016/j.rser.2011.01.004.
- [12] K. Alanne and A. Saari, "Distributed energy generation and sustainable development,"



- Renew. Sustain. Energy Rev.*, vol. 10, no. 6, pp. 539–558, 2006, doi: 10.1016/j.rser.2004.11.004.
- [13] N. L. Panwar, S. C. Kaushik, and S. Kothari, “Role of renewable energy sources in environmental protection: A review,” *Renew. Sustain. Energy Rev.*, vol. 15, no. 3, pp. 1513–1524, 2011, doi: 10.1016/j.rser.2010.11.037.
- [14] J. M. Kwon, K. H. Nam, and B. H. Kwon, “Photovoltaic power conditioning system with line connection,” *IEEE Trans. Ind. Electron.*, vol. 53, no. 4, pp. 1048–1054, 2006, doi: 10.1109/TIE.2006.878329.
- [15] S. Lee, J. E. Kim, and H. Cha, “Design and implementation of photovoltaic power conditioning system using a current-based maximum power point tracking,” *J. Electr. Eng. Technol.*, vol. 5, no. 4, pp. 606–613, 2010, doi: 10.5370/JEET.2010.5.4.606.
- [16] N. Kannan and D. Vakeesan, “Solar energy for future world: - A review,” *Renew. Sustain. Energy Rev.*, vol. 62, pp. 1092–1105, 2016, doi: 10.1016/j.rser.2016.05.022.
- [17] M. A. G. De Brito, L. P. Sampaio, L. G. Junior, and C. A. Canesin, “Research on photovoltaics: Review, trends and perspectives,” *COBEP 2011 - 11th Brazilian Power Electron. Conf.*, pp. 531–537, 2011, doi: 10.1109/COBEP.2011.6085198.
- [18] D. M. Chapin, C. S. Fuller, and G. L. Pearson, “A new silicon p-n junction photocell for converting solar radiation into electrical power,” *J. Appl. Phys.*, vol. 25, no. 5, pp. 676–677, 1954, doi: 10.1063/1.1721711.
- [19] A. Bahrami, S. Mohammadnejad, and S. Soleimaninezhad, “Photovoltaic cells technology: Principles and recent developments,” *Opt. Quantum Electron.*, vol. 45, no. 2, pp. 161–197, 2013, doi: 10.1007/s11082-012-9613-9.
- [20] R. L. Easton and M. J. Votaw, “Vanguard I IGY satellite (1958 beta),” *Rev. Sci. Instrum.*, vol. 30, no. 2, pp. 70–75, 1959, doi: 10.1063/1.1716492.
- [21] M. Wolf, “Limitations and Possibilities for Improvement of Photovoltaic Solar Energy Converters: Part I: Considerations for Earth’s Surface Operation,” *Proc. IRE*, vol. 48, no. 7, pp. 1246–1263, 1960, doi: 10.1109/JRPROC.1960.287647.
- [22] S. Guha, K. L. Narasimhan, and S. M. Pietruszko, “On light-induced effect in amorphous hydrogenated silicon,” *J. Appl. Phys.*, vol. 52, no. 2, pp. 859–860, 1981, doi: 10.1063/1.328849.
- [23] R. W. Miles, K. M. Hynes, and I. Forbes, “Photovoltaic solar cells: An overview of state-of-the-art cell development and environmental issues,” *Prog. Cryst. Growth Charact. Mater.*, vol. 51, no. 1–3, pp. 1–42, 2005, doi: 10.1016/j.pcrysgrow.2005.10.002.
- [24] H. M. Wagner, S., Shay, J. L., Migliorato, P., & Kasper, “CuInSe<sub>2</sub>/CdS heterojunction photovoltaic detectors,” *Appl. Phys. Lett.*, vol. 25, no. 8, pp. 434–435, 1974, doi: doi.org/10.1063/1.1655537.
- [25] Martin A. Green, “The Path to 25% Silicon Solar Cell Efficiency: History of Silicon Cell

- Evolution," *Prog. Photovoltaics Res. Appl.*, vol. 17, no. 3, pp. 183–189, 2009, doi: 10.1002/pip.
- [26] T. Saga, "Advances in crystalline silicon solar cell technology for industrial mass production," *NPG Asia Mater.*, vol. 2, no. 3, pp. 96–102, 2010, doi: 10.1038/asiamat.2010.82.
- [27] K. Ranabhat, L. Patrikeev, A. A. evna Revina, K. Andrianov, V. Lapshinsky, and E. Sofronova, "An introduction to solar cell technology," *J. Appl. Eng. Sci.*, vol. 14, no. 4, pp. 481–491, 2016, doi: 10.5937/jaes14-10879.
- [28] B. G. Gribov and K. V Zinov, "PreparationOfHigh-PuritySilicon for Solar Cells," vol. 39, no. 7, pp. 653–662, 2003, doi: <https://doi-org.gaelnomade-2.grenet.fr/10.1023/A:1024553420534>.
- [29] L. C. Andreani, A. Bozzola, P. Kowalczewski, M. Liscidini, and L. Redorici, "Silicon solar cells: Toward the efficiency limits," *Adv. Phys. X*, vol. 4, no. 1, p. 1548305, 2019, doi: 10.1080/23746149.2018.1548305.
- [30] M. Imamzai, M. Aghaei, and Y. H. Thayoob, "A Review on Comparison between Traditional Silicon Solar Cells and Thin-Film CdTe Solar Cell," *Proc. Natl. Grad. Conf.*, pp. 1–5, 2012.
- [31] S. Frontier, "Solar frontier achieves world record thin-film solar cell efficiency of 23.35%," 2015, [Online]. Available: <https://www.solar-frontier.eu/uploads/media/SFE-Thin-Film-Solar-Cell-Efficiency-EN.pdf>.
- [32] S. Rajendran, M. Naushad, K. Raju, and R. Boukherroub, "Emerging nanostructured materials for energy and environmental science," *Environ. Chem. a Sustain. World*, vol. 23, p. 565, 2019, doi: <https://doi.org/10.1007/978-3-030-04474-9>.
- [33] M. L. Parisi, S. Maranghi, L. Vesce, A. Sinicropi, A. Di Carlo, and R. Basosi, "Prospective life cycle assessment of third-generation photovoltaics at the pre-industrial scale: A long-term scenario approach," *Renew. Sustain. Energy Rev.*, vol. 121, no. 2019, p. 109703, 2020, doi: 10.1016/j.rser.2020.109703.
- [34] M. Gratzel, "A low-cost, high-efficiency solar cell based on dye-sensitized colloidal TiO<sub>2</sub> films," *Nat. .*, vol. 353, no. 6346, p. 737, 1991, doi: 10.1016/0146-5724(84)90144-4.
- [35] J. Gong, K. Sumathy, Q. Qiao, and Z. Zhou, "Review on dye-sensitized solar cells (DSSCs): Advanced techniques and research trends," *Renew. Sustain. Energy Rev.*, vol. 68, no. 2016, pp. 234–246, 2017, doi: 10.1016/j.rser.2016.09.097.
- [36] G. Hashmi *et al.*, "Review of materials and manufacturing options for large area flexible dye solar cells," *Renew. Sustain. Energy Rev.*, vol. 15, no. 8, pp. 3717–3732, 2011, doi: 10.1016/j.rser.2011.06.004.
- [37] S. Mathew *et al.*, "Dye-sensitized solar cells with 13% efficiency achieved through the molecular engineering of porphyrin sensitizers," *Nat. Chem.*, vol. 6, no. 3, pp. 242–247,

- 2014, doi: 10.1038/nchem.1861.
- [38] C. W. Tang, "Two-layer organic photovoltaic cell," *Appl. Phys. Lett.*, vol. 48, no. 2, pp. 183–185, 1986, doi: 10.1063/1.96937.
- [39] B. Carsten *et al.*, "Examining the effect of the dipole moment on charge separation in donor-acceptor polymers for organic photovoltaic applications," *J. Am. Chem. Soc.*, vol. 133, no. 50, pp. 20468–20475, 2011, doi: 10.1021/ja208642b.
- [40] Y. J. Cheng, S. H. Yang, and C. S. Hsu, "Synthesis of conjugated polymers for organic solar cell applications," *Chem. Rev.*, vol. 109, no. 11, pp. 5868–5923, 2009, doi: 10.1021/cr900182s.
- [41] S. K. Hau, H. L. Yip, and A. K. Y. Jen, "A review on the development of the inverted polymer solar cell architecture," *Polym. Rev.*, vol. 50, no. 4, pp. 474–510, 2010, doi: 10.1080/15583724.2010.515764.
- [42] R. Vogel, K. Pohl, and H. Weller, "Sensitization of highly porous, polycrystalline titanium dioxide electrodes by quantum sized cadmium sulfide," *Chem. Phys. Lett.*, vol. 174, no. 3–4, pp. 241–246, 1990, doi: [https://doi.org/10.1016/0009-2614\(90\)85339-E](https://doi.org/10.1016/0009-2614(90)85339-E).
- [43] A. Badawy, W. A., & Mendez, "Quantum dots and nano-porous materials for solar energy conversion.," *Brown Walk. Press*, pp. 235–242, 2012.
- [44] J. Bisquert, "Modeling High-Efficiency Quantum Dot," *ACS Nano*, vol. 4, no. 10, pp. 5783–5790, 2010, doi: <https://doi-org.gaelnomade-2.grenet.fr/10.1021>.
- [45] P. V. Kamat, "Quantum dot solar cells. The next big thing in photovoltaics," *J. Phys. Chem. Lett.*, vol. 4, no. 6, pp. 908–918, 2013, doi: 10.1021/jz400052e.
- [46] L. Li *et al.*, "Highly efficient CdS quantum dot-sensitized solar cells based on a modified polysulfide electrolyte," *J. Am. Chem. Soc.*, vol. 133, no. 22, pp. 8458–8460, 2011, doi: 10.1021/ja201841p.
- [47] B. Gao *et al.*, "Green synthesis of highly efficient CdSe quantum dots for quantum-dots-sensitized solar cells," *J. Appl. Phys.*, vol. 115, no. 19, p. 193104, 2014, doi: 10.1063/1.4876118.
- [48] J. Yang and X. Zhong, "CdTe based quantum dot sensitized solar cells with efficiency exceeding 7% fabricated from quantum dots prepared in aqueous media," *J. Mater. Chem. A*, vol. 4, no. 42, pp. 16553–16561, 2016, doi: 10.1039/c6ta07399a.
- [49] A. Kojima, K. Teshima, Y. Shirai, and T. Miyasaka, "Organometal halide perovskites as visible-light sensitizers for photovoltaic cells," *J. Am. Chem. Soc.*, vol. 131, no. 17, pp. 6050–6051, 2009, doi: 10.1021/ja809598r.
- [50] J. H. Im, C. R. Lee, J. W. Lee, S. W. Park, and N. G. Park, "6.5% Efficient Perovskite Quantum-Dot-Sensitized Solar Cell," *Nanoscale*, vol. 3, no. 10, pp. 4088–4093, 2011, doi: 10.1039/c1nr10867k.

- [51] H. S. Kim *et al.*, “Lead iodide perovskite sensitized all-solid-state submicron thin film mesoscopic solar cell with efficiency exceeding 9%,” *Sci. Rep.*, vol. 2, no. 1, pp. 1–7, 2012, doi: 10.1038/srep00591.
- [52] M. M. Lee, J. Teuscher, T. Miyasaka, T. N. Murakami, and H. J. Snaith, “Efficient hybrid solar cells based on meso-superstructured organometal halide perovskites,” *Science (80-. )*, vol. 338, no. 6107, pp. 643–647, 2012, doi: 10.1126/science.1228604.
- [53] J. H. Heo *et al.*, “Efficient inorganic-organic hybrid heterojunction solar cells containing perovskite compound and polymeric hole conductors,” *Nat. Photonics*, vol. 7, no. 6, pp. 486–491, 2013, doi: 10.1038/nphoton.2013.80.
- [54] J. Burschka *et al.*, “Sequential deposition as a route to high-performance perovskite-sensitized solar cells,” *Nature*, vol. 499, no. 7458, pp. 316–319, 2013, doi: 10.1038/nature12340.
- [55] P. Roy, N. Kumar Sinha, S. Tiwari, and A. Khare, “A review on perovskite solar cells: Evolution of architecture, fabrication techniques, commercialization issues and status,” *Sol. Energy*, vol. 198, no. 2019, pp. 665–688, 2020, doi: 10.1016/j.solener.2020.01.080.
- [56] M. A. Green, A. Ho-Baillie, and H. J. Snaith, “The emergence of perovskite solar cells,” *Nat. Photonics*, vol. 8, no. 7, pp. 506–514, 2014, doi: 10.1038/nphoton.2014.134.
- [57] S. Ito, “Research Update: Overview of progress about efficiency and stability on perovskite solar cells,” *APL Mater.*, vol. 4, no. 9, 2016, doi: 10.1063/1.4961955.
- [58] C. Zuo, H. J. Bolink, H. Han, J. Huang, D. Cahen, and L. Ding, “Advances in perovskite solar cells,” *Adv. Sci.*, vol. 3, no. 7, pp. 1–16, 2016, doi: 10.1002/advs.201500324.
- [59] H. S. Kim, S. H. Im, and N. G. Park, “Organolead halide perovskite: New horizons in solar cell research,” *J. Phys. Chem. C*, vol. 118, no. 11, pp. 5615–5625, 2014, doi: 10.1021/jp409025w.
- [60] V. M. Goldschmidt, “Crystal structure and chemical constitution,” *Trans. Faraday Soc.*, vol. 25, pp. 253–283, 1929, doi: DOI <https://doi.org/10.1039/TF9292500253>.
- [61] Z. Li, M. Yang, J. S. Park, S. H. Wei, J. J. Berry, and K. Zhu, “Stabilizing Perovskite Structures by Tuning Tolerance Factor: Formation of Formamidinium and Cesium Lead Iodide Solid-State Alloys,” *Chem. Mater.*, vol. 28, no. 1, pp. 284–292, 2016, doi: 10.1021/acs.chemmater.5b04107.
- [62] C. Li, X. Lu, W. Ding, L. Feng, Y. Gao, and Z. Guo, “Formability of ABX<sub>3</sub> (X = F, Cl, Br, I) halide perovskites,” *Acta Crystallogr. Sect. B Struct. Sci.*, vol. 64, no. 6, pp. 702–707, 2008, doi: 10.1107/S0108768108032734.
- [63] A. Poglitsch and D. Weber, “Dynamic disorder in methylammoniumtrihalogenoplumbates (II) observed by millimeter-wave spectroscopy,” *J. Chem. Phys.*, vol. 87, no. 11, pp. 6373–6378, 1987, doi: 10.1063/1.453467.

- [64] K. Hong, Q. Van Le, S. Y. Kim, and H. W. Jang, "Low-dimensional halide perovskites: Review and issues," *J. Mater. Chem. C*, vol. 6, no. 9, pp. 2189–2209, 2018, doi: 10.1039/c7tc05658c.
- [65] M. A. Green, Y. Jiang, A. M. Soufiani, and A. Ho-Baillie, "Optical Properties of Photovoltaic Organic-Inorganic Lead Halide Perovskites," *J. Phys. Chem. Lett.*, vol. 6, no. 23, pp. 4774–4785, 2015, doi: 10.1021/acs.jpcclett.5b01865.
- [66] L. Dou *et al.*, "Solution-processed hybrid perovskite photodetectors with high detectivity," *Nat. Commun.*, vol. 5, no. 1, pp. 1–6, 2014, doi: 10.1038/ncomms6404.
- [67] J. S. Shaikh *et al.*, "Perovskite solar cells: In pursuit of efficiency and stability," *Mater. Des.*, vol. 136, pp. 54–80, 2017, doi: 10.1016/j.matdes.2017.09.037.
- [68] V. Sarritzu *et al.*, "Direct or Indirect Bandgap in Hybrid Lead Halide Perovskites?," *Adv. Opt. Mater.*, vol. 6, no. 10, p. 1701254, 2018, doi: 10.1002/adom.201701254.
- [69] A. M. A. Leguy *et al.*, "Experimental and theoretical optical properties of methylammonium lead halide perovskites," *Nanoscale*, vol. 8, no. 12, pp. 6317–6327, 2016, doi: 10.1039/c5nr05435d.
- [70] K. Mahmood, B. S. Swain, and A. Amassian, "16.1% Efficient Hysteresis-Free Mesostructured Perovskite Solar Cells Based on Synergistically Improved ZnO Nanorod Arrays," *Adv. Energy Mater.*, vol. 5, no. 17, pp. 1–11, 2015, doi: 10.1002/aenm.201500568.
- [71] N. Suresh Kumar and K. Chandra Babu Naidu, "A review on perovskite solar cells (PSCs), materials and applications," *J. Mater.*, vol. 7, no. 5, pp. 940–956, 2021, doi: 10.1016/j.jmat.2021.04.002.
- [72] J. Atanacio, A. J., Bak, T., Rahman, K. A., & Nowotny, "Defect engineering of photosensitive oxide materials. Example of TiO<sub>2</sub> solid solutions," *Adv. Inorg. Chem.*, vol. 72, pp. 1–47, 2018, doi: <https://doi.org/10.1016/bs.adioch.2018.05.006>.
- [73] Z. Song, S. C. Watthage, A. B. Phillips, and M. J. Heben, "Pathways toward high-performance perovskite solar cells: review of recent advances in organo-metal halide perovskites for photovoltaic applications," *J. Photonics Energy*, vol. 6, no. 2, p. 022001, 2016, doi: 10.1117/1.jpe.6.022001.
- [74] D. Bogachuk *et al.*, "Low-temperature carbon-based electrodes in perovskite solar cells," *Energy Environ. Sci.*, vol. 13, no. 11, pp. 3880–3916, 2020, doi: 10.1039/d0ee02175j.
- [75] Q. Wang, N. Phung, D. Di Girolamo, P. Vivo, and A. Abate, "Enhancement in lifespan of halide perovskite solar cells," *Energy Environ. Sci.*, vol. 12, no. 3, pp. 865–886, 2019, doi: 10.1039/c8ee02852d.
- [76] J. Y. Jeng *et al.*, "CH<sub>3</sub>NH<sub>3</sub>PbI<sub>3</sub> perovskite/fullerene planar-heterojunction hybrid solar cells," *Adv. Mater.*, vol. 25, no. 27, pp. 3727–3732, 2013, doi:

10.1002/adma.201301327.

- [77] H. Shen *et al.*, “Monolithic Perovskite/Si Tandem Solar Cells: Pathways to Over 30% Efficiency,” *Adv. Energy Mater.*, vol. 10, no. 13, p. 1902840, 2020, doi: 10.1002/aenm.201902840.
- [78] X. Zheng *et al.*, “Managing grains and interfaces via ligand anchoring enables 22.3%-efficiency inverted perovskite solar cells,” *Nat. Energy*, vol. 5, no. 2, pp. 131–140, 2020, doi: 10.1038/s41560-019-0538-4.
- [79] M. Saliba *et al.*, “Incorporation of rubidium cations into perovskite solar cells improves photovoltaic performance,” *Science (80-. )*, vol. 354, no. 6309, pp. 206–209, 2016, doi: DOI: 10.1126/science.aah5557.
- [80] Y. Chen *et al.*, “Design of an Inorganic Mesoporous Hole-Transporting Layer for Highly Efficient and Stable Inverted Perovskite Solar Cells,” *Adv. Mater.*, vol. 30, no. 52, pp. 1–9, 2018, doi: 10.1002/adma.201805660.
- [81] L. Fagiolari and F. Bella, “Carbon-based materials for stable, cheaper and large-scale processable perovskite solar cells,” *Energy Environ. Sci.*, vol. 12, no. 12, pp. 3437–3472, 2019, doi: 10.1039/c9ee02115a.
- [82] Z. Ku, Y. Rong, M. Xu, T. Liu, and H. Han, “Full printable processed mesoscopic CH<sub>3</sub>NH<sub>3</sub>PbI<sub>3</sub>/TiO<sub>2</sub> heterojunction solar cells with carbon counter electrode,” *Sci. Rep.*, vol. 3, no. 1, pp. 1–5, 2013, doi: 10.1038/srep03132.
- [83] X. Liu *et al.*, “High-efficiency perovskite solar cells based on self-assembly n-doped fullerene derivative with excellent thermal stability,” *J. Power Sources*, vol. 413, no. 2018, pp. 459–466, 2019, doi: 10.1016/j.jpowsour.2018.12.066.
- [84] X. Xu *et al.*, “Hole Selective NiO Contact for Efficient Perovskite Solar Cells with Carbon Electrode,” *Nano Lett.*, vol. 15, no. 4, pp. 2402–2408, 2015, doi: 10.1021/nl504701y.
- [85] H. Ye *et al.*, “17.78% efficient low-temperature carbon-based planar perovskite solar cells using Zn-doped SnO<sub>2</sub> electron transport layer,” *Appl. Surf. Sci.*, vol. 478, no. 1, pp. 417–425, 2019, doi: 10.1016/j.apsusc.2019.01.237.
- [86] J. Chen *et al.*, “Hole-Conductor-Free Fully Printable Mesoscopic Solar Cell with Mixed-Anion Perovskite CH<sub>3</sub>NH<sub>3</sub>PbI<sub>3-x</sub>(BF<sub>4</sub>)<sub>x</sub>,” *Adv. Energy Mater.*, vol. 6, no. 5, pp. 2–7, 2016, doi: 10.1002/aenm.201502009.
- [87] H. Chen and S. Yang, “Carbon-Based Perovskite Solar Cells without Hole Transport Materials: The Front Runner to the Market?,” *Adv. Mater.*, vol. 29, no. 24, p. 1603994, 2017, doi: 10.1002/adma.201603994.
- [88] T. Liu *et al.*, “Critical parameters in TiO<sub>2</sub>/ZrO<sub>2</sub>/Carbon-based mesoscopic perovskite solar cell,” *J. Power Sources*, vol. 293, pp. 533–538, 2015, doi: 10.1016/j.jpowsour.2015.05.106.
- [89] Z. Meng, D. Guo, J. Yu, and K. Fan, “Investigation of Al<sub>2</sub>O<sub>3</sub> and ZrO<sub>2</sub> spacer layers for

- fully printable and hole-conductor-free mesoscopic perovskite solar cells,” *Appl. Surf. Sci.*, vol. 430, pp. 632–638, 2018, doi: 10.1016/j.apsusc.2017.05.018.
- [90] J. Barichello, L. Vesce, F. Matteocci, E. Lamanna, and A. Di Carlo, “The effect of water in Carbon-Perovskite Solar Cells with optimized alumina spacer,” *Sol. Energy Mater. Sol. Cells*, vol. 197, pp. 76–83, 2019, doi: 10.1016/j.solmat.2019.03.029.
- [91] I. Zimmermann *et al.*, “Improved efficiency and reduced hysteresis in ultra-stable fully printable mesoscopic perovskite solar cells through incorporation of CuSCN into the perovskite layer,” *J. Mater. Chem. A*, vol. 7, no. 14, pp. 8073–8077, 2019, doi: 10.1039/c9ta00669a.
- [92] A. Verma, D. Martineau, S. Abdolhosseinzadeh, J. Heier, and F. Nüesch, “Inkjet printed mesoscopic perovskite solar cells with custom design capability,” *Mater. Adv.*, vol. 1, no. 2, pp. 153–160, 2020, doi: 10.1039/d0ma00077a.
- [93] R. Tsuji *et al.*, “Function of porous carbon electrode during the fabrication of multiporous-layered-electrode perovskite solar cells,” *Photonics*, vol. 7, no. 4, pp. 1–14, 2020, doi: 10.3390/photonics7040133.
- [94] E. Kobayashi, R. Tsuji, D. Martineau, A. Hinsch, and S. Ito, “Light-induced performance increase of carbon-based perovskite solar module for 20-year stability,” *Cell Reports Phys. Sci.*, vol. 2, no. 12, p. 100648, 2021, doi: 10.1016/j.xcrp.2021.100648.
- [95] L. W. Dmitry Bogachuk, Jessica Girard, Siddharth Tilala, David Martineau, Stephanie Narbey, Anand Verma, Andreas Hinsch, Markus Kohlstädt, “Nanoarchitectonics in fully printed perovskite solar cells with carbon-based electrodes,” *Nanoscale*, 2023, doi: 10.1039/D2NR05856A.
- [96] T. Ye *et al.*, “Cost-Effective High-Performance Charge-Carrier-Transport-Layer-Free Perovskite Solar Cells Achieved by Suppressing Ion Migration,” *ACS Energy Lett.*, vol. 6, pp. 3044–3052, 2021, doi: 10.1021/acsenergylett.1c01186.
- [97] D. Bogachuk *et al.*, “Remanufacturing Perovskite Solar Cells and Modules-a Holistic Case Study,” 2022, doi: <https://doi.org/10.21203/rs.3.rs-1767937/v1>.
- [98] Z. Ku, X. Xia, H. Shen, N. H. Tiep, and H. J. Fan, “A mesoporous nickel counter electrode for printable and reusable perovskite solar cells,” *Nanoscale*, vol. 7, no. 32, pp. 13363–13368, 2015, doi: 10.1039/c5nr03610k.
- [99] A. Binek *et al.*, “Recycling Perovskite Solar Cells to Avoid Lead Waste,” *ACS Appl. Mater. Interfaces*, vol. 8, no. 20, pp. 12881–12886, 2016, doi: 10.1021/acsmi.6b03767.
- [100] K. Z. Zhen Li, Talysa R. Klein, Dong Hoe Kim, Mengjin Yang, Joseph J. Berry, “Scaling Up Perovskite Photovoltaics: Progress, Challenges, and Outlook of a Transformational Technology,” *Nat. Rev. Mater.*, vol. 3, p. 18017, 2018.
- [101] Y. Zhang, W. Liu, F. Tan, and Y. Gu, “The essential role of the poly(3-hexylthiophene) hole transport layer in perovskite solar cells,” *J. Power Sources*, vol. 274, pp. 1224–1230,

- 2015, doi: 10.1016/j.jpowsour.2014.10.145.
- [102] X. Tong, F. Lin, J. Wu, and Z. M. Wang, "High performance perovskite solar cells," *Advanced Science*, vol. 3, no. 5. pp. 1–18, 2015, doi: 10.1002/advs.201500201.
- [103] L. Xiong *et al.*, "Review on the Application of SnO<sub>2</sub> in Perovskite Solar Cells," *Advanced Functional Materials*, vol. 28, no. 35. pp. 1–18, 2018, doi: 10.1002/adfm.201802757.
- [104] A. K. Jena, A. Kulkarni, and T. Miyasaka, "Halide Perovskite Photovoltaics: Background, Status, and Future Prospects," *Chem. Rev.*, vol. 119, no. 5, pp. 3036–3103, 2019, doi: 10.1021/acs.chemrev.8b00539.
- [105] Y. Zhao, A. M. Nardes, and K. Zhu, "Solid-State Mesostructured Perovskite CH<sub>3</sub>NH<sub>3</sub> PbI<sub>3</sub> Solar Cells: Charge Transport, Recombination, and Diffusion Length," *J. Phys. Chem. Lett.*, vol. 5, no. 3, pp. 490–494, 2014, doi: <https://doi-org.gaelnomade-2.grenet.fr/10.1021/jz500003v>.
- [106] Q. Wang, Y. Shao, Q. Dong, Z. Xiao, Y. Yuan, and J. Huang, "Large fill-factor bilayer iodine perovskite solar cells fabricated by a low-temperature solution-process," *Energy Environ. Sci.*, vol. 7, no. 7, pp. 2359–2365, 2014, doi: 10.1039/c4ee00233d.
- [107] I. Ermanova *et al.*, "Crystal engineering approach for fabrication of inverted perovskite solar cell in ambient conditions," *Energies*, vol. 14, no. 6, pp. 1–15, 2021, doi: 10.3390/en14061751.
- [108] P. Docampo, J. M. Ball, M. Darwich, G. E. Eperon, and H. J. Snaith, "Efficient organometal trihalide perovskite planar-heterojunction solar cells on flexible polymer substrates," *Nat. Commun.*, vol. 4, pp. 1–6, 2013, doi: 10.1038/ncomms3761.
- [109] W. Q. Wu, D. Chen, R. A. Caruso, and Y. B. Cheng, "Recent progress in hybrid perovskite solar cells based on n-type materials," *J. Mater. Chem. A*, vol. 5, no. 21, pp. 10092–10109, 2017, doi: 10.1039/c7ta02376f.
- [110] W. Qiu *et al.*, "High efficiency perovskite solar cells using a PCBM/ZnO double electron transport layer and a short air-aging step," *Org. Electron.*, vol. 26, pp. 30–35, 2015, doi: 10.1016/j.orgel.2015.06.046.
- [111] I. Hussain, H. P. Tran, J. Jaksik, J. Moore, N. Islam, and M. J. Uddin, "Functional materials, device architecture, and flexibility of perovskite solar cell," *Emergent Mater.*, vol. 1, no. 3–4, pp. 133–154, 2018, doi: 10.1007/s42247-018-0013-1.
- [112] N. J. Jeon *et al.*, "O-methoxy substituents in spiro-OMeTAD for efficient inorganic-organic hybrid perovskite solar cells," *J. Am. Chem. Soc.*, vol. 136, no. 22, pp. 7837–7840, 2014, doi: 10.1021/ja502824c.
- [113] J. A. Christians, R. C. M. Fung, and P. V. Kamat, "An inorganic hole conductor for Organolead halide perovskite solar cells. improved hole conductivity with copper iodide," *J. Am. Chem. Soc.*, vol. 136, no. 2, pp. 758–764, 2014, doi: 10.1021/ja411014k.
- [114] P. Qin *et al.*, "Inorganic hole conductor-based lead halide perovskite solar cells with



- 12.4% conversion efficiency," *Nat. Commun.*, vol. 5, no. 1, pp. 1–6, 2014, doi: 10.1038/ncomms4834.
- [115] C. Bi, Q. Wang, Y. Shao, Y. Yuan, Z. Xiao, and J. Huang, "Non-wetting surface-driven high-aspect-ratio crystalline grain growth for efficient hybrid perovskite solar cells," *Nat. Commun.*, vol. 6, no. 1, pp. 1–7, 2015, doi: 10.1038/ncomms8747.
- [116] J. Y. Jeng *et al.*, "Nickel oxide electrode interlayer in CH<sub>3</sub>NH<sub>3</sub>PbI<sub>3</sub> perovskite/PCBM planar-heterojunction hybrid solar cells," *Adv. Mater.*, vol. 26, no. 24, pp. 4107–4113, 2014, doi: 10.1002/adma.201306217.
- [117] S. Ye *et al.*, "CuSCN-Based Inverted Planar Perovskite Solar Cell with an Average PCE of 15.6%," *Nano Lett.*, vol. 15, no. 6, pp. 3723–3728, 2015, doi: 10.1021/acs.nanolett.5b00116.
- [118] H. Zhou *et al.*, "Interface engineering of highly efficient perovskite solar cells," *Science* (80-. ), vol. 345, no. 6196, pp. 542–546, 2014, doi: 10.1126/science.1254050.
- [119] M. M. H. Desoky, M. Bonomo, N. Barbero, G. Viscardi, C. Barolo, and P. Quagliotto, "Polymeric dopant-free hole transporting materials for perovskite solar cells: Structures and concepts towards better performances," *Polymers (Basel)*, vol. 13, no. 10, p. 1652, 2021, doi: 10.3390/polym13101652.
- [120] L. Yongsheng *et al.*, "Dopant-Free Organic Hole Transport Material for Efficient Planar Heterojunction Perovskite Solar Cells," *J. Mater. Chem. A*, vol. 2, no. 22, pp. 11940–11947, 2015, doi: DOI: 10.1039/C5TA02502H.
- [121] D. Bi, L. Yang, G. Boschloo, A. Hagfeldt, and E. M. J. Johansson, "Effect of different hole transport materials on recombination in CH<sub>3</sub>NH<sub>3</sub>PbI<sub>3</sub> perovskite-sensitized mesoscopic solar cells," *J. Phys. Chem. Lett.*, vol. 4, no. 9, pp. 1532–1536, 2013, doi: 10.1021/jz400638x.
- [122] K. P. Ong, T. W. Goh, Q. Xu, and A. Huan, "Structural Evolution in Methylammonium Lead Iodide CH<sub>3</sub>NH<sub>3</sub>PbI<sub>3</sub>," *J. Phys. Chem. A*, vol. 119, no. 44, pp. 11033–11038, 2015, doi: 10.1021/acs.jpca.5b09884.
- [123] M. Shirayama *et al.*, "Optical Transitions in Hybrid Perovskite Solar Cells: Ellipsometry, Density Functional Theory, and Quantum Efficiency Analyses for CH<sub>3</sub>NH<sub>3</sub>PbI<sub>3</sub>," *Phys. Rev. Appl.*, vol. 5, no. 1, pp. 1–25, 2016, doi: 10.1103/PhysRevApplied.5.014012.
- [124] W. J. Yin, J. H. Yang, J. Kang, Y. Yan, and S. H. Wei, "Halide perovskite materials for solar cells: A theoretical review," *J. Mater. Chem. A*, vol. 3, no. 17, pp. 8926–8942, 2015, doi: 10.1039/c4ta05033a.
- [125] J. Kim, S. H. Lee, J. H. Lee, and K. H. Hong, "The role of intrinsic defects in methylammonium lead iodide perovskite," *J. Phys. Chem. Lett.*, vol. 5, no. 8, pp. 1312–1317, 2014, doi: 10.1021/jz500370k.
- [126] F. Xu, T. Zhang, G. Li, and Y. Zhao, "Mixed cation hybrid lead halide perovskites with

- enhanced performance and stability," *J. Mater. Chem. A*, vol. 5, no. 23, pp. 11450–11461, 2017, doi: 10.1039/c7ta00042a.
- [127] Y. Liu *et al.*, "Two-Inch-Sized Perovskite CH<sub>3</sub>NH<sub>3</sub>PbX<sub>3</sub> (X = Cl, Br, I) Crystals: Growth and Characterization," *Adv. Mater.*, vol. 27, no. 35, pp. 5176–5183, 2015, doi: 10.1002/adma.201502597.
- [128] J. P. Correa-Baena *et al.*, "The rapid evolution of highly efficient perovskite solar cells," *Energy Environ. Sci.*, vol. 10, no. 3, pp. 710–727, 2017, doi: 10.1039/c6ee03397k.
- [129] P. P. Boix, S. Agarwala, T. M. Koh, N. Mathews, and S. G. Mhaisalkar, "Perovskite solar cells: Beyond methylammonium lead iodide," *J. Phys. Chem. Lett.*, vol. 6, no. 5, pp. 898–907, 2015, doi: 10.1021/jz502547f.
- [130] E. Edri, S. Kirmayer, D. Cahen, and G. Hodes, "High open-circuit voltage solar cells based on organic-inorganic lead bromide perovskite," *J. Phys. Chem. Lett.*, vol. 4, no. 6, pp. 897–902, 2013, doi: 10.1021/jz400348q.
- [131] A. R. B. M. Yusoff and M. K. Nazeeruddin, "Organohalide Lead Perovskites for Photovoltaic Applications," *J. Phys. Chem. Lett.*, vol. 7, no. 5, pp. 851–866, 2016, doi: 10.1021/acs.jpcclett.5b02893.
- [132] W. S. Yang *et al.*, "Iodide management in formamidinium-lead-halide-based perovskite layers for efficient solar cells," *Science (80-. )*, vol. 356, no. 6345, pp. 1376–1379, 2017, doi: 10.1126/science.aan2301.
- [133] J. W. Lee, D. H. Kim, H. S. Kim, S. W. Seo, S. M. Cho, and N. G. Park, "Formamidinium and cesium hybridization for photo- and moisture-stable perovskite solar cell," *Adv. Energy Mater.*, vol. 5, no. 20, 2015, doi: 10.1002/aenm.201501310.
- [134] G. E. Eperon, S. D. Stranks, C. Menelaou, M. B. Johnston, L. M. Herz, and H. J. Snaith, "Formamidinium lead trihalide: A broadly tunable perovskite for efficient planar heterojunction solar cells," *Energy Environ. Sci.*, vol. 7, no. 3, pp. 982–988, 2014, doi: 10.1039/c3ee43822h.
- [135] H. Choi *et al.*, "Cesium-doped methylammonium lead iodide perovskite light absorber for hybrid solar cells," *Nano Energy*, vol. 7, pp. 80–85, 2014, doi: 10.1016/j.nanoen.2014.04.017.
- [136] T. Matsui *et al.*, "Effect of rubidium for thermal stability of triple-cation perovskite solar cells," *Chem. Lett.*, vol. 47, no. 6, pp. 814–816, 2018, doi: 10.1246/cl.180211.
- [137] Michael Saliba *et al.*, "Incorporation of rubidium cations into perovskite solar cells improves photovoltaic performance," *Science (80-. )*, vol. 354, no. 6309, pp. 203–206, 2016, doi: DOI: 10.1126/science.aah5557.
- [138] N. Pellet *et al.*, "Mixed-organic-cation perovskite photovoltaics for enhanced solar-light harvesting," *Angew. Chemie - Int. Ed.*, vol. 53, no. 12, pp. 3151–3157, 2014, doi: 10.1002/anie.201309361.

- [139] Y. Zhou, M. Yang, S. Pang, K. Zhu, and N. P. Padture, "Exceptional Morphology-preserving evolution of formamidinium lead triiodide perovskite thin films via organic-cation displacement," *J. Am. Chem. Soc.*, vol. 138, no. 17, pp. 5535–5538, 2016, doi: 10.1021/jacs.6b02787.
- [140] D. B. Mitzi, C. A. Feild, W. T. A. Harrison, and A. M. Guloy, "Conducting tin halides with a layered organic-based perovskite structure," *Nature*, vol. 369, no. 6480, pp. 467–469, 1994, doi: 10.1038/369467a0.
- [141] N. K. Noel *et al.*, "Lead-free organic-inorganic tin halide perovskites for photovoltaic applications," *Energy Environ. Sci.*, vol. 7, no. 9, pp. 3061–3068, 2014, doi: 10.1039/c4ee01076k.
- [142] N. J. Jeon *et al.*, "Compositional engineering of perovskite materials for high-performance solar cells," *Nature*, vol. 517, no. 7535, pp. 476–480, 2015, doi: 10.1038/nature14133.
- [143] Y. C. Kim *et al.*, "Beneficial Effects of PbI<sub>2</sub> Incorporated in Organo-Lead Halide Perovskite Solar Cells," *Adv. Energy Mater.*, vol. 6, no. 4, pp. 1–8, 2016, doi: 10.1002/aenm.201502104.
- [144] T. Jesper Jacobsson *et al.*, "Exploration of the compositional space for mixed lead halogen perovskites for high efficiency solar cells," *Energy Environ. Sci.*, vol. 9, no. 5, pp. 1706–1724, 2016, doi: 10.1039/c6ee00030d.
- [145] F. H. Isikgor, B. Li, H. Zhu, Q. Xu, and J. Ouyang, "High performance planar perovskite solar cells with a perovskite of mixed organic cations and mixed halides, MA<sub>1-x</sub>FaxPbI<sub>3-y</sub>Cl<sub>y</sub>," *J. Mater. Chem. A*, vol. 4, no. 32, pp. 12543–12553, 2016, doi: 10.1039/c6ta03381d.
- [146] B. Conings *et al.*, "Intrinsic Thermal Instability of Methylammonium Lead Trihalide Perovskite," *Adv. Energy Mater.*, vol. 5, no. 15, pp. 1–8, 2015, doi: 10.1002/aenm.201500477.
- [147] M. Saliba *et al.*, "Cesium-containing triple cation perovskite solar cells: Improved stability, reproducibility and high efficiency," *Energy Environ. Sci.*, vol. 9, no. 6, pp. 1989–1997, 2016, doi: 10.1039/c5ee03874j.
- [148] P. W. Liang *et al.*, "Additive enhanced crystallization of solution-processed perovskite for highly efficient planar-heterojunction solar cells," *Adv. Mater.*, vol. 26, no. 22, pp. 3748–3754, 2014, doi: 10.1002/adma.201400231.
- [149] T. Li, Y. Pan, Z. Wang, Y. Xia, Y. Chen, and W. Huang, "Additive engineering for highly efficient organic-inorganic halide perovskite solar cells: Recent advances and perspectives," *J. Mater. Chem. A*, vol. 5, no. 25, pp. 12602–12652, 2017, doi: 10.1039/c7ta01798g.
- [150] C. Y. Chang *et al.*, "Tuning perovskite morphology by polymer additive for high efficiency solar cell," *ACS Appl. Mater. Interfaces*, vol. 7, no. 8, pp. 4955–4961, 2015,

doi: 10.1021/acsami.5b00052.

- [151] Y. Zhao *et al.*, “A polymer scaffold for self-healing perovskite solar cells,” *Nat. Commun.*, vol. 7, no. 1, pp. 1–9, 2016, doi: 10.1038/ncomms10228.
- [152] N. Tripathi, Y. Shirai, M. Yanagida, A. Karen, and K. Miyano, “Novel Surface Passivation Technique for Low-Temperature Solution-Processed Perovskite PV Cells,” *ACS Appl. Mater. Interfaces*, vol. 8, no. 7, pp. 4644–4650, 2016, doi: 10.1021/acsami.5b11286.
- [153] Y. Guo, K. Shoyama, W. Sato, and E. Nakamura, “Polymer Stabilization of Lead(II) Perovskite Cubic Nanocrystals for Semitransparent Solar Cells,” *Adv. Energy Mater.*, vol. 6, no. 6, pp. 1–9, 2016, doi: 10.1002/aenm.201502317.
- [154] C. H. Chiang and C. G. Wu, “Bulk heterojunction perovskite-PCBM solar cells with high fill factor,” *Nat. Photonics*, vol. 10, no. 3, pp. 196–200, 2016, doi: 10.1038/nphoton.2016.3.
- [155] K. M. Boopathi *et al.*, “Synergistic improvements in stability and performance of lead iodide perovskite solar cells incorporating salt additives,” *J. Mater. Chem. A*, vol. 4, no. 5, pp. 1591–1597, 2016, doi: 10.1039/c5ta10288j.
- [156] S. Bag and M. F. Durstock, “Large Perovskite Grain Growth in Low-Temperature Solution-Processed Planar p-i-n Solar Cells by Sodium Addition,” *ACS Appl. Mater. Interfaces*, vol. 8, no. 8, pp. 5053–5057, 2016, doi: 10.1021/acsami.5b11494.
- [157] Y. Chen, Y. Zhao, and Z. Liang, “Nonvolatile chlorinated additives adversely influence CH<sub>3</sub>NH<sub>3</sub>PbI<sub>3</sub> based planar solar cells,” *J. Mater. Chem. A*, vol. 3, no. 17, pp. 9137–9140, 2015, doi: 10.1039/c5ta01198a.
- [158] J. H. Heo *et al.*, “Planar CH<sub>3</sub>NH<sub>3</sub>PbI<sub>3</sub> perovskite solar cells with constant 17.2% average power conversion efficiency irrespective of the scan rate,” *Adv. Mater.*, vol. 27, no. 22, pp. 3424–3430, 2015, doi: 10.1002/adma.201500048.
- [159] J. Huang, M. Wang, L. Ding, Z. Yang, and K. Zhang, “Hydrobromic acid assisted crystallization of MAPbI<sub>3</sub>-xCl<sub>x</sub> for enhanced power conversion efficiency in perovskite solar cells,” *RSC Adv.*, vol. 6, no. 61, pp. 55720–55725, 2016, doi: 10.1039/c6ra07536c.
- [160] L. Li, Y. Chen, Z. Liu, Q. Chen, X. Wang, and H. Zhou, “The Additive Coordination Effect on Hybrids Perovskite Crystallization and High-Performance Solar Cell,” *Adv. Mater.*, vol. 28, no. 44, pp. 9862–9868, 2016, doi: 10.1002/adma.201603021.
- [161] C. G. Wu, C. H. Chiang, Z. L. Tseng, M. K. Nazeeruddin, A. Hagfeldt, and M. Grätzel, “High efficiency stable inverted perovskite solar cells without current hysteresis,” *Energy Environ. Sci.*, vol. 8, no. 9, pp. 2725–2733, 2015, doi: 10.1039/c5ee00645g.
- [162] S. S. Li *et al.*, “Intermixing-seeded growth for high-performance planar heterojunction perovskite solar cells assisted by precursor-capped nanoparticles,” *Energy Environ. Sci.*, vol. 9, no. 4, pp. 1282–1289, 2016, doi: 10.1039/c5ee03229f.
- [163] W. Zhang *et al.*, “Enhancement of perovskite-based solar cells employing core-shell

- metal nanoparticles,” *Nano Lett.*, vol. 13, no. 9, pp. 4505–4510, 2013, doi: 10.1021/nl4024287.
- [164] T. H. Chang *et al.*, “Planar Heterojunction Perovskite Solar Cells Incorporating Metal-Organic Framework Nanocrystals,” *Adv. Mater.*, vol. 27, no. 44, pp. 7229–7235, 2015, doi: 10.1002/adma.201502537.
- [165] P. Docampo *et al.*, “Solution deposition-conversion for planar heterojunction mixed halide perovskite solar cells,” *Adv. Energy Mater.*, vol. 4, no. 14, pp. 1–6, 2014, doi: 10.1002/aenm.201400355.
- [166] H. L. Hsu, C. C. Chang, C. P. Chen, B. H. Jiang, R. J. Jeng, and C. H. Cheng, “High-performance and high-durability perovskite photovoltaic devices prepared using ethylammonium iodide as an additive,” *J. Mater. Chem. A*, vol. 3, no. 17, pp. 9271–9277, 2015, doi: 10.1039/c5ta01563d.
- [167] S. Liu *et al.*, “A Review on Additives for Halide Perovskite Solar Cells,” *Adv. Energy Mater.*, vol. 10, no. 13, pp. 1–28, 2020, doi: 10.1002/aenm.201902492.
- [168] D. Zheng, C. Tong, T. Zhu, Y. Rong, and T. Pauporté, “Effects of 5-ammonium valeric acid iodide as additive on methyl ammonium lead iodide perovskite solar cells,” *Nanomaterials*, vol. 10, no. 12, pp. 1–15, 2020, doi: 10.3390/nano10122512.
- [169] X. Li *et al.*, “Outdoor Performance and Stability under Elevated Temperatures and Long-Term Light Soaking of Triple-Layer Mesoporous Perovskite Photovoltaics,” *Energy Technol.*, vol. 3, no. 6, pp. 551–555, 2015, doi: 10.1002/ente.201500045.
- [170] E. V. Péan *et al.*, “Investigating the Superoxide Formation and Stability in Mesoporous Carbon Perovskite Solar Cells with an Aminovaleric Acid Additive,” *Adv. Funct. Mater.*, vol. 30, no. 12, p. 1909839, 2020, doi: 10.1002/adfm.201909839.
- [171] A. Mei *et al.*, “Stabilizing Perovskite Solar Cells to IEC61215:2016 Standards with over 9,000-h Operational Tracking,” *Joule*, vol. 4, no. 12, pp. 2646–2660, 2020, doi: 10.1016/j.joule.2020.09.010.
- [172] M. Shahiduzzaman, K. Yamamoto, Y. Furumoto, T. Kuwabara, K. Takahashi, and T. Taima, “Ionic liquid-assisted growth of methylammonium lead iodide spherical nanoparticles by a simple spin-coating method and photovoltaic properties of perovskite solar cells,” *RSC Adv.*, vol. 5, no. 95, pp. 77495–77500, 2015, doi: 10.1039/c5ra08102e.
- [173] Y. Chen, Y. Zhao, and Z. Liang, “Non-thermal annealing fabrication of efficient planar perovskite solar cells with inclusion of NH<sub>4</sub>Cl,” *Chem. Mater.*, vol. 27, no. 5, pp. 1448–1451, 2015, doi: 10.1021/acs.chemmater.5b00041.
- [174] C. Qin, T. Matsushima, T. Fujihara, and C. Adachi, “Multifunctional Benzoquinone Additive for Efficient and Stable Planar Perovskite Solar Cells,” *Adv. Mater.*, vol. 29, no. 4, pp. 1–8, 2017, doi: 10.1002/adma.201603808.

- [175] N. J. Jeon, J. H. Noh, Y. C. Kim, W. S. Yang, S. Ryu, and S. Il Seok, "Solvent engineering for high-performance inorganic-organic hybrid perovskite solar cells," *Nat. Mater.*, vol. 13, no. 9, pp. 897–903, 2014, doi: 10.1038/nmat4014.
- [176] K. L. Gardner *et al.*, "Nonhazardous Solvent Systems for Processing Perovskite Photovoltaics," *Adv. Energy Mater.*, vol. 6, no. 14, p. 1600386, 2016, doi: 10.1002/aenm.201600386.
- [177] N. K. Noel *et al.*, "A low viscosity, low boiling point, clean solvent system for the rapid crystallisation of highly specular perovskite films," *Energy Environ. Sci.*, vol. 10, no. 1, pp. 145–152, 2017, doi: 10.1039/c6ee02373h.
- [178] K. H. Hendriks, J. J. Van Franeker, B. J. Bruijnaers, J. A. Anta, M. M. Wienk, and R. A. J. Janssen, "2-Methoxyethanol as a new solvent for processing methylammonium lead halide perovskite solar cells," *J. Mater. Chem. A*, vol. 5, no. 5, pp. 2346–2354, 2017, doi: 10.1039/C6TA09125C.
- [179] J. W. Lee and N. G. Park, "Two-step deposition method for high-efficiency perovskite solar cells," *MRS Bull.*, vol. 40, no. 8, pp. 654–659, 2015, doi: 10.1557/mrs.2015.166.
- [180] C. qing Xu *et al.*, "Anomalous electro-absorption in the low-temperature phase of  $(\text{C}_{10}\text{H}_{21}\text{NH}_3)_2\text{PbI}_4$ ," *Solid State Commun.*, vol. 77, no. 12, pp. 923–926, 1991, doi: 10.1016/0038-1098(91)90347-X.
- [181] K. O. Brinkmann *et al.*, "Extremely Robust Gas-Quenching Deposition of Halide Perovskites on Top of Hydrophobic Hole Transport Materials for Inverted (p-i-n) Solar Cells by Targeting the Precursor Wetting Issue," *ACS Appl. Mater. Interfaces*, vol. 11, no. 43, pp. 40172–40179, 2019, doi: 10.1021/acsami.9b15867.
- [182] G. E. Eperon, V. M. Burlakov, P. Docampo, A. Goriely, and H. J. Snaith, "Morphological control for high performance, solution-processed planar heterojunction perovskite solar cells," *Adv. Funct. Mater.*, vol. 24, no. 1, pp. 151–157, 2014, doi: 10.1002/adfm.201302090.
- [183] K. Liang, D. B. Mitzi, and M. T. Prikas, "Synthesis and Characterization of Organic-Inorganic Perovskite Thin Films Prepared Using a Versatile Two-Step Dipping Technique," *Chem. Mater.*, vol. 10, no. 1, pp. 403–411, 1998, doi: 10.1021/cm970568f.
- [184] F. Huang, M. Li, P. Siffalovic, G. Cao, and J. Tian, "From scalable solution fabrication of perovskite films towards commercialization of solar cells," *Energy Environ. Sci.*, vol. 12, no. 2, pp. 518–549, 2019, doi: 10.1039/c8ee03025a.
- [185] J. H. Im, I. H. Jang, N. Pellet, M. Grätzel, and N. G. Park, "Growth of  $\text{CH}_3\text{NH}_3\text{PbI}_3$  cuboids with controlled size for high-efficiency perovskite solar cells," *Nat. Nanotechnol.*, vol. 9, no. 11, pp. 927–932, 2014, doi: 10.1038/nnano.2014.181.
- [186] J. H. Im, H. S. Kim, and N. G. Park, "Morphology-photovoltaic property correlation in perovskite solar cells: One-step versus two-step deposition of  $\text{CH}_3\text{NH}_3\text{PbI}_3$ ," *APL Mater.*, vol. 2, no. 8, p. 081510, 2014, doi: 10.1063/1.4891275.

- [187] Y. Wu *et al.*, “Retarding the crystallization of PbI<sub>2</sub> for highly reproducible planar-structured perovskite solar cells via sequential deposition,” *Energy Environ. Sci.*, vol. 7, no. 9, pp. 2934–2938, 2014, doi: 10.1039/c4ee01624f.
- [188] Y. Zhou *et al.*, “Growth control of compact CH<sub>3</sub>NH<sub>3</sub>PbI<sub>3</sub> thin films via enhanced solid-state precursor reaction for efficient planar perovskite solar cells,” *J. Mater. Chem. A*, vol. 3, no. 17, pp. 9249–9256, 2015, doi: 10.1039/c4ta07036d.
- [189] M. Liu, M. B. Johnston, and H. J. Snaith, “Efficient planar heterojunction perovskite solar cells by vapour deposition,” *Nature*, vol. 501, no. 7467, pp. 395–398, 2013, doi: 10.1038/nature12509.
- [190] J. Feng *et al.*, “High-throughput large-area vacuum deposition for high-performance formamidine-based perovskite solar cells,” *Energy Environ. Sci.*, vol. 14, no. 5, pp. 3035–3043, 2021, doi: 10.1039/d1ee00634g.
- [191] Q. Chen *et al.*, “Planar heterojunction perovskite solar cells via vapor-assisted solution process,” *J. Am. Chem. Soc.*, vol. 136, no. 2, pp. 622–625, 2014, doi: 10.1021/ja411509g.
- [192] D. Wang *et al.*, “Improvement on the performance of perovskite solar cells by doctor-blade coating under ambient condition with hole-transporting material optimization,” *J. Energy Chem.*, vol. 38, pp. 207–213, 2019, doi: 10.1016/j.jechem.2019.03.023.
- [193] Y. Zhang *et al.*, “Major impediment to highly efficient, stable and low-cost perovskite solar cells,” *Metals (Basel)*, vol. 8, no. 11, pp. 1–33, 2018, doi: 10.3390/met8110964.
- [194] S. Tang *et al.*, “Composition Engineering in Doctor-Blading of Perovskite Solar Cells,” *Adv. Energy Mater.*, vol. 7, no. 18, pp. 1–7, 2017, doi: 10.1002/aenm.201700302.
- [195] Y. Deng, E. Peng, Y. Shao, Z. Xiao, Q. Dong, and J. Huang, “Scalable fabrication of efficient organolead trihalide perovskite solar cells with doctor-bladed active layers,” *Energy Environ. Sci.*, vol. 8, no. 5, pp. 1544–1550, 2015, doi: 10.1039/c4ee03907f.
- [196] N. B. Muslim, A. F. Hamzah, and A. E. Al-kawaz, “Study of mechanical properties of wollastonite filled epoxy functionally graded composite,” *Int. J. Mech. Eng. Technol.*, vol. 9, no. 8, pp. 669–677, 2018, [Online]. Available: <http://www.iaeme.com/ijmet/issues.asp?JType=IJMET&VType=9&IType=8>.
- [197] D. Vak *et al.*, “3D Printer Based Slot-Die Coater as a Lab-to-Fab Translation Tool for Solution-Processed Solar Cells,” *Adv. Energy Mater.*, vol. 5, no. 4, pp. 1–8, 2014, doi: 10.1002/aenm.201401539.
- [198] D. Burkitt, J. Searle, T. Watson, B. Campus, F. Way, and C. Burrows, “Perovskite solar cells in N-I-P structure with four slot-die-coated layers,” *R. Soc. Open Sci.*, vol. 5, no. 5, p. 172158, 2018, doi: <https://doi.org/10.1098/rsos.172158>.
- [199] J. E. Kim *et al.*, “Slot die coated planar perovskite solar cells via blowing and heating assisted one step deposition,” *Sol. Energy Mater. Sol. Cells*, vol. 179, pp. 80–86, 2018, doi: 10.1016/j.solmat.2018.02.003.

- [200] H. C. Hsieh, J. Yu, S. P. Rwei, K. F. Lin, Y. C. Shih, and L. Wang, "Ultra-compact titanium oxide prepared by ultrasonic spray pyrolysis method for planar heterojunction perovskite hybrid solar cells," *Thin Solid Films*, vol. 659, no. 2017, pp. 41–47, 2018, doi: 10.1016/j.tsf.2018.05.002.
- [201] A. T. Barrows, A. J. Pearson, C. K. Kwak, A. D. F. Dunbar, A. R. Buckley, and D. G. Lidzey, "Efficient planar heterojunction mixed-halide perovskite solar cells deposited via spray-deposition," *Energy Environ. Sci.*, vol. 7, no. 9, pp. 2944–2950, 2014, doi: 10.1039/c4ee01546k.
- [202] C. Zuo *et al.*, "Self-Assembled 2D Perovskite Layers for Efficient Printable Solar Cells," *Adv. Energy Mater.*, vol. 9, no. 4, pp. 1–9, 2019, doi: 10.1002/aenm.201803258.
- [203] S. Mastroianni *et al.*, "Towards a Sustainable Energy Future: Fully Printable Carbon-Based Perovskite Solar Cells with Overcome Charge Transport Limitation and Improved Light-Harvesting Efficiency," *Asia-Pacific Int. Conf. Perovskite, Org. Photovoltaics Optoelectron.*, 2020, doi: 10.29363/nanoge.ipero.2020.106.
- [204] L. Zhang, C. Zuo, and L. Ding, "Efficient MAPbI<sub>3</sub> solar cells made via drop-coating at room temperature," *J. Semicond.*, vol. 42, no. 7, p. 072201, 2021, doi: 10.1088/1674-4926/42/7/072201.
- [205] H. Xiao, C. Zuo, F. Liu, and L. Ding, "Drop-coating produces efficient CsPbI<sub>2</sub>Br solar cells," *Journal of Semiconductors*, vol. 42, no. 5, pp. 8–11, 2021, doi: 10.1088/1674-4926/42/5/050502.
- [206] C. Zuo *et al.*, "Crystallisation control of drop-cast quasi-2D/3D perovskite layers for efficient solar cells," *Commun. Mater.*, vol. 1, no. 1, pp. 1–10, 2020, doi: 10.1038/s43246-020-0036-z.
- [207] W. Nie *et al.*, "High-efficiency solution-processed perovskite solar cells with millimeter-scale grains," *Science (80-. )*, vol. 347, no. 6221, pp. 522–525, 2015, doi: DOI: 10.1126/science.aaa0472.
- [208] C. Zuo and L. Ding, "Drop-Casting to Make Efficient Perovskite Solar Cells under High Humidity," *Angew. Chemie*, vol. 133, no. 20, pp. 11342–11346, 2021, doi: 10.1002/ange.202101868.
- [209] A. J. Huckaba *et al.*, "Inkjet-Printed Mesoporous TiO<sub>2</sub> and Perovskite Layers for High Efficiency Perovskite Solar Cells," *Energy Technol.*, vol. 7, no. 2, pp. 317–324, 2019, doi: 10.1002/ente.201800905.
- [210] S. G. Li *et al.*, "Inkjet printing of CH<sub>3</sub>NH<sub>3</sub>PbI<sub>3</sub> on a mesoscopic TiO<sub>2</sub> film for highly efficient perovskite solar cells," *J. Mater. Chem. A*, vol. 3, no. 17, pp. 9092–9097, 2015, doi: 10.1039/c4ta05675b.
- [211] E. Tekin, H. Wijlaars, E. Holder, D. A. M. Egbe, and U. S. Schubert, "Film thickness dependency of the emission colors of PPE-PPVs in inkjet printed libraries," *J. Mater. Chem.*, vol. 16, no. 44, pp. 4294–4298, 2006, doi: 10.1039/b610996a.



- [212] B. Gao and J. Meng, "Flexible CH<sub>3</sub>NH<sub>3</sub>PbI<sub>3</sub> perovskite solar cells with high stability based on all inkjet printing," *Sol. Energy*, vol. 230, pp. 598–604, 2021, doi: 10.1016/j.solener.2021.10.072.
- [213] Z. Li *et al.*, "Ink Engineering of Inkjet Printing Perovskite," *ACS Appl. Mater. Interfaces*, vol. 12, no. 35, pp. 39082–39091, 2020, doi: 10.1021/acscami.0c09485.
- [214] Z. Wei, H. Chen, K. Yan, and S. Yang, "Inkjet printing and instant chemical transformation of a CH<sub>3</sub>NH<sub>3</sub>PbI<sub>3</sub>/nanocarbon electrode and interface for planar perovskite solar cells," *Angew. Chemie - Int. Ed.*, vol. 53, no. 48, pp. 13239–13243, 2014, doi: 10.1002/anie.201408638.
- [215] L. Wagner *et al.*, "Distinguishing crystallization stages and their influence on quantum efficiency during perovskite solar cell formation in real-time," *Sci. Rep.*, vol. 7, no. 1, pp. 1–6, 2017, doi: 10.1038/s41598-017-13855-6.
- [216] Y. C. Ho, M. N. F. Hoque, E. Stoneham, J. Warzywoda, T. Dallas, and Z. Fan, "Reduction of Oxygen Vacancy Related Traps in TiO<sub>2</sub> and the Impacts on Hybrid Perovskite Solar Cells," *J. Phys. Chem. C*, vol. 121, no. 43, pp. 23939–23946, 2017, doi: 10.1021/acs.jpcc.7b08384.
- [217] G. Liu *et al.*, "Irreversible light-soaking effect of perovskite solar cells caused by light-induced oxygen vacancies in titanium oxide," *Appl. Phys. Lett.*, vol. 111, no. 15, pp. 1–6, 2017, doi: 10.1063/1.4994085.
- [218] A. Schneider, S. Alon, and L. Etgar, "Evolution of Photovoltaic Performance in Fully Printable Mesoscopic Carbon-Based Perovskite Solar Cells," *Energy Technol.*, vol. 7, no. 7, pp. 1–9, 2019, doi: 10.1002/ente.201900481.
- [219] R. T. Ginting, M. K. Jeon, K. J. Lee, W. Y. Jin, T. W. Kim, and J. W. Kang, "Degradation mechanism of planar-perovskite solar cells: correlating evolution of iodine distribution and photocurrent hysteresis," *J. Mater. Chem. A*, vol. 5, no. 9, pp. 4527–4534, 2017, doi: 10.1039/c6ta09202k.
- [220] N. Wu, C. Shi, N. Li, Y. Wang, and M. Li, "Preparation of ZnO nanorod arrays by hydrothermal procedure and its application in perovskite solar cells," *Mater. Res. Innov.*, vol. 20, no. 5, pp. 338–342, 2016, doi: 10.1080/14328917.2016.1144247.
- [221] D. Commandeur, T. Draper, Z. T. Y. Alabdulla, R. Qian, and Q. Chen, "Dramatic Maturing Effects on All Inorganic CsPbBr<sub>3</sub> Perovskite Solar Cells under Different Storage Conditions," *J. Phys. Chem. C*, vol. 125, no. 36, pp. 19642–19652, 2021, doi: 10.1021/acs.jpcc.1c05714.
- [222] J. You *et al.*, "Moisture assisted perovskite film growth for high performance solar cells," *Appl. Phys. Lett.*, vol. 105, no. 18, p. 183902, 2014, doi: 10.1063/1.4901510.
- [223] Y. Wang *et al.*, "Encapsulation and Stability Testing of Perovskite Solar Cells for Real Life Applications," *ACS Mater. Au*, vol. 2, no. 3, pp. 215–236, 2021, doi: 10.1021/acsmaterialsau.1c00045.

- [224] R. Wang, M. Mujahid, Y. Duan, Z. K. Wang, J. Xue, and Y. Yang, "A Review of Perovskites Solar Cell Stability," *Advanced Functional Materials*, vol. 29, no. 47, p. 1808843, 2019, doi: 10.1002/adfm.201808843.
- [225] M. Aranda, C. A., Calìò, L., & Salado, "Toward Commercialization of Stable Devices : An Overview on Solar Cells," *Crystals*, vol. 11, no. 5, p. 519, 2021, doi: <https://doi.org/10.3390/cryst11050519>.
- [226] H. C. Weerasinghe, Y. Dkhissi, A. D. Scully, R. A. Caruso, and Y. B. Cheng, "Encapsulation for improving the lifetime of flexible perovskite solar cells," *Nano Energy*, vol. 18, pp. 118–125, 2015, doi: 10.1016/j.nanoen.2015.10.006.
- [227] S. Castro-Hermosa, M. Top, J. Dagar, J. Fahlteich, and T. M. Brown, "Quantifying Performance of Permeation Barrier—Encapsulation Systems for Flexible and Glass-Based Electronics and Their Application to Perovskite Solar Cells," *Adv. Electron. Mater.*, vol. 5, no. 10, pp. 1–11, 2019, doi: 10.1002/aelm.201800978.
- [228] L. Shi *et al.*, "Accelerated Lifetime Testing of Organic-Inorganic Perovskite Solar Cells Encapsulated by Polyisobutylene," *ACS Appl. Mater. Interfaces*, vol. 9, no. 30, pp. 25073–25081, 2017, doi: 10.1021/acsami.7b07625.
- [229] K. A. Bush *et al.*, "23.6%-Efficient Monolithic Perovskite/Silicon Tandem Solar Cells With Improved Stability," *Nat. Energy*, vol. 2, no. 4, pp. 1–7, 2017, doi: 10.1038/nenergy.2017.9.
- [230] H. Liu *et al.*, "Predicting the reliability of polyisobutylene seal for photovoltaic application," *Reliab. Photovolt. Cells, Modul. Components, Syst. V*, vol. 8472, p. 84720Y, 2012, doi: 10.1117/12.931240.
- [231] F. Matteocci *et al.*, "Encapsulation for long-term stability enhancement of perovskite solar cells," *Nano Energy*, vol. 30, pp. 162–172, 2016, doi: 10.1016/j.nanoen.2016.09.041.
- [232] E. Ramasamy, V. Karthikeyan, K. Rameshkumar, and G. Veerappan, "Glass-to-glass encapsulation with ultraviolet light curable epoxy edge sealing for stable perovskite solar cells," *Mater. Lett.*, vol. 250, pp. 51–54, 2019, doi: 10.1016/j.matlet.2019.04.082.
- [233] R. Cheacharoen, N. Rolston, D. Harwood, K. A. Bush, R. H. Dauskardt, and M. D. McGehee, "Design and understanding of encapsulated perovskite solar cells to withstand temperature cycling," *Energy Environ. Sci.*, vol. 11, no. 1, pp. 144–150, 2018, doi: 10.1039/c7ee02564e.
- [234] J. Li *et al.*, "Encapsulation of perovskite solar cells for enhanced stability: Structures, materials and characterization," *J. Power Sources*, vol. 485, p. 229313, 2021, doi: 10.1016/j.jpowsour.2020.229313.
- [235] M. Bonomo *et al.*, "Thermosetting Polyurethane Resins as Low-Cost, Easily Scalable, and Effective Oxygen and Moisture Barriers for Perovskite Solar Cells," *ACS Appl. Mater. Interfaces*, vol. 12, no. 49, pp. 54862–54875, 2020, doi: 10.1021/acsami.0c17652.

- [236] "ENLIGHT™ Polyolefin Back Encapsulant Composite Films –Dow® Technical paper," *Dow Chem. Co. Tech. Pap.*, pp. 1–14, 2012.
- [237] R. K. Raman, S. A. Gurusamy Thangavelu, S. Venkataraj, and A. Krishnamoorthy, "Materials, methods and strategies for encapsulation of perovskite solar cells: From past to present," *Renew. Sustain. Energy Rev.*, vol. 151, p. 111608, 2021, doi: 10.1016/j.rser.2021.111608.
- [238] Z. Huang, X. Hu, C. Liu, L. Tan, and Y. Chen, "Nucleation and Crystallization Control via Polyurethane to Enhance the Bendability of Perovskite Solar Cells with Excellent Device Performance," *Adv. Funct. Mater.*, vol. 27, no. 41, pp. 1–9, 2017, doi: 10.1002/adfm.201703061.
- [239] M. Kaltenbrunner *et al.*, "Flexible high power-per-weight perovskite solar cells with chromium oxide-metal contacts for improved stability in air," *Nat. Mater.*, vol. 14, no. 10, pp. 1032–1039, 2015, doi: 10.1038/nmat4388.
- [240] Z. Fu *et al.*, "Encapsulation of Printable Mesoscopic Perovskite Solar Cells Enables High Temperature and Long-Term Outdoor Stability," *Adv. Funct. Mater.*, vol. 29, no. 16, pp. 1–7, 2019, doi: 10.1002/adfm.201809129.
- [241] R. Cheacharoen *et al.*, "Encapsulating perovskite solar cells to withstand damp heat and thermal cycling," *Sustain. Energy Fuels*, vol. 2, no. 11, pp. 2398–2406, 2018, doi: 10.1039/c8se00250a.
- [242] G. Oreski *et al.*, "Properties and degradation behaviour of polyolefin encapsulants for photovoltaic modules," *Prog. Photovoltaics Res. Appl.*, vol. 28, no. 12, pp. 1277–1288, 2020, doi: 10.1002/pip.3323.
- [243] "ENLIGHT™ Polyolefin Back Encapsulant Composite Films," *Dow Chem. Co. Tech. Pap.*, no. Form No. 877-00334-0812 SMG, pp. 1–4.
- [244] D. A. R. Barkhouse, O. Gunawan, T. Gokmen, T. K. Todorov, and D. B. Mitzi, "Yield predictions for photovoltaic power plants: empirical validation, recent advances and remaining uncertainties," *Prog. Photovoltaics Res. Appl.*, vol. 20, no. 1, pp. 6–11, 2015, doi: 10.1002/pip.
- [245] M. V. Khenkin *et al.*, "Consensus statement for stability assessment and reporting for perovskite photovoltaics based on ISOS procedures," *Nat. Energy*, vol. 5, no. 1, pp. 35–49, 2020, doi: 10.1038/s41560-019-0529-5.
- [246] N. K. Kim *et al.*, "Investigation of Thermally Induced Degradation in CH<sub>3</sub>NH<sub>3</sub>PbI<sub>3</sub> Perovskite Solar Cells using In-situ Synchrotron Radiation Analysis," *Sci. Rep.*, vol. 7, no. 1, pp. 1–9, 2017, doi: 10.1038/s41598-017-04690-w.
- [247] F. Lang, O. Shargaieva, V. V. Brus, H. C. Neitzert, J. Rappich, and N. H. Nickel, "Influence of radiation on the properties and the stability of hybrid perovskites," *Adv. Mater.*, vol. 30, no. 3, pp. 1–22, 2018, doi: 10.1002/adma.201702905.

- [248] S. W. Lee *et al.*, “UV Degradation and Recovery of Perovskite Solar Cells,” *Sci. Rep.*, vol. 6, no. 1, pp. 1–10, 2016, doi: 10.1038/srep38150.
- [249] J. Yang, B. D. Siempelkamp, D. Liu, and T. L. Kelly, “Investigation of CH<sub>3</sub>NH<sub>3</sub>PbI<sub>3</sub> degradation rates and mechanisms in controlled humidity environments using in situ techniques,” *ACS Nano*, vol. 9, no. 2, pp. 1955–1963, 2015, doi: 10.1021/nn506864k.
- [250] M. V. Khenkin, K. M. Anoop, E. A. Katz, and I. Visoly-Fisher, “Bias-dependent degradation of various solar cells: Lessons for stability of perovskite photovoltaics,” *Energy Environ. Sci.*, vol. 12, no. 2, pp. 550–558, 2019, doi: 10.1039/c8ee03475c.
- [251] D. Bryant *et al.*, “Light and oxygen induced degradation limits the operational stability of methylammonium lead triiodide perovskite solar cells,” *Energy Environ. Sci.*, vol. 9, no. 5, pp. 1655–1660, 2016, doi: 10.1039/c6ee00409a.
- [252] M. Anaya, J. F. Galisteo-López, M. E. Calvo, J. P. Espinós, and H. Míguez, “Origin of Light-Induced Photophysical Effects in Organic Metal Halide Perovskites in the Presence of Oxygen,” *J. Phys. Chem. Lett.*, vol. 9, no. 14, pp. 3891–3896, 2018, doi: 10.1021/acs.jpcclett.8b01830.
- [253] G. Divitini, S. Cacovich, F. Matteocci, L. Cinà, A. Di Carlo, and C. Ducati, “In situ observation of heat-induced degradation of perovskite solar cells,” *Nat. Energy*, vol. 1, no. 2, pp. 1–6, 2016, doi: 10.1038/NENERGY.2015.12.
- [254] T. Malinauskas *et al.*, “Enhancing thermal stability and lifetime of solid-state dye-sensitized solar cells via molecular engineering of the hole-transporting material spiro-OMeTAD,” *ACS Appl. Mater. Interfaces*, vol. 7, no. 21, pp. 11107–11116, 2015, doi: 10.1021/am5090385.
- [255] A. Firman, M. Cáceres, A. R. González Mayans, and L. H. Vera, “Photovoltaic Qualification and Approval Tests,” *Standards*, vol. 2, no. 2, pp. 136–156, 2022, doi: 10.3390/standards2020011.
- [256] D. R. Ceratti *et al.*, “Self-Healing Inside APbBr<sub>3</sub> Halide Perovskite Crystals,” *Adv. Mater.*, vol. 30, no. 10, pp. 1–7, 2018, doi: 10.1002/adma.201706273.
- [257] W. Nie *et al.*, “Light-activated photocurrent degradation and self-healing in perovskite solar cells,” *Nat. Commun.*, vol. 7, no. 1, pp. 1–9, 2016, doi: 10.1038/ncomms11574.
- [258] T. Duong *et al.*, “Light and Electrically Induced Phase Segregation and Its Impact on the Stability of Quadruple Cation High Bandgap Perovskite Solar Cells,” *ACS Appl. Mater. Interfaces*, vol. 9, no. 32, pp. 26859–26866, 2017, doi: 10.1021/acsami.7b06816.
- [259] T. Leijtens, G. E. Eperon, S. Pathak, A. Abate, M. M. Lee, and H. J. Snaith, “Overcoming ultraviolet light instability of sensitized TiO<sub>2</sub> with meso-superstructured organometal tri-halide perovskite solar cells,” *Nat. Commun.*, vol. 4, no. 1, pp. 1–8, 2013, doi: 10.1038/ncomms3885.
- [260] M. Koehl, M. Heck, D. Philipp, K.-A. Weiss, C. Ferrara, and W. Herrmann, “Indoor and

- outdoor weathering of PV-modules,” *Reliab. Photovolt. Cells, Modul. Components, Syst.*, vol. 7048, pp. 37–44, 2008, doi: 10.1117/12.794569.
- [261] J. A. Schwenzler *et al.*, “Temperature Variation-Induced Performance Decline of Perovskite Solar Cells,” *ACS Appl. Mater. Interfaces*, vol. 10, no. 19, pp. 16390–16399, 2018, doi: 10.1021/acsami.8b01033.
- [262] C. Zhao, B. Chen, X. Qiao, L. Luan, K. Lu, and B. Hu, “Revealing Underlying Processes Involved in Light Soaking Effects and Hysteresis Phenomena in Perovskite Solar Cells,” *Adv. Energy Mater.*, vol. 5, no. 14, pp. 1–6, 2015, doi: 10.1002/aenm.201500279.
- [263] F. Huang *et al.*, “Fatigue behavior of planar CH<sub>3</sub>NH<sub>3</sub>PbI<sub>3</sub> perovskite solar cells revealed by light on/off diurnal cycling,” *Nano Energy*, vol. 27, pp. 509–514, 2016, doi: 10.1016/j.nanoen.2016.07.033.
- [264] M. Hadadian, J. H. Smått, and J. P. Correa-Baena, “The role of carbon-based materials in enhancing the stability of perovskite solar cells,” *Energy Environ. Sci.*, vol. 13, no. 5, pp. 1377–1407, 2020, doi: 10.1039/c9ee04030g.
- [265] M. Que, B. Zhang, J. Chen, X. Yin, and S. Yun, “Carbon-based electrodes for perovskite solar cells,” *Mater. Adv.*, vol. 2, no. 17, pp. 5560–5579, 2021, doi: 10.1039/d1ma00352f.
- [266] B. Honsberg, Christiana and S. Bowden, “IV Curve | PVEducation,” *PVEducation*, 2019. <https://www.pveducation.org/pvcdrom/solar-cell-operation/iv-curve>-Date Accessed: November 2022.
- [267] Z. Zhou, S. Pang, Z. Liu, H. Xu, and G. Cui, “Interface engineering for high-performance perovskite hybrid solar cells,” *J. Mater. Chem. A*, vol. 3, no. 38, pp. 19205–19217, 2015, doi: 10.1039/c5ta04340a.
- [268] I. Zarazua *et al.*, “Surface Recombination and Collection Efficiency in Perovskite Solar Cells from Impedance Analysis,” *J. Phys. Chem. Lett.*, vol. 7, no. 24, pp. 5105–5113, 2016, doi: 10.1021/acs.jpcllett.6b02193.
- [269] I. Zarazúa *et al.*, “Operating Mechanisms of Mesoscopic Perovskite Solar Cells through Impedance Spectroscopy and J-V Modeling,” *J. Phys. Chem. Lett.*, vol. 8, no. 24, pp. 6073–6079, 2017, doi: 10.1021/acs.jpcllett.7b02848.
- [270] SAYPhysics, “How to calculate band gap energy from UV-Vis reflection (DRS) data in origin,” 2021. <https://www.youtube.com/watch?v=YYVoG0030cl>-Date Accessed November 2022.
- [271] T. Wang *et al.*, “Indirect to direct bandgap transition in methylammonium lead halide perovskite,” *Energy Environ. Sci.*, vol. 10, no. 2, pp. 509–515, 2017, doi: 10.1039/c6ee03474h.
- [272] E. Planes, M. Spalla, S. Juillard, L. Perrin, and L. Flandin, “Absolute Quantification of Photo-/Electroluminescence Imaging for Solar Cells: Definition and Application to Organic and Perovskite Devices,” *ACS Appl. Electron. Mater.*, vol. 1, no. 12, pp. 2489–

- 2501, 2019, doi: 10.1021/acsaelm.9b00450.
- [273] G. S. Bumbrah and R. M. Sharma, "Raman spectroscopy – Basic principle, instrumentation and selected applications for the characterization of drugs of abuse," *Egypt. J. Forensic Sci.*, vol. 6, no. 3, pp. 209–215, 2016, doi: 10.1016/j.ejfs.2015.06.001.
- [274] K. Aitola *et al.*, "Encapsulation of commercial and emerging solar cells with focus on perovskite solar cells," *Sol. Energy*, vol. 237, pp. 264–283, 2022, doi: 10.1016/j.solener.2022.03.060.
- [275] F. Corsini and G. Griffini, "Recent progress in encapsulation strategies to enhance the stability of organometal halide perovskite solar cells," *J. Phys. Energy*, vol. 2, no. 3, p. 031002, 2020, doi: 10.1088/2515-7655/ab8774.
- [276] D. Wang, M. Wright, N. K. Elumalai, and A. Uddin, "Stability of perovskite solar cells," *Sol. Energy Mater. Sol. Cells*, vol. 147, pp. 255–275, 2016, doi: 10.1016/j.solmat.2015.12.025.
- [277] S. Jiang, K. Wang, H. Zhang, Y. Ding, and Q. Yu, "Encapsulation of PV Modules Using Ethylene Vinyl Acetate Copolymer as the Encapsulant," *Macromol. React. Eng.*, vol. 9, no. 5, pp. 522–529, 2015, doi: 10.1002/mren.201400065.
- [278] P. Holzhey and M. Saliba, "A full overview of international standards assessing the long-term stability of perovskite solar cells," *J. Mater. Chem. A*, vol. 6, no. 44, pp. 21794–21808, 2018, doi: 10.1039/C8TA06950F.
- [279] S. A. Fateev *et al.*, "Solution Processing of Methylammonium Lead Iodide Perovskite from  $\gamma$ -Butyrolactone: Crystallization Mediated by Solvation Equilibrium," *Chem. Mater.*, vol. 30, no. 15, pp. 5237–5244, 2018, doi: 10.1021/acs.chemmater.8b01906.
- [280] A. Lertngim *et al.*, "Preparation of surlyn films reinforced with cellulose nanofibres and feasibility of applying the transparent composite films for organic photovoltaic encapsulation," *R. Soc. Open Sci.*, vol. 4, no. 10, p. 170792, 2017, doi: 10.1098/rsos.170792.
- [281] G. Oreski, J. Stein, G. Eder *et al.*, "Designing New Materials for Photovoltaics: Opportunities for Lowering Cost and Increasing Performance through Advanced Material Innovations," *IEA PVPS Task 13 Performance, Oper. Reliab. Photovolt. Syst. Des.*, 2021, doi: doi:10.2172/1779380.
- [282] G. C. Eder and Y. Voronko, "Reliability testing of new Polyolefin Encapsulants and Backsheets," *Conf. 12th SOPHIA PV-Module Reliab. Work. Neuchâtel, Switz.*, 2022.
- [283] Y. Ge *et al.*, "Polyolefin Elastomer as the Anode Interfacial Layer for Improved Mechanical and Air Stabilities in Nonfullerene Solar Cells," *ACS Appl. Mater. Interfaces*, vol. 12, no. 9, pp. 10706–10716, 2020, doi: 10.1021/acsaami.9b18095.
- [284] M. S. Kim, W. Jang, S. C. Mun, B. G. Kim, and D. H. Wang, "Suppressed oxidation in organic photovoltaics via hydrogen-bonded polyurethane acrylate resin

- encapsulation,” *J. Power Sources*, vol. 528, p. 231206, 2022, doi: 10.1016/j.jpowsour.2022.231206.
- [285] T. Oku, “Crystal Structures of CH<sub>3</sub>NH<sub>3</sub>PbI<sub>3</sub> and Related Perovskite Compounds Used for Solar Cells,” *Sol. Cells - New Approaches Rev.*, vol. 1, pp. 77–92, 2015, doi: 10.5772/59284.
- [286] J. Qin *et al.*, “Enabling Self-passivation by Attaching Small Grains on Surfaces of Large Grains toward High-Performance Perovskite LEDs,” *iScience*, vol. 19, pp. 378–387, 2019, doi: 10.1016/j.isci.2019.07.044.
- [287] W. Raja *et al.*, “Photon recycling in perovskite solar cells and its impact on device design,” *Nanophotonics*, vol. 10, no. 8, pp. 2023–2042, 2021, doi: 10.1515/nanoph-2021-0067.
- [288] J. Zhao *et al.*, “Band Alignment Strategy for Printable Triple Mesoscopic Perovskite Solar Cells with Enhanced Photovoltage,” *ACS Appl. Energy Mater.*, vol. 2, no. 3, pp. 2034–2042, 2019, doi: 10.1021/acsaem.8b02104.
- [289] S. I. Ryuki Tsuji, Kenichirou Tanaka, Kota Oishi, Takaya Shioki, Seigo Ito, “Effect of Graphite and Carbon Black in Carbon Back Contacts of Carbon-based Multi-Porous-Layered-Electrode Perovskite Solar Cells (IPEROP23),” *Proc. Asia-Pacific Int. Conf. Perovskite, Org. Photovoltaics Optoelectron.*, 2023.
- [290] A. M. Mhatre, S. Chappa, S. Ojha, and A. K. Pandey, “Functionalized glass fiber membrane for extraction of iodine species,” *Sep. Sci. Technol.*, vol. 54, no. 9, pp. 1469–1477, 2019, doi: 10.1080/01496395.2018.1520729.
- [291] S. Seethamraju, A. D. Rao, P. C. Ramamurthy, and G. Madras, “Layer-by-layer assembly of Nafion on Surlyn with ultrahigh water vapor barrier,” *Langmuir*, vol. 30, no. 48, pp. 14606–14611, 2014, doi: 10.1021/la503302f.
- [292] B. C. Smith, “The Infrared Spectra of Polymers II: Polyethylene,” *Spectroscopy*, vol. 36, no. 9, pp. 24–29, 2021, [Online]. Available: <https://www.spectroscopyonline.com/view/the-infrared-spectra-of-polymers-ii-polyethylene>-Date Accessed January 2023.
- [293] L. López-Vilanova, I. Martinez, T. Corrales, and F. Catalina, “Photoreversible crosslinking of poly-(ethylene-butyl-acrylate) copolymers functionalized with coumarin chromophores using microwave methodology,” *React. Funct. Polym.*, vol. 85, pp. 28–35, 2014, doi: 10.1016/j.reactfunctpolym.2014.10.001.
- [294] H. R. Nafchi, M. Abdouss, S. K. Najafi, R. M. Gargari, and M. Mazhar, “Effects of nano-clay particles and oxidized polypropylene polymers on improvement of the thermal properties of wood plastic composite,” *Maderas Cienc. y Tecnol.*, vol. 17, no. 1, pp. 45–54, 2015, doi: 10.4067/S0718-221X2015005000005.
- [295] A. Tcharkhtchi, S. Farzaneh, S. Abdallah-Elhirtsi, B. Esmaellou, F. Nony, and A. Baron, “Thermal Aging Effect on Mechanical Properties of Polyurethane,” *Int. J. Polym. Anal.*

- Charact.*, vol. 19, no. 7, pp. 571–584, 2014, doi: 10.1080/1023666X.2014.932644.
- [296] J. M. Cauich-Rodríguez, J. V., Chan-Chan, L. H., Hernandez-Sánchez, F., & Cervantes-Uc, “Degradation of polyurethanes for cardiovascular applications,” *Adv. Biomater. Sci. Biomed. Appl.*, vol. 245, pp. 51–82, 2013, doi: 10.5772/56420.
- [297] Q. Chen *et al.*, “Controllable self-induced passivation of hybrid lead iodide perovskites toward high performance solar cells,” *Nano Lett.*, vol. 14, no. 7, pp. 4158–4163, 2014, doi: 10.1021/nl501838y.
- [298] A. Bonadio, L. S. De Oliveira, A. S. Polo, and J. A. Souza, “Liquid water-induced growth of the 1D morphology of CH<sub>3</sub>NH<sub>3</sub>PbI<sub>3</sub> hybrid perovskites,” *CrystEngComm*, vol. 21, no. 48, pp. 7365–7372, 2019, doi: 10.1039/c9ce01275c.
- [299] A. M. A. Leguy *et al.*, “Reversible hydration of CH<sub>3</sub>NH<sub>3</sub>PbI<sub>3</sub> in films, single crystals, and solar cells,” *Chem. Mater.*, vol. 27, no. 9, pp. 3397–3407, 2015, doi: 10.1021/acs.chemmater.5b00660.
- [300] M. Al Katrib, E. Planes, and L. Perrin, “Effect of Chlorine Addition on the Performance and Stability of Electrodeposited Mixed Perovskite Solar Cells,” *Chem. Mater.*, vol. 34, no. 5, pp. 2218–2230, 2022, doi: 10.1021/acs.chemmater.1c04021.
- [301] T. Ye *et al.*, “Efficient and Ambient-Air-Stable Solar Cell with Highly Oriented 2D@3D Perovskites,” *Adv. Funct. Mater.*, vol. 28, no. 30, pp. 1–8, 2018, doi: 10.1002/adfm.201801654.
- [302] M. Al Katrib, L. Perrin, and E. Planes, “Optimizing Perovskite Solar Cell Architecture in Multistep Routes Including Electrodeposition,” *ACS Appl. Energy Mater.*, vol. 5, no. 4, pp. 4461–4474, 2022, doi: 10.1021/acsaem.1c04063.
- [303] M. A. Green and A. Ho-Baillie, “Perovskite Solar Cells: The Birth of a New Era in Photovoltaics,” *ACS Energy Lett.*, vol. 2, no. 4, pp. 822–830, 2017, doi: 10.1021/acsenergylett.7b00137.
- [304] M. Kim *et al.*, “Methylammonium Chloride Induces Intermediate Phase Stabilization for Efficient Perovskite Solar Cells,” *Joule*, vol. 3, no. 9, pp. 2179–2192, 2019, doi: 10.1016/j.joule.2019.06.014.
- [305] D. Zhao *et al.*, “Four-Terminal All-Perovskite Tandem Solar Cells Achieving Power Conversion Efficiencies Exceeding 23%,” *ACS Energy Lett.*, vol. 3, no. 2, pp. 305–306, 2018, doi: 10.1021/acsenergylett.7b01287.
- [306] Z. El Jouad *et al.*, “Ca/Alq<sub>3</sub> hybrid cathode buffer layer for the optimization of organic solar cells based on a planar heterojunction,” *J. Phys. Chem. Solids*, vol. 98, pp. 128–135, 2016, doi: 10.1016/j.jpcs.2016.06.014.
- [307] J. Kim *et al.*, “Overcoming the Challenges of Large-Area High-Efficiency Perovskite Solar Cells,” *ACS Energy Lett.*, vol. 2, no. 9, pp. 1978–1984, 2017, doi: 10.1021/acsenergylett.7b00573.



- [308] M. Mujahid, C. Chen, W. Hu, Z. K. Wang, and Y. Duan, "Progress of High-Throughput and Low-Cost Flexible Perovskite Solar Cells," *Sol. RRL*, vol. 4, no. 8, p. 1900556, 2020, doi: 10.1002/solr.201900556.
- [309] N. G. Park, "Perovskite solar cells: An emerging photovoltaic technology," *Mater. Today*, vol. 18, no. 2, pp. 65–72, 2015, doi: 10.1016/j.mattod.2014.07.007.
- [310] M. E. Kayesh *et al.*, "Coadditive Engineering with 5-Ammonium Valeric Acid Iodide for Efficient and Stable Sn Perovskite Solar Cells," *ACS Energy Lett.*, vol. 4, no. 1, pp. 278–284, 2019, doi: 10.1021/acseenergylett.8b02216.
- [311] A. Q. Alanazi *et al.*, "Atomic-Level Microstructure of Efficient Formamidinium-Based Perovskite Solar Cells Stabilized by 5-Ammonium Valeric Acid Iodide Revealed by Multinuclear and Two-Dimensional Solid-State NMR," *J. Am. Chem. Soc.*, vol. 141, no. 44, pp. 17659–17669, 2019, doi: 10.1021/jacs.9b07381.
- [312] M. Bidikoudi, C. Simal, V. Dracopoulos, and E. Stathatos, "Exploring the effect of ammonium iodide salts employed in multication perovskite solar cells with a carbon electrode," *Molecules*, vol. 26, no. 19, p. 5737, 2021, doi: 10.3390/molecules26195737.
- [313] N. Wei *et al.*, "5-Ammonium Valeric Acid Iodide to Stabilize MAPbI<sub>3</sub> via a Mixed-Cation Perovskite with Reduced Dimension," *J. Phys. Chem. Lett.*, vol. 11, no. 19, pp. 8170–8176, 2020, doi: 10.1021/acs.jpcclett.0c02528.
- [314] R. Lu, Y. Liu, J. Zhang, D. Zhao, X. Guo, and C. Li, "Highly efficient (200) oriented MAPbI<sub>3</sub> perovskite solar cells," *Chem. Eng. J.*, vol. 433, p. 133845, 2022, doi: 10.1016/j.cej.2021.133845.
- [315] M. Spalla, L. Perrin, E. Planes, M. Matheron, S. Berson, and L. Flandin, "Effect of the Hole Transporting/Active Layer Interface on the Perovskite Solar Cell Stability," *ACS Appl. Energy Mater.*, vol. 3, no. 4, pp. 3282–3292, 2020, doi: 10.1021/acsaem.9b02281.
- [316] M. Spalla, E. Planes, L. Perrin, M. Matheron, S. Berson, and L. Flandin, "Alternative Electron Transport Layer Based on Al-Doped ZnO and SnO<sub>2</sub> for Perovskite Solar Cells: Impact on Microstructure and Stability," *ACS Appl. Energy Mater.*, vol. 2, no. 10, pp. 7183–7195, 2019, doi: 10.1021/acsaem.9b01160.
- [317] A. Karavioti, E. Vitoratos, and E. Stathatos, "Improved performance and stability of hole-conductor-free mesoporous perovskite solar cell with new amino-acid iodide cations," *J. Mater. Sci. Mater. Electron.*, vol. 31, no. 8, pp. 6109–6117, 2020, doi: 10.1007/s10854-020-03164-6.
- [318] A. Pockett, D. Raptis, S. M. P. Meroni, J. Baker, T. Watson, and M. Carnie, "Origin of Exceptionally Slow Light Soaking Effect in Mesoporous Carbon Perovskite Solar Cells with AVA Additive," *J. Phys. Chem. C*, vol. 123, no. 18, pp. 11414–11421, 2019, doi: 10.1021/acs.jpcc.9b01058.
- [319] J. Bing, S. Huang, and A. W. Y. Ho-Baillie, "A Review on Halide Perovskite Film Formation by Sequential Solution Processing for Solar Cell Applications," *Energy Technol.*, vol. 8,

no. 4, pp. 1–22, 2020, doi: 10.1002/ente.201901114.

- [320] Y. Tian and I. G. Scheblykin, “Artifacts in absorption measurements of organometal halide perovskite materials: What are the real spectra?,” *J. Phys. Chem. Lett.*, vol. 6, no. 13, pp. 3466–3470, 2015, doi: 10.1021/acs.jpcclett.5b01406.
- [321] F. Liu *et al.*, “Is Excess PbI<sub>2</sub> Beneficial for Perovskite Solar Cell Performance?,” *Adv. Energy Mater.*, vol. 6, no. 7, pp. 1–9, 2016, doi: 10.1002/aenm.201502206.
- [322] M. Lubas, J. J. Jasinski, M. Sitarz, L. Kurpaska, P. Podsiad, and J. Jasinski, “Raman spectroscopy of TiO<sub>2</sub> thin films formed by hybrid treatment for biomedical applications,” *Spectrochim. Acta - Part A Mol. Biomol. Spectrosc.*, vol. 133, pp. 867–871, 2014, doi: 10.1016/j.saa.2014.05.045.
- [323] S. M. Jain *et al.*, “Vapor phase conversion of PbI<sub>2</sub> to CH<sub>3</sub>NH<sub>3</sub>PbI<sub>3</sub>: Spectroscopic evidence for formation of an intermediate phase,” *J. Mater. Chem. A*, vol. 4, no. 7, pp. 2630–2642, 2016, doi: 10.1039/c5ta08745g.
- [324] P. Selvarajan, G. Chandra, S. Bhattacharya, S. Sil, A. Vinu, and S. Umapathy, “Potential of Raman spectroscopy towards understanding structures of carbon-based materials and perovskites,” *Emergent Mater.*, vol. 2, no. 4, pp. 417–439, 2019, doi: 10.1007/s42247-019-00052-6.
- [325] A. Guerrero *et al.*, “Properties of Contact and Bulk Impedances in Hybrid Lead Halide Perovskite Solar Cells Including Inductive Loop Elements,” *J. Phys. Chem. C*, vol. 120, no. 15, pp. 8023–8032, 2016, doi: 10.1021/acs.jpcc.6b01728.
- [326] B. Suarez, V. Gonzalez-Pedro, T. S. Ripolles, R. S. Sanchez, L. Otero, and I. Mora-Sero, “Recombination study of combined halides (Cl, Br, I) perovskite solar cells,” *J. Phys. Chem. Lett.*, vol. 5, no. 10, pp. 1628–1635, 2014, doi: 10.1021/jz5006797.
- [327] L. Contreras-Bernal *et al.*, “Impedance analysis of perovskite solar cells: A case study,” *J. Mater. Chem. A*, vol. 7, no. 19, pp. 12191–12200, 2019, doi: 10.1039/c9ta02808k.
- [328] Y. Cheng *et al.*, “Revealing the Degradation and Self-Healing Mechanisms in Perovskite Solar Cells by Sub-Bandgap External Quantum Efficiency Spectroscopy,” *Adv. Mater.*, vol. 33, no. 3, pp. 1–9, 2021, doi: 10.1002/adma.202006170.

## Etude des mécanismes de maturation et de dégradation au sein des cellules solaires pérovskites à base carbone

Récemment, les matériaux pérovskites hybrides organométalliques ont connu une progression dans les applications des cellules solaires. Grâce à leurs propriétés particulièrement intéressantes : bande interdite modulable, cristallinité élevée, capacité de transport de charge élevée et efficacité élevée en couches minces, ces matériaux ont le potentiel de dépasser les limites de performance des technologies actuelles. Parmi les structures de dispositifs alternatives, les cellules solaires pérovskite à base de carbone semblent très prometteuses en raison de leur faible coût et de leurs matériaux abondamment disponibles ( $\text{TiO}_2$ ,  $\text{ZrO}_2$ , poudre noire de carbone et de graphite), de méthodes de fabrication évolutives rentables et de la grande stabilité inhérente. Une solution de pérovskite  $(\text{CH}_3\text{NH}_3)_x(\text{AVA})_{1-x}\text{PbI}_3$  (avec l'additif AVA = acide valérique d'ammonium) a été ajoutée par pipette ou par la méthode d'impression jet d'encre pour infiltrer les couches mp- $\text{TiO}_2$ /mp- $\text{ZrO}_2$  à travers une épaisse couche de carbone poreuse. Afin de révéler leurs performances photovoltaïques maximales, ces cellules doivent d'abord être maturées sous humidité et température. Cette étape dure environ 100-150 h et améliore les performances de la cellule. Dans cette thèse, les deux méthodes d'infiltration ont été comparées en utilisant des cellules avant et après maturation afin de mettre en évidence le rôle de cette étape sur les performances des cellules. Pour mieux étudier la stabilité de ces cellules, des campagnes de vieillissement à une température de 85°C et une humidité relative de 85% ont été menées. De plus, de nombreuses campagnes de vieillissement ont également été réalisées avec différents systèmes d'encapsulation tels qu'un joint en ionomère Surlyn, un film en ionomère Surlyn, une polyoléfine élastomère, un polyuréthane thermoplastique, un film multicouche de polyoléfine et finalement l'addition d'un joint périphérique en polyisobutylène. Ces encapsulants ont été utilisés afin de limiter la perméation de l'humidité jusqu'aux cellules solaires, ce qui induirait une dégradation accélérée. Grâce à des techniques de caractérisation dédiées telles que les mesures J(V), les performances PV ont été évaluées. Avec les mesures de courant induit par faisceau laser (LBIC) et l'imagerie par photoluminescence, les performances locales ont été corrélées à l'inhomogénéité de la dégradation. Les modifications de la couche de pérovskite ont été enfin évaluées avec d'autres techniques plus courantes (diffraction des rayons X, absorption UV-visible et spectroscopie de photoluminescence).

Mots-clés : Pérovskites, cellules solaires, maturation, stabilité, systèmes d'encapsulation, dégradation

## Study of the mechanisms of maturation and degradation within carbon-based perovskite solar cells

Recently, organometallic hybrid perovskite materials are experiencing a real progress for solar cell applications. Due to particularly interesting properties: adaptable band gap, high crystallinity, high charge transport capacity and high thin film efficiency, these materials have the potential to exceed the performance limits of current technologies. Among alternative device structures, carbon-based perovskite solar cells look highly promising due to their low cost and abundantly available materials ( $\text{TiO}_2$ ,  $\text{ZrO}_2$ , carbon black and graphite powders), cost-efficient scalable fabrication methods and their inherent high stability. A one step  $(\text{CH}_3\text{NH}_3)_x(\text{AVA})_{1-x}\text{PbI}_3$  perovskite solution (with AVA= ammonium valeric acid, as additive) was added by pipetting or by inkjet printing method to infiltrate mp- $\text{TiO}_2$ /mp- $\text{ZrO}_2$  through a thick porous carbon layer. In order to reveal their maximum photovoltaic performance, these devices should be first matured under humidity and temperature. This step lasts of approximately 100-150 h and improves the cell's performance. In this thesis, the two infiltration methods were compared using cells before and after maturation in order to highlight the role of this step on the cells' performance. To further investigate their stability, aging campaigns at damp heat conditions 85°C/85%RH have been conducted. Moreover, many aging campaigns were also realized using different encapsulation systems such as a Surlyn ionomer gasket, a Surlyn film, a polyolefin elastomer, a polyurethane thermoplastic, a multilayered polyolefin and finally with the addition of a polyisobutylene external gasket. These sealants were used to limit the humidity permeation up to solar cells which would induce an acceleration of devices degradation. Thanks to dedicated characterization techniques such as J(V) measurements, the PV performance were evaluated. With laser beam induced current (LBIC) measurements and photoluminescence imaging, the local performances have been correlated to the degradation inhomogeneity. Finally, the modifications of the perovskite layer have been evaluated with others more common techniques (X-Ray diffraction, UV-visible absorption and photoluminescence spectroscopy).

Keywords: Perovskite, solar cell, maturation, stability, encapsulation systems, degradation